

Study of non-radiative decay processes in weakly bound systems using post Hartree-Fock methods

by

Ravi Kumar
10CC18A26018

A thesis submitted to the
Academy of Scientific and Innovative Research
for the award of the degree of
DOCTOR OF PHILOSOPHY
in
SCIENCE

Under the supervision of
Dr. Nayana Vaval



CSIR-National Chemical Laboratory, Pune



Academy of Scientific and Innovative Research
AcSIR Headquarters, CSIR-HRDC campus
Sector 19, Kamla Nehru Nagar,
Ghaziabad, U.P. - 201002, India

November 2023

Certificate

This is to certify that the work incorporated in this Ph.D. thesis entitled, “Study of non-radiative decay processes in weakly bound systems using post Hartree-Fock methods,” submitted by Ravi Kumar to the Academy of Scientific and Innovative Research (AcSIR), in fulfillment of the requirements for the award of the Degree of Doctor of Philosophy in Science, embodies original research work carried-out by the student. We further certify that this work has not been submitted to any other University or Institution in part or full for the award of any degree or diploma. Research material(s) obtained from other source(s) and used in this research work has/have been duly acknowledged in the thesis. Image(s), illustration(s), figure(s), table(s), etc., used in the thesis from other source(s) have also been duly cited and acknowledged.



Ravi Kumar

(Signature of Student)

31st October, 2023



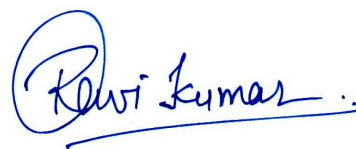
Dr. Nayana Vaval

(Signature of Supervisor)

31st October, 2023

STATEMENTS OF ACADEMIC INTEGRITY

I, Ravi Kumar, a Ph.D. student of the Academy of Scientific and Innovative Research (Ac-SIR) with Registration No. 10CC18A26018, hereby undertake that the thesis entitled "Study of non-radiative decay processes in weakly bound systems using post Hartree-Fock methods" has been prepared by me and that the document reports original work carried out by me and is free of any plagiarism in compliance with the UGC Regulations on "Promotion of Academic Integrity and Prevention of Plagiarism in Higher Educational Institutions (2018)" and the CSIR Guidelines for "Ethics in Research and in Governance (2020)".



Signature of Student

Date: **31st October, 2023**

Place: CSIR-NCL, Pune

It is hereby certified that the work done by the student, under my/our supervision, is plagiarism-free in accordance with the UGC Regulations on "*Promotion of Academic Integrity and Prevention of Plagiarism in Higher Educational Institutions (2018)*" and the CSIR Guidelines for "*Ethics in Research and in Governance (2020)*".

NA

**Signature of Co
-supervisor**

Name:

Date:

Place:



Signature of Supervisor

Name: Dr. Nayana Vaval

Date: **31st October, 2023**

Place: CSIR-NCL, Pune

**This thesis is dedicated to my parents for
their endless love, support, and
inspiration.**

The love and support of parents can turn a child's
ordinary abilities into extraordinary achievements.

- Brad Henry

Acknowledgement

I want to express my sincere gratitude to everyone who has contributed to completing this thesis in the field of quantum chemistry.

First and foremost, I am deeply thankful to my advisor, Dr. Nayana Vaval, for her unwavering guidance, support, and motivation throughout this academic odyssey. Her meticulous training in problem definition, critical thinking, scientific analysis, paper writing, and presentation skills have honed my technical and intellectual abilities. I am profoundly grateful for her expertise and the flexibility she provided, allowing me to work seamlessly from both home and the lab. This support has been pivotal in shaping my research pursuits. Our discussions, whether in formal meetings or casual encounters within the academic corridors and in the canteen, have been intellectually stimulating and enriched my Ph.D. experience. I also thank the esteemed members of my doctoral advisory committee (DAC) - Dr. Sailaja Krishnamurty, Dr. Kumar Vanka, and Dr. N. Y. Kadoo (Chairperson) – for their consistent evaluation of my research endeavors and invaluable suggestions offered during each DAC meeting.

I am grateful to my seniors, Dr. Aryya Ghosh (from Ashoka University), Dr. Turbasu Sengupta, Dr. Achintya Kumar Datta (from IIT-Bombay), and others for helping me to overcome computational challenges. I am also grateful to Dr. Sailja Krishnamuty (CSIR-NCL) and Dr. Mudit Dixit (CSIR-CLRI) for their invaluable assistance in crafting my research proposal. I also acknowledge Andreas M. Köster (deMon2k software developer) for helping

me with the BOMD simulation issue, which helps me finish my fourth article. I also thank Lorenz S. Cederbaum (Heidelberg University) for his invaluable comments and corrections to my first article.

I acknowledge the Council of Scientific and Industrial Research (CSIR), India, for their generous research fellowship and the Director of CSIR-National Chemical Laboratory, Pune, for providing essential research infrastructure. Additionally, I am grateful to the Academy of Scientific & Innovative Research (AcSIR) for their consistent administrative support, which has been invaluable to my academic pursuit.

I appreciate the support from Amit Naglekar, Soumya Ranjan Dash (Motu), Dr. Vipin Raj K, Himanshu Sharma, Asha Kiran Maibam, Sheena Aggarwal, Dr. Mohammed Ghadiyali, Dr. Sweta Mehta, Siddharth Ghule, Jignesh Dhumal, Trideep C., Minal Bhalerao and other colleagues from various labs of MSM building. Their diverse perspectives and collective efforts have helped me during my Ph.D. journey and enriched my understanding of quantum chemistry. I am grateful for the invaluable advice and companionship of Minal Bhalerao and Amit Naglekar, who have been constant guides in navigating life's decisions and sharing memorable adventures.

Contents

Contents	vi
List of Figures	x
List of Tables	xiv
1 An Overview of Various Non-Radiative Decay Processes and Ab-Initio Methods	1
1.1 Introduction	1
1.2 Non Radiative Decay processes (NRDP)	2
1.2.1 Auger Decay	3
1.2.2 Interatomic or Intermolecular Coulombic Decay (ICD)	5
1.2.3 Electron Transfer Mediated Decay (ETMD)	8
1.2.4 Other Non Radiative Decay Processes	11
1.3 Temporary Bound state (TBS)	13
1.4 Applications of Temporary Bound states formed during non-radiative decay processes	14
1.5 Electronic structure methods	15
1.5.1 Hartree Fock methods	16
1.5.2 Electron Correlation	22
1.5.3 Size Consistency and Size extensivity	23

1.5.4	Configuration Interaction (CI)	24
1.5.5	Perturbation Theory (PT)	27
1.5.6	Coupled Cluster (CC) methods	31
1.6	Equation of Motion Coupled cluster (EOM-CC) Method	36
1.7	Challenges of Temporary Bound State (TBS) & its solutions	39
1.7.1	Complex Absorbing Potential (CAP) Method	41
1.7.2	Complex Scaling Method	44
1.7.3	Fano Theory for decay width	45
2	Decay Processes in Cationic Alkali Metals in Microsolvated Clusters: A Complex Absorbing Potential Based Equation-of-Motion Coupled Cluster Investigation	48
2.1	Abstract	48
2.2	Introduction	49
2.3	Theory	52
2.3.1	Complex absorbing potential based equation-of-motion coupled cluster	52
2.4	Results and discussion	56
2.4.1	Choice of basis set for ETMD process of 1s state of Li^+ in $\text{Li}^+\text{-H}_2\text{O}$.	57
2.4.2	Effect of different molecular environments on the ETMD process . .	58
2.4.3	Li^+ -water clusters: Effect of the increasing number of water molecules in surrounding on the ETMD process	60
2.4.4	Na^+ -water cluster: Effect of distance and increasing number of water molecules on the ICD process	61
2.4.5	Auger Decay process for the 2s and 2p ionized states of K in K^+ -water	64
2.4.6	Polarized Surrounding effect on ETMD and ICD	66
2.5	Conclusions	66
3	Effect of Protonation and Deprotonation on Electron Transfer Mediated Decay	

and Interatomic Coulombic Decay	69
3.1 Abstract	70
3.2 Introduction	70
3.3 Theory and Computational Details	73
3.4 Results and Discussion	75
3.4.1 Effect of protonation and deprotonation on the IP and DIP	76
3.4.2 Effect of protonation and deprotonation on the lifetime of Li-1s and O-2s/N-2s TBSs in LiH-H ₂ O and LiH-NH ₃	81
3.5 Conclusion	86
4 Effect of Charge and Solvation Shell on Non-Radiative Decay Processes in s- Block Cationic Metal Ion Water Clusters	88
4.1 Abstract	89
4.2 Introduction	89
4.3 Computational Methods	92
4.3.1 Fano approach for decay width	92
4.4 Results and Discussion	93
4.4.1 Cluster geometries and basis set	93
4.4.2 Solvation shell's effect on IP and DIP of Na ⁺ -(H ₂ O) ₁₋₅ and Mg ²⁺ - (H ₂ O) ₁₋₅ clusters	97
4.4.3 Solvation shell's effect on lifetimes of Na-2s and Mg-2s TBSs	101
4.5 Conclusions	108
5 Intermolecular Coulombic Decay in Water Dimer: Electronic versus Nuclear Motion	110
5.1 Abstract	111
5.2 Introduction	112
5.3 Theory	114

5.3.1	Born-Oppenheimer Molecular Dynamics	114
5.3.2	Complex Absorbing Potential (CAP)	115
5.3.3	Equation of Motion Coupled Cluster Singles and Doubles (EOM- CCSD) Methods for Ionization Potential	117
5.3.4	Computational details	119
5.4	Results and Discussion	120
5.4.1	IP and DIP of PDMW and PAWM in a water dimer	120
5.4.2	Decay width of PDMW and PAWM in a water dimer	124
6	Summary and Future Scope	128
6.1	Future scope	134
	Bibliography	135

List of Figures

1.1	Auger Decay.	4
1.2	Intermolecular or Interatomic Coulombic Decay (ICD).	6
1.3	Electron Transfer Mediated Decay (ETMD): 2 and 3 in ETMD(2) and ETMD(3) represent the number of molecules involved during the process.	10
1.4	Types of Resonant ICD - Participator ICD and Spectator ICD.	12
2.1	Various non-radiative decay processes: 1a Auger decay, 1b ICD, both 1c and 1d ETMD processes. 3 and 2 represent the number of atoms in 1c and 1d, respectively.	52
2.2	a) Orientation of lone pair in $\text{Li}^+\text{-NH}_3$ is toward Li atom, making electron transfer easier, hence a shorter lifetime. b) The direction of the lone pair in $\text{Li}^+\text{-H}_2\text{O}$ is perpendicular to the molecular plane, making electron transfer difficult and, thus, a more significant lifetime. The above picture is generated for isosurface value 0.02 eA^{-3} . Atom colour code Pink: Lithium, Blue: Nitrogen, Red: Oxygen, and White: Hydrogen.	59
2.3	Effect of the increased number of surrounding water molecules on ETMD process using an aug-cc-pVDZ basis set.	62
2.4	Effect of bond length on ICD process for the 2s state of Na in $\text{Na}^+\text{-H}_2\text{O}$ using maug-cc-pV(T+d)Z basis set.	63

-
- 3.1 Visual representation of electronic decay processes. (1a.) In ETMD(2), an inner valence vacancy is filled by an outer valence electron of the neighboring molecule B, and another valence electron is emitted from the same molecule B, leaving a final AB^{2+} molecular state. (1b.) ICD, a valence electron from molecule A, fills the vacancy, and the released energy is transferred to an outer valence electron of neighboring molecule B. Thus forming A^+B^+ as the final state. (1c.) ETMD(3) process in which the vacancy in molecule A is filled by an outer valence electron of the neighboring molecule B, and ejection of the second electron occurs from another adjacent molecule C, leaving AB^+C^+ as the final state. The number 2 and 3 represents the number of molecules involved in the ETMD process. 72
- 3.2 The IPs of neutral LiH-H₂O and its deprotonated and protonated species. The smaller black line denotes the lowest DIP value. The structure of the respective system is shown on the right of each panel. Atom color code : Red: Oxygen, Pink: Lithium, and White: Hydrogen. 76
- 3.3 The IPs of deprotonated, protonated, and neutral LiH-NH₃. The smaller black line denotes the lowest DIP value. The structure of the respective system is shown on the right of each panel. Atom color code : Blue: Nitrogen, Pink: Lithium, and White: Hydrogen. 77
- 3.4 a and b show HOMO and LUMO in Li⁻-NH₃. c shows HOMO and LUMO are together in one picture in Li⁻-NH₃. d shows the same for Li⁻-H₂O. This figure (c and d) demonstrates these orbitals partially overlap in space. Images are generated for 0.02 eÅ⁻³ isosurface value. Atom color code:- Blue: Nitrogen, Red: Oxygen, Pink: Lithium, and White: Hydrogen. 80

-
- 3.5 a, b, and c show the partially overlapping in space between Li-1s orbital and the lone pair orbital of oxygen/nitrogen, which are perpendicular to the molecular axis in LiH-H₂O, LiH-OH⁻, and LiH-NH₂⁻, respectively. It shows that the orbital's partial overlapping in space increases from LiH-H₂O to LiH-OH⁻. Images are generated for 0.02 eÅ⁻³ isosurface value. Atom color code-: Red: Oxygen, Pink: Lithium, Blue: Nitrogen, and White: Hydrogen. 82
- 4.1 Geometries of the first and second solvation shells of Na⁺-(H₂O)_{n=1-5} and Mg²⁺-(H₂O)₁₊₁ clusters. Atom colour code Yellow: Magnesium, Violet: Sodium, Red: Oxygen, and White: Hydrogen. 95
- 4.2 Geometries of the first (shown by a) and second solvation shells (shown by b) for n=2 in Na⁺-(H₂O)_n clusters. c shows the geometry-A, formed by changing the O-Na bond distances of the first solvation shell structures. The O-Na bond lengths of geometry-A are equal to those in the second solvation shell structure. A decay width (or lifetime) comparison between a and c provides the effect of bond length on decay width. In contrast, comparing b and c offers the impact of position on decay width. A decay width comparison among these geometries helps us understand what affects the lifetime of Na-2s TBS more: the O-Na bond length or the position of the water molecule. Atom colour code Violet: Sodium, Red: Oxygen, and White: Hydrogen. 104

-
- 5.1 Single and double ionization potentials of water dimer along the proton transfer coordinates. These coordinates are taken from geometry obtained during the BOMD simulation when vacancy was generated in the O-2s orbital of a proton-donating water molecule (PDWM). The $2a_1$ state's IP of PDWM has been calculated using CASPT2 (15,8) and an aug-cc-pVTZ basis set, represented by a solid red line. All DIPs have been computed using state-averaged (SA-15) CASPT2(14,8) and an aug-cc-pVTZ basis set. Dashed lines of different colors show DIPs corresponding to different ICD channels. The letters S and T represent the singlet and triplet states, respectively. 121
- 5.2 Single and Double ionization potentials of water dimer along the O-O bond coordinates. All DIPs belong to the ICD channels. The coordinates are taken from geometry obtained during the BOMD simulation when vacancy was generated in the O-2s orbital of a proton-accepting water molecule. In this case, no proton transfer occurs. The IP of $2a_1$ state of accepting water has been calculated using CASPT2 (15,8) and an aug-cc-pVTZ basis set, represented by a solid violet line. All DIPs have been computed using state-averaged (SA-15) CASPT2(14,8) and an aug-cc-pVTZ basis set. Dashed lines of different colors show DIPs corresponding to different ICD channels. The letters S and T represent the singlet and triplet states, respectively. 123
- 5.3 η trajectory for the $2a_1$ ionized state of proton-accepting water in the ground state geometry of a water dimer calculated using CAP-EOM-CCSD/ aug-cc-pVTZ+[1s1p1d] level of theory. 124
- 5.4 η trajectory for the $2a_1$ ionized state of proton-donating water in the ground state geometry of a water dimer calculated using CAP-EOM-CCSD/ aug-cc-pVTZ+[1s1p1d] level of theory. 125

List of Tables

1.1	Name of truncated Coupled Cluster methods	36
1.2	Various types of Complex Absorbing Potentials	44
2.1	Effect of variation of basis set on decay width of the Li 1s state in Li ⁺ -H ₂ O for ETMD process	57
2.2	Effect of different molecular surroundings on ETMD process for Li 1s state in Li ⁺ -H ₂ O and Li ⁺ -NH ₃ using aug-cc-pVTZ+1f basis set.	59
2.3	Different decay process in different systems: Auger decay in K ⁺ -H ₂ O, ICD in Na ⁺ -(H ₂ O) _n and ETMD in Li ⁺ -(H ₂ O) _n (where n=1,2).	64
2.4	Polarization effect on decay width in ETMD and ICD processes for X ⁺ -H ₂ O system (X = Li, Na).	66
3.1	Energetic position of the decaying state and the decay width after Li-1s and O-2s ionization of LiH-H ₂ O along with its protonated and deprotonated sys- tems.	82
3.2	Energetic position of the decaying state and the decay width after Li-1s and N-2s ionization of LiH-NH ₃ along with its protonated and deprotonated sys- tems.	85

4.1	It shows the ionization potentials (IP) of Na-2s and Na-2p and the lowest double ionization potential (DIP) in $\text{Na}^+(\text{H}_2\text{O})_n$ $n=1,5$ clusters. All the values are in eV.	99
4.2	It shows the ionization potentials (IP) of Mg-2s and Mg-2p and the lowest double ionization potential (DIP) in $\text{Mg}^{2+}(\text{H}_2\text{O})_n$ $n=1,5$ clusters. All the values are in eV.	100
4.3	Shows the total decay width due to ICD and ETMD processes and the total lifetime of Na-2s TBS in $\text{Na}^+(\text{H}_2\text{O})_n$; $n=1,5$ clusters.	102
4.4	Shows the total decay width due to ICD and ETMD processes and the total lifetime of Mg-2s TBS in $\text{Mg}^{2+}(\text{H}_2\text{O})_n$; $n=1,5$ clusters.	103
4.5	Partial decay widths (for ICD and ETMD) of Na-2s ionized state in various geometries (see figure 4.2) of $\text{Na}^+(\text{H}_2\text{O})_n$ clusters for $n=2$	107

Acronyms

Acronym	Meaning
ADC	Algebraic Diagrammatic Construction
AES	Auger Electron Spectroscopy
BOMD	Born-Oppenheimer Molecular Dynamics
BOA	Born Oppenheimer Approximation
CAP	Complex Absorbing Potential
CAS	Complete Active Space
CC	Coupled Cluster
CCSD	Coupled Cluster Singles and Doubles
CI	Configuration Interaction
CK	Coster-Kronig
CT	Charge Transfer
DIP	Double Ionization Potential
DFT	Density Functional Theory
ENC	Effective Nuclear Charge
EOM-CCSD	Equation of Motion Coupled Cluster Singles and Doubles
ETMD	Electron Transfer Mediated Decay
eV	Electron Volt
fs	Femtosecond(s)
HF	Hartree-Fock
HOMO	Highest Occupied Molecular Orbital

Acronym	Meaning
ICD	Interatomic or Intermolecular Coulombic Decay
IP	Ionization Potential
KE	Kinetic energy
LEE	Low Energy Electrons
LUMO	Lowest Unoccupied Molecular Orbital
MO	Molecular Orbital
MPPT or MP	Møller-Plesset Perturbation Theory
MRCC	Multi-Reference Coupled Cluster
MS-CASPT2	Multi-State Complete-Active-Space Second-Order Perturbation Theory
NBO	Natural Bond Order
NRDP	Non Radiative Decay Process(es)
OE	Self Consistent Field
SCK	Super Coster-Kronig
TBS	Temporary Bound State
Z	Atomic Number
1h	1 Hole Configurations
2h1p	2-Hole 1-Particle Configurations

Chapter 1

An Overview of Various Non-Radiative Decay Processes and Ab-Initio Methods

1.1 Introduction

When a molecule absorbs a photon, it enters an electronically excited or ionized state. The relaxation of an excited molecule involves transitioning from an excited/ionized state to a lower energy state; it could either be an ionized or ground state. There are a few ways for an excited molecule to lose its energy. It can emit a photon, convert excess energy into heat through vibrational relaxation, emit an electron (ionization), or undergo some chemical reaction. However, the relaxation processes can be divided into two main categories: radiative decay and non-radiative decay processes (NRDP). Radiative decay involves the emission of a photon (of a lower energy or longer wavelength than the absorbed photon) as the excited molecule returns to its ground state. Depending on the spin characteristics of the excited state, this process is known as fluorescence or phosphorescence. Fluorescence occurs within nanoseconds, while phosphorescence takes longer (microseconds to minutes). Non-radiative decay processes do not involve the emission of a photon. Instead, the excess energy of the excited molecule is dissipated in other ways, such as through vibrational relaxation, colli-

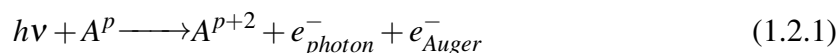
sional quenching, or emitting an electron. It is a much faster process than the radiative decay process and usually takes place at femtosecond or less. NRDP involves energy transfer to the solvent or another molecule. The study of non-radiative decay processes is essential for many reasons. It can help improve optoelectronic devices' efficiency, enhance the photostability of materials, optimize materials, understand energy transfer processes, explore chemical and biological systems, and advance fundamental scientific knowledge. Here are some specific examples of how the study of non-radiative decay processes is essential: (a.) In optoelectronics, non-radiative decay processes can limit the efficiency of solar cells and LEDs. By understanding and controlling non-radiative decay pathways, researchers can improve energy conversion efficiency.^{1,2} (b.) In materials science, NRDP can lead to the degradation of materials. By studying these pathways, researchers can develop strategies to enhance the photostability of materials, ensuring their long-term functionality under light exposure.³ (c.) In chemistry, NRDP can play a role in photochemical reactions. Researchers can unravel complex reaction mechanisms and explore reaction pathways by studying these processes.⁴ (d.) Studying NRDP can reveal the role of excited states in chemical and biological systems.^{5,6} Researchers can develop strategies to control and manipulate the relaxation pathways by understanding the underlying mechanisms and factors.

1.2 Non Radiative Decay processes (NRDP)

Many non-radiative decay processes (NRDP) exist that are stimulated by different energies of light. We are interested in X-ray-induced types of non-radiative decay processes. Most non-radiative decay processes (X-ray-induced) can be understood in three parts: ionization, relaxation, and ejection of a secondary electron. The final state formed in most decay processes is a 2-hole state. The location of these 2-hole (2h) states varies from process to process. These processes are also known as the autoionization process⁷ because, during these processes, the system ionizes itself without absorbing energy from outside the system.

1.2.1 Auger Decay

Auger decay was observed by Lise Meitner⁸ and Pierre Auger⁹ independently. In Auger decay,¹⁰⁻¹⁴ an electron from core orbitals of a chemical species A gets ejected upon X-rays or high energy electron bombardment. This creates a hole/vacancy in the core orbitals of the chemical species. The valance electron then fulfills this vacancy by emitting a virtual photon. This virtual photon again ejects an electron from the valance shells of the chemical species. The secondary ejected electron is known as an "auger electron". The A^{2+} type of state (2-hole) is formed after Auger decay. As illustrated in figure-1.1 and given as



This equation's importance comes into the picture to calculate the kinetic energy (KE) of Auger electrons. Computationally, the KE of Auger electrons can be calculated using the orbital energies (OE) with the given equation 1.2.2. It provides a rough estimate because it neglects many other factors, like the contributions from coulomb repulsion between two holes in a chemical species.

$$KE_{\text{Auger-e}^-} \approx OE_{\text{core}} - OE_{1\text{st-hole}} - OE_{2\text{nd-hole}} \quad (1.2.2)$$

An application of Auger decay is Auger Electron Spectroscopy (AES). Here, KE of Auger electrons identify elements and provides information about their chemical environment. AES helps analyze the composition, thickness, and bonding of thin films, nanoparticles, and nanostructures.¹⁵⁻¹⁷ This knowledge is essential for understanding the properties and behavior of materials at the nanoscale. AES also determines the concentration of impurities or dopants in semiconductors, which are necessary for electrical conductivity¹⁸ in semiconductors.¹⁹⁻²¹ This information is vital for optimizing device performance and ensuring the reliability of semiconductor devices. Also, help to understand corrosion pattern and depth.^{22,23} These are a few examples based on the application of Auger decay. The Coster-Kronig and Super

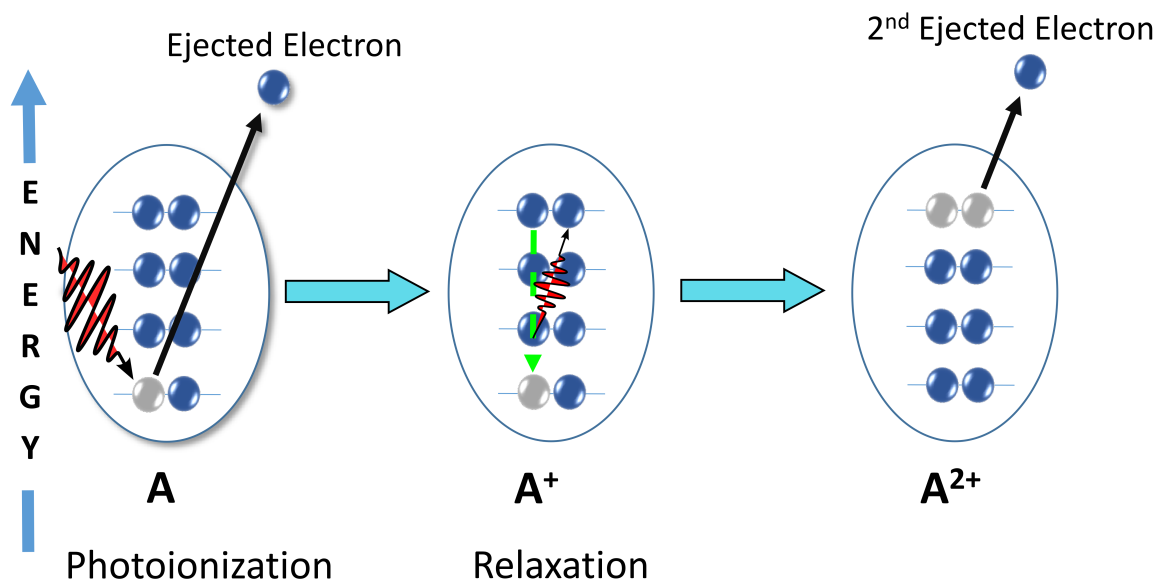


Figure 1.1: Auger Decay.

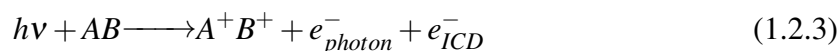
Coster-Kronig decays are special types of Auger decay processes.^{24–26} If the initial vacancy in Auger decay is filled by an electron of a higher subshell within the same shell, the process is known as Coster-Kronig (CK). Suppose the second electron (Auger electron) ejection also occurs from any higher subshell of the same shell where the initial vacancy has been generated. It means both holes are present in the same shell. In that case, it is said to be the Super Coster-Kronig (SCK). It has been observed that CK and SCK occur in chemical systems if an element's atomic number (Z) is higher than 30. Even though for $Z > 30$, the probability of CK and SCK's occurring is lesser than Auger decay. Auger decay only starts appearing in higher principal quantum number shells²⁷ for $Z > 30$ because a single vacancy in core orbitals (1s) will lead to a cascade effect^{28,29} than Auger decay. In the cascade effect, a new vacancy is created in a higher-lying orbital once a core vacancy is filled. This new vacancy is promptly filled by transitions from even higher orbitals, and the process continues. Here, the system continuously relaxes by filling the previously empty orbital while generating new vacancies in higher orbitals. A single vacancy in the K shell can result in hundreds of potential transitions for high- Z elements. Each transition leads to the emission of X-rays or electrons, contributing to the rich emission spectrum (X-ray fluorescence spectra) associated with these

elements.

Auger decay is a local or intra-molecular decay, meaning that it does not affect the environment. However, variables like temperature³⁰ and others^{31–34} can affect this decay. Contrasting to the Auger decay, some processes can be affected by their surroundings, and the environment can influence and modulate their occurrence. In the following discussion, I will discuss these non-local NRDP.

1.2.2 Interatomic or Intermolecular Coulombic Decay (ICD)

The Interatomic or Intermolecular Coulombic Decay (ICD) process^{35–38} is a non-local decay process that occurs in the chemical environment. So, it is highly dependent on the presence of neighboring molecules, and the decay process becomes faster as the number of molecules in the surroundings increases.³⁹ This makes ICD a sensitive tool for understanding the chemical environment. Like Auger decay, ICD begins in a molecule (named molecule-A) when high-energy electrons or X-rays create a vacancy in an inner shell. A valence electron from the same molecule can fill this hole by emitting a virtual photon. This virtual photon then ejects a secondary electron from a neighboring molecule B. As a result, a two-centered two-hole species (A^+B^+ type) is formed. The +1 charge on each molecule leads to a Coulomb explosion, causing the molecules to move apart. Because of this coulomb repulsion, this process gets its name Interatomic or Intermolecular Coulombic Decay (ICD). The second ejected electron, known as the ICD electron, typically has an energy of a few electron volts. ICD is illustrated in Figure-1.2. Note A and B could be atoms or molecules that depend on the system. For example, in the Neon dimers system, A and B are atoms; for sodium ions in water, one is an atom, and the other a molecule; for water dimer systems, both A and B will be molecules. ICD can be described in an equation form as



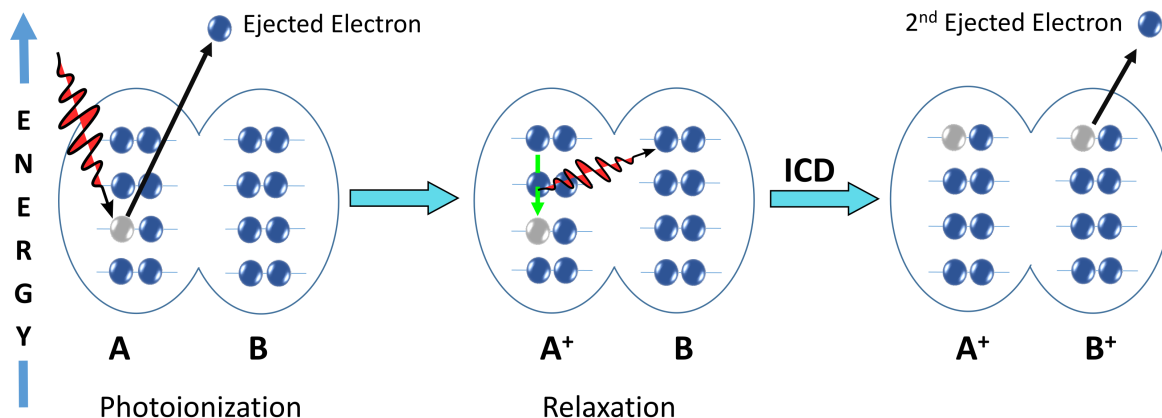


Figure 1.2: Intermolecular or Interatomic Coulombic Decay (ICD).

There are a few differences between ICD and Auger decay. The first difference is that Auger decay is a local process, which means it won't involve the neighboring atom/molecule. In other words, it is a process of a single atom or molecule, while ICD is non-local, which means it involves neighboring atoms or molecules and is a two atoms or two-molecule process. The initial vacancy formed in Auger decay involves the core orbitals, while in ICD, the orbital involves non-core orbitals. If you see it at the atomic level, it is usually a $2s$ atomic orbital (inner valance shell). Third, an ejected secondary electron's kinetic energy is very high, making it easy to detect. In contrast, in the ICD process, these electrons have low energy, which makes these non-local non-radiative processes hard to detect. It took ten years to notice non-local processes experimentally after the theoretical prediction of these processes. It's important to note that the distinction between Auger and ICD processes goes beyond the kinetic energies of the emitted electrons. These processes differ in their underlying mechanisms and dynamics. Auger decay involves the rearrangement of electrons within an atom or molecule, while ICD occurs through electron transfer between neighboring atoms or molecules. If Auger decay is energetically feasible, it will be the dominant decay channel over ICD decay. However, if there is a surrounding and the distance between molecule A and molecule B is less, ICD can be the dominant decay channel. This is because ICD requires spatial overlap between the excited atom or molecule and neighboring atoms or molecules. The presence of nearby atoms or molecules with appropriate energy levels and spatial prox-

imity is necessary for efficient energy transfer through ICD.

ICD is a general and usual way of relaxation in nature since every molecule is a neighbor of other molecules in nature. Due to this neighborhood, ICD generates two separate holes present on two different chemical species. It lowers the DIP values of the system by lessening the coulomb repulsion between these two holes. At the same time, there is no such neighbor in Auger decay. Therefore, this is another reason for the dominance of ICDs in nature over Auger decay. ICD has been explored extensively from both theoretical^{40–46} and experimental^{39,47–50} angles. Its existence was first³⁵ theoretically predicted by Cederbaum et al. in 1997, using hydrogen bonding systems. Subsequently, experimental evidence^{47,48} supported the existence of ICD. Various theoretical methods have been developed to study ICD in different systems. For instance, Santra et al.⁵¹ introduced the CAP/CI approach to analyze the ICD rate in small hydrogen-bonded systems. They discovered that ICD happens rapidly in (HF)₂, taking just femtoseconds. It has also been established that mixed hydrogen-bonded clusters like HF(H₂O)₂ include ICD.⁵⁰

In the past 25 years, thousands of articles have been published on ICD. It is not feasible to discuss each article individually. Therefore, reading review articles is the best way to explore past work on ICD. Until now, several important review articles have been written on ICD, each focusing on different aspects of the topic. Let's take a brief look at each of these articles. First, Hergenbahn's articles^{52,53} summarize the early ICD experimental research. They talk about experiments on ICD in rare gas clusters, cascade ICD followed by Auger decay, and ICD of satellite states. They have mostly focused on rare gas clusters but also studied the first experiment on water clusters. Next, Jahnke⁵⁴ looked at the experimental ICD research that followed Hergenbahn's work. Jahnke also talked about ICD's importance in biological systems and how it might harm these systems through radiation. Then, Santra and Cederbaum gave an early summary of the theory behind ICD in 2002.⁴² Additionally, in 2009, Dias⁵⁵ provided a short review of changes made to the way we understand the energy distribution of electrons emitted during ICD decay. In 2011, Averbukh and colleagues⁵⁶

reviewed more recent theoretical researches on ICD in singly and multiply ionized clusters. Following that, Frühling et al.⁵⁷ offered a brief overview of advancements in the time domain facets of ICD in a 2015 article. They focused on summarizing experiments that have become achievable thanks to the advances in free-electron lasers. In 2020, Jahnke's⁵⁸ most recent work encompassed a comprehensive review of more than 500 articles. This review includes the theoretical approaches for explaining ICD, ICD-like or similar decay processes, and discusses the experimental methods developed and utilized to investigate it. In each chapter, we'll talk about different studies that have been conducted on the topic of this thesis.

1.2.3 Electron Transfer Mediated Decay (ETMD)

Like ICD, electron transfer-mediated decay (ETMD)⁵⁹⁻⁶³ is also a non-local, non-radiative decay process affected by its environment. In the ETMD process, molecule-A's initial inner valance vacancy is filled by an electron of neighboring molecule B. This vacancy-filling process emits a virtual photon or excess energy that ejects a second electron from either the lending molecule B or another nearby molecule C. If this extra energy removes the second electron from molecule B, we call it ETMD(2). If it knocks out an electron from the neighboring molecule C, it's ETMD(3).⁶⁴ The numbers 2 and 3 show how many molecules are involved during the process. The final doubly ionized (or two holes) states in ETMD(2) and ETMD(3) processes are AB^{2+} and AB^+C^+ types, respectively. Check the mentioned equation form or Figure-1.3 to understand the ETMD process more clearly.



ETMD is slower compared to ICD for two main reasons. First, ICD is driven by energy transfer that occurs faster than the electron transfer process in ETMD. Second, because of less repulsion between charges in ICD, the doubly ionized state in ICD is more stable than in

ETMD. This extra stability in ICD makes it even faster. This is why we usually observe less lifetime for ICD than ETMD.⁵⁹ The way non-radiative decay processes differ is in the way they create two-hole or doubly ionized states. In Auger decay, two holes are localized on the same initial molecule from where the process initially started. In ICD, one hole is localized on the neighboring molecule, and the other is on the initial molecule. In ETMD, holes are not located on the initial molecule; instead, they are located on neighboring molecules. It means an initial molecule that remains neutral in the ETMD process. One of the advantages is that it can neutralize an ion's charge.⁶⁵ Normally, when excited ions need to return to a neutral state, charge transfer is assumed to be the route. This involves the ion becoming neutral by swapping an electron with a neighboring particle. This process occurs if the potential curves^{66,67} of the ion's charged state and the charge transfer state intersect. Alternatively, when no notable curve intersection is present, the neutralization follows Radiative Charge Transfer (RCT), which generally happens at the nano-second timeframe. In contrast, the ETMD process doesn't require any movement of atomic nuclei to neutralize the ion. ETMD's primary driving factor is the interaction between electrons, unlike charge transfer decays, which involve coupling with the electromagnetic field. Consequently, the energy involved in ETMD is much higher than in charge transfer (CT) decay, contributing to its significantly faster nature.

The concept of ETMD was initially introduced for Neon-Argon dimers by Zobeley et al.⁵⁹ In their study, they presented ETMD as an alternative to ICD and found that, for that specific system, ETMD was about 10^4 times less efficient than ICD. However, as the distance between molecules becomes smaller, the importance of ETMD increases. ICD is only about ten times more efficient at short distances than ETMD. It means the ETMD efficiency increases as bond distance decreases. Therefore, ETMD is highly affected by nuclear dynamics. This I have shown in Chapter 5. The reason behind the lower efficiency of ETMD than ICD lies in the fact that electron transfer relies heavily on the overlapping of orbitals. In contrast, ICD's efficiency follows a dependency of R^{-6} (where R is the distance between nuclei) and does

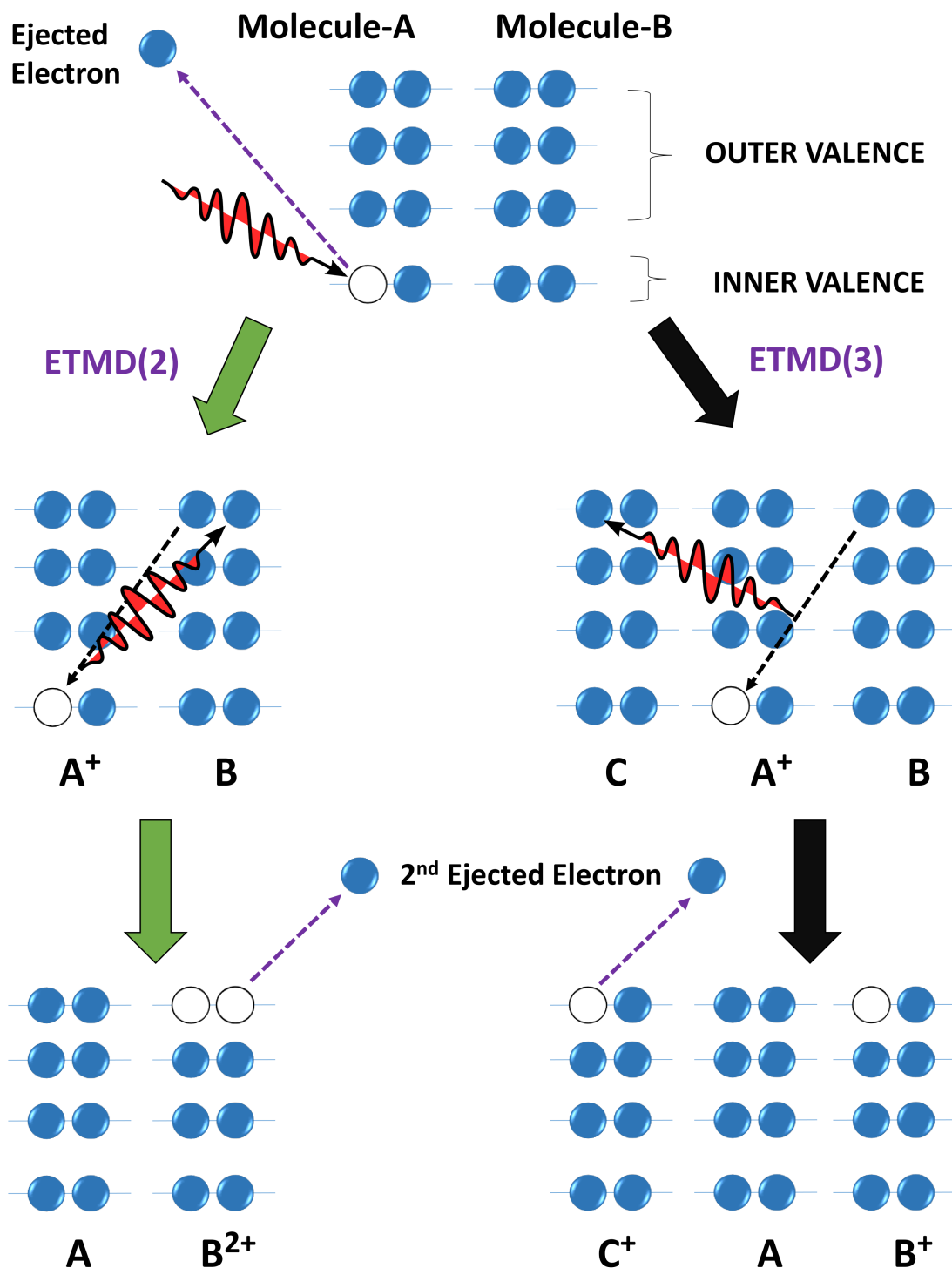


Figure 1.3: Electron Transfer Mediated Decay (ETMD): 2 and 3 in ETMD(2) and ETMD(3) represent the number of molecules involved during the process.

not require orbital overlap.

Now, you might be wondering when ETMD will become the dominant process. ETMD becomes the main process in two situations: first, when our system has certain chemicals like He, Li⁺,⁶⁸⁻⁷¹ Be²⁺ which don't have extra valence electrons to fill a respective atom's (He/Li/Be) 1s hole. Second, when the AB²⁺ DIP is lower than A⁺B⁺ DIP, like what happens with an Ar atom's 3s vacancy in a group of Kr-Ar-Kr atoms.⁷² ETMD process is also frequent in Auger-ETMD cascade decay.^{29,65}

1.2.4 Other Non Radiative Decay Processes

Our primary focus will be the study of ICD and ETMD processes, which I have already described. However, there are many more different types of non-radiative decay processes⁵⁸ that I will explain without going too much in-depth. When a molecule absorbs a photon, it can either be excited to a higher energy state or ionized. In ICD, molecules get ionized. However, in the case of **Resonant ICD (RICD)**,⁷³⁻⁷⁵ the molecule becomes excited, causing an inner valence electron to occupy an unoccupied orbital. The RICD process can be divided into two main categories: **spectator Resonant ICD** and **participator Resonant ICD**. The categorization is based on whether the excited electrons are directly involved in the ICD process. Check figure-1.4 for more clarity. In **participator RICD**, the excited electron gets de-excited and fills the inner valence vacancy created by its excitation in molecule A. The extra energy is transferred to a neighboring molecule B and leads to its ionization. The final state of participator RICD is of AB⁺ type. For **spectator RICD**, the scenario is different. In this case, a non-excited electron of molecule A fills the inner valence vacancy. The excess energy is then passed on to a neighboring unit (molecule B), causing it to eject an outer valence electron. Consequently, the final state of spectator RICD is characterized by two outer valence holes positioned on two different parts of the system, like ICD. However, the initial molecule remains in the excited state. The excited electrons observe the whole process

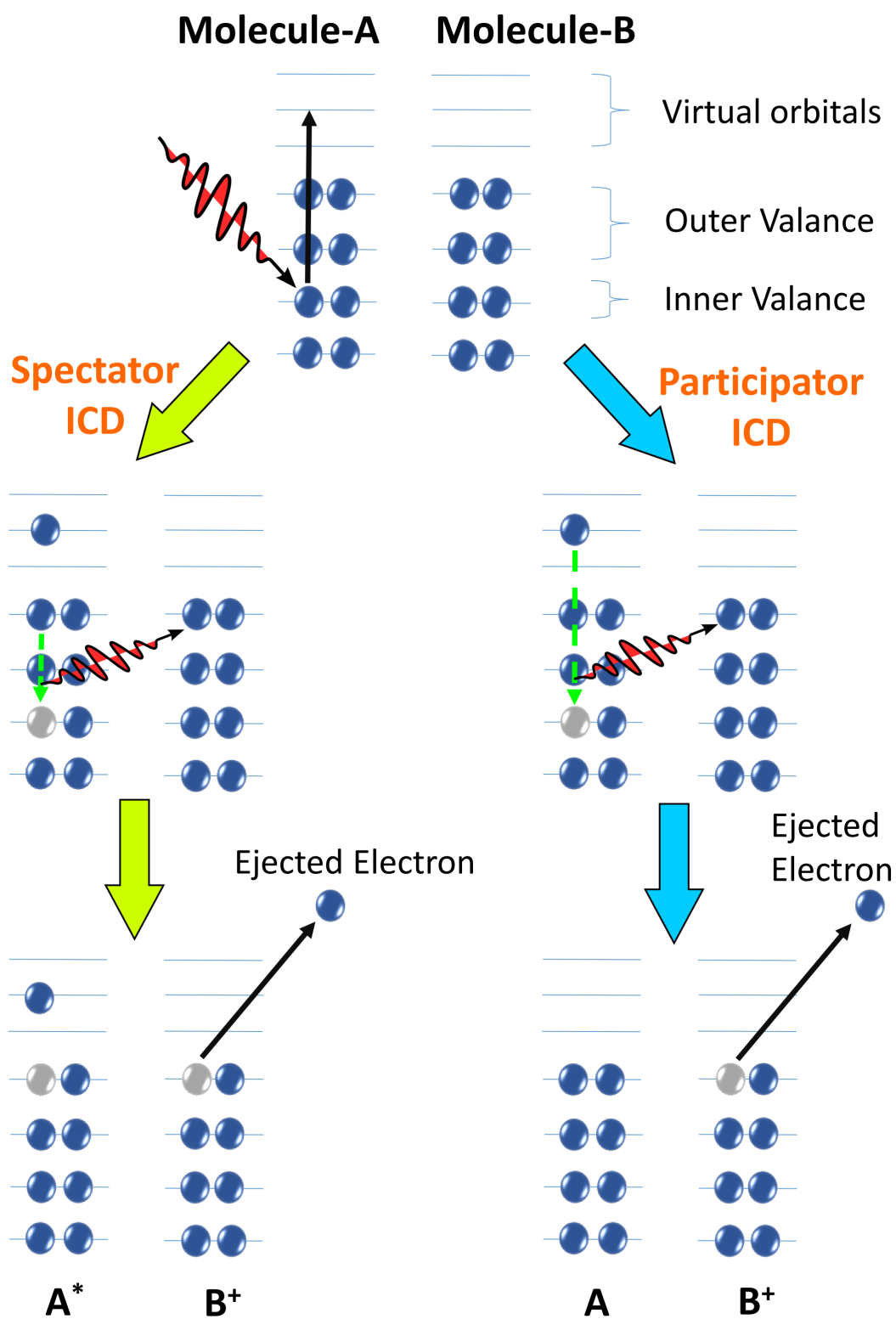


Figure 1.4: Types of Resonant ICD - Participator ICD and Spectator ICD.

as a spectator.



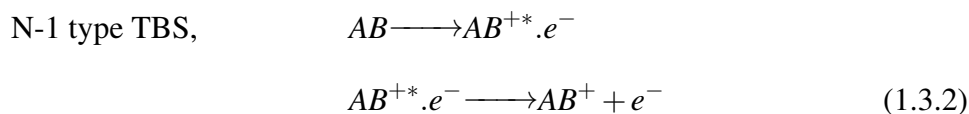
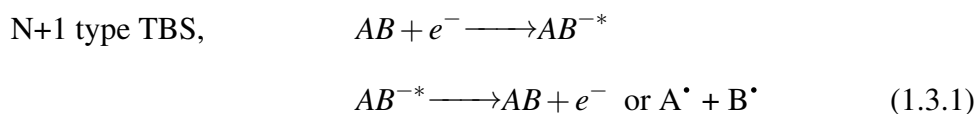
Resonant ICD processes were initially discovered by Barth et al.⁷³ in extensive Neon clusters. Further investigations into various forms of RICD were conducted by Gokhberg et al., who focused on Ne(2s \rightarrow 3p) excitation within MgNe clusters.⁷⁵ The Magnesium atom is an ideal neighbor for Neon due to its low thresholds for single and double ionization, which are comparable to the inner-valence IP of Neon.

1.3 Temporary Bound state (TBS)

Temporary bound states (TBS), also known as virtual or resonance states, possess characteristics resembling bound states but are inherently short-lived. These states emerge when particles or fields interact in quantum systems, resulting in a temporary binding effect. While their energy levels closely resemble those of stable bound states, they are not stable due to their proximity to the continuum. Consequently, they possess finite lifetimes (in femtosecond timescale or less) and can quickly decay upon encountering perturbations. TBSs are associated with resonance phenomena because they arise when the energy of the incoming particle matches that of an intermediate configuration in a quantum system. These resonant energy matchings lead to enhanced interactions, affecting processes like scattering, energy transfer, and ionization and providing valuable information regarding the behavior of particles and systems. TBSs play a crucial role in determining the probability and dynamics of electron ejection. TBSs are also significant in understanding the behavior of particles in strong external fields, such as interactions with intense laser pulses. Furthermore, TBSs are relevant to understanding nuclear reactions and decay processes in nuclear physics. They help describe

how particles and nuclei interact and transform in various nuclear processes. In other words, TBS are also formed during non-radiative decay processes.

Let's understand the concept of TBS with an example. Imagine an AB molecule and a free electron that becomes associated with the AB molecule and forms an attached state (TBS) referred to as AB^{-*} . This N+1 type of TBS is formed during a process known as resonance. On the other hand, the N-1 type of TBS is formed during non-radiative decay processes, where ejected electrons, which are now in a continuum, can be considered attached to the N-1 molecular system.



1.4 Applications of Temporary Bound states formed during non-radiative decay processes

We are aware that non-radiative decay processes generate low-energy free electrons, which can create reactive oxygen species⁷⁶ or free radicals within the human body. This poses significant health risks. These free radicals are known to cause DNA damage,⁷⁷⁻⁸³ first highlighted by Sanchez and coworkers' research.⁷⁷ A few published articles demonstrated the breakage of a DNA strand⁸⁴⁻⁹⁰ using a free electron of very low^{91,92} (1.8 eV) energy. Now, you may wonder about the underlying mechanism of electron involvement and entering into small biomolecular systems. Datta and his coworkers⁹³ present a novel perspective on this matter, where they discussed the interplay between dipole bound and valance bound states in Cytosine-Guanine (GC pair) and Adenine-Thymine (AT) DNA base pairs leads to the transfer of an electron into the small biomolecular system.

Additionally, free electrons can act as catalysts in various applications.^{94–100} One such instance is shown by J. Richard Wagner, where dissociation occurs in a neutral dissociative manner.⁹² Daly Davis’s article offers more insights if you’re curious about the neutral dissociative^{94–99} than non-neutral dissociative^{101–104} approaches. The exciting thing is that both types of dissociations take place only after a generation of TBS. Beyond catalysis, TBSs play a pivotal role in exploring diverse domains. They facilitate the investigation of plasma, multi-photon processes, and even interstellar chemistries, underscoring their significance in a broader scientific context.

1.5 Electronic structure methods

Computational chemistry is an emerging field. It has become a crucial tool for researchers in various areas of chemistry, offering insights that are often difficult to obtain through traditional experimental methods alone. For example, it can predict molecular properties, reaction mechanisms, and material behaviors. It has revolutionized the fields like drug discovery, materials science, catalysis, and many more. Computational chemistry employs quantum mechanical and molecular dynamics simulations to understand the interactions of molecules with biological systems. It also aids in designing efficient catalysts, understanding complex biological processes, predicting spectra, and analyzing environmental impacts. However, you can only get good results once you are fully aware of the method used to get the results. However, the results of computational chemistry simulations can only be as good as the method and the level of theory used. It is essential to be aware of these factors when interpreting the results of a computational chemistry study. Let’s understand the various theories used to predict molecular properties in brief.

1.5.1 Hartree Fock methods

In computational chemistry, everything begins with optimizing the structure and finding its energy. In chemistry, scientists are interested in the energy difference. We need more accurate calculated energy to get a good energy difference. The first attempt to find the energy for a molecular system was made by two scientists named Douglas Hartree and Vladimir Fock using Hartree-Fock theory.¹⁰⁵⁻¹⁰⁸ To get the energy, we must solve the time-independent Schrödinger wave equation ($H\Psi = E\Psi$). H is the Hamiltonian operator, and Ψ is the system's wave function. For any molecular system, H is a sum of five terms:

- Kinetic energy (KE) of electrons $\left[- \sum_{i=1}^n \hbar^2 \cdot \nabla_{r_i} / 2m_i \right]$
- KE of the nucleus $\left[- \sum_{A=1}^M \hbar^2 \cdot \nabla_{R_A} / 2M_A \right]$
- Electron-nucleus attraction $\left[- \sum_{i=1}^n \sum_{A=1}^M Z_A / r_{iA} \right]$
- Nucleus-nucleus repulsion $\left[\sum_{A=1}^M \sum_{B>A}^M Z_A Z_B / \vec{R}_{AB} \right]$
- Electron-electron repulsion $\left[\sum_{i=1}^n \sum_{j>i}^n 1 / r_i - r_j \right]$

The first two terms define the system's KE, whereas the last three terms contribute to potential energy. By applying the Born Oppenheimer approximation (BOA), we can simplify our definition of Hamiltonian by eliminating the second and fourth terms. BOA says the nucleus's mass is way larger than an electron's. Therefore, the nuclear motion does not affect the electronic motions for a specific geometry. After BOA implementation, the Hamiltonian only contains the first, third, and fifth terms and can be defined as

$$\hat{H}_{elec} = \sum_{i=1}^n \frac{\hbar^2 \cdot \nabla_{r_i}}{2m_i} + \sum_{i=1}^n \sum_{A=1}^M \frac{Z_A}{r_i - \vec{R}_A} + \sum_{i=1}^n \sum_{j>i}^n \frac{1}{r_i - r_j} \quad (1.5.1)$$

The Hamiltonian now has only the electronic part. Equation 1.5.1 can also be written as

$$\hat{H}_{\text{elec}} = \sum_{i=1}^n h(i) + \sum_{i=1}^n \sum_{j>i}^n \frac{1}{|\vec{r}_i - \vec{r}_j|} \quad (1.5.2)$$

Where $h(i)$ is a 1-electron operator, and $1/|\vec{r}_i - \vec{r}_j|$ is a two-electron operator. Let's look at the wave function description for the electronic part. We know that electrons cannot be defined by space coordinates alone. We must include the spin part in the wave function to define electrons completely. A spin orbital ($\chi_i(x)$) is an orbital that has both space ($\Psi_i(r)$) and spin parts [$\alpha(\omega)$ or $\beta(\omega)$] and where $x = (r, \omega)$. A wave function for an electron can then be written as $\chi(x) = \Psi(r)\alpha(\omega)$ or $\Psi(r)\beta(\omega)$.

Before discussing the actual situation, let's imagine a hypothetical system where electrons do not interact. It means the two-electron term is zero. Let's call this system a non-interacting system. Then equation 1.5.2 will become

$$\hat{H}_{\text{elec}} = \sum_{i=1}^n h(i) = h(1) + h(2) + \dots + h(n). \quad (1.5.3)$$

To get the energy, we need to solve $\hat{H}_{\text{elec}}\Psi = E_{\text{elec}}\Psi$ for the non-interacting system. For that, we must know the form of Ψ . Hartree proposed a form of a wavefunction for N electronic system known as Hartree-product wavefunction (Ψ^{HP}), which can be written as

$$\Psi_{HP}(x_1, x_2, \dots, x_n) = \chi_1(x_1) \cdot \chi_2(x_2) \cdot \dots \cdot \chi_n(x_n). \quad (1.5.4)$$

The energy of the non-interacting system is found to be the sum of the individual energy of each electron and can be written as

$$E_{\text{elec}} = \epsilon_1 + \epsilon_2 + \dots + \epsilon_n. \quad (1.5.5)$$

According to the above equation 1.5.4, the definition of Hartree product wavefunction (Ψ^{HP}) tells that electron-one occupies the spin-orbital χ_i , electron-two occupies the spin-orbital χ_j , and so on. We know the probability of finding an electron is the square of the wavefunction. Based on equation 1.5.4, the probability can be defined as:

$$|\Psi^{HP}(x_1, x_2, \dots, x_n)|^2 \cdot dx_1, dx_2, \dots, dx_n = |\chi_i(x_1)|^2 dx_1 \cdot |\chi_j(x_2)|^2 dx_2 \dots |\chi_m(x_n)|^2 dx_n. \quad (1.5.6)$$

This tells us that the probability of finding electron-one in the volume element dx_1 , electron-two in dx_2 , etc., is equal to the product of the probabilities of the individual electrons in their respective volume elements. This means that the probability of finding electron-one at a given point in space is independent of the position of electron-two when the Hartree product wavefunction is used. However, in reality, the motion of electrons is correlated. Electron-one will be repelled by electron-two, and vice versa. Each electron will also avoid the space occupied by other electrons. This is one problem with the Hartree product wavefunction. We can ignore this point for now since we are discussing the non-interacting system. Another problem is that it treats electrons as distinguishable particles. In reality, we cannot distinguish between any two electrons. We must introduce antisymmetry to the wavefunction to address the indistinguishability of electrons. A wavefunction is considered antisymmetric if the interchange of the position of two electrons changes the wavefunction's sign. For example, a wavefunction $\Psi(x_1, x_2, x_3, x_4)$ is antisymmetric if $\Psi(x_1, x_2, x_3, x_4) = -\Psi(x_1, x_4, x_3, x_2)$. Mathematically, antisymmetry can be introduced to the wavefunction by writing it in a determinant form. Slater did this, and the wavefunction can be written in Slater determinant form

as:

$$\Psi(x_1, x_2, \dots, x_N) = \frac{1}{\sqrt{N!}} \begin{vmatrix} \chi_1(x_1) & \chi_2(x_1) & \dots & \chi_N(x_1) \\ \chi_1(x_2) & \chi_2(x_2) & \dots & \chi_N(x_2) \\ \vdots & \vdots & \ddots & \vdots \\ \chi_1(x_N) & \chi_2(x_N) & \dots & \chi_N(x_N) \end{vmatrix} \quad (1.5.7)$$

In short, A Slater determinant is a wavefunction that is the product of one-electron wavefunctions with the antisymmetry principle applied, which also accounts for the indistinguishability of electrons. Slater determinant also ensures that no two electrons occupy the same spin orbitals. If this occurs, two columns of the determinant become equal, making the determinant's value zero. Therefore, no more than 1 electron with the same spin can occupy the same spin-orbital, which is the Pauli Exclusion Principle. A Slater determinant is a wavefunction that is the product of one-electron wavefunctions with the antisymmetry principle applied. The one-electron wavefunctions in the Slater determinant are called orbitals. We choose these orbitals to be orthonormal, meaning they are orthogonal to each other.

A Slater determinant is the exact form of a wavefunction for a non-interaction system. But for interacting systems, a single Slater determinant will not be the exact form of a wavefunction because the electron-electron repulsion term is another problem to consider. Two electron term is the electron's influence on each other's behavior due to their motion within a molecule, making it necessary to calculate the electron correlation energy, which accounts for the potential energy resulting from the mutual influence of electrons. Hartree and Fock propose a mean-field approximation to tackle this problem (two electron terms). In this approximation, Hartree and Fock assume that the electrons in a molecule can be treated as independent particles, and each electron moves in an average field or mean-field (V_{HF}) created by all other electrons. It means that each electron is treated as if it were stationary and experiences the potential created by the average field of all the other N-1 electrons. After the

Hartree-Fock approximation, the form of Hamiltonian (equation) changes to

$$\text{for 1 electron} \quad f(i) = h(i) + \sum_{j=1}^n V_{\text{HF}}(x_j)$$

OR

$$\text{for n electrons} \quad \sum_{i=1}^n f(i) = \sum_{i=1}^n h(i) + \sum_{i=1}^n \sum_{j=1}^n V_{\text{HF}}(x_j) \quad (1.5.8)$$

Where

$$V_{\text{HF}}(x_j) = \sum_{j \neq i}^n J_j(x_i) + \sum_{j \neq i}^n K_j(x_i) \quad (1.5.9)$$

$$J_j(x_1)\chi_i(x_1) = \int [\chi_j^*(x_2) \cdot \frac{1}{\vec{r}_i - \vec{r}_j} \chi_j(x_2) dx_2] \chi_i(x_1) \quad (1.5.10)$$

$$K_j(x_1)\chi_i(x_1) = \int [\chi_j^*(x_2) \cdot \frac{1}{\vec{r}_i - \vec{r}_j} \chi_i(x_2) dx_2] \chi_j(x_1) \quad (1.5.11)$$

They called this modified \hat{H}_{elec} an effective one-electron Fock operator [f(i)]. The expectation value of electronic energy can be calculated as

$$f(i)\chi_i(x_i) = \epsilon_i\chi_i(x_i) \quad (1.5.12)$$

The first step in the Self Consistent Field (SCF) procedure is to make an initial guess about the molecular orbitals (Ψ_{elec}). Then, a set of these orbitals is used to construct the Fock operator f(i) in matrix form. The electron density is calculated for this set of orbital. A specific set of orbital describes a distribution of electrons in a specific way in space. Diagonalization of the Fock matrix is performed in this procedure to get a new spin-orbital set. These new orbitals are chosen in a way that should provide a better approximation to the true electronic wavefunctions. It means electronic arrangement (V_{elec}) is changed in space. Now that we have the new orbitals, we can construct an updated Fock matrix using these improved orbitals. This updated Fock matrix incorporates the changes in electron distribution due to the new orbitals. This iterative process continues until a self-consistent solution is achieved, where the elec-

tron density and the orbitals no longer change significantly between iterations. The electronic energy is then calculated using the final set of orbitals and represents an approximation to the true electronic energy of the system. The HF method is a theoretical framework for solving the electronic structure problem. It provides a formalism for obtaining a molecular system's approximate wavefunction and energy. But Roothan was the first scientist who solved the HF problem numerically.^{109,110} Roothan's equations are used because they provide a practical way to find the HF energy, molecular orbitals, and their coefficients for real molecular systems.

In short, a two-electron term converted into one electronic form in the HF equation. By achieving this transformation, the interacting system's wavefunction can be written as the linear combination of a complete set of wavefunctions. Then, total M^n number of determinants are obtained out of which only ${}^M C_n$ numbers of determinants are the antisymmetric determinant. Here, M is the no. of spin-orbital (later called Basis set), and n is the no. of electrons. It means the wave function is the sum of ${}^M C_n$ determinants, where each determinant will correspond to a different state. For example, one will be the ground state, and the other could belong to the 1st excited, 2nd excited state, and ionized states. The ground state determinant can be described by a single determinant which is contributing most out of ${}^M C_n$ determinants. That's why Hartree Fock's theory is also known as one determinant theory. One can find this one determinant by SCF procedure. You will see the complete expansion of wavefunction on a given basis in the Configuration Interaction (CI) method. The HF approximation simplifies the problem but does not accurately describe the true electron-electron interactions. The Hartree-Fock method performs relatively well for systems with weak electron correlation, such as closed-shell molecules. However, it fails to accurately describe strongly correlated systems where electron-electron interactions play a significant role, such as molecules with open-shell configurations, transition metal complexes, and systems with multiple bond dissociation. The post-Hartree-Fock methods take care of the missing correlation problem, and we will see how these methods take care of it.

1.5.2 Electron Correlation

In quantum mechanics, electrons in atoms and molecules don't behave independently of each other. Their movements are correlated,^{111,112} meaning the behavior of one electron is directly related to the behavior of another. This correlation arises due to the electrostatic repulsion between electrons; they tend to avoid each other to minimize energy. In terms of the system's energy, it is the difference between exact energy and that system's Hartree-Fock energy $E_{corr} = E_{exact} - E_{HF}$. Electron faces a different level of repulsion when they are in parallel spin (Coulomb correlation) and anti-parallel spin (Fermi correlation). This repulsion generates an area of space around each electron with a lower chance of running into another electron. This area with lower electron finding probability is known as the Fermi hole for electrons with the same spin and the Coulomb hole for electrons with opposite spin.

Types of Electron Correlation: **Static correlation** deals with situations with a significant change in electron configuration, leading to different electronic states. This type of correlation is common in systems with multiple near-degenerate electronic states. **Dynamic correlation** focuses on the continuous motion of electrons. It accounts for the instantaneous correlation between electron positions and momenta. Dynamic correlation becomes essential when describing excited states and chemical reactions. The dissociation of the H_2 molecule is often used as an example to illustrate the differences between dynamic and static electron correlation. The correlation is primarily dynamic at equilibrium geometry because the gap between the singlet and triplet states is large. The singlet state is a good description of the ground state at equilibrium geometry. However, as the distance between the two H atoms increases, the energy gap between the singlet and triplet states disappears. This leads to a point (the dissociation limit) where the system can show both types of spins (singlet and triplet). At the dissociation limit, the system's correlation is dominated by static correlation.

Importance of Electron Correlation: Hartree-Fock (HF) calculations can accurately capture about 99% of a system's energy, especially when using large basis sets. The subsequent methods I'll discuss account for this 1% remaining correlation energy, which is vital for

precise calculations of various chemical properties. This remaining fraction becomes crucial, especially when dealing with subtle energy differences between systems during formation, dissociation, or interaction processes. If the computational method lacks accuracy, it may fail to explain problems adequately, potentially leading to misleading results. For instance, in scenarios like gas adsorption on a 2D surface, using an inappropriate correlation method can even yield contradictory outcomes, emphasizing the significance of accurate correlation modeling. Electron correlation is very important in various fields. For example, in diatomic molecules like $^2\text{O}_2$, accurate bond length and dissociation energy predictions require methods considering strong electron correlation. Enzymatic reactions, crucial in drug design, heavily depend on the correlation between metal and ligand electrons. In high-temperature superconductors, intricate behaviors arise due to electron correlation, impacting applications in power transmission. Quantum dots, with unique properties at the nanoscale, exhibit strong electron correlation effects, vital in advanced technologies like solar cells. Electron correlation in systems like transition metal oxides also leads to emergent phenomena like high-temperature superconductivity. Accurate treatment of these correlations is essential for accuracy across fields, from chemistry to condensed matter physics, shaping innovations in materials science, electronics, and energy technologies. Understanding and controlling electron correlation remains a cornerstone for future scientific advancements.

Hartree-Fock is an uncorrelated method; therefore, any method that improves HF wave function by adding correlation is known as the post Hartree-Fock method or correlated method.

1.5.3 Size Consistency and Size extensivity

There are many criteria that a computational method must follow to be considered a correlated method.^{113,114} Among these criteria, size consistency and size extensivity are the most important. Let's understand them. **Size Consistency (strict separability¹¹⁵)** is a computational method property that ensures that the energy calculation for molecule AB at infinite separation gives the same result as the sum of energy from the separate calculations on A and

B. In equation form, it can be written as $E_{AB} = E_A + E_B$ when $R_{AB} \rightarrow \infty$. This property ensures the correct behavior of dissociation curves of a molecule at dissociation limits.

Size Extensivity: A property of a computational method that ensures that the system's energy scales properly with size (number of electrons in the system). On moving smaller to large molecules, energy calculation errors must not increase. It can be written as $E \propto N$, where E is the system's energy, and N is the Particle's (electrons) number. Size- Extensivity is a major factor involved in electron correlation.

Importance of Size-Extensivity

- It allows straightforward comparisons between calculations involving various numbers of electrons.
- The lack of this property implies that errors in exact energy increase as more electrons enter the calculation.

1.5.4 Configuration Interaction (CI)

HF method is the one determinant and partially correlated method. The first correlated method after HF theory was the Configuration Interaction (CI) method.^{116–123} This method includes the correlation to the HF method by adding the new excited determinants. The CI wavefunction for the ground state can be written as

$$\Psi_{\text{CI}} = c_0|\Psi_{\text{HF}}\rangle + \sum_{i,a} c_i^a|\Psi_i^a\rangle + \sum_{\substack{i<j \\ a>b}} c_{ij}^{ab}|\Psi_{ij}^{ab}\rangle + \sum_{\substack{i<j<k \\ a<b<c}} c_{ijk}^{abc}|\Psi_{ijk}^{abc}\rangle + \dots \quad (1.5.13)$$

i,j,k.. set of spin orbitals represent the occupied orbitals, and a,b,c.. set represent the virtual orbitals. If we replace the i^{th} single spin-orbital in the HF determinant with the a^{th} , we obtain a single excited determinant. The total number of electrons remains the same during the replacement of the spin-orbital, which is equivalent to exciting an electron from the i^{th} orbital to the a^{th} orbital. Similarly, we can construct higher-order excited determinants

by replacing multiple spin-orbitals in the HF determinant. The p^{th} excited determinant will differ from the HF determinant from p spin orbitals.

We understand that for $2K$ spin orbitals and n -electron system, a total of ${}^{2K}C_n$ antisymmetric determinants contribute to the full CI wavefunction. Within these ${}^{2K}C_n$ determinants, we can discern the count of determinants contributing to single, double, and other excitations. In simpler terms, how many determinants will form from distinct n -tuple excitations from a Hartree-Fock (HF) determinant? If we have $2K$ spin orbitals (or K no. of basis), with N spin-orbitals occupied in the Hartree-Fock (HF) determinant, then $2K-N$ orbitals will be unoccupied. Therefore, ${}^N C_M$ are ways to select M spin orbitals from the occupied set. Similarly, M orbitals can be chosen from the $2K-N$ virtual orbitals in ${}^{2K-N} C_M$ ways. Therefore, the number of determinants formed from M -tuple excitation is ${}^N C_M \cdot {}^{2K-N} C_M$. The value of $M=1$ for single excitation, whereas it will be 2 and 3 for double and triple excitation, and so on. The CI matrix, a matrix form of Hamiltonian of a full CI,¹⁰⁸ can be written as

$$\mathbf{H}_{CI} = \begin{bmatrix} \langle \Psi_{HF} | H | \Psi_{HF} \rangle & 0 & \langle \Psi_{HF} | H | D \rangle & 0 & 0 & \dots \\ 0 & \langle S | H | S \rangle & \langle S | H | D \rangle & \langle S | H | T \rangle & 0 & \dots \\ \langle D | H | \Psi_{HF} \rangle & \langle D | H | S \rangle & \langle D | H | D \rangle & \langle D | H | T \rangle & \langle D | H | Q \rangle & \dots \\ 0 & \langle T | H | S \rangle & \langle T | H | D \rangle & \langle T | H | T \rangle & \langle T | H | Q \rangle & \dots \\ \vdots & \vdots & \vdots & \vdots & \ddots & \vdots \end{bmatrix} \quad (1.5.14)$$

Where $S (= \Psi_i^a)$, $D (= \Psi_{ij}^{ab})$, and $T (= \Psi_{ijk}^{abc})$ represent the single, double, and triple excited determinants. In the CI matrix, some elements are zero ($\langle \Psi_{HF} | H | S \rangle = \langle S | H | \Psi_{HF} \rangle = 0$) and that is due to Brillouin's theorem, which states that ground state determinant and first excited determinant can not be coupled. That does not mean that they have no impact on the CI energy. Via doubles, the amplitude of singles is indirectly mixed and affects the CI energy.

According to the Slater-Condon rule, any Hamiltonian matrix element that differs by more than two spin orbitals is also zero. This is the reason for the zero value of other elements in the CI matrix.

The CI amplitude's value can be found using two methods. First is diagonalizing the CI matrix, which is the most straightforward approach. Once the CI matrix has been diagonalized, the amplitudes of the CI wavefunctions can be determined from the eigenvectors. However, it is only feasible for very small systems. The second is the iterative method. For larger systems, it is not possible to diagonalize the CI matrix directly. Instead, we must use iterative methods like the Lanczos^{124,125,125,126} or Davidson algorithm.¹²⁷⁻¹³⁰ Iterative methods also diagonalize the CI matrix but in a small subspace of determinants. The subspace is then expanded to include more determinants until the desired accuracy is achieved. It's important to note that the size of the CI matrix (and consequently, the number of amplitudes to be determined) grows rapidly with the number of basis functions and the size of the active space. As a result, CI calculations can become computationally expensive for large systems, especially when considering extensive configurations.

CI offers an exact solution to the Schrödinger equation for many-electron systems when all possible N-electron configurations are included in the CI wavefunction expansion (full CI). However, the number of possible N-electron configurations is enormous, even for small molecules. This makes full CI calculations impractical for most systems. To make CI calculations more practical, truncated CI methods come into the picture, which only includes a subset of all possible N-electron configurations. However, truncated CI methods have some drawbacks. They are not size extensive or size consistent, which means that their accuracy does not scale well with the size of the system. Additionally, truncated CI methods struggle to account for dynamic correlation effects, which can lead to inaccurate results for more complex systems.

1.5.5 Perturbation Theory (PT)

Perturbation Theory (PT),^{131,132} a fundamental mathematical technique in quantum mechanics, is used to refine any system's energy beyond the Hartree-Fock (HF) approximation by adding dynamic correlation. Its core concept is solving complex problems by breaking them into manageable parts. The method separates the total Hamiltonian into two components: a solvable (whose solution is known) zeroth order unperturbed part (denoted as $\hat{H}^{(0)}$) and a perturbed component (represented as V), which usually is very small. This partition of total Hamiltonian can be written as

$$\hat{H} = \hat{H}^{(0)} + \lambda \hat{V} \quad (1.5.15)$$

where λ varies from 0 (completely unperturbed $\hat{H}^{(0)}$) to 1 (exact \hat{H}). Therefore, the Schrödinger equation for the perturbed system will be

$$(\hat{H}^{(0)} + \lambda \hat{V})|\Psi_n\rangle = E_n|\Psi_n\rangle \quad (1.5.16)$$

where $|\Psi_n\rangle$ and E_n represent the perturbed system's eigenfunction and eigenvalues, respectively. The wavefunction $|\Psi_n\rangle$ and the related energy E_n can both be expanded in a Taylor series of λ in the following manner, presuming that a perturbation is weak (λ is small):

$$E_n = E_n^{(0)} + \lambda E_n^{(1)} + \lambda^2 E_n^{(2)} + \lambda^3 E_n^{(3)} + \dots + \lambda^m E_n^{(m)} \quad (1.5.17)$$

$$|\Psi_n\rangle = |\Psi_n^{(0)}\rangle + \lambda |\Psi_n^{(1)}\rangle + \lambda^2 |\Psi_n^{(2)}\rangle + \lambda^3 |\Psi_n^{(3)}\rangle + \dots + \lambda^m |\Psi_n^{(m)}\rangle \quad (1.5.18)$$

In the above two equations, m (for $m > 0$) represents the m^{th} order correction to wavefunction and energy. $|\Psi_n^{(0)}\rangle$ and $E_n^{(0)}$ are the unperturbed (or $\hat{H}^{(0)}$) system's wavefunction and energy, whose solution we know. Putting the value of $|\Psi_n\rangle$ and E_n from equations 1.5.18 and 1.5.17 into equation 1.5.16 and dissociating the resulting equation in a separate power of

λ . We will get m^{th} order of λ equations, but I have shown up to the second order, which can be expressed as

$$\begin{aligned}
 \text{For } \lambda^0, \quad & \hat{H}^{(0)}|\Psi_n^{(0)}\rangle = E_n^{(0)}|\Psi_n^{(0)}\rangle \\
 \text{For } \lambda^1, \quad & \hat{H}^{(0)}|\Psi_n^{(1)}\rangle + \hat{V}|\Psi_n^{(0)}\rangle = E_n^{(0)}|\Psi_n^{(1)}\rangle + E_n^{(1)}|\Psi_n^{(0)}\rangle \\
 \text{For } \lambda^2, \quad & \hat{H}^{(0)}|\Psi_n^{(2)}\rangle + \hat{V}|\Psi_n^{(1)}\rangle = E_n^{(0)}|\Psi_n^{(2)}\rangle + E_n^{(1)}|\Psi_n^{(1)}\rangle + E_n^{(2)}|\Psi_n^{(0)}\rangle.
 \end{aligned} \tag{1.5.19}$$

We already know the solution of equation 1.5.19 when $\lambda=0$. After premultiply 1.5.19 by $\Psi_n^{(0)}$ (for $\lambda=1$) and $\Psi_i^{(0)}$ (for $\lambda=2$), respectively. We get a first-order and second-order correction to energy after using the hermeticity condition ($\langle\phi|\hat{A}|\Psi\rangle = \langle\Psi|\hat{A}|\phi\rangle^*$) with intermediate normalization ($\langle\Psi_n^{(0)}|\hat{H}|\Psi_n^{(1,2,\dots)}\rangle = 0$) on the resulting equations. These corrections can be expressed as

$$\begin{aligned}
 E_n^{(1)} &= \langle\Psi_n^{(0)}|\hat{V}|\Psi_n^{(0)}\rangle \\
 E_n^{(2)} &= \langle\Psi_n^{(0)}|\hat{V}|\Psi_n^{(1)}\rangle
 \end{aligned} \tag{1.5.20}$$

Equation 1.5.20 shows that to know the n^{th} order energy correction we must have to calculate $n-1^{th}$ order wavefunction correction. We can also expand $|\Psi_n^{(1)}\rangle$ as $\hat{H}^{(0)}$'s eigenfunctions as

$$|\Psi_n^{(1)}\rangle = \sum_{m \neq n} c_m |\Psi_m^{(0)}\rangle. \tag{1.5.21}$$

To find the 2^{nd} order energy correction, first, we need to find the 1^{st} order wavefunction correction and the coefficient c_m of eq. 1.5.21. The coefficient can be found by putting the value of $|\Psi_n^{(1)}\rangle$ from eq. 1.5.21 into eq. 1.5.19 and after solving the resulting equation, we will get the value of coefficient, which can be expressed as

$$c_m = \frac{\langle\Psi_m^{(0)}|\hat{V}|\Psi_n^{(0)}\rangle}{E_n^{(0)} - E_m^{(0)}} \tag{1.5.22}$$

After putting c_m value from eq. 1.5.22 into eq. 1.5.21, eq. 1.5.21 will become

$$\Psi_n^{(1)} = \sum_{m \neq n} \frac{\langle \Psi_m^{(0)} | \hat{V} | \Psi_n^{(0)} \rangle}{E_n^{(0)} - E_m^{(0)}} \Psi_m^{(0)} \quad (1.5.23)$$

After putting the value of $\Psi_n^{(1)}$ eq. 1.5.23 into eq. 1.5.20, we will get the 2nd order energy correction, which can be expressed as

$$E_n^{(2)} = \sum_{m \neq n} \frac{|\langle \Psi_m^{(0)} | \hat{V} | \Psi_n^{(0)} \rangle|^2}{E_n^{(0)} - E_m^{(0)}} \quad (1.5.24)$$

The approach we have discussed till now is known as **Rayleigh-Schrödinger Perturbation (RSP) theory**.^{133–135} A special case of RSP theory is proposed by Møller and Plesset (known as **Møller-Plesset Perturbation Theory (MPPT)**¹³⁶), where they have defined the unperturbed Hamiltonian as the sum of the Fock operator (see eq. 1.5.8), which is a one-electron operator.

$$\hat{H}^{(0)} = \sum_{i=1}^N f(i) \quad (1.5.25)$$

The perturbation \hat{V} is the difference between the \hat{H}_{elec} (see eq. 1.5.2) and $\hat{H}^{(0)}$ (the unperturbed \hat{H}). It can be expressed as

$$\hat{V} = \sum_{i=1}^n \sum_{j>i}^n \frac{1}{\vec{r}_i - \vec{r}_j} - \sum_{i=1}^n \sum_{j=1}^n V_{\text{HF}}(x_j) \quad (1.5.26)$$

The $|\Psi_n^{(0)}\rangle$ is the Hartree Fock wavefunction $|\Psi_{\text{HF}}\rangle$, which is equal to the sum of the orbital energies.

$$\begin{aligned} E_n^{(0)} + E_n^{(1)} &= \langle \Psi_n^{(0)} | \hat{H}^{(0)} | \Psi_n^{(0)} \rangle + \langle \Psi_n^{(0)} | \hat{V} | \Psi_n^{(0)} \rangle \\ &= \langle \Psi_n^{(0)} | \hat{H}^{(0)} + \hat{V} | \Psi_n^{(0)} \rangle \\ &= \langle \Psi_{\text{HF}} | \hat{H} | \Psi_{\text{HF}} \rangle \\ &= E_{\text{HF}} \end{aligned} \quad (1.5.27)$$

After adding the first-order energy correction to the zeroth order, it provides the Hartree Fock energy (shown in 1.5.27). Therefore, the first correction to the system's energy starts after adding a second-order energy correction. Hence, MP(2)¹³⁷⁻¹⁴² is the minimum correlated method in perturbation theory, where two in MP(2) refer to the second-order energy correction. The second-order energy correction can be written as

$$E_n^{(2)} = \sum_{\substack{i < j \\ a < b}} \frac{\langle ij || ab \rangle^2}{\epsilon_i + \epsilon_j - \epsilon_a - \epsilon_b} \quad (1.5.28)$$

MP(2), a cost-effective method, captures 80-90% of electron correlation. It scales with N^5 for system size N . MP(2) refines the Hartree-Fock (HF) wave function but tends to overestimate correlation energy slightly, whereas MP(3) method^{113,143,144} underestimates electron correlation, leading to inferior properties compared to the second order. MP4^{145,146} also overestimates correlation effects but performs better than MP(2). In short, higher-order variants of PT (like MP(3) and MP(4)) are computationally expensive and show abnormal and oscillating convergence behavior with a larger basis set, especially when using diffuse basis sets. This oscillating convergence^{147,148} behavior makes results predictions for higher-order MP(n) problematic. You can check the review by Cremer,¹⁴⁹ which beautifully explained and covered all aspects (like convergence issues) of perturbation series methods. MP(2) is size-extensive, providing reliable results for various systems. However, perturbation methods lack a variational principle, affecting their accuracy in handling static correlation effects. A variational principle ensures that any approximation to the true wave function will have an energy higher than or equal to the true ground-state energy. This property is crucial because it guarantees that the calculated energy is not artificially lower than the actual physical energy. Consequently, the MP(n) series might not always improve energy as higher orders are considered. The lack of variationality also emphasizes considering other methods for accurate and reliable predictions, such as coupled cluster methods.

1.5.6 Coupled Cluster (CC) methods

The Coupled Cluster (CC) method is a powerful and widely used quantum chemical technique that provides highly accurate energy and the best description for correlated electronic wavefunctions. It was first developed in the mid-1900s by Cöester and Kümmel to study the phenomena of nuclear physics.^{150,151} In the late 1960s, Čížek and Paldus introduced this method in the quantum chemistry community for the first time.^{152–154} In their article, they used second quantization and a Feynman-like diagram, which makes CC method programmable. Jiří Čížek made substantial contributions by introducing excitation operators and formulating a Coupled Cluster with Single and Double excitations (CCSD). Later, in the 1980s, Bartlett and others made CCSD even more accurate by introducing CCSD(T)^{155,156} and CCSDT¹⁵⁷ methods. CCSD(T) includes perturbative Triple excitations to CCSD, whereas CCSDT includes CC-triple excitations to CCSD. In 1987, Bartlett and others also introduced molecular properties (like dipole moments, quadrupole moments, polarizabilities, hyperpolarizabilities, and spin properties (hyperfine splitting constants and nuclear magnetic coupling constant)) evaluation using CC methods.¹⁵⁸ Today, the CC methods¹⁵⁹ are a powerful tool for understanding how electrons behave in molecules.

In CC methods, a wave function is defined as

$$\Psi_{\text{CC}} = e^{\hat{T}} |\Psi_{\text{HF}}\rangle. \quad (1.5.29)$$

The operator \hat{T} is an excitation operator, which is a combination of many excitation operators (single (\hat{T}_1), double (\hat{T}_2), triple (\hat{T}_3) excitation and so on). It can be written as

$$\hat{T} = \hat{T}_1 + \hat{T}_2 + \dots + \hat{T}_n. \quad (1.5.30)$$

where

$$\begin{aligned}\hat{T}_1 &= \sum_{i,a} t_i^a a_a^\dagger a_i \\ \hat{T}_2 &= \sum_{\substack{i>j \\ a>b}} t_{ij}^{ab} a_a^\dagger a_b^\dagger a_j a_i \\ \text{In general, } \hat{T}_n &= \sum_{\substack{i>j>k>l\dots \\ a>b>c>d\dots}} t_{ijkl\dots}^{abcd\dots} a_a^\dagger a_b^\dagger a_c^\dagger a_d^\dagger \dots a_l a_k a_j a_i\end{aligned}\quad (1.5.31)$$

The coefficients $t_{ijkl\dots}^{abcd\dots}$ are known as the CC-amplitudes of the \hat{T}_n operator. These CC-amplitudes determine the excitation operator's contribution to the overall wavefunction. The CC amplitudes of the full CC method are equivalent to the expansion coefficients of full CI wavefunction. If the \hat{T}_1 operator acts on the HF determinant, it excites an electron from occupied to virtual orbitals. The \hat{T}_2 operator is a two-electron operator that can excite two electrons simultaneously. Note that i,j,k,\dots represents filled orbitals, and a,b,c,\dots represents the virtual orbital. The summation of 'i' is over all occupied orbitals, whereas the summation of 'a' is over all the virtual orbitals.

$$\begin{aligned}\hat{T}_1 |\Psi_{\text{HF}}\rangle &= \sum_{i,a} t_i^a |\Psi_i^a\rangle \\ \hat{T}_1^2 |\Psi_{\text{HF}}\rangle &= 2 \sum_{\substack{i>j \\ a>b}} (t_i^a t_j^b - t_i^b t_j^a) |\Psi_{ij}^{ab}\rangle \\ \hat{T}_2 |\Psi_{\text{HF}}\rangle &= \sum_{\substack{i>j \\ a>b}} t_{ij}^{ab} |\Psi_{ij}^{ab}\rangle \quad \text{and so on.}\end{aligned}\quad (1.5.32)$$

The \hat{T}_n operator is an n-electron operator that simultaneously excites n electrons. This excitation can also be shown with the help of annihilation and creation operators of the second quantization representation method. a_a^\dagger represents the creation of a particle in virtual orbitals, whereas a_i represents the destruction of a particle in occupied orbitals. Equation 1.5.29 shows that the \hat{T}_1 operator operates on the HF determinant, which is one determinant. We have used a single determinant as a reference. Therefore, it is also known as the Single Reference Cou-

pled Cluster (SRCC) method. If one uses two or more determinants in equation 1.5.29, the process will be known as the multireference CC method (MRCC). MRCC^{160–162} is mostly necessary for the study of the excited state, ionized states, and degenerated states. A solution of full CC wavefunction is computationally very expensive. Therefore, in practice, truncated CC methods are used. For example, CCSD is a CC method that is truncated at $\hat{T}_n = \hat{T}_1 + \hat{T}_2$. Normally, the truncation of a method unsatisfied a few conditions that a computational method must follow. For instance, truncated CI is not size-consistent. However, CCSD (a truncated CC method) is size consistent and size extensive. This is because the operator operates on wavefunction exponentially (non-linear) rather than linearly (as in CI).

Let's find out the energy expression by putting the value of Ψ_{CC} from equation 1.5.29 in the Schrödinger wave equation.

$$\hat{H}e^{\hat{T}}|\Psi_{HF}\rangle = E_{cc}e^{\hat{T}}|\Psi_{HF}\rangle. \quad (1.5.33)$$

Pre-multiplication of equation 1.5.33 by Ψ_{HF} , equation 1.5.33 will become 1.5.29 in the Schrödinger wave equation.

$$\langle\Psi_{HF}|\hat{H}e^{\hat{T}}|\Psi_{HF}\rangle = E_{cc}\langle\Psi_{HF}|e^{\hat{T}}|\Psi_{HF}\rangle. \quad (1.5.34)$$

We know that the expansion of the exponential of x in the Tylor series is written as

$$e^x = 1 + x + \frac{x^2}{2!} + \frac{x^3}{3!} + \frac{x^4}{4!} + \dots \quad (1.5.35)$$

Similarly, $e^{\hat{T}}$ can be expanded the same as above, and after the rearranging the terms, the expanded form will look like

$$e^{\hat{T}} = 1 + \hat{T}_1 + [\hat{T}_2 + \frac{\hat{T}_1^2}{2}] + [\hat{T}_3 + \frac{\hat{T}_1^3}{6} + \hat{T}_2\hat{T}_1] + [\hat{T}_4 + \hat{T}_1\hat{T}_3 + \frac{\hat{T}_2^2}{2} + \frac{\hat{T}_1^4}{24}] + \dots \quad (1.5.36)$$

After putting the value of $e^{\hat{T}}$ in the right-hand term of equation 1.5.34, it is clear that only

the first term will survive, which does not contain \hat{T} . Rest all terms will become zero [$\langle \Psi_{\text{HF}} | \Psi_{ijkl\dots}^{abcd\dots} \rangle = 0$ (orthogonality)] because of orthonormality. So equation 1.5.34 will become

$$\langle \Psi_{\text{HF}} | \hat{H} e^{\hat{T}} | \Psi_{\text{HF}} \rangle = E_{\text{cc}}. \quad (1.5.37)$$

The above equation can also be written in expanded form as

$$E_{\text{cc}} = \langle \Psi_{\text{HF}} | \hat{H} | \Psi_{\text{HF}} \rangle + \langle \Psi_{\text{HF}} | \hat{H} \hat{T}_1 | \Psi_{\text{HF}} \rangle + \langle \Psi_{\text{HF}} | \hat{H} (\hat{T}_2 + \frac{\hat{T}_1^2}{2}) | \Psi_{\text{HF}} \rangle + \langle \Psi_{\text{HF}} | \hat{H} (\hat{T}_3 + \frac{\hat{T}_1^3}{6} + \hat{T}_2 \hat{T}_1) | \Psi_{\text{HF}} \rangle + \dots \quad (1.5.38)$$

The Hamiltonian operator deals explicitly with one- and two-particle interactions or operators, following Slater's rules, which state that when comparing determinants, they should not differ by more than two spin orbitals for non-zero matrix elements. Consequently, any terms beyond the third power of the T operator in equation 1.5.38, where applying the \hat{T} operator creates excited determinants with three or more electron changes compared to the reference, also vanishes. As a result, the expansion will truncate naturally, and the energy expression will include only terms up to a certain level, which can be written as

$$E_{\text{cc}} = \langle \Psi_{\text{HF}} | \hat{H} | \Psi_{\text{HF}} \rangle + \langle \Psi_{\text{HF}} | \hat{H} \hat{T}_1 | \Psi_{\text{HF}} \rangle + \langle \Psi_{\text{HF}} | \hat{H} (\hat{T}_2 + \frac{\hat{T}_1^2}{2}) | \Psi_{\text{HF}} \rangle \quad (1.5.39)$$

The truncation of terms is due to the Hamiltonian and not because of \hat{T} or the number of electrons. According to the Brillouin theorem in quantum mechanics, the matrix elements of the Hamiltonian operator between two Slater determinants that differ by a single excitation are equal to zero. Therefore, the middle term in the above equation will become zero. After using equation 1.5.32, the energy value will be

$$E_{\text{cc}} = E_{\text{HF}} + \sum_{\substack{i>j \\ a>b}} (t_{ij}^{ab} + t_i^a t_j^b - t_i^b t_j^a) \langle \Psi_{\text{HF}} | \hat{H} | \Psi_{ij}^{ab} \rangle \quad (1.5.40)$$

The values of cc-amplitude (like t_i^a , t_{ij}^{ab}) can be obtained by an equation generated from pro-

jecting $\langle \Psi_{ijkl\dots}^{abcd\dots} |$ on equation 1.5.33. The amplitude equation can be written as

$$\begin{aligned} \langle \Psi_{ijkl\dots}^{abcd\dots} | \hat{H} e^{\hat{T}} | \Psi_{\text{HF}} \rangle &= E_{\text{cc}} \langle \Psi_{ijkl\dots}^{abcd\dots} | e^{\hat{T}} | \Psi_{\text{HF}} \rangle. \\ &= 0 \end{aligned} \quad (1.5.41)$$

Equations 1.5.40 and 1.5.41 have one problem: they contain disconnected and connected terms. Even though disconnected terms get canceled in the above equations and provided only closed and connected terms. However, the equation 1.5.40 and 1.5.41 can also be expressed in another form where disconnected terms won't exist. We have premultiplied equation 1.5.33 by $\Psi_{\text{HF}} e^{-\hat{T}}$ and $\Psi_{ijkl\dots}^{abcd\dots} e^{-\hat{T}}$ to get energy (equation 1.5.42) and cc-amplitudes (equation 1.5.43).

$$\begin{aligned} \langle \Psi_{\text{HF}} | e^{-\hat{T}} \hat{H} e^{\hat{T}} | \Psi_{\text{HF}} \rangle &= E_{\text{cc}} \langle \Psi_{\text{HF}} | e^{-\hat{T}} e^{\hat{T}} | \Psi_{\text{HF}} \rangle \\ &= E_{\text{cc}} \end{aligned} \quad (1.5.42)$$

$$\begin{aligned} \langle \Psi_{ijkl\dots}^{abcd\dots} | e^{-\hat{T}} \hat{H} e^{\hat{T}} | \Psi_{\text{HF}} \rangle &= E_{\text{cc}} \langle \Psi_{ijkl\dots}^{abcd\dots} | e^{-\hat{T}} e^{\hat{T}} | \Psi_{\text{HF}} \rangle \\ &= E_{\text{cc}} \langle \Psi_{ijkl\dots}^{abcd\dots} | \Psi_{\text{HF}} \rangle \\ &= 0 \end{aligned} \quad (1.5.43)$$

The operator $(e^{-\hat{T}} \hat{H} e^{\hat{T}})$ in equation 1.5.42 looks like a similarity-transformed Hamiltonian. Let's call it \bar{H} . It's important to note that such a transformation doesn't alter the operator's eigenvalues. This transformation causes the Hamiltonian to lose its hermitian property, making it unsuitable for energy calculation through variational methods. However, this similarity transformation has an advantage. This transformation gains computational efficiency when employing the Baker–Campbell–Hausdorff (BCH) formula. Through this formula, the operator $\bar{H} = e^{-\hat{T}} \hat{H} e^{\hat{T}}$ operator can be expressed as a linear combination of \hat{H} and \hat{T} , as

shown in equation 1.5.44.

$$e^{-\hat{T}}\hat{H}e^{\hat{T}} = \hat{H} + [\hat{H}, \hat{T}] + \frac{1}{2!}[[\hat{H}, \hat{T}], \hat{T}] + \frac{1}{3!}[[[\hat{H}, \hat{T}], \hat{T}], \hat{T}] + \frac{1}{4!}[[[[\hat{H}, \hat{T}], \hat{T}], \hat{T}], \hat{T}] + \dots \quad (1.5.44)$$

This series will truncate after the first five terms (or the first four commutations). That is due to Hamiltonian's two-body nature, which has two holes and two particles. \hat{H} can be represented by two up and two down lines, connecting with the \hat{T} operator through these four lines. Therefore, four such connections are possible. It means \hat{H} can commute only four times with \hat{T} . Therefore, the equation will terminate after five terms, simplifying the calculation. The equation 1.5.44 also shows the importance of commutation of \hat{H} and \hat{T} to connecting and open terms for correlation energy.

The truncated CC method's name is given in the table 1.1. CCSD(T) is CCSD + triples

Table 1.1: Name of truncated Coupled Cluster methods

S. No	Value of \hat{T}	CC-Method's Name
1	\hat{T}_2	CCD
2	$\hat{T}_1 + \hat{T}_2$	CCSD
3	$\hat{T}_1 + \hat{T}_2 + \hat{T}_3$	CCSDT
4	$\hat{T}_1 + \hat{T}_2 + \hat{T}_3 + \hat{T}_4$	CCSDTQ

correction added through perturbation theory.

1.6 Equation of Motion Coupled cluster (EOM-CC) Method

In the EOM-CC method,^{163–166} the term "equation of motion" does not refer to classical physics's traditional equations of motion. Instead, it refers to mathematical equations that describe the movement of particles or electrons. In other words, it describes how certain observables, such as excitation energies and transition moments, change in response to perturbations in a quantum mechanical system. The EOM-CC method calculates the energy

and other properties of excited,¹⁶⁷ ionized,^{168,169} and electron-attached¹⁷⁰ states. In the past three decades, the EOM-CC scheme has been developed quite a lot. It underwent expansions to include triply excited configurations partially^{171–174} (EOM-CCSD(T)) and fully (EOM-CCSDT) for excited,^{174–177} ionized,^{169,178–180} and electron-attached^{180–182} states. Since the EOM-CC method uses Ψ_{CC} (see equation 1.5.29) as a reference, that makes it a single reference approach. If a different wavefunction (Ψ_X) is chosen as the reference instead, the method is called EOM-X, where X is the name of a method. To calculate energy, one needs wavefunction. The EOM-CC method generates the wavefunction for a p^{th} excited, ionized, and electron-attached states (Ψ_p) with the help of an $\hat{R}(p)$ operator.

$$\Psi_p = \hat{R}(p)|\Psi_{\text{cc}}\rangle. \quad (1.6.1)$$

The $\hat{R}(p)$ operator is a linear operator, and its form varies depending on the type of state being calculated. The form of the $R(p)$ operator for various states can be written as

$$R^{IP}(p) = \sum_i \hat{R}_i(p)a_i + \sum_{a,i>j} \hat{R}_{ij}^a(p)a_a^\dagger a_j a_i + \dots \quad (1.6.2)$$

$$R^{EA}(p) = \sum_a \hat{R}^a(p)a_a^\dagger + \sum_{a>b,i} \hat{R}_i^{ab}(p)a_a^\dagger a_b^\dagger a_i + \dots \quad (1.6.3)$$

$$R^{DIP}(p) = \sum_{i>j} \hat{R}_{ij}(p)a_i a_j + \sum_{a,i>j>k} \hat{R}_{ijk}^a(p)a_a^\dagger a_k a_j a_i + \dots \quad (1.6.4)$$

$$R^{EE}(p) = \hat{R}_0(p) + \sum_i \hat{R}_i^a(p)a_a^\dagger a_i + \sum_{a>b,i>j} \hat{R}_{ij}^{ab}(p)a_a^\dagger a_b^\dagger a_j a_i + \dots \quad (1.6.5)$$

Since the non-radiative decay processes involve the ionization of a state, we will use the $\hat{R}(p)$'s form for ionized states in the upcoming calculation. Energy for the ground state and other p^{th} state can be written using the Schrödinger equation as

$$\hat{H}\Psi_{\text{cc}} = E_{\text{cc}}\Psi_{\text{cc}}. \quad (1.6.6)$$

$$\hat{H}\Psi_p = E_p\Psi_p. \quad (1.6.7)$$

Using equation 1.6.1, above equation 1.6.7 will become

$$\hat{H}\hat{R}(p)\Psi_{cc} = E_p\hat{R}(p)\Psi_{cc} \quad (1.6.8)$$

Premultiply equation 1.6.6 with $\hat{R}(p)$ operator and subtraction resulting equation from equation 1.6.8.

$$\begin{aligned} (\hat{H}\hat{R}(p) - \hat{R}(p)\hat{H})\Psi_{cc} &= (E_p - E_{cc})\hat{R}(p)\Psi_{cc} \\ \text{OR} \quad [\hat{H}, \hat{R}(p)]\Psi_{cc} &= \Delta E_p\hat{R}(p)\Psi_{cc} \end{aligned} \quad (1.6.9)$$

$\hat{R}(p)$ and \hat{T} operator commute with each other. Thus, we can replace \hat{H} with $\bar{H} = e^{-\hat{T}}\hat{H}e^{\hat{T}}$ in the above equation and it can be written as

$$[\bar{H}, \hat{R}(p)]\Psi_{cc} = \Delta E_p\hat{R}(p)\Psi_{cc} \quad (1.6.10)$$

One of the advantages of this method is that we can get direct energy differences between the ground state and other states like ionized, excited, electron-attached, and double-ionized states. Diagonalization of \bar{H} matrix in 1h + 2h1p and 1p + 2p1h subspaces provides the ionization potential (IP) and electron affinity (EA) values, respectively. A different approach is applied to DIP values. These values are acquired through a non-symmetric diagonalization procedure of the \bar{H} matrix within the subspace encompassing 2h + 3h1p configurations.

1.7 Challenges of Temporary Bound State (TBS) & its solutions

Mainly, there are only two challenges to the TBS problem. First, TBSs are metastable states, which makes the wave function non-square integrable. It means that $\int \psi \cdot \psi^* d\tau$ is not a finite number, and particles can also be found outside the box. Second, we have to calculate the continuum and electron correlation simultaneously. You can understand the situation's gravity from the fact that the molecules have discrete or quantized energies, whereas free electrons have continuous energy. It is like we are trying to combine two opposite things. Solving this problem requires finding a harmonious middle ground between these two. One proposed solution is to confine the system within a potential box, similar to the particle-in-a-box scenario. This confinement yields discrete energy levels and ensures the wavefunction becomes square integrable. However, still, one problem remains unsolved. That is, the solution to our problem lies in a complex domain. We need complex eigenvalues (or complex energy) as a solution, while the hermitian Hamiltonian operator only gives real values. Analytic continuation is the solution to this problem. Analytic continuation of a real function involves extending the domain of a real-valued function defined over a limited range of real numbers to a larger domain in the complex plane while preserving its analytical properties. This process allows us to explore the behavior of the real wavefunction in regions beyond its original definition.

In any quantum mechanical method, the computational space is divided into the inner and outer regions. The inner region is where the physical interaction or phenomena of interest occur, while the outer region represents the asymptotic region at a large distance away from the interaction. Specific boundary conditions are applied at the boundary separating the inner and outer regions to ensure a smooth transition between the two regions. The boundary conditions serve the critical role of ensuring a seamless connection between these regions while accommodating the distinct behaviors of wavefunctions in both scattering and bound states.

In simple words, boundary conditions ensure wavefunction behaves well in inner regions and remains square integrable.¹⁸³ For scattering states (states that describe particles scattering off to infinity, where wavefunction behaves differently and is not square integrable), the boundary conditions aim to ensure the wavefunction behaves appropriately as it reaches the outer region. This typically involves specifying the behavior of the wavefunction at large distances. The boundary condition of square integrability is important in non-hermitian Hamiltonian methods¹⁸⁴ because it allows us to associate the resonance phenomenon¹⁸⁵ with the discrete part of the spectrum of the complex scaled Hamiltonian. This means that we can treat resonances using standard quantum mechanics methods. The specific form of the boundary conditions can vary depending on the problem and the chosen methods.

We know the Hamiltonian operator is hermitian and always leads to real eigenvalues (or energy). Therefore, we cannot get complex energies using a hermitian Hamiltonian. Thus, we have to modify our Hamiltonian and make it non-hermitian,¹⁸⁴ then it will lead to complex energies. We will learn various ways to make a hermitian \hat{H} into non-hermitian \hat{H} in upcoming methods like complex absorbing potential (CAP) based methods, complex scaling, and Fano-ADC type methods. Using these methods, we can get complex energy or Siegert energy,¹⁸⁶ and the complex part of this Siegert energy tells us about the decay width of TBSs. Siegert energy can be written as

$$E_{\text{TBS}} = E_{\text{real}} - i\frac{\Gamma}{2} \quad (1.7.1)$$

Depending upon the process you are studying, E_{real} can be IP, EA, or any other energy, whereas Γ of the complex part provides details about the decay rate or the lifetime of the metastable state. The lifetime (τ) and decay width (Γ) of metastable state are related to each other by

$$\tau = \frac{\hbar}{\Gamma} \quad (1.7.2)$$

Siegert energy is important in nuclear and atomic physics, particularly when studying TBS-

related (or resonance) phenomena. These tools provide physicists with a robust framework for understanding and characterizing the behavior of particles in metastable states. The Siegert states, which arise from the non-hermitian Hamiltonian, offer a basis for describing the outgoing wave behavior of resonance states, which is crucial for calculating decay widths and quantifying the speed at which resonances decay or scatter into other states. This insight into decay processes is essential for various applications, from nuclear reactions and decay to atomic processes involving unstable states. In general, it helps to gain deeper insights into the dynamics of resonant systems, ultimately enhancing our understanding of fundamental processes in the subatomic world and facilitating the development of advanced technologies in various fields like quantum mechanics and nuclear physics. Next, we will study the CAP, complex scaling, and FANO-ADC methods that make hermitian Hamiltonian into non-hermitian and provide complex energies. We will try to understand how these methods work in brief.

1.7.1 Complex Absorbing Potential (CAP) Method

The CAP approach^{187–194} is a powerful tool for calculating TBSs energies in quantum chemistry. However, it is also computationally expensive, especially for large molecules and high-level electronic structure methods. A one-particle complex potential ($-i\eta\hat{W}$) is added to the original Hamiltonian (H), making it a non-Hermitian $\hat{H}(\eta)$. However, $\hat{H}(\eta)$ remains complex-symmetric. After adding CAP, the non-hermitian Hamiltonian can be written as

$$\hat{H}(\eta) = H - i\eta\hat{W} \quad (1.7.3)$$

where η represents the strength of applied potential and \hat{W} is a semi-definite one-particle

operator with a positive value and can be written as

$$W(x, c) = \sum_{i=1}^3 W_i(x_i, c_i) = \begin{cases} 0 & |x_i| \leq c_i \\ (|x_i| - c_i)^2 & |x_i| > c_i \end{cases} \quad (1.7.4)$$

where c_i ($i=1,2,3$) represents the CAP box length in different directions and x_i ($i=1,2,3$) is the bond length of the molecule in different coordinate axes from the center of the coordinate axis. The CAP-augmented Hamiltonian ($\hat{H}(\eta)$) provides the complex energy values. For the appropriate form of CAP, the asymptotic damping of the Siegert eigenfunction is possible (see figure 1.5) after adding CAP, making the wave function square-integrable and eigenvalues discrete. A box shape CAP, which we have used and shown by equation 1.7.4, is applied in the molecule's peripheral region so that the molecule remains unperturbed, yet scattered electrons get absorbed. $\hat{H}(\eta)$ is solved for various values of η , where η varies from 0.0 to 0.1 with a desired step size. Usually, the step size of η is 10^{-5} . It means that the CAP-EOM-CC calculations^{195–206} are performed thousands of times to generate η trajectory. At each time, we are perturbing the original Hamiltonian with a small CAP value to obtain energy value at every η value. This process makes calculation computationally expensive. A plot between the obtained energy's real and imaginary parts provides η trajectory for non radiative decay problems. Whereas, the η trajectories for resonance problems are examined by using logarithmic velocity $v_i(\eta)$, which can be written as

$$v_i(\eta) = \eta \frac{\partial E}{\partial \eta}. \quad (1.7.5)$$

The η 's value at which $v_i(\eta)$ is minimum gives the optimal CAP strength. At this point, TBS is also found. The optimal value of η is significant because, for a finite basis, if CAP is weak (η is too small), the TBS will not stabilize, resulting in not obtaining the Siegert energy. If CAP is too strong, reflection affects the TBS significantly, unable to obtain the

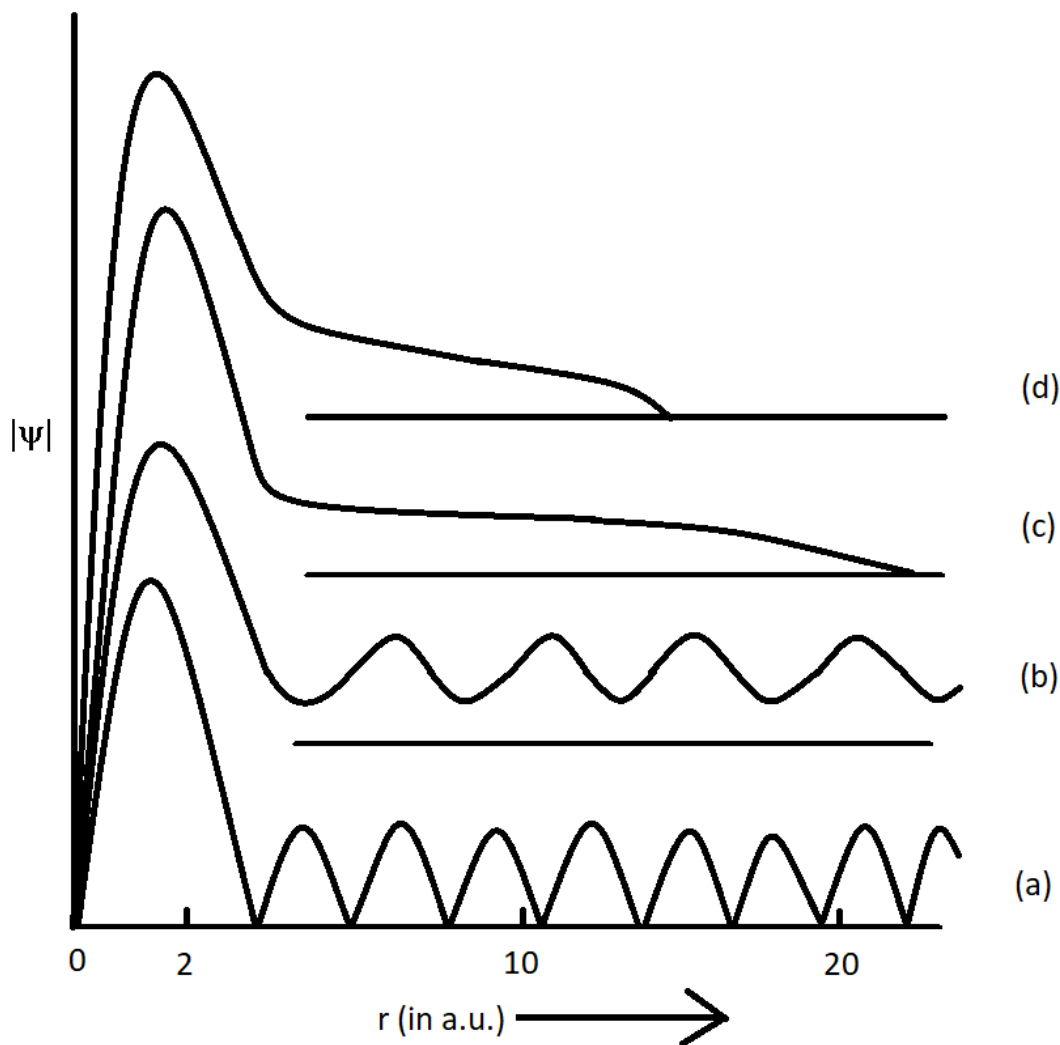


Figure 1.5: Plot shows change in wavefunction after CAP implementation. Caption a represents the wavefunction for $\eta = 0$ (original wave function), whereas b, c, and d represent the wavefunction at various values of $\eta = 5 \times 10^{-4}$, $\eta = 5 \times 10^{-3}$, and $\eta = 5 \times 10^{-2}$ respectively. This graph is a copy of figure-4 of reference¹⁸⁷. I have used this for better understanding. I do not claim that this graph and its data are produced by me (Graph is redrawn with permission).

TBS energy.

In principle, CAP can be applied at any level of electronic methods,^{207,208} like at the self-consistent field (SCF)/Hartree-Fock, coupled cluster (CC),¹⁹⁶ or even at the EOM-CC^{40,41,68} level. Because the N electron ground state cannot be disturbed, we add CAP at the EOM-CC level. Now, a question comes to your mind: what if we add CAP at other levels? Adding CAP at the CC¹⁹⁶ or SCF levels makes the cluster amplitudes complex, and it perturbs the ground

state of the N electron system. Then, to get the correct decay width, we need to correct the N electron ground state by removing the perturbation. In short, we have to perform extra calculations, and in this case, we also lose the advantage of the CC theory of getting direct energy difference. Then, the correct energy is given by

$$E_{TBS}(\eta) = \Delta E_p(\eta) + E_{cc}(\eta) - E_{cc}(\eta = 0). \quad (1.7.6)$$

Various (CAP,¹⁸⁷ Continuum removal CAP,^{209,210} Reflection-free CAP,^{211–213} Transformative CAP,²¹⁴ Voronoi-CAP^{215–217}) types of complex potentials are used worldwide. The basic principle of all complex potential is the same. I have presented a list of various groups that used this CAP. If you are interested in the details of various CAPs, check the details in the mentioned article.

Table 1.2: Various types of Complex Absorbing Potentials

S. No	Type of CAP	FORM	First Proposed by
1	Optical potential	$iV_i(r) = -iAr_8$	Austin & Jolicard in 1985 ²¹⁸
2	CAP	$\hat{H}(\eta) = H - i\eta\hat{W}$	Riss & Meyer in 1993 ¹⁸⁷
3	Reflection Free	Extra added potential term in CAP	Riss & Meyer in 1995 ²¹¹
4	Transformative CAP	Modified K.E. operator in CAP	Riss & Meyer in 1995 ²¹⁴
5	Continuum removal	$\hat{H}(\eta, \lambda) = H + (\lambda - i\eta)\hat{W}$	Nimrod & Sajeev in 2009 ²⁰⁹
6	Voronoi CAP	CAP is applied to Voronoi cells	Sommerfeld & Ehara in 2015 ²¹⁵

1.7.2 Complex Scaling Method

Aguilar, Balslev, and Combes proposed the complex scaling method (CSM).^{219–221} In the CSM method,^{222–227} the coordinates and Hamiltonian undergo a process called "complexification" or "complex scaling," where it is modified to accommodate the complex scaling parameter (θ). θ is a real number. Complexification takes place with the help of the transformation (dilation) operator $U(\theta)$. The coordinates r_i change into $r_i e^{i\theta}$ using the dilation

operator as

$$U r_i U^{-1} = r_i e^{i\theta} \quad (1.7.7)$$

Here, i denotes the number of particles and $U = e^{i\theta r \partial / \partial r}$. Similarly, Hamiltonian also transformed from real (\hat{H}) to complex Hamiltonian $\hat{H}(\theta)$. A point to note is that after the complex transformation of Hamiltonian, the kinetic energy term gets a phase factor (complex part) of $e^{-2i\theta}$ whereas $e^{-i\theta}$ is the phase factor for potential energy. Wavefunction never transforms using the dilation operator directly but gets changed indirectly since wavefunction depends on r_i , which has changed. This indirect scaling makes wavefunction square integrable. TBSs lie in a group of continuum eigenstates if we look from the point of Hermitian Hamiltonian, whereas it becomes a single square integrable state if we use a non-hermitian operator with proper boundary conditions. In this method, the boundary condition of square integrability is preserved during the complex scaling of coordinates when $|\theta| \geq \pi/2$. In general, continuum states that are connected to bound states, such as TBSs, normally remain hidden. By hidden, I mean that we cannot observe them and study their properties using the normal quantum mechanical methods used to study bound states. Complex scaling,^{190,228–231} a non-hermitian Hamiltonian-based method, is a way to study them.

1.7.3 Fano Theory for decay width

Ugo Fano²³² and Herman Feshbach²³³ independently developed the Fano-Feshbach theory, also known as the Fano-Resonance theory, in the 1960s and has since been widely applied in various areas of quantum physics to describe the interaction between a discrete quantum state and continuum. It is a robust framework for understanding the processes originating from the interaction between discrete and continuum states, like resonance, autoionization, etc. As discussed earlier, TBS are metastable states that are stable for a few femtoseconds.

The decay width Γ provided by Fano can be expressed as

$$\Gamma = 2\pi \sum_f |\langle \phi | H | \chi_{f,\varepsilon} \rangle|^2 \quad (1.7.8)$$

where $\chi_{f,\varepsilon}$ is the continuum wavefunction of the ionized state, ϕ is the exact wavefunction of the ground state, H is the total electronic Hamiltonian, and f indicates the number of open decay channels (number of DIPs lower than IP of the targeted state) that belong to the continuum subspace, and ε is the asymptotic ICD/ETMD electron's kinetic energy. This theory uses Green's function-based electron propagator to get the wavefunction of the ionized state.

This approach divides the Hilbert space into the Q subspace representing the bound configurations and the P subspace representing the continuum configurations. These P and Q subspaces must satisfy the following conditions: $P + Q = 1$ and $P * Q = 0$. The algebraic diagrammatic construction (ADC) Hamiltonian (\hat{H}) is projected onto the P and Q subspaces, yielding interaction matrices PHP and QHQ , respectively. Diagonalization of these interaction matrices produces the continuum states and the bound component. Bound and continuum part can be expressed as

$$QHQ|\phi\rangle = E_b|\phi\rangle \quad (1.7.9)$$

$$PHP|\chi_{f,\varepsilon}\rangle = E_f|\chi_{f,\varepsilon}\rangle \quad (1.7.10)$$

The extended second-order algebraic diagrammatic construction (ADC(2)X)^{234–237} scheme of Green's function is used to build H . This scheme is specified in the region bounded by the one-hole (1h) and two-hole one-particle (2h1p) configurations. The coupling between the 1h configurations is treated with the second-order perturbation theory in the ADC(2)X method whereas, first-order perturbation theory is used to treat the coupling between the 1h and 2h1p configurations as well as the coupling between the 2h1p configurations. To build the P subspace, representing the ultimate double-ionized state with an outgoing free electron,

we have considered the 2h1p configurations matrix block of ADC \hat{H} . Usually, the Q subspace includes all occupied orbitals in one hole block. The partitioning of the 2h1p configurations places the open decay channels (i.e., DIPs lower than IP) in the P subspace and the remaining configurations in the Q subspace. We may obtain the entire and partial decay width using this method. Please refer to the references^{234–237} for further information on the Fano-ADC approach.

The L^2 basis set has been employed in all our upcoming calculations; hence, the continuum states we derived using equation 1.7.10 are not a true continuum. They exhibit asymptotic behavior and incorrect normalization. Therefore, they are pseudo-continuum in nature. We used the Stieltjes imaging approach to get an exact estimate for decay width as well as the proper normalization.²³⁸ This technique also enhances the convergence of calculations, improves the description of TBS's properties, and simplifies the treatment of complex energy spectra, ultimately leading to more accurate and physically meaningful results in studying atomic and molecular systems. Details regarding the Stieltjes imaging technique is provided by reference.²³⁸

Chapter 2

Decay Processes in Cationic Alkali Metals in Microsolvated Clusters: A Complex Absorbing Potential Based Equation-of-Motion Coupled Cluster Investigation

2.1 Abstract

We have employed the highly accurate complex absorbing potential based ionization potential equation-of-motion coupled cluster singles and doubles (CAP-IP-EOM-CCSD) method to study the various intermolecular decay processes in ionized metals (Li^+ , Na^+ , K^+) microsolvated by water molecules. For the Li atom, the electron is ionized from the 1s subshell. However, for Na and K atoms, the electron is ionized from 2s and both 2s and 2p subshells, respectively. We have investigated decay processes for the $\text{Li}^+(\text{H}_2\text{O})_n$; ($n=1-3$) systems as well as $\text{Na}^+(\text{H}_2\text{O})_n$; ($n=1,2$), and $\text{K}^+-\text{H}_2\text{O}$. The Lithium cation in water can decay only via

electron transfer mediated decay (ETMD) as there are no valence electrons in Lithium. We have investigated how the various decay processes change in the presence of different alkali metal atoms and how the increasing number of water molecules play a significant role in the decay of microsolvated systems. To see the effect of the environment, We have studied the $\text{Li}^+ \text{-NH}_3$ (in comparison to $\text{Li}^+ \text{-H}_2\text{O}$). In the case of $\text{Na}^+ \text{-H}_2\text{O}$, We have studied the impact of bond distance on the decay width. The effect of polarization on decay width is checked for the $\text{X}^+ \text{-H}_2\text{O}$; $\text{X}=\text{Li, Na}$. We have used the PCM model to study the polarization effect. We have compared our results with the existing theoretical and experimental results wherever available in the literature.

2.2 Introduction

There are various ways in which an excited/ionized atom/molecule can relax, either via non-radiative processes or radiative decay processes. A radiative decay like fluorescence or a non-radiative process like Auger decay has been well known for a long time. Auger spectroscopy^{8,9} has various applications in material and surface science. In 1997, Cederbaum *et al.*^{35,42} proposed a new decay mechanism for inner valence ionized/excited states, called Interatomic/molecular Coulomb decay (ICD). This non-local complex relaxation process happens in atomic/molecular clusters. In the original formulation of this process, a single inner-valence hole state in an atom or molecule, which cannot decay locally via the Auger mechanism due to energetic considerations, decays through energy transfer to the neighbouring atom. This knocks out an outer valence electron from the adjacent atom or molecule. Contrary to the Auger decay process, ICD is driven by the correlation between electrons located on different species, often a few nanometers apart. The ejected ICD electrons have low energy, whose value strongly depends on the initial state and chemical nature of the neighbour. In the ICD process, two positive charges are produced in close proximity to each other, leading to a Coulomb explosion.

Electron transfer mediated decay (ETMD)⁵⁹ is another interatomic decay process initiated by ionizing radiation. In this process, an electron acts as a mediator transfer between two sub-units rather energy. In ETMD, an electron is a neighbour donated by a neighbour to an initially ionized atom or molecule, while excess energy is transferred either to the donor or to another neighbour, which emits a secondary electron to the continuum. Li^+ has only electrons in its core orbital, so it is the best example to study the ETMD process.⁶⁸ Being an electron transfer process, ETMD is usually considerably slower than the energy-transfer-driven ICD process. However, it becomes a vital decay pathway in a medium if ICD is energetically forbidden. Since its original formulation, ICD has been investigated theoretically^{42–46,58} and experimentally^{39,47,48} in a variety of system such as rare-gas^{36,38} clusters, hydrogen-bonded clusters³⁷ and water solutions.^{50,239,240} It has been found that not only inner-valence ionized states may undergo ICD, but any localized electronic excitation whose energy lies above the ionization potential of a neighbour can undergo ICD. Thus, the ICD of ionized-excited,^{7,40,41} doubly ionized, or neutral-excited states of clusters have been observed and investigated theoretically. Moreover, it turns out that this decay process can be initiated not only by photons but also by energetic electrons and positive heavy ions. Experimentally, the ETMD process has been observed in rare gas clusters^{60,62,72,241,242} and alkali-doped helium droplets.^{66,243–245} Recently, Unger *et al.*⁷¹ have investigated the ETMD process in LiCl aqueous solution. The ETMD process has been studied theoretically in hydrogen bonded clusters.^{69,246} Recently, Ghosh *et al.*⁶⁷ have investigated the ETMD process in the HeLi_2 cluster. Their investigation has shown that the multi-mode nuclear dynamics play a significant role in the ETMD process. The ETMD process has also been investigated theoretically in microsolvated clusters.²⁴⁷

The high efficiency of interatomic decay processes (i.e. ICD, ETMD) makes it imperative to take these interatomic decay processes into account for proper understanding of physico-chemical phenomena induced in biological systems by ionizing radiation and related to radiation damage. First, ICD and ETMD result in the production of low energy electrons (LEEs) through ionization of the medium. LEEs are known to be very effective in causing

DNA strands to break through the resonant dissociative attachment mechanism.²⁴⁸ Second, the ionization of the medium produces genotoxic radicals such as the hydroxyl radical OH. Third, both LEE and radicals are produced locally close to where an ionizing particle initially deposits energy. If this happens close to the DNA molecule, the probability of the complex being damaged significantly increases. The feasibility of ICD and ETMD among biologically relevant species was investigated theoretically.^{76-82,84-88,91,92} Microsolvated clusters with alkali metal cations serve as a model system for a natural biological system because ions can impact the intracellular and extracellular activities, i.e., the movement of enzymes²⁴⁹ and activities and conformers of proteins.²⁵⁰ Na⁺ and K⁺ ions are the key components of the sodium-potassium pump in the human body. These ions also help to transmit the signals inside the brain.²⁵¹ The proper functioning of Na⁺ and K⁺ ions helps us to avoid neurological diseases.²⁵² Therefore, the investigation of interatomic or intermolecular decay processes in microsolvated clusters will shed light on chemistry related to radiation damage. The decay rate of the interatomic decay process specifically depends on the energy of the initially ionized or excited state. Therefore, the proper treatment of the initially ionized or excited state is necessary to calculate the lifetime of the interatomic decay process. The ionization potential equation-of-motion coupled-cluster method¹⁶³⁻¹⁶⁶ augmented by complex absorbing potential^{187-190,193,194,207,208,218} (CAP-IP-EOM-CC) method provides proper treatment of ionized states or excited states with the inclusion of correlation effects (dynamic and non-dynamic) as well as continuum ones. Therefore, the CAP-IP-EOM-CCSD method¹⁹⁵⁻²⁰⁰ is promising to describe the interatomic decay process efficiently.

In this chapter, We have reported the implementation of the highly correlated CAP-IP-EOM-CCSD method, which is a combination of the CAP approach and equation-of-motion coupled cluster²⁰¹⁻²⁰⁶ approach to study the ETMD decay mechanism in microsolvated Li⁺-(H₂O)_n (n=1,3) systems, ICD in Na⁺-(H₂O)_n;n=1,2 and Auger decay in K⁺-(H₂O). To see the effect of the environment on the decay of Li 1s state, We have chosen two iso-electronic systems, i.e., Li⁺-NH₃ and Li⁺-H₂O. I compare my findings with the existing theoretical and

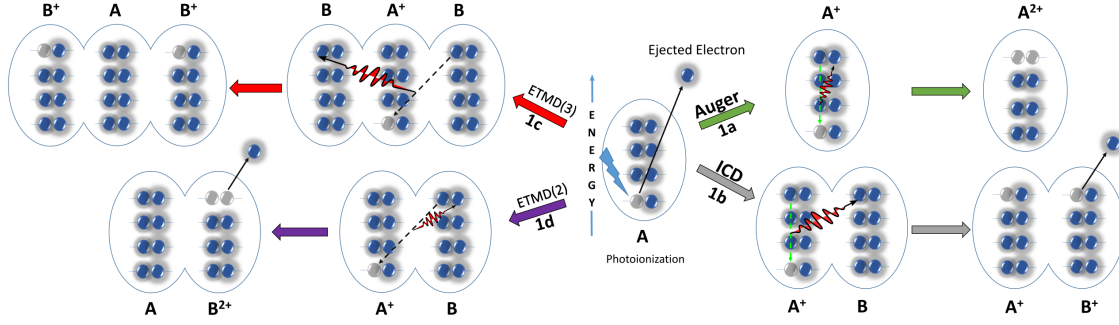


Figure 2.1: Various non-radiative decay processes: 1a Auger decay, 1b ICD, both 1c and 1d ETMD processes. 3 and 2 represent the number of atoms in 1c and 1d, respectively.

experimental data. This chapter is organized as follows: in Section 2.3, We briefly discuss the equation-of-motion coupled-cluster theory along with the CAP approach. Results and discussion are presented in Section 2.4. In Section 2.5, we conclude our findings.

2.3 Theory

2.3.1 Complex absorbing potential based equation-of-motion coupled cluster

To calculate the position and lifetime of the decaying state, We have used the CAP-IP-EOM-CCSD method. In this section, We discuss the CAP-IP-EOM-CCSD method briefly. The decaying states are associated with the complex eigenvalues within the formulation of Siegert.¹⁸⁶

$$E_{res} = E_R - i\frac{\Gamma}{2} \quad (2.3.1)$$

where E_R represents the resonance position and Γ is the decay width. The relation between decay width and lifetime τ is given by

$$\tau = \frac{\hbar}{\Gamma} \quad (2.3.2)$$

The meta-stable states are not square-integrable. They can also be seen as discrete states embedded into the continuum. Hence to describe the metastable states, we require a method that can simultaneously treat electron correlation and the continuum. CAP and complex scaling^{190,219–231} are two well-known methods used for the calculation of resonance energies. Complex absorbing potential (CAP)^{187–190,193,194,207,208,218} along with quantum chemical methods is one of the simplest and the favoured approach. CAP has been implemented in many of the quantum chemical methods for the calculation of resonance states.^{41,43,45,201–208} CAP along with EOM-CCSD has been used very successfully for the study of ICD and the shape resonance phenomena.

In the CAP approach, a one-particle potential $-i\eta W$ is added to the physical Hamiltonian, making the original Hamiltonian complex symmetric and non-hermitian (i.e., $\hat{H}(\eta) = \hat{H} - i\eta W$). As a result, we obtain complex eigenvalues from the CAP augmented Hamiltonian ($\hat{H}(\eta)$). The real part denotes the resonance position, and the imaginary part gives half of the decay width. In $\hat{H}(\eta) = \hat{H} - i\eta W$, η represents the CAP strength, and W is a local positive-semidefinite one-particle operator. With the appropriate choice of CAP, the eigenfunctions of the complex symmetric Hamiltonian become square-integrable, and eigenvalues are discrete. ($\hat{H}(\eta)$) is solved for various η values. The resonance energy is obtained by diagonalizing the complex Hamiltonian matrix $\hat{H}(\eta)$ for multiple values of η . The η trajectory is obtained by plotting the real and imaginary parts of energy. The local minimum of trajectory is associated with the position and half decay width of the decaying state.

$$v_i(\eta) = \eta \frac{\delta E_i}{\delta \eta} \quad (2.3.3)$$

The value of η for which $v_i(\eta)$ is minimum gives the optimal CAP strength. We have used

a box shape CAP. CAP is applied in the peripheral region so that the target remains unperturbed, yet scattered electrons are absorbed.

In the EOM-CC approach, the target state is generated by the action of a CI-like linear operator onto the initial reference state (closed shell coupled cluster reference state). The wavefunction for the k^{th} ionized state $|\Psi_k\rangle$ is expressed as

$$|\Psi_k\rangle = \hat{R}(k)|\Phi_{cc}\rangle \quad (2.3.4)$$

where $\hat{R}(k)$ is an ionization operator. The form of the linear operator for the electron ionized state can be written as

$$\hat{R}(k) = \sum_i r_i(k) i + (1/2) \sum_{ija} r_{ij}^a(k) a^\dagger j i \quad (2.3.5)$$

The reference CC wave function, $|\Phi_{cc}\rangle$ can be written as

$$|\Phi_{cc}\rangle = e^{\hat{T}} |\Phi_0\rangle \quad (2.3.6)$$

where $|\Phi_0\rangle$ is the N-electron closed-shell reference determinant (restricted Hartree-Fock determinant (RHF)) and T is the cluster operator. In the coupled cluster singles and doubles (CCSD) approximation, the T operator can be defined as follows:

$$\hat{T} = \sum_{ia} t_i^a a_a^\dagger a_i + 1/4 \sum_{ab} \sum_{ij} t_{ij}^{ab} a_a^\dagger a_b^\dagger a_i a_j \quad (2.3.7)$$

The indices denoted as a, b, and so on are the virtual spin orbitals, while indices i, j, and so on are the occupied spin orbitals. In IP-EOM-CCSD framework, the final ionized states

are obtained by diagonalizing the coupled cluster similarity transformed Hamiltonian within a $(N - 1)$ electron space.

$$\bar{H}_N \hat{R}(k) |\Phi_0\rangle = \omega_k \hat{R}(k) |\Phi_0\rangle \quad (2.3.8)$$

Where

$$\bar{H}_N = e^{-\hat{T}} \hat{H}_N e^{\hat{T}} - E_{cc} \quad (2.3.9)$$

\bar{H}_N is the similarity transformed Hamiltonian and ω_k is the energy change connected with the ionization process. In the IP-EOM-CCSD approach, the matrix is generated in the 1hole and 2hole 1particle (2h-1p) subspace. Diagonalization of the matrix gives us ionization potential values.

In principle, CAP can be implemented at the self-consistent field (SCF)/ Hartree-Fock, coupled cluster (CC) or EOMCC level. Adding CAP at the coupled cluster level makes the cluster amplitudes complex; hence, all the further calculations are complex. The N electron ground state should be unperturbed. Adding CAP at the CC or SCF level perturbs the N electron ground state. In this case, we need to correct the N electron ground state by removing the perturbation to get the correct decay width.

$$|\Phi_{cc}(\eta)\rangle = e^{\hat{T}(\eta)} |\Phi_0\rangle \quad (2.3.10)$$

$$\bar{H}_N(\eta) = e^{\hat{T}(\eta)} \hat{H}_N(\eta) e^{\hat{T}(\eta)} - \langle \Phi_0 | e^{\hat{T}(\eta)} \hat{H}_N(\eta) e^{\hat{T}(\eta)} | \Phi_0 \rangle \quad (2.3.11)$$

The resonance energy is obtained as

$$E_{res}(\eta) = \omega_k(\eta) + E_{cc}(\eta) - E_{cc}(\eta = 0) \quad (2.3.12)$$

Thus, we lose the advantage of computing resonance energy as the direct energy difference obtained as eigenvalues of $\bar{H}_N(\eta)$ using the IP-EOM-CCSD approach. Our previous study of resonance,¹⁹⁶ shows that the results are not affected when we implement CAP at the IP-EOM-CCSD level. In our calculation for the decay width, we have added the CAP potential in the particle-particle block of the one-particle \bar{H}_N matrix, leaving our N electron ground state unaffected. Therefore, the $\bar{H}_N(\eta)$ can be written as

$$\bar{H}_N(\eta) = e^{\hat{T}(\eta=0)} \hat{H}_N(\eta) e^{\hat{T}(\eta=0)} - \langle \Phi_0 | e^{\hat{T}(\eta=0)} \hat{H}_N(\eta=0) e^{\hat{T}(\eta=0)} | \Phi_0 \rangle \quad (2.3.13)$$

To generate the η trajectory for locating the stationary point, we need to run the CAP-IP-EOM-CCSD calculations thousands of times. We start with $\eta = 0$ and then proceed with small incremental η values. Since IP-EOM-CCSD scales as N^6 , it makes our calculations computationally intensive. Convergence of the equations for various η values may be difficult as we are interested in the inner valence state, and the presence of a metal ion may add to the problem. Hence, we have used the full diagonalization of the matrix using BLAS routines. The dimension of the matrix usually is $NH + NH * NH * NP$ in a given basis for a system where NH and NP represent the number of occupied and unoccupied orbitals.

2.4 Results and discussion

This chapter has studied the decay mechanism of the microsolvated clusters of small cations like Li^+ , Na^+ , K^+ with water. The bond distance, different environments, and the number of neighbours play an important role in the decay process. So, we have studied the behaviour of the decay width in microsolvated clusters as a function of the following parameters:

a) Effect of different molecular environments on decay width for ETMD: We have studied the decay of the Lithium 1s state in Li^+ -water and Li^+ -ammonia. Ammonia resembles the amino group found in bio-molecules and it is iso-electronic with water also. This is the main

Table 2.1: Effect of variation of basis set on decay width of the Li 1s state in $\text{Li}^+\text{-H}_2\text{O}$ for ETMD process

Basis	Energy (eV)	Width(meV)	lifetime(fs)
aug-cc-pVDZ	72.36	11	60
aug-cc-pVDZ+F(O)	72.32	12	56
aug-cc-pVTZ	71.89	6.6	98
aug-cc-pVTZ+F(O)	72.16	7	96

reason to choose these systems to study the effect of different environments on the ETMD process. b) To check the impact of an increasing number of surrounding molecules on the decay width for ETMD: We have studied the decay of the Li^+ 1s state in $\text{Li}^+\text{-(H}_2\text{O)}_n$; $n=1,3$. c) To see the effect of bond distance on the decay width for ICD: We have studied the decay of the 2s state of Na^+ in $\text{Na}^+\text{-H}_2\text{O}$ at various bond lengths. The distance between sodium and oxygen is varied. d) To study the effect of polarization on the decay width, we have studied $\text{Li}^+\text{-water}$ and $\text{Na}^+\text{-water}$ systems in the gaseous and liquid phases. We have used the PCM model²⁵³ to study the liquid phase.

We have studied ICD of the Sodium 2s state in $\text{Na}^+\text{-(H}_2\text{O)}_n$; $n=1,2$ and Auger decay of potassium 2s and 2p states in $\text{K}^+\text{-(H}_2\text{O)}$. Geometries were optimized using the Gaussian09²⁵⁴ software package. For the rest of the calculations, the codes used are homegrown.

2.4.1 Choice of basis set for ETMD process of 1s state of Li^+ in $\text{Li}^+\text{-H}_2\text{O}$

We have studied $\text{Li}^+\text{-water}$ in four different basis sets. Basis-A is an aug-cc-pVDZ basis set.²⁵⁵ Basis-B is constructed by adding an extra Rydberg type f function on the oxygen atom of the water molecule in Basis-A. In the $\text{Li}^+\text{-water}$ system, after ionizing the electron from the 1s orbital of lithium, an electron will be transferred from oxygen to fill the 1s vacancy created on lithium. The excess energy will be used to knock out a secondary electron from oxygen. Thus, it is important to have a Rydberg-type function on oxygen to get the continuum effect. The exponent of the f function is constructed according to the method of Kaufmann et

al.²⁵⁶ Basis-C is an aug-cc-pVTZ basis set.²⁵⁷ Basis-D is constructed using the aug-cc-pVTZ basis set on lithium and oxygen atoms and the cc-pVTZ basis set for the hydrogen atom. In basis-D, an extra Rydberg f function is added to the oxygen atom, similar to the basis-B. The CAP box side lengths are chosen to be $C_x = C_y = \delta c$ and $C_z = \delta c + R/2$ a.u. The δc value is chosen to be 5.0 a.u for the aug-cc-pVDZ basis set and 6 a.u for the aug-cc-pVTZ basis set. Table 2.1 reports the resonance position and decay width (lifetime) for the Lithium 1s state in all four basis sets. The triple zeta (TZ) quality basis reduces the decay position by 0.5 eV. The addition of the Rydberg f function on oxygen has minimal effect on the decay position (i.e., ionization potential) and the decay width in double zeta and triple zeta basis sets. For the Li^+ -water dimer and trimer study, we have used basis-A (i.e., aug-cc-pVDZ basis²⁵⁵) as the method scales N^6 , making it computationally expensive with the higher basis set.

2.4.2 Effect of different molecular environments on the ETMD process

To see the impact of different molecular environments on the decay of the lithium 1s state, we have chosen Li^+ - NH_3 and Li^+ - H_2O as study systems. Since they are iso-electronic systems, they are relevant systems to study the effect of different molecular environments on the decay width of lithium 1s state for the ETMD process. We have used the aug-cc-pVTZ + Rydberg 1f function on oxygen and nitrogen. The δc value is chosen to be 6.0 a.u. We have presented our results in Table 2.2.

The ionization potential of the Li 1s state is 71.89 eV and 71.18 eV in Li^+ - H_2O and Li^+ - NH_3 , respectively. The decay widths are 7 meV and 8 meV, respectively. The decay is faster in Li^+ - NH_3 (lifetime of 81 fs) than the Li^+ - H_2O (lifetime of 96 fs). It means that the transfer of the electron to the 1s vacant position of the Li atom is faster in the case of ammonia than water. It can be explained on the following basis a.) Electronegativity: Oxygen is a more electronegative atom than nitrogen, making the electron transfer slower in case of water than ammonia. b.) Position of lone pair electron: The position of the lone pair electron in the Li^+ - NH_3 is between Li^+ and nitrogen. In Li^+ - H_2O , the position of lone pair

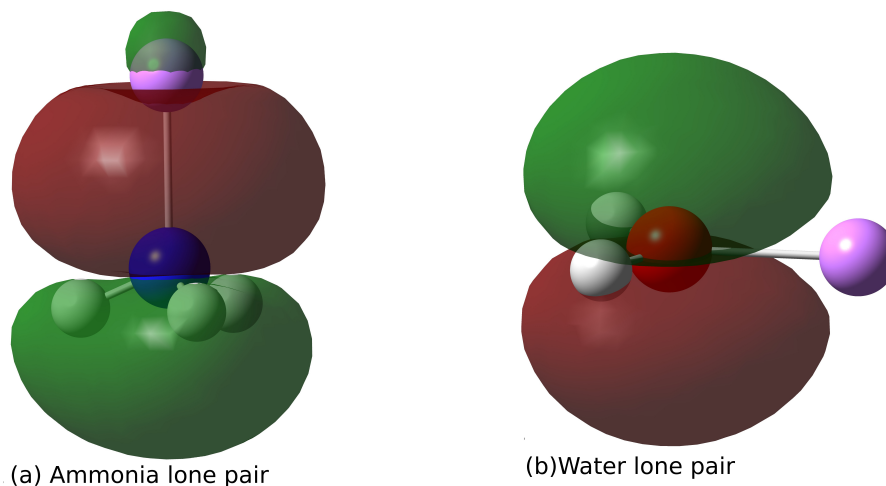


Figure 2.2: a) Orientation of lone pair in $\text{Li}^+ - \text{NH}_3$ is toward Li atom, making electron transfer easier, hence a shorter lifetime. b) The direction of the lone pair in $\text{Li}^+ - \text{H}_2\text{O}$ is perpendicular to the molecular plane, making electron transfer difficult and, thus, a more significant lifetime. The above picture is generated for isosurface value 0.02 eA^{-3} . Atom colour code Pink: Lithium, Blue: Nitrogen, Red: Oxygen, and White: Hydrogen.

Table 2.2: Effect of different molecular surroundings on ETMD process for Li 1s state in $\text{Li}^+ - \text{H}_2\text{O}$ and $\text{Li}^+ - \text{NH}_3$ using aug-cc-pVTZ+1f basis set.

System	Energy (eV)	Width (meV)	lifetime(fs)
$\text{Li}^+ - \text{H}_2\text{O}$	71.89	7	96
$\text{Li}^+ - \text{NH}_3$	71.18	8	81

is perpendicular to $\text{Li}^+ - \text{H}_2\text{O}$ molecular plane (not in between Li^+ and oxygen); see figure-2.2. Because of the directional nature of the p-orbital and lone pair's orientation toward lithium, electron transfer is much faster in case of ammonia than water. Orbitals of figure-2.2 are generated by Gaussian09²⁵⁴ software package using density functional theory with B3LYP functional²⁵⁸⁻²⁶¹ and aug-cc-pVTZ basis set.²⁵⁷ The error bar of the IP-EOM-CCSD method is larger than 1meV. However, the trend should remain the same. To confirm this, we have calculated the ionization potential (IP) for both systems using CCSD(T) method. The IP values are 71.81 eV and 71.18 eV for $\text{Li}^+ - \text{H}_2\text{O}$ and $\text{Li}^+ - \text{NH}_3$ with partial inclusion of triples, respectively. We hope that the qualitative trend for decay width will be similar. Hence concluding that the $\text{Li}^+ - \text{NH}_3$ decays faster than the $\text{Li}^+ - \text{H}_2\text{O}$ should remain the same.

2.4.3 Li^+ -water clusters: Effect of the increasing number of water molecules in surrounding on the ETMD process

For the Li^+ -water dimer and trimer systems aug-cc-pVDZ basis set has used. The CAP box size used for the dimer is $C_x = 8$ a.u; $C_y = C_z = 5$ a.u. and $C_x = C_y = 10$ a.u; $C_z = 5$ a.u for the trimer. The Li^+ ion is a good example to study the ETMD process since it has only core electrons. Therefore, ICD and Auger decay processes cannot occur in this system.

If the Li^+ -water cluster is ionized by removing an electron from the 1s subshell of the Li^+ ion, then the molecule relaxes via the ETMD process. The ETMD process of $\text{Li}^{2+}(1s^{-1}2s^{-1})$ state in Li^+ -water clusters can be described as follows. After removing an electron from the 1s orbital of Li^+ ion in $\text{Li}^+-\text{H}_2\text{O}$ (i.e., formation of $\text{Li}^{2+}-\text{H}_2\text{O}$), the 1s vacancy of $\text{Li}^{2+}(1s^{-1}2s^{-1})$ ion is filled up by a 2p outer valence electron of the oxygen atom of one of the water molecules. Then, the released energy emits a secondary outer valence electron from the same or another water molecule. Therefore, the final state ($\text{Li}^+-\text{H}_2\text{O}^{2+}$ or $\text{H}_2\text{O}^+-\text{Li}^+-\text{H}_2\text{O}^+$) of the ETMD process is a double ionized state (with respect to our initial system, i.e., $\text{Li}^+-\text{H}_2\text{O}$). The $\text{Li}^+-\text{H}_2\text{O}^{2+}$ final state is produced via an ETMD(2) process, where both the positive charges are present on one water molecule. The $\text{H}_2\text{O}^+-\text{Li}^+-\text{H}_2\text{O}^+$ double ionized final state (with respect to our initial system, i.e. $\text{Li}^+-\text{H}_2\text{O}$) is produced via ETMD(3). The ETMD channel is open for the 1s ionized state of Li^+ ion because the energy of the $\text{Li}^{2+}(1s^{-1}2s^{-1})$ state lies above the double ionized final states (i.e. $\text{Li}^+-\text{H}_2\text{O}^{2+}$ or $\text{H}_2\text{O}^+-\text{Li}^+-\text{H}_2\text{O}^+$). Thus, the positively charged water molecules will repel the positively charged Lithium ion leading to a Coulomb explosion. The different variants of ETMD (i.e. ETMD(2) or ETMD(3)) may be possible with an increasing number of water molecules surrounding the Li^+ ion. The 1s ionization energy of the Li^+ ion in Li^+ -water cluster varies from 72.35 to 67.45 eV depending on the number of water molecules present in the surroundings of Li^+ ion. Here, we have calculated the lifetime of 1s ionized state of Li^+ ion in various Li^+ -water clusters.

In figure-2.3, we have plotted the decay values for the $\text{Li}^+-(\text{H}_2\text{O})_n; n=1,3$ system, where

the aug-cc-pVDZ basis set is used. As we move from the monomer to the trimer, the decay position reduces from 72.35 eV to 67.45 eV. On the other hand, the decay width increases from 11 meV to 63 meV. There are two factors that can affect the decay width: first, the bond distance between the Li^+ and H_2O molecules and second, the number of surrounding water molecules. The bond length does not seem to have much effect as we move from the monomer (1.867 Å) to the dimer (1.86 Å). Therefore, the number of decay channels play a significant role in increasing the decay width as we move from monomer to dimer. From figure-2.3, we have noticed that the decay width increases nonlinearly. The possible reason for the nonlinear growth of the decay width is that the number of decay channels increases nonlinearly with an increasing number of water molecules surrounding the Li^+ ion. Cederbaum and Müller⁶⁹ have studied $\text{Li}^+-\text{H}_2\text{O}$ with up to five water molecules using a perturbation theory ansatz with SCF integrals. They estimated lifetimes in the range of 100-20 fs. Our results give the decay time range from 60 fs to 10 fs from monomer to trimer in the aug-cc-pVDZ basis.²⁵⁵ In the aug-cc-pVTZ basis set,²⁵⁷ we obtained a lifetime of 98 fs, which is in good agreement with the Cederbaum and Müller. See reference²⁶² for details of the IP and DIP spectra of the $\text{Li}^+(\text{H}_2\text{O})_n$ complex.

2.4.4 Na^+ -water cluster: Effect of distance and increasing number of water molecules on the ICD process

The 2s ionized state of the Na atom in the $\text{Na}^+-\text{H}_2\text{O}$ system can relax via the ICD process. The ICD process of the 2s ionized state of the Na atom in the $\text{Na}^+-\text{H}_2\text{O}$ system can be described as follows: after removing an electron from the 2s subshell of Na atom, the 2s vacancy of the Na atom in the $\text{Na}^{2+}-\text{H}_2\text{O}$ is filled up by a 2p outer valence electron of the Na atom. Then the released energy is transferred to the neighbouring H_2O molecule which emits a secondary electron. Therefore, the final state of the ICD process is characterized by the $\text{Na}^{2+} (2p^{-1}3s^{-1}) \text{O}^+\text{H}_2 (2p^{-1})$ triple ionized state. Energetically, the ICD process is possible in the $\text{Na}^+-\text{H}_2\text{O}$ system because the energy of the 2s ionized state of the Na atom

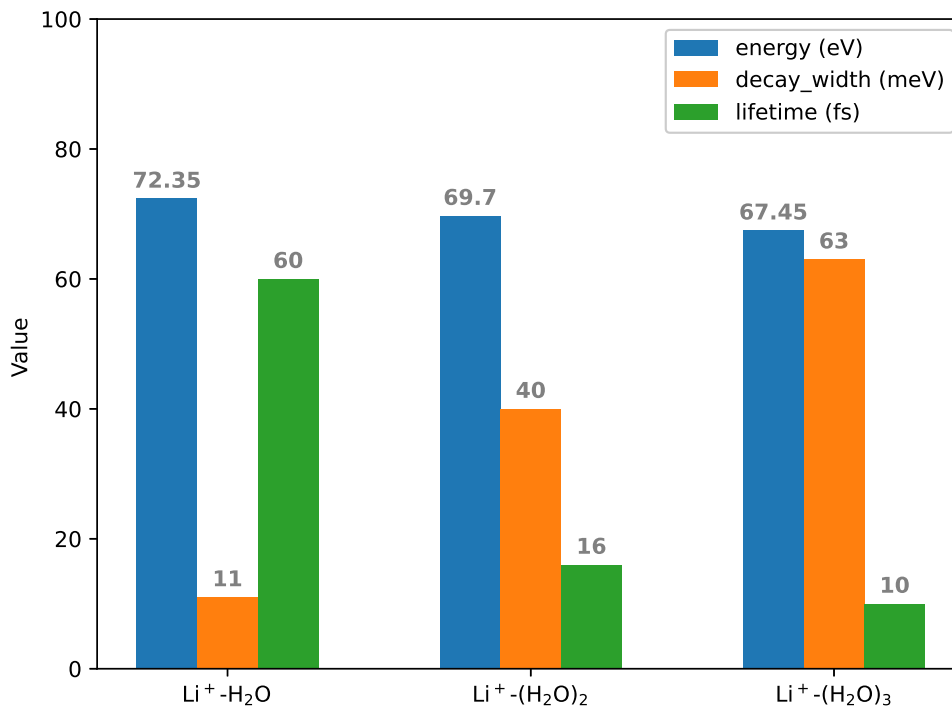


Figure 2.3: Effect of the increased number of surrounding water molecules on ETMD process using an aug-cc-pVDZ basis set.

lies above the energy of the $\text{Na}^{2+} (2p^{-1}3s^{-1}) \text{O}^+\text{H}_2(2p^{-1})$ final state.

The decay of the Sodium 2s state in the $\text{Na}^+\text{-H}_2\text{O}$ system is studied in a modified maug-cc-pV(T+d)Z²⁶³ basis set and augmented by 3s3p1d functions for Oxygen atom only (taken from the basis set exchange library,²⁶⁴ then modified) for sodium and oxygen and cc-pVDZ²⁵⁵ for hydrogen. The detailed basis set used for the system is described in supporting information. To see the effect of bond length on the decay width, we have studied the $\text{Na}^+\text{-water}$ system for various bond lengths, i.e. 2.24988 Å to 5.0 Å between the sodium and the oxygen atom. The geometry was optimized using the CCSD method in the aug-cc-pVDZ basis²⁵⁵ and the bond distance between sodium and oxygen was found to be 2.24988 Å. Thus, we have used this bond distance. The CAP box size used in our calculation is $C_x = 8.7$, $C_y = 6.5$ and $C_z = 5.0$ a.u. Figure-2.4 summarizes the results for various bond lengths. We know from equation 2 that the decay width and lifetime of a temporary bound state (TBS) are inversely proportional to each other. We observe that the lifetime increases rapidly as the bond length

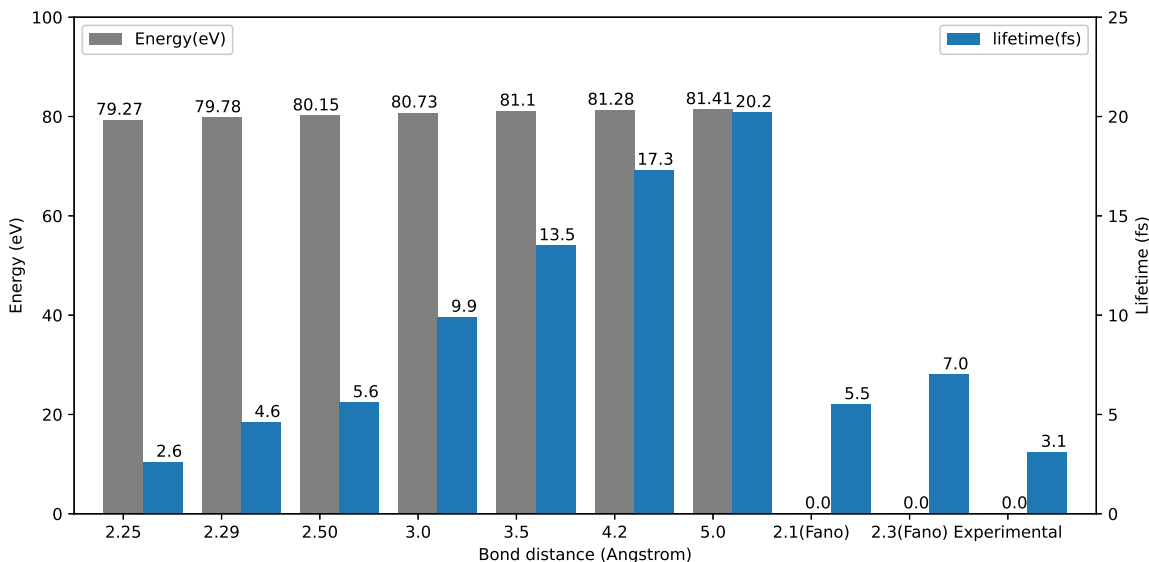


Figure 2.4: Effect of bond length on ICD process for the 2s state of Na in $\text{Na}^+\text{-H}_2\text{O}$ using maug-cc-pV(T+d)Z basis set.

increases or the decay width rapidly decreases with an increase in the bond length. A sharp change in decay width from 251 meV (2.6 fs) at 2.24988 Å to 142 meV (4.6 fs) at 2.29 Å is observed. Then it saturates at 33 meV (20 fs) at 5.0 Å. It may become bound with a further increase in the bond length. We also report the Fano-ADC²⁴⁶ results at 2.30 Å, which uses cc-pCVTZ+2s2p2d1f KBJ²⁵⁶ basis for sodium and oxygen and cc-pVTZ+1s1p1d KBJ²⁵⁶ for hydrogen. The lifetime of 7 fs was reported using the Fano-ADC method. The experimental²⁶⁵ value of the decay time of the Na 2s state is 3.1 fs. Our results predict the decay time to be 2.6 fs at the equilibrium bond length which shows good agreement with the experimental value.

To see the effect of the increased number of surrounding molecules on the decay width in the ICD process, we also studied the $\text{Na}^+\text{-water}$ dimer. The optimized geometry was obtained using the B3LYP functional²⁵⁸⁻²⁶¹ and the 6-311++g(3d,2p) basis set²⁶⁶ in the Gaussian09²⁵⁴ software package. The CAP box size used for the $\text{Na}^+\text{-water}$ system in our calculation is $C_x = 12$, $C_y = 7$ and $C_z = 7$ a.u. We have used a spherical basis set for the $\text{Na}^+\text{-water}$ dimer due to scaling of the CC equations (i.e., in a cartesian basis, the $\text{Na}^+\text{-water}$ dimer is

Table 2.3: Different decay process in different systems: Auger decay in K^+-H_2O , ICD in $Na^+-(H_2O)_n$ and ETMD in $Li^+-(H_2O)_n$ (where $n=1,2$).

Basis	System	Energy (eV)	Width in meV (fs)
maug-cc-pV(T+d)Z [@]	Li ⁺ -H ₂ O	71.81	7.64 (86)
maug-cc-pV(T+d)Z [@]	Li ⁺ -(H ₂ O) ₂	69.03	16.12 (40.8)
maug-cc-pV(T+d)Z ^{**}	Na ⁺ -H ₂ O	79.49	129 (5.1)
maug-cc-pV(T+d)Z ^{**}	Na ⁺ -(H ₂ O) ₂	78.19	305 (2.1)
aug-cc-pVDZ-X2C	K ⁺ -H ₂ O (2s)	396	423 (1.5) 278 (2.4)*
aug-cc-pVDZ-X2C	K ⁺ -H ₂ O (2p)	315	74.86 (8.8) 246 (2.7)*

* represents the 2nd decay value that we have observed.

** represents the maug-cc-pV(T+d)Z + 3s3p1d on O atom in Spherical basis.

@ represents the maug-cc-pV(T+d)Z + 3s3p1d on O atom in Cartesian basis.

computationally very expensive). To compare $Na^+-(H_2O)_2$ with Na^+-H_2O , we again run Na^+-H_2O in a spherical basis set. In $Na^+-(H_2O)_2$ and Na^+-H_2O , the bond distances between sodium and oxygen are 2.2453 and 2.24988 Å, respectively. The decay width of the 2s state of Sodium in $Na^+-(H_2O)_2$ is 305 meV (2.1 fs) compared to 129 meV (5.1 fs) in Na^+-H_2O .

2.4.5 Auger Decay process for the 2s and 2p ionized states of K in K⁺-water

The 2s and 2p ionized states of the K atom in the K^+-H_2O can relax via the Auger process. In our calculations, we have used the optimized geometry for K^+-H_2O obtained using the B3LYP functional²⁵⁸⁻²⁶¹ and the 6-311++g(3d,2p) basis set²⁶⁷ in the Gaussian09²⁵⁴ software package. For the computation of the decay width, we have employed the aug-cc-pVDZ-X2C basis set²⁶⁸ for potassium, aug-cc-pVDZ²⁵⁵ for oxygen and the cc-pVDZ basis set²⁵⁵ for hydrogen. The results for the 2s and 2p ionized states are presented in Table-2.3 along with $Li^+-(H_2O)_n$ and $Na^+-(H_2O)_n$; $n=1,2$. Here, for the $Li^+-(H_2O)_n$; $n=1,2$, we have used the

maug-cc-pV(T+d)Z²⁶³ + 3s3p1d basis set on Oxygen while for Li we have used maug-cc-pV(T+d)Z basis set²⁶³ to maintain consistency. The CAP box size used for K⁺-water system in our calculation is $C_x = 7$, $C_y = 4$ and $C_z = 4$ a.u. In the case of the K⁺-H₂O system, we observed two stationary points on the η trajectory indicating decay through a cascade mechanism. Experimentally, a similar kind of two stationary points (cascade decay type effect) was observed.²⁶⁹ The η trajectory shows only one stationary point for the other two systems (Li⁺-H₂O, Na⁺-H₂O).

The Auger process of the (2s, 2p) ionized state of the K atom in K⁺-H₂O (4s⁻¹) can be rationalized as follows: After removing an electron from the 2s or 2p subshell of the K atom in K⁺-H₂O (formation of K²⁺-H₂O)(2s⁻¹ 4s⁻¹ or 2p⁻¹ 4s⁻¹), the 2s or 2p vacancy is filled up by a 3p or 3s outer valence electron of the K atom. Then the released energy is used to knock out another secondary outer valence electron from the 3p or 3s subshell of the K atom (formation of K³⁺-H₂O). This two-hole state (K³⁺(3p⁻² 4s⁻¹)H₂O or K³⁺(3p⁻¹ 3s⁻¹ 4s⁻¹)H₂O or K³⁺(3s⁻² 4s⁻¹)H₂O) (which is with respect to our initial system K⁺-H₂O) is unstable and further relax via another decay process which is a three-hole state. Energetically the Auger process will be viable if the energy of the 2s or 2p ionized state of the K atom lies above the triple ionized final states. The calculation of the three-hole state is beyond the scope of this thesis.

The Auger decay width for the 2p ionized state is 75 meV (i.e. 8.8 fs) which undergoes further decay with a decay width of 246 meV corresponding to a lifetime of 2.7 fs. Similarly, the Auger decay width for the 2s ionized state is 423 meV with a lifetime of 1.5 fs which undergoes further decay with a decay width of 278 meV corresponding to a lifetime of 2.4 fs. Pokapanich et al.²⁷⁰ have studied the Auger decay in potassium chloride surrounded by water molecules.

Table 2.4: Polarization effect on decay width in ETMD and ICD processes for $X^+ - H_2O$ system ($X = Li, Na$).

Basis	System	medium	Energy (eV)	Width in meV(fs)
aug-cc-pVDZ +F(O)	$Li^+ - H_2O$	GAS	72.36	12 (56)
aug-cc-pVDZ+F(O)	$Li^+ - H_2O$	PCM	72.3	9.7 (67)
m-aug-cc-PV(T+d)Z	$Na^+ - H_2O$	GAS	79.78	143 (4.6)
m-aug-cc-PV(T+d)Z	$Na^+ - H_2O$	PCM	79.73	108 (6.0)

2.4.6 Polarized Surrounding effect on ETMD and ICD

We have studied the Li^+ -water and Na^+ -water in the gaseous and aqueous medium to see the effect of a polarized surrounding on the decay width in the ETMD and ICD processes, respectively. We have used the PCM model²⁵³ for the aqueous phase, where water is the solvent. The bond distance and CAP box size were kept identical for the gaseous and aqueous phases. The results are presented in Table 2.4. For the Li^+ -water 1s state, the decay position remains almost identical; however, the decay width changes from 12 meV (56 fs) for the gaseous medium to 9.7 meV (67 fs) for the aqueous medium. The decay is slower in the aqueous medium compared to the gaseous medium. A similar trend was observed for the Na^+ -water's 2s state and the decay width changes from 143 meV (4.6) for the gaseous medium to 108 meV (6 fs) for the aqueous medium. The slow decay in the aqueous medium is due to the polarization provided by the medium which makes the ionized state more stable than the gaseous medium.

2.5 Conclusions

This chapter has used the CAP-IP-EOM-CCSD method to study the various decay processes in microsolvated alkali metal ions i.e. Li^+ , Na^+ and K^+ . The CAP-IP-EOM-CCSD method is used for the first time to explore the ETMD lifetimes for the Li 1s state in $Li^+ - H_2O$ clusters. It is observed that the decay widths are sensitive to the bond length, surrounding atoms,

medium (gas or liquid) and the number of neighboring molecules. We have studied the effect of all these parameters on the decay width of $\text{Li}^+\text{-H}_2\text{O}$ and $\text{Na}^+\text{-H}_2\text{O}$ clusters.

We have studied the decay of 1s, 2s, and both 2s and 2p states in Li^+ , Na^+ and K^+ with water, respectively. The Li 1s state undergoes ETMD whereas the Na 2s state decays via ICD. The K 2s and 2p states undergo Auger decay. To study the impact of different molecular environments, the 1s ionized state of the Li atom was studied in $\text{Li}^+\text{-NH}_3$ and $\text{Li}^+\text{-H}_2\text{O}$. Since water and ammonia are isoelectronic, it will be interesting to study the effect of the environment on the decay width. We found that decay is faster in $\text{Li}^+\text{-NH}_3$ (81 fs) than in $\text{Li}^+\text{-H}_2\text{O}$ (96 fs). The possible explanation for this could be, first, the higher electronegativity of oxygen than nitrogen, making electron transfer more difficult than nitrogen. Second, the location of the lone pair. In $\text{Li}^+\text{-NH}_3$, it is between Li^+ and nitrogen, whereas in $\text{Li}^+\text{-H}_2\text{O}$, it is perpendicular to the molecular plane. Because of the directional nature of p-orbitals and the orientation of the lone pair toward lithium, electron transfer is much faster in the case of ammonia than water (See Figure-2.2 for details).

We have studied the ETMD lifetime for the 1s ionized state of the Li atom in the $\text{Li}^+\text{-(H}_2\text{O)}_n$ ($n=1,3$) system to see the effect of the number of water molecules on the decay. The lifetime obtained for the $\text{Li}^+\text{-(H}_2\text{O)}_n$ system is 60 fs, 16 fs and drops further to 10 fs as n increases from 1 to 3. The lifetime of an ETMD exhibits a considerable drop as the number of neighbors increases. This is due to a nonlinear increase in the number of decay channels with an increasing number of surrounding atoms.

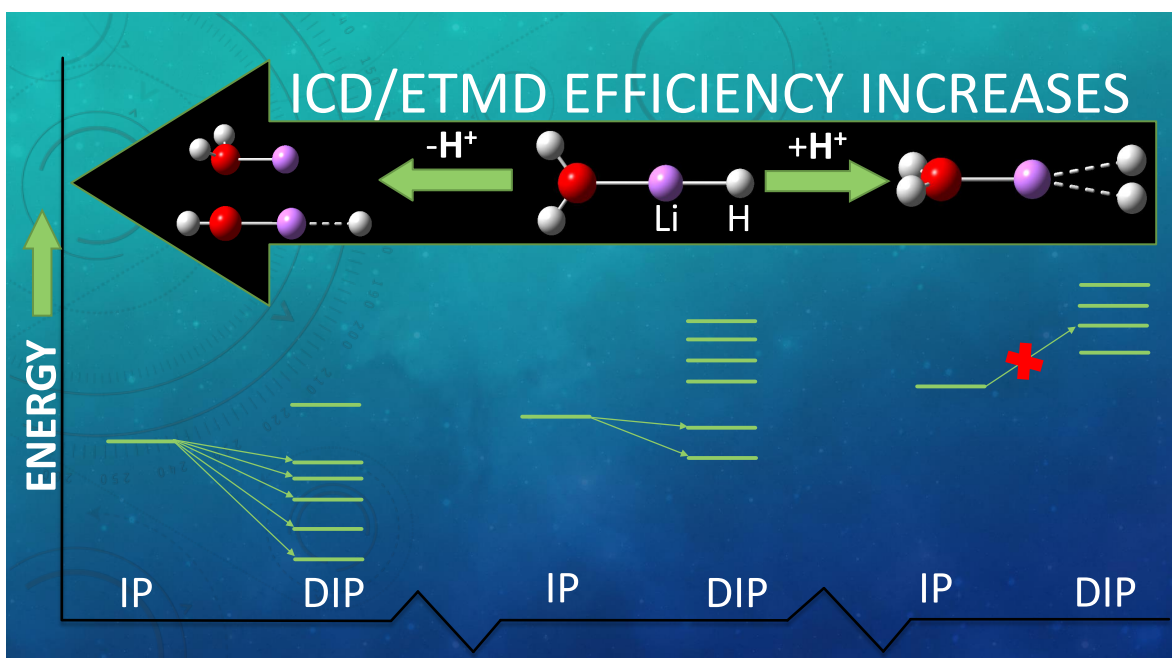
To see the effect of bond length on the decay width for the ICD process, we studied the 2s ionized state of Na atom in $\text{Na}^+\text{-H}_2\text{O}$ at various bond lengths, i.e. 2.2489 Å to 5.0 Å. We observe that as the bond length increases, the decay width reduces and the lifetime increases from 2.6 fs at 2.24 Å to 20 fs at 5.0 Å. A similar trend was observed using the Fano ADC method.²⁴⁷ The authors report a lifetime of 5.5 fs at 2.21 Å and 7 fs at 2.30 Å. Our results for sodium 2s state are in good agreement with the experiment²⁶⁵ and the Fano ADC²⁴⁷ method. We have also investigated the ICD lifetime for the 2s ionized state of the Na atom in the $\text{Na}^+\text{-}$

$(\text{H}_2\text{O})_n$ ($n=1,2$) systems to study the effect of increased water molecules in the surrounding on ICD. The computed ICD lifetime for the $\text{Na}^+-\text{H}_2\text{O}$ system is 5.1 fs, and it decreases strongly to 2.1 fs for the $\text{Na}^+(\text{H}_2\text{O})_2$ system. We have used a spherical Gaussian basis set here for monomer and dimer to have a proper comparison. The sensitivity of the decay width to the spherical or cartesian basis is also observed. We have investigated the Auger lifetime for the 2s and 2p ionized state of the K atom in the $\text{K}^+(\text{H}_2\text{O})$ system. The computed Auger lifetimes for the 2s and 2p ionized states are 2.36 fs and 2.67 fs, respectively. The η trajectory indicates a cascade decay for the $\text{K}^+(\text{H}_2\text{O})$ system. The Auger decay initiates another decay after a short-lived state leading to a more stable state. Since the Auger decay is a localized decay, we do not expect much change with bond length or number of neighbours.

To know the polarization effect on the ICD and ETMD processes, we studied the decay of the 1s state of the Li atom and the 2s state of Na in $\text{Li}^+(\text{H}_2\text{O})$ and $\text{Na}^+(\text{H}_2\text{O})$, respectively. We used the PCM model²⁵³ in our study. In both cases, our results show that the polarization stabilizes the system, i.e., decay time is increased in the liquid phase compared to the gaseous phase. In this chapter, we studied the decay width of alkali metal ions as a function of different molecular environments, increase of surrounding molecules in a system, bond distance, basis set and polarization of the medium.

Chapter 3

Effect of Protonation and Deprotonation on Electron Transfer Mediated Decay and Interatomic Coulombic Decay



3.1 Abstract

Electronically excited atoms or molecules in an environment are often subject to interatomic/intermolecular Coulombic decay (ICD) and/or electron transfer mediated decay (ETMD) mechanisms. A few of the numerous variables that can impact these non-radiative decay mechanisms include bond distance, the number of nearby atoms or molecules, and the polarisation effect. In this chapter, we have studied the effect of protonation and deprotonation on the ionization potential (IP), double ionization potential (DIP), and lifetime (or decay width) of the temporary bound state in these non-radiative decay processes. We have chosen LiH-NH₃ and LiH-H₂O as test systems. The equation of motion coupled cluster singles and doubles method augmented by complex absorbing potential (CAP-EOM-CCSD) has been used in calculating the energetic position of the decaying state and the system's decay rate. Deprotonation of LiH-NH₃/LiH-H₂O either from the metal center (LiH) or from ammonia/water lowers the IP and DIP compared to the neutral systems. In contrast, protonation increases these quantities compared to neutral systems. The protonation closes the inner valence state relaxation channels for ICD/ETMD. For example, the decay of the O-2s/N-2s state stops in protonated systems (LiH₂⁺-H₂O, LiH₂⁺-NH₃, and LiH-NH₄⁺). Our study also shows that the efficiency, i.e., the rate of ICD/ETMD, can be altered by protonation and deprotonation. It is expected to have implications for chemical and biological systems.

3.2 Introduction

The knowledge on the importance of non-radiative processes like interatomic and intermolecular coulombic decay (ICD)^{35,42} and electron transfer mediated decay (ETMD)^{59,60,69,241,242,246} has substantially increased over the past two decades. ICD, first proposed by Cederbaum *et al.*,^{35,42} is a nonlocal and efficient decay mechanism that occurs at the femtosecond timescale. During this process, when an ionized/excited system relaxes non-radiatively in an environment, an electron from an outer valence shell fills the inner valence shell's vacancy, resulting

in a virtual photon emission that knocks out a valence electron from an adjacent atom or molecule. This situation leads to a Coulomb explosion due to the proximity of two positively charged species. The energy transfer happens quickly, i.e. in a few to a hundred femtoseconds. ICD was initially studied theoretically⁴³⁻⁴⁵ and experimentally^{47,48,50,54,70,71} in hydrogen-bonded,³⁷ and weakly bound rare gas clusters.^{36,38} In ETMD, an electron is transferred from a neighboring atom to an initially ionized atom or molecule. The excess energy can knock out a second electron from the same donor atom/molecule in ETMD(2) process. While in ETMD(3), secondary electron ejection occurred from the second adjacent atom/molecule. Since ETMD involves the transfer of electrons from a neighboring species to an initially ionized species, it is usually slower than the ICD. See figure 3.1 for a better understanding of the difference between ICD and ETMD. The low-energy electrons generated during ICD and ETMD have different kinetic energies. One can use this information to identify the specific local environment. Thus, the study of ICD and ETMD is essential to understanding the decay of the ionized inner valence state in an environment. Recent studies^{40,58} show that various factors influence the ICD/ETMD process, like the number of surrounding atoms or molecules, bond distance, geometry, and the medium in which energy/electron transfer happens. The environment can change the lifetime of a temporary bound state (TBS) undergoing ICD / ETMD by stabilizing or destabilizing it. Thus, environmental effects/properties play a particularly relevant role. In this chapter, we explore an important environmental effect: the protonation and deprotonation effect on ICD and ETMD. Specifically, we will study the impact of protonation and deprotonation on ionization potential (IP), Double ionization potential (DIP), and decay width (or the lifetime of TBS). Recently, the effect of protonation and deprotonation on IP and DIP in pure ammonia clusters²⁷¹ has been studied. Still, the impact of protonation and deprotonation on the lifetime of TBS has not been studied. We are the first ones to learn it through this study. The reason to choose LiH-H₂O-related systems is that the effect of protonation and deprotonation (as studied in Chapter 3) on ETMD can only be analyzed using a Li⁺ ion-related system without interference of other decay processes

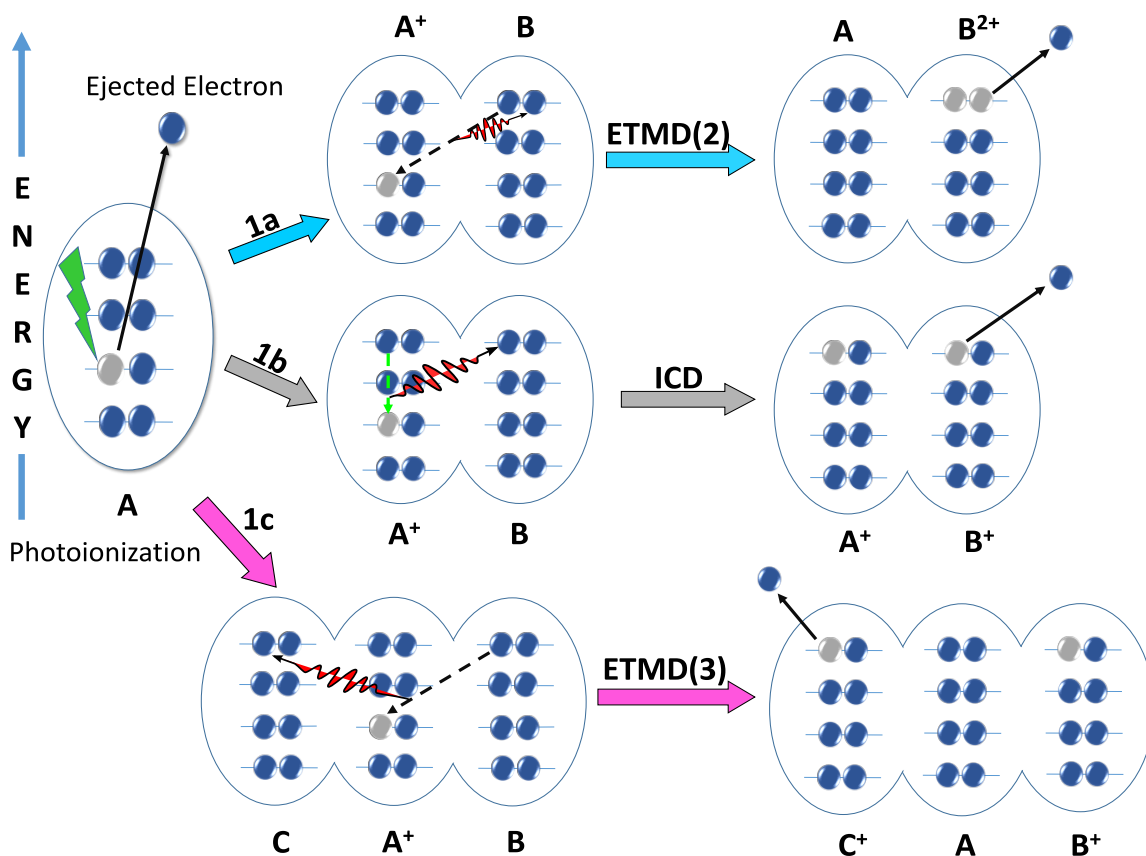


Figure 3.1: Visual representation of electronic decay processes. (1a.) In ETMD(2), an inner valence vacancy is filled by an outer valence electron of the neighboring molecule B, and another valence electron is emitted from the same molecule B, leaving a final AB^{2+} molecular state. (1b.) ICD, a valence electron from molecule A, fills the vacancy, and the released energy is transferred to an outer valence electron of neighboring molecule B. Thus forming A^+B^+ as the final state. (1c.) ETMD(3) process in which the vacancy in molecule A is filled by an outer valence electron of the neighboring molecule B, and ejection of the second electron occurs from another adjacent molecule C, leaving AB^+C^+ as the final state. The number 2 and 3 represents the number of molecules involved in the ETMD process.

because there is no valence electron in Li^+ ion. Since $LiH-H_2O$ -related systems do not exist in biological systems, however, by using these systems, one can gain a high understanding of the behavior of the ETMD process upon protonation and deprotonation, which is very important.

Our aim is to understand the effect of protonation/deprotonation on the ICD/ETMD using alkali metal ions microsolvated in water and ammonia. Understanding this may help us control the relevant process in a chemical environment. This tells us how a change in sur-

rounding and protonation/deprotonation affects the decay process and lifetime of the TBS. The first step towards this will be doing these calculations accurately for a metal ion-water system and its protonated/ deprotonated form with the coupled-cluster methods, which scale as N^6 . To get the decay width, we need to solve the CC equation thousands of times, which makes it computationally expensive. Thus, we wanted to study the smallest possible metal-related system. Therefore, we chose Lithium, although we know that the alkali metals Na^+ , K^+ , etc., are more relevant biologically. Also, as the first step towards this, gas-phase calculations are done. We may have to implement some approximate method for the actual interesting systems. We have discussed our finding and their possible reasons in the results and discussion section, followed by the Conclusion. Last, we have discussed the Computational and Theoretical details of the Equation of motion coupled cluster methods.

3.3 Theory and Computational Details

We will initially examine the computational specifics before going through the decay processes' theory and procedures. Geometries of all molecules were optimized in the Gaussian09 software package²⁵⁴ using B3LYP^{258–261} functional and 6-311++g(2d,p) basis set.²⁷² The IPs of neutral, protonated, and deprotonated clusters are calculated using the equation of motion coupled-cluster singles and doubles (EOM-CCSD) method.^{159,160,167,170} The DIP values are computed using the diagonalization of the 2-hole block of EOM-CCSD. The decay position and width of the system are calculated using the EOM-CCSD method augmented by the complex absorbing potential (CAP).^{187–190,214,218} The aug-cc-pVTZ basis set²⁵⁷ is used for CAP-EOM-CCSD calculations. For information on the CAP-EOM-CCSD technique for ICD, ETMD(2), and ETMD(3), see reference.⁴⁰ For both neutral systems, the CAP-EOM-CCSD computations have been performed with various box sizes. The dimension of optimum box size was found to be $C_x = C_y = C_z = 9$ a.u and δC in protonated, deprotonated, and neutral LiH-NH_3 . $\delta C = R/2$ was added along the molecular axis. For protonated, deprotonated, and

neutral LiH-H₂O systems, box dimensions were $C_x = C_y = C_z = 11$ a.u and δC . Again, the $\delta C = R/2$ value was added along the molecular axis, where R is the length of the molecule in atomic units. Calculations of IP, DIP, and decay widths are done using homegrown codes. We will now quickly go over the CAP-EOM-CCSD methodology.

The target state, which is one hole state, is generated by the action of a linear operator $\hat{R}(k)$ on the ground state wavefunction. The equation for the target state $|\Psi_k\rangle$ can be written as

$$|\Psi_k\rangle = \hat{R}(k)|\Phi_{cc}\rangle \quad (3.3.1)$$

where $|\Phi_{cc}\rangle$ is the coupled-cluster wavefunction. It can be defined as

$$|\Phi_{cc}\rangle = e^{\hat{T}}|\Phi_0\rangle \quad (3.3.2)$$

Where $|\Phi_0\rangle$ is the ground state Hartree-Fock wavefunction, $\hat{R}(k)$ is an ionization operator, and T's ($T = T_1 + T_2$ for CCSD) are hole-particle excitation operators. T and R commute with each other. The linear operator $\hat{R}(k)$ within singles and doubles approximation is written as

$$\hat{R}(k) = \sum_i r_i(k)i + \sum_{i,j,a} r_{ij}^a(k)a^\dagger ji \quad (3.3.3)$$

The similarity transformed Hamiltonian \bar{H}_N is formed as below.

$$\bar{H}_N = e^{-\hat{T}}\hat{H}_N e^{\hat{T}} - \langle\Phi_0|e^{-\hat{T}}\hat{H}_N e^{\hat{T}}|\Phi_0\rangle \quad (3.3.4)$$

The ionization potential values are obtained by diagonalizing the coupled-cluster similarity transformed Hamiltonian within $(N - 1)$ electron space. This similarity transformed Hamil-

tonian is formed within 1-hole and 2-hole one particle space.

$$\bar{H}_N \hat{R}(k) |\Phi_0\rangle = \omega_k \hat{R}(k) |\Phi_0\rangle \quad (3.3.5)$$

Where ω_k is the difference between the N and (N-1) electronic state, which is the IP of the k^{th} state. The position and lifetime of the decaying state are obtained by augmenting the EOM-CCSD by complex absorbing potential (CAP). CAP approach adds a one-particle potential to the physical Hamiltonian $-i\eta W$. This makes the original Hamiltonian complex and non-hermitian $\hat{H}(\eta) = \hat{H} - i\eta W$. Where W is the real potential and η is the strength of CAP. The complex eigenvalues of the non-hermitian Hamiltonian give us the system's position and half decay width. In CAP-EOM-CCSD, we get the total decay width, i.e., the contribution from all possible decay channels. We do not get the decay width for the individual decay process. We solve the $\hat{H}(\eta) = \hat{H} - i\eta W$ equation for various values of η to obtain complex energies that are η dependent. Real part vs. imaginary part of energy plotted in energy plot that shows the η trajectory. The stationary point on the trajectory provides the stabilization point.

3.4 Results and Discussion

We will study the effect of protonation and deprotonation on the IP, DIP, and lifetime of O-2s, N-2s, and Li-1s TBS in the gaseous state. We have chosen LiH-H₂O and LiH-NH₃ as test systems for our study. Protonation and deprotonation can occur either from LiH (metal center) or H₂O/NH₃. Thus, LiH₂⁺-NH₃ and LiH-NH₄⁺ will be formed by the protonation of LiH-NH₃ and Li⁻-NH₃ and LiH-NH₂⁻ by deprotonation. Similarly, for the LiH-H₂O system, we have Li⁻-H₂O and LiH-OH⁻ as deprotonated and LiH₂⁺-H₂O only as a protonated system. Due to the instability of LiH-H₃O⁺, global minima could not be found. Understanding the impact of deprotonation and protonation on ICD and ETMD in microsolvated systems is a step toward helping us control these relevant and abundant processes in various chemical environments and may also be in biological systems. We will first study, analyze and then

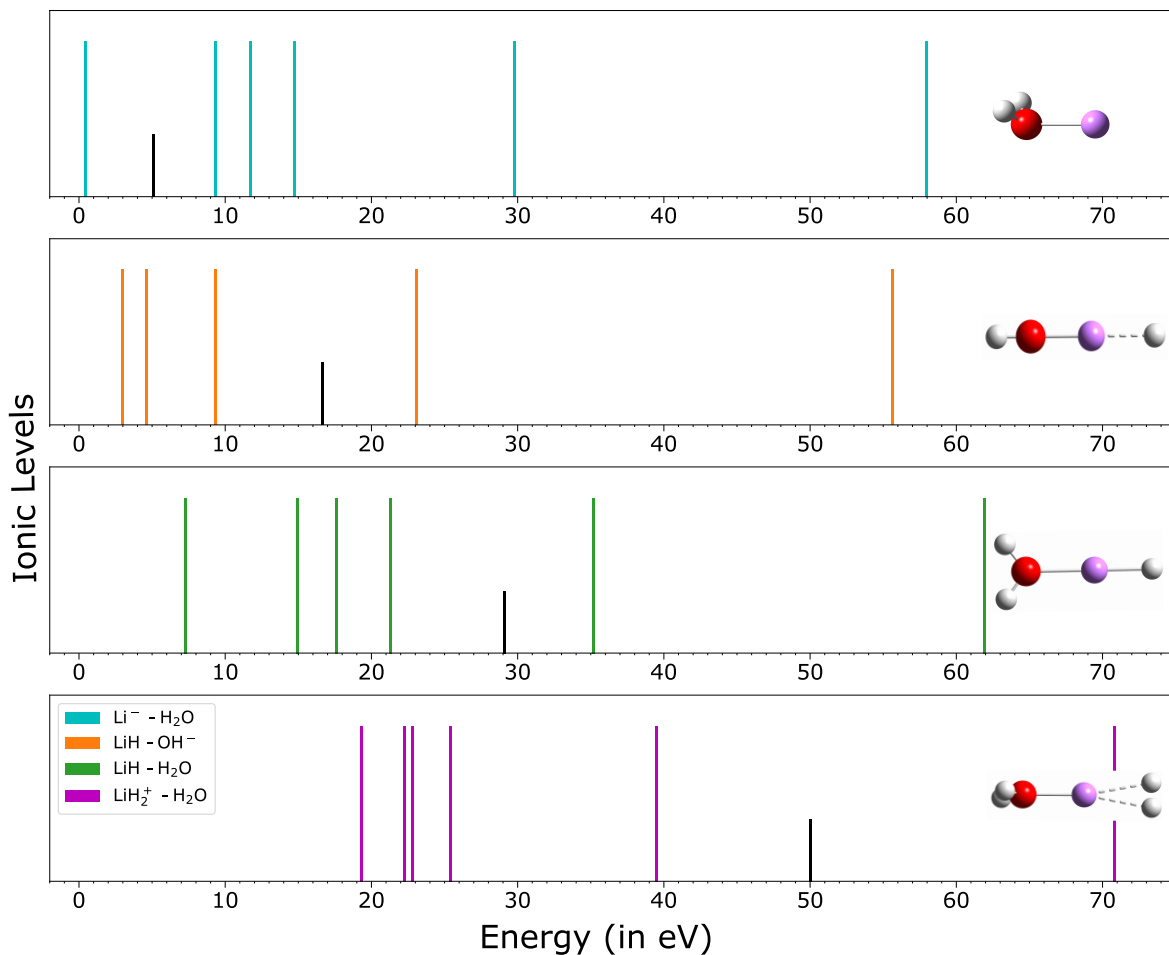


Figure 3.2: The IPs of neutral LiH-H₂O and its deprotonated and protonated species. The smaller black line denotes the lowest DIP value. The structure of the respective system is shown on the right of each panel. Atom color code : Red: Oxygen, Pink: Lithium, and White: Hydrogen.

compare the effect of the protonation and deprotonation on IP and DIP for LiH-NH₃, LiH-H₂O, along with their protonated and deprotonated systems. Later, we will examine the factors that affect TBS lifetime and whether it is possible to find a general trend in the lifetime of TBS on protonation and deprotonation.

3.4.1 Effect of protonation and deprotonation on the IP and DIP

Figures 3.2 and 3.3 display all the IPs (except O-1s) and the lowest DIP values of the neutral, protonated, and deprotonated LiH-H₂O and LiH-NH₃ systems, respectively. We have

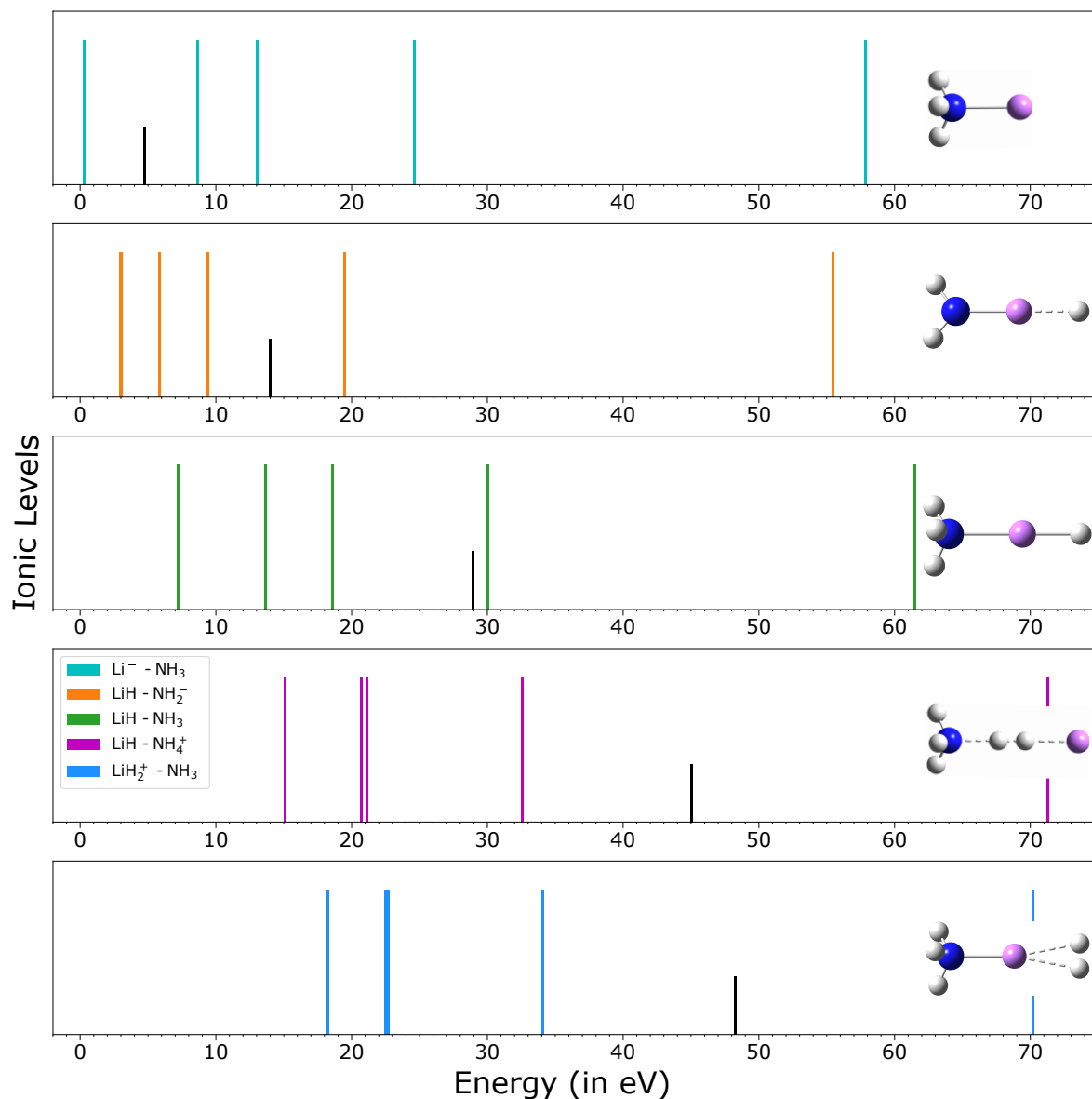


Figure 3.3: The IPs of deprotonated, protonated, and neutral LiH-NH₃. The smaller black line denotes the lowest DIP value. The structure of the respective system is shown on the right of each panel. Atom color code : Blue: Nitrogen, Pink: Lithium, and White: Hydrogen.

written down a few observations from both figures (3.2 and 3.3) and will provide possible explanations for them. First, we observe the decrease in system's IP and DIP values with deprotonation and an increase after protonation. This is due to the change in effective nuclear charge on deprotonation and protonation. Protonation increases the effective nuclear charge (ENC) while deprotonation decreases it. Electron ejection becomes challenging as ENC rises. As a result, we saw that IP and DIP value increased on protonation and decreased after deprotonation. Second, from figure 3.3, if we compare the IP values of the two deprotonated systems of LiH-NH₃, i.e., Li⁻-NH₃ and LiH-NH₂⁻. The IP values for all the states of Li⁻-NH₃ are higher than the corresponding LiH-NH₂⁻, except for the IP of HOMO. HOMO's IP of LiH-NH₂⁻ (3.06 eV) is more than HOMO's IP of Li⁻-NH₃ (0.33 eV), which is just opposite of the rest of the IP trend. A similar trend is observed between deprotonated systems of LiH-H₂O (see Figure 3.2).

The IP values of HOMO in the metal-centered deprotonated systems (Li⁻-NH₃ and Li⁻-H₂O) almost drop to zero. The lowest IP (HOMO's IP) values of metal-centered deprotonated systems are so small that both systems may lose their outer-valance electron vibrationally. To know that, we have calculated these system's ionization energy (IE) and zero point energy. The IE value was found to be 0.54 eV and 0.46 eV for the Li⁻-H₂O and Li⁻-NH₃, respectively. But the zero point energy is 0.62 eV for Li⁻-H₂O and 0.99 eV for Li⁻-NH₃. It is clear that the zero-point energy of the metal-centered deprotonated systems is higher than its ionization energy. Thus, we conclude that the metal-centered deprotonated systems can lose electrons vibrationally in their ground state and are not electronically stable. Therefore, we will not further study the metal-centered deprotonated systems for the decay width. We have used the CCSD(T) method (a gold standard in theory) for the ionization energy and zero-point energy with the aug-cc-pVTZ basis set.²⁵⁷

Till now, it's clear that electrons can lose vibrationally, but it does not tell why the HOMO's IP values of metal-centered deprotonated systems are so low than HOMO's IP of their respective neutral systems and other deprotonated systems (LiH-NH₂⁻ and LiH-OH⁻).

To understand that, we will discuss both systems' geometric and electronic structures before returning to the ionization spectra. Our primary focus will be the HOMO since HOMO does not fit the rest of the IP trend.

We must know about the HOMO and its constituting atomic orbitals in neutral and metal-centered deprotonated systems to understand the changes clearly. Lithium-2s and hydrogen-1s atomic orbitals form the HOMO in neutral systems (LiH-NH₃ and LiH-H₂O). After deprotonation from the metal center, HOMO is mainly Li-2s in metal-centered deprotonated systems (Li⁻-NH₃ and Li⁻-H₂O). However, the HOMO of other deprotonated systems (LiH-NH₂⁻/LiH-OH⁻) is similar to the corresponding neutral systems. The LiH bond is ionic, so electron density is mainly towards the more electronegative atom in the Li-H bond, which is the hydrogen atom. Figure 3.4(a,b, and c) shows the location of HOMO (Li-2s), the lowest unoccupied molecular orbital (LUMO) (N-H antibonding), and both in one frame for Li⁻-NH₃. There is a partial overlapping in space between the HOMO and LUMO, which indicates the possibility of electron density transfer from HOMO to LUMO. Natural bond order (NBO) analysis proves this possibility, showing that the system stabilizes by $8.66 \times 3 = 25.98$ kcal/mol by delocalizing the electron density to 3 degenerate N-H antibonding orbitals from HOMO. Since the HOMO of Li-2s is spherical, all three delocalizations can happen simultaneously. One more interaction stabilizing the system by 3.61 kcal/mol occurs between HOMO and Rydberg states (3s orbital) of N. Resulting in HOMO will have negligible electron density. Hence, the IP of HOMO is lowered dramatically to 0.33 eV in Li⁻-NH₃. The NBO analysis has been done using the CCSD(T) level of theory and aug-cc-pVTZ basis set²⁵⁷ in the Gaussian09 software package.²⁵⁴ MOs in figure 3.4, has been generated after NBO analysis. A similar kind of partial overlapping in space (shown in figure 3.4d) and interaction between HOMO and LUMO is observed in Li⁻-H₂O. Here, the system stabilizes by $17.18 \times 2 = 34.36$ kcal/mol by delocalizing Li-2s electron density to 2 O-H antibonding orbitals, drastically lowering the IP of HOMO to 0.42 eV. A similar interaction between HOMO and LUMO did not observe in the rest of the systems.

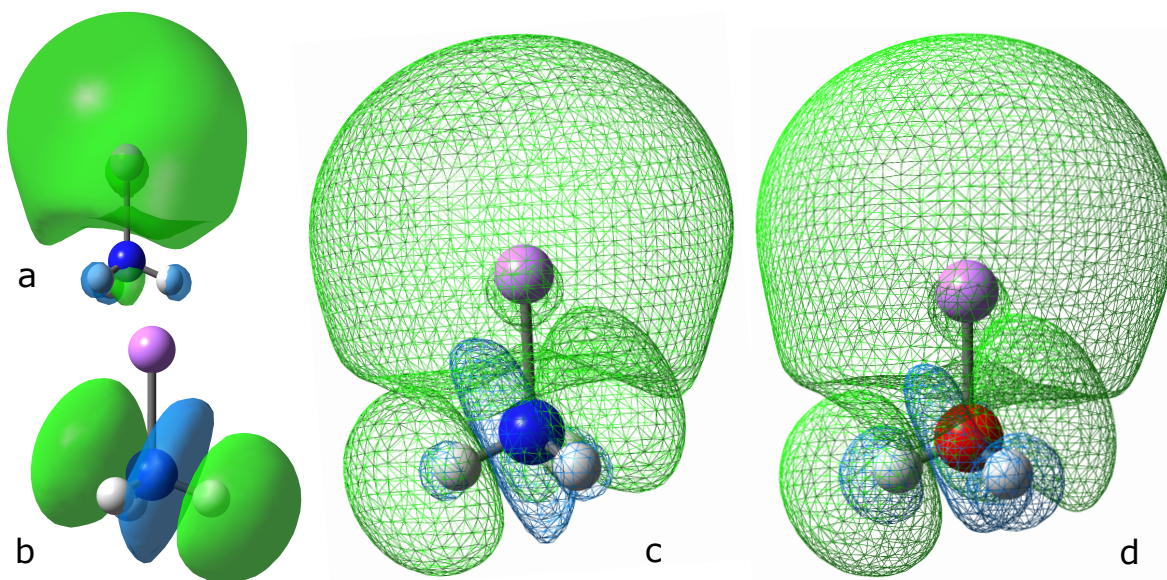


Figure 3.4: a and b show HOMO and LUMO in Li^- - NH_3 . c shows HOMO and LUMO are together in one picture in Li^- - NH_3 . d shows the same for Li^- - H_2O . This figure (c and d) demonstrates these orbitals partially overlap in space. Images are generated for $0.02 \text{ e}\text{\AA}^{-3}$ isosurface value. Atom color code-: Blue: Nitrogen, Red: Oxygen, Pink: Lithium, and White: Hydrogen.

In Li^- - NH_3 and Li^- - H_2O , we have seen delocalization of the electron density. However, despite the fact that both LiH-OH^- and LiH-NH_2^- are deprotonated systems, why is there no delocalization in these systems? This can be explained by the fact that lithium is less electronegative than oxygen and nitrogen in water and ammonia, respectively. As a result, the lone pair stays close to the oxygen/nitrogen atoms. Second, Li is bound to the p_z -orbitals of nitrogen and oxygen in LiH-OH^- and LiH-NH_2^- . The electron density after deprotonation is still present in the p_x and p_y orbitals of nitrogen/oxygen. Unlike the s-orbital of Li-2s in Li^- - NH_3 and Li^- - H_2O , which is spherical, p-orbitals are directional. Therefore, in LiH-OH^- and LiH-NH_2^- , we do not observe delocalization on deprotonation from ammonia/water.

Third, we noted that the IP was increased more by protonation from the metal center (IP's in LiH_2^+ - NH_3) than by protonation from ammonia (IP's in LiH-NH_4^+). For example, the IP of HOMO is higher in LiH_2^+ - NH_3 (18.24 eV) than in LiH-NH_4^+ (15.10 eV). The reason is the charge transfer. The location of a H^+ ion is critical within the molecule because it can help promote and demote the charge transfer between lithium and nitrogen. Let's understand

how the H^+ ion affects charge transfer. As discussed earlier, HOMO in $LiH-NH_3$ is more localized on hydrogen than lithium. An extra added H^+ ion shifts the lithium's 2s electron density. Thus, almost all-electron density will be on H_2^+ in $LiH_2^+-NH_3$ and $LiH-NH_4^+$, and lithium will be left with nearly nothing. However, the direct sharing of a lone pair of ammonia in $LiH_2^+-NH_3$ overcomes this lack of electron density on Li and stabilizes the system. $LiH_2^+-NH_3$ geometry shows (see Figure 3.3) that the additional H^+ ion is located far from the ammonia, facilitating charge transfer even more. Such direct electron sharing is impossible from ammonia to lithium in $LiH-NH_4^+$ since H_2^+ is between lithium and nitrogen. Fourth, we observe that the DIP value is the lowest (4.73 eV for $Li^- -NH_3$) and highest (48.26 eV for $LiH_2^+-NH_3$) when deprotonation and protonation occur from the metal center (LiH), respectively. That's because HOMO, which corresponds to the lowest DIP orbital, is a combination of lithium and hydrogen atomic orbitals. Thus, any change to these orbitals can lead to a considerable shift in DIP. We have so far talked about how protonation and deprotonation affect IP and DIP values. We have observed that protonation increases the IP and DIP values, resulting in a few decay (inner valence) channels closing. For example, N-2s TBS in $LiH_2^+-NH_3$ and $LiH-NH_4^+$, and O-2s TBS in $LiH_2^+-H_2O$ stop showing the decay. Note that the IP and DIP of the protonated/deprotonated system tell us whether a system is temporarily bound or not. In other words, if decay is possible or not. Decay is only possible when a state's IP exceeds the lowest DIP. This means whether a lifetime of a decaying state will increase or decrease on protonation or deprotonation cannot be concluded based only on the IP and DIP values. To know that, we will now study how the protonation and deprotonation affect the decay width (in meV) and lifetime (in fs) of the TBS, along with the possible reasons.

3.4.2 Effect of protonation and deprotonation on the lifetime of Li-1s and O-2s/N-2s TBSs in $LiH-H_2O$ and $LiH-NH_3$

The visual representation of the ICD and ETMD processes for a general system ABC is shown in figure 3.1. Since ICD and ETMD(2) include two atoms/molecules, we are not

Table 3.1: Energetic position of the decaying state and the decay width after Li-1s and O-2s ionization of LiH-H₂O along with its protonated and deprotonated systems.

System	Li-1s		O-2s	
	Energy(eV)	Width in meV (fs)	Energy (eV)	Width in meV (fs)
LiH-OH ⁻	55.56	64.27 (10.24)	23.10	16.6 (39.62)
LiH-H ₂ O	61.93	13.41 (49)	35.22	4.7 (139.6)
LiH ₂ ⁺ -H ₂ O	70.79	50.17 (13.17)	—	—

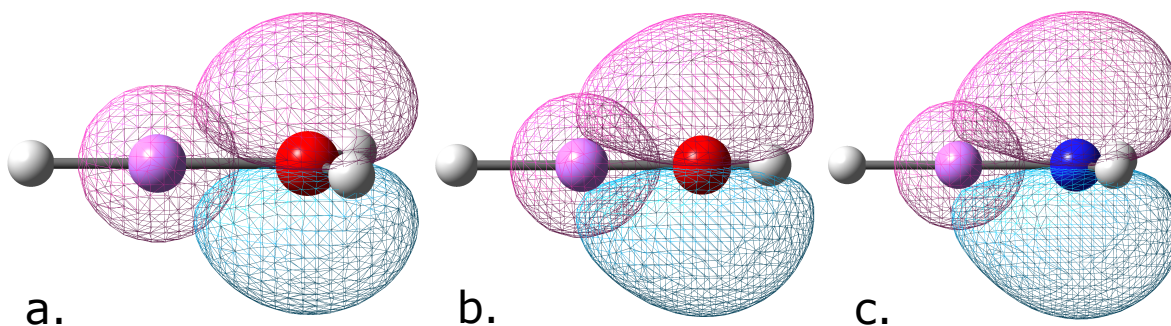


Figure 3.5: a, b, and c show the partially overlapping in space between Li-1s orbital and the lone pair orbital of oxygen/nitrogen, which are perpendicular to the molecular axis in LiH-H₂O, LiH-OH⁻, and LiH-NH₂⁻, respectively. It shows that the orbital's partial overlapping in space increases from LiH-H₂O to LiH-OH⁻. Images are generated for 0.02 eÅ⁻³ isosurface value. Atom color code-: Red: Oxygen, Pink: Lithium, Blue: Nitrogen, and White: Hydrogen.

mentioning molecule C there. You can distinguish between various decay mechanisms by identifying their final DIP states. The final two-hole states are localized on two separate molecules in ICD, i.e., A⁺B⁺, but in ETMD(2), they are localized on one atom/molecules, i.e., AB²⁺ or A²⁺B. The two-hole localization in ETMD(3) is on the pair of neighboring molecules, i.e., C⁺AB⁺. DIP eigenvalues and eigenvectors offer information on the localization of two holes in molecules. Specifically, eigenvalues tell us whether decay is feasible, whereas eigenvectors predict whether a process will be ICD, ETMD(2), or ETMD(3). In the following section, we will compare the systems in tables 3.1 & 3.2 and examine potential explanations for any variations in the lifetime of Li-1s and O-2s/N-2s TBS on protonation and deprotonation.

Lifetime of Li-1s TBS in LiH-H₂O, LiH-NH₃ and their deprotonated systems

When we compare the lifetime of Li-1s TBS in deprotonated LiH-OH⁻ and neutral LiH-H₂O systems in Table 3.1, we observe a decrease in the lifetime of Li-1s TBS. That's due to an increase in the orbital's partial overlapping in space (see fig. 3.5(a and b) that facilitates a faster electron transfer from p-orbitals of oxygen to Li-1s orbital. This partial orbital overlap is influenced by three different causes. First is the charge. In LiH-OH⁻, oxygen has an entirely negative charge, while lithium has a high positive charge. Here two adjacent atoms have opposite charges on them. We know opposite charges attract each other. Therefore, there will be an increase in attraction force (or partial overlapping of orbitals). The O-Li bond distance is the second. We observed a reduction in the O-Li bond length while switching from LiH-H₂O (1.924 Å) to LiH-OH⁻ (1.690 Å). This further increases the partial overlapping between orbitals. The third is electron-electron repulsion. After LiH-H₂O deprotonated, an additional lone pair appeared on OH⁻ in LiH-OH⁻, which is perpendicular to the molecular plane. The Li-H bond's electron density is mostly on hydrogen (more electronegative than Li) because it is an ionic bond. Therefore, an incoming oxygen's electrons may feel substantially less repulsion from Li-2s electrons. This makes the shift of lone pair electrons of oxygen toward lithium more favorable. This shift of lone pairs increases further when there is a vacancy formation on Li during the decay, making electron transfer faster between oxygen and lithium. Thus, we are getting a low lifetime for Li-1s TBS in LiH-OH⁻ than LiH-H₂O. Similar reasoning can explain a decrease in Li-1s TBS lifespan in LiH-NH₂⁻ compared to LiH-NH₃.

Additionally, we've seen that the decrease in Li-1s TBS lifetime in LiH-NH₂⁻ relative to its neutral system is less pronounced than the decrease in Li-1s TBS lifetime in LiH-OH⁻ relative to its neutral system. Two factors can explain this. First is the number of lone pairs. LiH-OH⁻ has two lone pairs, which are perpendicular to the molecular plane, while LiH-NH₂⁻ has one such lone pair. As a result, electron transfer from the oxygen/nitrogen lone pair to the Li-1s orbital will happen twice as quickly in LiH-OH⁻ as in LiH-NH₂⁻. Bond

distance is the second. The O-Li bond distance (1.69 Å) in LiH-OH^- is shorter than the N-Li bond distance (1.85 Å) in LiH-NH_2^- . Therefore, the partial overlapping between the lone pair orbital of oxygen and the lithium 1s orbital will be greater than that between the lone pair orbital of nitrogen and the lithium 1s orbital. This strong partial overlapping makes electron transfer faster between O/N and Li-1s in LiH-OH^- than in LiH-NH_2^- . The lone pair of oxygen/nitrogen that we are talking about are the ones that are perpendicular to the molecular axis of each system. Hence, observing a significant reduction in LiH-OH^- than in LiH-NH_2^- compared to their neutral systems.

Lifetime of O-2s and N-2s TBS in $\text{LiH-H}_2\text{O}$, LiH-NH_3 and their deprotonated systems

We have seen a large shift in the lifetime of O-2s TBS and a minor decrease in N-2s TBS in LiH-OH^- and LiH-NH_2^- compared to their respective neutral systems. There are three reasons for that. First, LiH-OH^- has two lone pairs, which are perpendicular to the molecular plane, while LiH-NH_2^- has one such lone pair. It means LiH-OH^- and LiH-NH_2^- each have one lone pair extra than their respective neutral systems. We are aware that bonded electron density is governed by two attractive forces from two separate nuclei, whereas lone pair electrons are affected by one nucleus (atom specific). It means the O-2s or N-2s vacancy can be filled faster in deprotonated systems than in respective neutral systems. Hence, we observed that the decay becomes faster, and the lifetime will reduce. Second, oxygen is more electronegative than nitrogen. Thus, attraction felt by electrons is higher in LiH-OH^- than LiH-NH_2^- , making decay faster. The third is the eigenvector analysis. We observe that N-2s have two possible decay channels in LiH-NH_2^- , while O-2s have four possible decay channels in LiH-OH^- . Based on eigenvector analysis, N-2s TBS decays by the ICD process only. In contrast, O-2s TBS decays by ETMD and ICD. Besides these three reasons, huge geometry and symmetry change may also be the reason for a large drop in the lifetime of O-2s in LiH-OH^- and a minor change in the lifetime of N-2s in LiH-NH_2^- compared to their respective neutral systems. In water-related systems, the H-O-Li bond angle changes from

Table 3.2: Energetic position of the decaying state and the decay width after Li-1s and N-2s ionization of LiH-NH₃ along with its protonated and deprotonated systems.

System	Li-1s		N-2s	
	Energy(eV)	Width in meV (fs)	Energy (eV)	Width in meV (fs)
LiH-NH ₃	61.48	39.18 (16.79)	30.00	7.19 (91.48)
LiH ₂ ⁺ -NH ₃	70.17	10.39 (63.32)	—	—
protonation and deprotonation on nitrogen				
LiH-NH ₂ ⁻	55.50	65.52 (10.45)	19.51	7.48 (87.90)
LiH-NH ₃	61.48	39.18 (16.79)	30.00	7.19 (91.48)
LiH-NH ₄ ⁺	71.01	144.06 (4.57)	—	—

126.6° (in LiH-H₂O) to 180° (in LiH-OH⁻), and symmetry changes from C_{2v} to C_{∞v}. While in ammonia-related systems, the H-N-Li bond angle changes from 112.4° (in LiH-NH₃) to 127.9° (in LiH-NH₂⁻), and symmetry changes from C_{3v} to C_{2v}. This change in the geometry of the ammonia-related system is not profound compared to the geometry change of LiH-OH⁻ form LiH-H₂O.

Lifetime of Li-1s TBS in LiH-H₂O, LiH-NH₃ and their protonated systems

The situation changes in LiH₂⁺-H₂O and LiH₂⁺-NH₃ because the molecule can be seen as three separate units, namely H₂O/NH₃, Li⁺, and H₂. You might wonder if it makes a difference whether a molecule has two or three subunits. It matters because the prerequisites for the ETMD(3) process are met (two nearby atoms or molecules in addition to the atom or molecule that forms the TBS). The ETMD(3) decay process can be described for Li-1s TBS in LiH₂⁺-H₂O and LiH₂⁺-NH₃, as the lithium atom receives a second positive charge due to photoionization (Li-1s vacancy formation). Then an electron from the H₂ subunit will fill the Li-1s vacancy, and the released virtual photon will eject a secondary electron from either NH₃ or H₂O. The directional nature of p-orbitals is critical in explaining increases and decreases in the lifetime of the Li-1s TBS in the protonated systems (LiH₂⁺-H₂O, LiH₂⁺-NH₃,

and LiH-NH_4^+). The nitrogen/oxygen lone pair orbital is oriented toward the Li-1s TBS in $\text{LiH}_2^+-\text{NH}_3$ and perpendicular to the molecular plane in $\text{LiH}_2^+-\text{H}_2\text{O}$. As a result, charge transfer in $\text{LiH}_2^+-\text{NH}_3$ is eased, and we can observe that lone pairs of ammonia stabilize Li-1s TBS while $\text{LiH}_2^+-\text{H}_2\text{O}$ does not experience this stabilization from water. This explains why the Li-1s TBS lifetime in $\text{LiH}_2^+-\text{H}_2\text{O}$ and $\text{LiH}_2^+-\text{NH}_3$ differs from those of their neutral systems. Since H_2 sits between Li and ammonia in LiH-NH_4^+ , there is no direct stabilizing effect by ammonia's lone pair in this compound. As a result, LiH-NH_4^+ has a lower Li-1s TBS lifetime than LiH-NH_3 . Protonation raises the IP and DIP values, which shuts the decay channel for the O-2s and N-2s in their respective protonated systems ($\text{LiH}_2^+-\text{H}_2\text{O}$, LiH-NH_4^+ , and $\text{LiH}_2^+-\text{NH}_3$). This explains the absence of N-2s and O-2s peaks in their respective protonated systems.

3.5 Conclusion

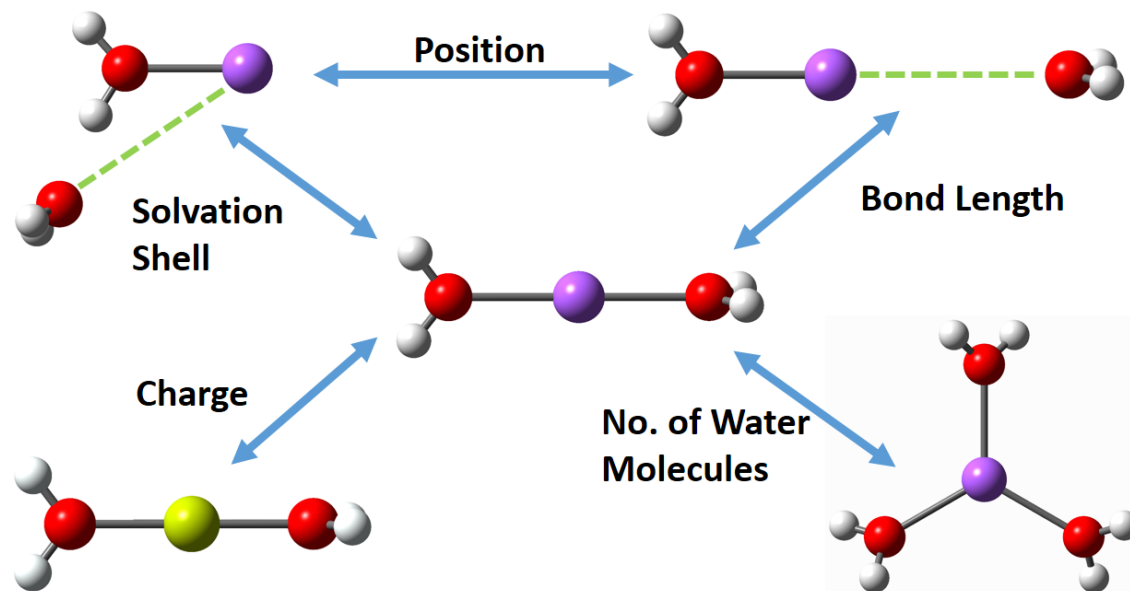
The impact of protonation and deprotonation on the system's IP, DIP, and lifetime has been examined in this chapter. LiH-NH_3 and $\text{LiH-H}_2\text{O}$ have been selected as test systems. For our research, we employed the EOM-CCSD approach with CAP potential. Our investigation found that protonation raises IP and DIP values relative to the neutral system, while deprotonation decreases IP and DIP values. However, we do not see such a general trend for the decay width/lifetime on protonation or deprotonation. In general, a molecule's protonation or deprotonation impacts its structural stability, which results in noticeable changes to the system's geometry and charge distribution. For example, due to protonation/deprotonation, geometry changes dominate the decay widths in water-related systems. However, in ammonia-related systems, we observe that charge transfer makes the system stable (i.e., $\text{LiH}_2^+-\text{NH}_3$), causing a significant difference in decay width. These two elements influence the difference in the decay width of the system. We cannot state that protonation or deprotonation will cause an increase or decrease in decay width, unlike the IP/DIP values. We find that protonation

(either from the metal center (LiH) or from H₂O/NH₃) shuts N-2s and O-2s (inner valence) decay pathways. However, the decay channel remains open for the core state Li-1s even after protonation. Li-1s TBS decays more quickly in deprotonated systems than in the corresponding neutral system because deprotonation increases the number of potential decay channels relative to the neutral system. Since the ammonia lone pair orbital is oriented toward Li and facilitates faster electron transmission, the Li-1s TBS decays in LiH-NH₃ more quickly than in LiH-H₂O. We draw the conclusion that the Li-1s TBS decays in neutral and deprotonated systems through ICD and ETMD(2) based on eigenvector analysis of the DIP. However, Li-1s decays via ETMD(2 & 3) in LiH₂⁺-NH₃ and LiH₂⁺-H₂O following protonation. O-2s and N-2s TBS decay via ICD and ETMD(2) in the neutral system. But in deprotonated systems, N-2s decay via ICD (in LiH-NH₂⁻) only, whereas O-2s (in LiH-OH⁻) decay via ICD and ETMD(2). All three decays are feasible for the decay of Li-1s in LiH-NH₄⁺.

Chapter 4

Effect of Charge and Solvation Shell on Non-Radiative Decay Processes in s-Block Cationic Metal Ion Water Clusters

Factors Affecting Non-Radiative Decay Process's Rate



4.1 Abstract

Intermolecular coulombic decay (ICD) or electron transfer-mediated decay (ETMD) are the autoionization processes through which a molecule can relax. This relaxation is only possible if the inner valence's ionization potential (IP) exceeds the system's double ionization potential (DIP). To study the effects of charge and solvation shell, we have calculated the IP, DIP values, and the lifetime of Na-2s and Mg-2s temporary bound states (TBSs) in various optimized structures of $\text{Na}^+(\text{H}_2\text{O})_n$ and $\text{Mg}^{2+}(\text{H}_2\text{O})_n$ ($n=1-5$) micro-solvated clusters, where n water molecules are distributed in a way that some are directly bound to the metal ion and the rest to the water molecules. The first and second solvation shells are the names for the former water-binding positions and the latter. For a given number n , the lifetime of decaying states is longer when water molecules are in the second solvation shell. We found that the Mg-2p state can decay for all n values in $\text{Mg}^{2+}(\text{H}_2\text{O})_n$ clusters, whereas the Na-2p state's decay is possible for $n \geq 2$ in $\text{Na}^+(\text{H}_2\text{O})_n$ clusters. Our findings highlight the influence of metal ions' charge, different solvation shell structures, and the number of water molecules on the decay rate. These systems are relevant to the human body, which makes this study significant.

4.2 Introduction

In nature, we find various metal ions that act as catalysts and are necessary for enzymatic activity. Few metal ions play an essential role in many biological processes. Sodium and Magnesium ions are such ions, out of a few (i.e., Na, Mg, K, Ca, Zn, Fe, Cu, etc.), that are essential for the human body. Studies²⁷³⁻²⁷⁵ have shown that magnesium ion alone has been involved in more than 300 enzymatic systems as a cofactor. For example, magnesium is required in the human body for making proteins, maintaining the health of muscles and neurons, controlling blood glucose levels, and structural development of bone. Additionally, magnesium aids in the active movement of calcium and potassium ions across cell membranes, which is necessary for the conduction of nerve impulses, the contraction of muscles,

and a regular heartbeat. Magnesium also helps in adenosine triphosphate (ATP) production (the energy currency of the human body). Three sodium and two potassium ions use this energy currency to move in and out of the cells. Na^+ ion is one of the main elements of the sodium-potassium pump in the human body. Na^+ ion also plays an important role in neural signaling²⁵¹ and preventing brain disease.²⁵² Studying non-radiative decay processes in micro-solvated clusters will provide insight into the chemistry involved in radiation damage in the human body.

Most of the human body's chemical and biological reactions occur in the liquid phase. But studying the reactions in the liquid phase is more challenging than in the gaseous phase because of the large number of solvent molecules and weak interactions (solvent-solute and solvent-solvent weak interactions) between these large numbers of molecules in the liquid phase. But, understanding these weak interactions is essential for more accurate results. Thus one can use the concept of micro-solvation, where calculations are performed in the gaseous phase using a few molecules of solvent (at least up to 1st solvation shell). Micro-solvation includes weak interaction, is not too computationally expensive, and provides good-quality results.

Our chosen study system is so versatile that many studies^{40,276–280} have been conducted. Most of these investigations target the spectra, thermal stability, and global minimum for the ground state structure of the clusters. Micro-solvated metal ions can serve as a valuable model for studying solution chemistry at the molecular level. These studies are essential for solvation chemistry, electron transfer, charge-induced reactivity, and other properties. However, only a few studies^{246,279} have explored the non-radiative decay process using micro-solvated cationic metal ion water systems. Non-radiative decay processes, characterized by the absence of radiation or photon emission, have short lifetimes in the femtosecond range, making them challenging to detect. Intermolecular or interatomic coulombic decay^{35,58} (ICD), Electron transfer-mediated decay⁵⁹ (ETMD) are examples of non-radiative decay processes. You can check details on ETMD and ICD in section-1.2.2 and 1.2.3 (or figures-1.2 and 1.3).

Recently, various factors^{40,41,58,68,281} that affect the non-radiative decay process have been studied, for example, the effect of protonation and deprotonation,^{68,271} bond length,^{198,247} polarization, different molecular environment effect,⁴⁰ etc. Stumpf et al.²⁴⁷ studied the decay width of the $\text{Na}^+(\text{H}_2\text{O})_n$; $n=1,4$ and $\text{Mg}^{2+}(\text{H}_2\text{O})_m$; $m=1,6$ clusters as a function of metal-oxygen distance and the number of nearest neighbors. They initiated their study with the optimized geometry of the cluster containing the highest number of water molecules, namely $\text{Na}^+(\text{H}_2\text{O})_4$ and $\text{Mg}^{2+}(\text{H}_2\text{O})_6$. They gradually removed one water molecule at a time while maintaining the high number of cis-pairs to retain the position and bond distance for subsequent geometries. There is no unique way to remove water molecules from these clusters; one can follow any method. However, removing the water molecules from various positions in a cluster will lead to different geometries. It is known that the bond length⁴⁰ and geometry affect the decay width. Using three different geometries of $\text{Na}^+(\text{H}_2\text{O})_2$, our study shows that the position of the water molecules contributes significantly to the decay width. In this study, we have used the various optimized structures of $\text{Na}^+(\text{H}_2\text{O})_n$ and $\text{Mg}^{2+}(\text{H}_2\text{O})_n$ ($n=1-5$) micro-solvated clusters, where the n water molecules are distributed such that some are directly bound to the metal ion and the rest to water molecules. We refer to the former arrangement as the first solvation shell and the latter as the second. Check Section III-A for further details regarding different solvation shell structures. In this chapter, our primary goal is to understand the influence of metal ions' charge, different solvation shell structures (water molecule's position), and the number of water molecules on the decay rate using $\text{Na}^+(\text{H}_2\text{O})_n$ and $\text{Mg}^{2+}(\text{H}_2\text{O})_n$ clusters. How all these factors affect the IP and DIP trend within clusters also have been studied.

4.3 Computational Methods

4.3.1 Fano approach for decay width

The metastable states generated via photoionization can decay through Auger decay, ICD, and ETMD. The decay happens through two-electron autoionization mechanisms; hence, these processes can belong to the Feshbach-type resonance states. The characteristic of these metastable states is governed by the system's decay width Γ . According to Fano-Feshbach's theory, the resonance states are a combination of continuum and bound states. The coupling between the bound and continuum part of the resonance state gives us the decay width. The decay width Γ in this approach is provided by

$$\Gamma = 2\pi \sum_f |\langle \phi | \hat{H} | \chi_{f,\varepsilon} \rangle|^2 \quad (4.3.1)$$

where \hat{H} is the total electronic Hamiltonian, f indicates open decay channels that belong to the continuum subspace, and ε is the asymptotic kinetic energy of the ICD/ETMD electron. To construct the bound and continuum parts of the resonance state, we have divided the Hilbert space into the Q subspace for bound configurations and the P subspace for continuum configurations. P and Q subspace would have to fulfill the following conditions, which are $P + Q = 1$ and $P * Q = 0$. We have obtained the bound part of the resonance state through the diagonalization of \hat{H} projected on the Q subspace. Q subspace included

$$Q\hat{H}Q|\phi\rangle = E_b|\phi\rangle \quad (4.3.2)$$

We have obtained the continuum part of the resonance state through the diagonalization of \hat{H} projected on the P subspace.

$$P\hat{H}P|\chi_{f,\varepsilon}\rangle = E_f|\chi_{f,\varepsilon}\rangle \quad (4.3.3)$$

The continuum states we obtained using equation-3 are not true continuum because the L^2 basis set has been used in our calculations. They show wrong normalization and asymptotic behavior. Therefore, they are pseudo-continuum in nature. To obtain the correct normalization and accurate value of decay width, we have employed the Stieltjes imaging technique.^{238,282}

For the construction of \hat{H} , we have used the extended second-order algebraic diagrammatic construction (ADC(2)X) scheme of the Green's function (defined within the space spanned by the one-hole (1h) and two-hole one particle (2h1p) configurations). In ADC(2)X approach,^{234–237} the coupling between the 1h configurations is treated as the second order of perturbation theory. However, the coupling between 1h and 2h1p configurations and the coupling between 2h1p configurations is treated to first-order perturbation theory. We considered the 2h1p configurations to construct the P subspace, representing the final double-ionized state with an outgoing free electron. In one hole block (part of Q subspace), we include all occupied orbitals except for the core orbitals of the metal and oxygen atoms. The 2h1p configurations are partitioned in such a way that the ones which are open decay channels (i.e., DIPs lower than IP) are in the P subspace, and the rest are in the Q subspace. In this approach, we can get the total and partial decay width. For details on the Fano-ADC method, please see the reference.^{234–237}

4.4 Results and Discussion

4.4.1 Cluster geometries and basis set

We must familiarize ourselves with the solvation shell's concept since we are examining its impact through this chapter. The solute's solvation shell refers to the number of water molecules (solvent molecules) surrounding a solute (a metal ion in our case). The distinction between these two structures (first and second solvation) lies in the positioning of water molecules within the cluster. In the first solvation shell structure, all the water molecules are directly connected to the metal ion. Conversely, in the second solvation shell structure,

a few water molecules are not directly linked to the metal ion but rather connected to the water molecules of the first solvation shell. To denote the different solvation shell structures in our clusters, we use a general notation: $\text{Na}^+(\text{H}_2\text{O})_{p+q}$ and $\text{Mg}^{2+}(\text{H}_2\text{O})_{p+q}$, where p and q represent the number of water molecules in the first and second solvation shells. The sum of p and q is n , the total number of water molecules in any cluster. To illustrate this notation with examples of sodium-water clusters, let's consider the case when $n = 2$. The $\text{Na}^+(\text{H}_2\text{O})_{2+0}$ cluster denotes the first solvation shell geometry, where both water molecules directly interact with the Na^+ ion. On the other hand, $\text{Na}^+(\text{H}_2\text{O})_{1+1}$ is the second solvation shell geometry, where one water molecule is directly connected to Na^+ (present in the first solvation shell). The second water molecule is linked to the first water molecule or indirectly connected to a metal ion (makes it in 2nd solvation shell). Similarly, for $n=3$, $\text{Na}^+(\text{H}_2\text{O})_{3+0}$ and $\text{Na}^+(\text{H}_2\text{O})_{2+1}$ are the first and second solvation geometries, respectively. Numerous structural possibilities²⁷⁸ exist for the first and second solvation shells when $n \geq 3$. We solely consider the lowest energy structure for each solvation shell.

The number of water molecules in the first solvation shell of Na^+ ion is reported differently by different articles. You can find these studies through reference²⁷⁸ and references within it. The coordination number of Na^+ ion in the gaseous phase is close to 4, while in bulk, it is between 5 and 6. This means that in the gaseous phase, the first solvation shell structure for $n \leq 4$ will be the lowest minimum structure, whereas the second solvation shell structure will be the lowest energy structure for $n \geq 5$ in $\text{Na}^+(\text{H}_2\text{O})_n$. As for $\text{Mg}^{2+}(\text{H}_2\text{O})_n$ clusters, the coordination number is close to 6. The Mg^{2+} 's coordination number in $\text{Mg}^{2+}(\text{H}_2\text{O})_n$ tells that the first solvation shell structure will be the lowest minimum structure up to $n \leq 6$.

Geometries of $\text{Na}^+(\text{H}_2\text{O})_n$ and $\text{Mg}^{2+}(\text{H}_2\text{O})_n$ clusters were optimized using the Gaussian09 software package²⁵⁴ with B3LYP^{258–261} functional and 6-311++g(2d,p) basis set.²⁷² Grimme's GD3 dispersion correction has been used while optimizing geometries. To ensure accurate results, we employed tight convergence criteria for optimizing all structures in

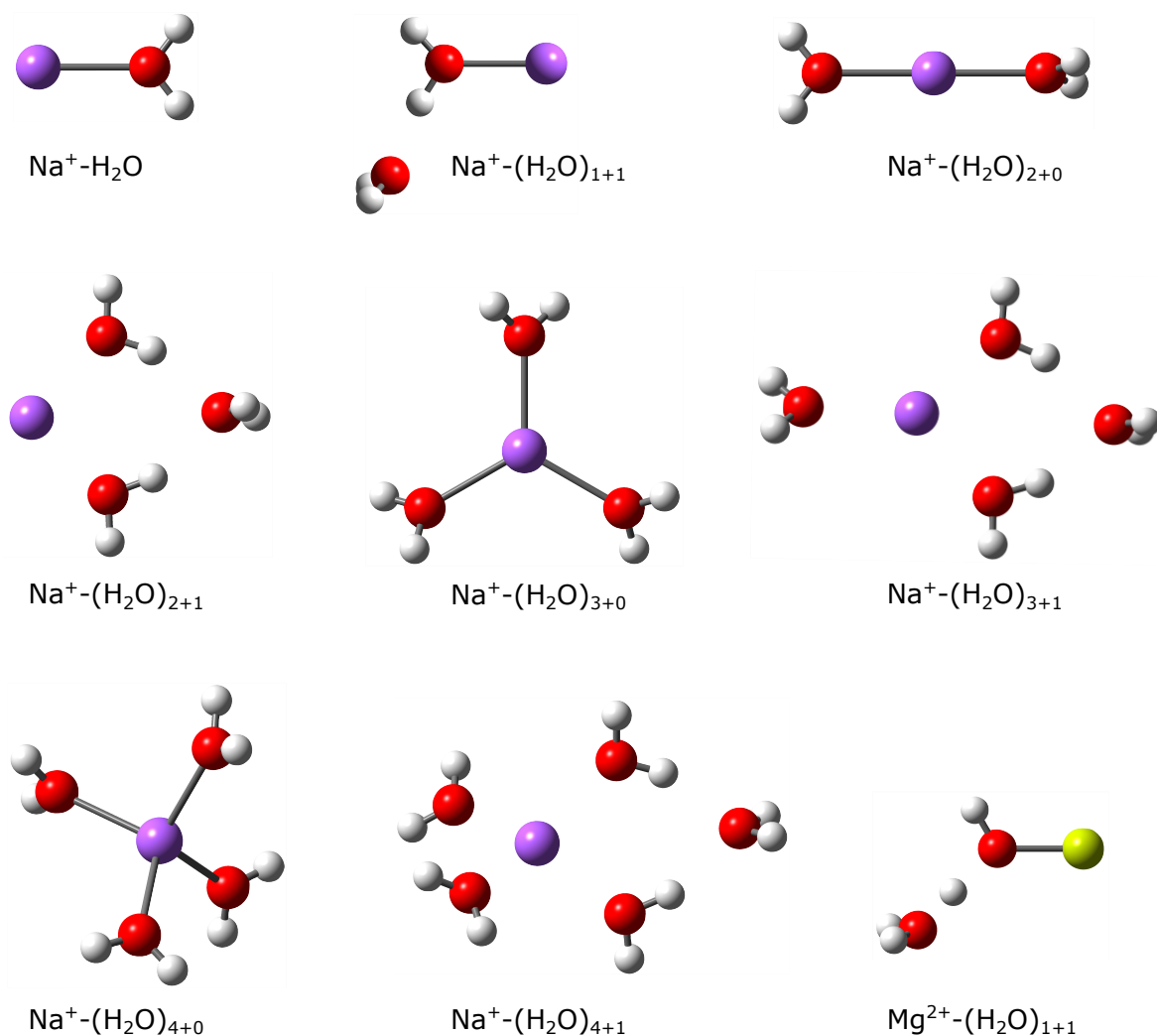


Figure 4.1: Geometries of the first and second solvation shells of Na⁺-(H₂O)_{n=1-5} and Mg²⁺-(H₂O)₁₊₁ clusters. Atom colour code Yellow: Magnesium, Violet: Sodium, Red: Oxygen, and White: Hydrogen.

our study. The maximum and RMS forces were constrained below 15×10^{-6} and 10×10^{-6} atomic units, respectively, while the maximum and RMS displacements were limited to 60×10^{-6} and 40×10^{-6} atomic units. Symmetry was not enforced during the optimization process, allowing for unrestricted exploration of the cluster geometries. Figure 4.1 shows sodium-water clusters' optimized 1st and 2nd solvation shell structures for different n values. The optimized geometries of magnesium-water clusters' are similar to the corresponding geometries of sodium-water clusters, except for the second solvation shell geometry when $n=2$. The Mg²⁺-(H₂O)₁₊₁ geometry differs significantly from Na⁺-(H₂O)₁₊₁ even though

both have the same symmetry, as depicted in the second and last geometries shown in figure 4.1. The bonding between two water molecules is different in both structures. In $\text{Mg}^{2+}-(\text{H}_2\text{O})_{1+1}$, because of the +2 charge of magnesium, the water molecule in 1st solvation shell gets partial charge, and the O-H bond becomes elongated, which is stabilized by the water of the second solvation shell. Considering the significance of symmetry in determining a cluster's geometry, let us delve into the symmetries observed in sodium and magnesium water clusters. Except for $p=2$, where $\text{Na}^+-(\text{H}_2\text{O})_{2+0}$ and $\text{Mg}^{2+}-(\text{H}_2\text{O})_2$ exhibit D_2 and D_{2d} symmetries, respectively, the symmetries of $\text{Na}^+-(\text{H}_2\text{O})_{p+0}$ and $\text{Mg}^{2+}-(\text{H}_2\text{O})_{p+0}$ are identical for $p=1,3,4$, which are C_{2v} , D_3 and S_4 . Symmetries of $\text{Na}^+-(\text{H}_2\text{O})_{p+0}$ for $p=5$ and 6 are C_1 and S_6 , whereas for $\text{Mg}^{2+}-(\text{H}_2\text{O})_{p+0}$ they are C_{2v} , and T_H . The second solvation shell structures of sodium and magnesium-water clusters ($\text{Na}^+-(\text{H}_2\text{O})_{p+1}$ and $\text{Mg}^{2+}-(\text{H}_2\text{O})_{p+1}$) were also found to have the same symmetries. The symmetries are C_s for $p=1$, C_{2v} for $p=2$, C_2 for $p=3$ and C_2 for $p=4$. In the second solvation shell structure for $n=6$, the 4+2 structure type ($p=4$, $q=2$) has smaller energy than the 5+1 type structure ($p=5$, $q=1$). D_{2d} is the symmetry for 4+2 type structure of Na^+ and Mg^{2+} water clusters.

We have already discussed the basis set for geometry optimization. The CAS-SCF²⁸³⁻²⁹⁰ and MS-CASPT2 methods²⁹¹⁻²⁹³ have been used to calculate the IP and DIP in MOLCAS 8.4 version.²⁹⁴ We have used the cc-pVTZ basis²⁵⁷ for Hydrogen atom, aug-cc-pVTZ basis²⁵⁷ for Oxygen atom, and ANO-L basis²⁹⁵ for Mg^{2+} and Na^+ metal ions. IP have computed using aug-cc-pVTZ basis set²⁵⁷ for all chemical species (H, O, Na^+ , and Mg^{2+}) using the EOM-CCSD method.²⁹⁶ We have used the FANO-ADC(2)X approach²³⁴⁻²³⁷ for the decay width calculations. Decay widths are very sensitive to the basis set. The accurate calculation of decay width requires a proper description of the continuum wave function. Therefore, we added 4 s-type 4 p-type 4 d-type continuum-like basis functions (4s4p4d) to the cc-pVTZ basis set for Oxygen and Sodium atoms, and the cc-pVTZ basis set augmented by 1s1p1d functions are used for the Hydrogen atom in $\text{Na}^+-(\text{H}_2\text{O})_{1-3}$ clusters. Basis functions addition is done using Kaufmann-Baumeister-Jungen (KBJ)²⁵⁶ continuum-like basis functions ap-

proach. Adding the extra functions will provide a good description of the pseudo-continuum. However, adding extra KBJ functions also increases the calculation's cost. Thus one has to choose the basis set by keeping the cost of calculation and the result's accuracy in mind. Therefore, for the decay width calculation of $\text{Na}^+(\text{H}_2\text{O})_{4,5}$ clusters, the cc-pVTZ basis set augmented with 2s2p KBJ continuum like basis functions for Oxygen, cc-pVTZ basis set for Hydrogen and the cc-pVTZ basis set plus 3s3p1d KBJ continuum like basis functions for the Sodium atom has been used. For $\text{Mg}^{2+}(\text{H}_2\text{O})_{1-5}$ clusters, we have used the cc-pVTZ basis set for Hydrogen, cc-pCVTZ basis set + 2s2p KBJ functions for Oxygen, and cc-pCVTZ basis set²⁶⁴ + 3s3p1d KBJ functions for Magnesium atom.

4.4.2 Solvation shell's effect on IP and DIP of $\text{Na}^+(\text{H}_2\text{O})_{1-5}$ and $\text{Mg}^{2+}(\text{H}_2\text{O})_{1-5}$ clusters

It is well known that the core IP is dominated by relaxation, whereas outer valence IP is governed by correlation. In the case of inner valence ionization, relaxation, and correlation²⁹⁷ both play an important role. In some cases, the interplay of these effects causes Koopmans' approximation²⁹⁸ to fail. The inner valence ionized state in a surrounding has a finite lifetime and decays via ICD or ETMD. These decay processes form double-ionized states, resulting in significant reorganization and relaxation within the system. Shake-up states usually accompany the double ionization potentials, highlighting the importance of considering many-body effects in DIP calculations. There are two possibilities within double ionized states. First is the single site double ionized states (ss-DIP), where two holes are confined on a single site (A^{2+}B or AB^{2+}). Second is two sited-doubly ionized states (ts-DIP), where two holes are localized on two different sites (A^+B^+ or AB^+C^+). You can see these two types of two-hole states in figure 1.2 and 1.3. The ss-DIP states are usually larger in energy than the ts-DIP because two positive charges repel each other more strongly if they are on the same molecule rather than two different molecules. The ts-DIP states are usually responsible for the non-radiative decay process since they are likely to be smaller than the IP of the inner

valence state. This implies that decay occurs only when the lowest DIP is smaller than the target state's IP. The count of DIPs smaller than the target state's IP provides the number of potential decay channels. The IPs (Na^+-2s , Na^+-2p , $\text{Mg}^{2+}-2s$, and $\text{Mg}^{2+}-2p$) and the lowest DIPs of $\text{Na}^+(\text{H}_2\text{O})_{1-5}$ and $\text{Mg}^{2+}(\text{H}_2\text{O})_{1-5}$ clusters, are reported in table 4.1 and table 4.2, respectively. The CASSCF and MS-CASPT2 method involves Complete-active space (CAS or CA space) that contains the number of active orbital and active electrons. We have excluded the 1s orbitals of metal ions(Mg, Na) and Oxygen atoms from CAS, and the remaining orbitals are in CAS. For example, the total number of electrons in $\text{Na}^+(\text{H}_2\text{O})_2$ is 30 in 15 orbitals. Out of these 2+1 1s-orbitals contains, six electrons belong to Na and O. CA space for IP will be CAS(12,23). Where 12 represents the number of active orbitals and 23 ($30-6-1(\text{for IP})=23$) active electrons. Similarly, for DIP, this space will be CAS(12,22). In this way, we have calculated the CA space for every cluster. To ensure the accuracy of the IP values obtained from the MS-CASPT2 method, we also performed IP calculations using the EOM-CCSD method. The trend observed in the IP values obtained from both methods is consistent. It also supports the reliability of the MS-CASPT2 results. However, it should be noted that calculating double ionization potentials (DIPs) using the EOM-CCSD method is computationally expensive. Consequently, we employed the MS-CASPT2 method to calculate the DIP values, as it balances the accuracy and computational cost. One will need two different solvation shell structures to study the solvation shell effect. The construction of the first and second solvation shells requires a minimum of two water molecules. Therefore, we focused on the lowest energy structures of the first and second solvation for our study. For $\text{Na}^+(\text{H}_2\text{O})_{2-4}$ and $\text{Mg}^{2+}(\text{H}_2\text{O})_{2-4}$, we have studied two different geometries which correspond to the first and second solvation.

Tables 4.1 and 4.2 provide valuable insights, leading to the following observations. We will try to understand the reasons behind them. First, in sodium-water clusters, we observe a decreasing trend in IP values as the number of water molecules in the first solvation shell of Na^+ ion increases. The decrease in effective nuclear charge (ENC) is the key here. As the

Table 4.1: It shows the ionization potentials (IP) of Na-2s and Na-2p and the lowest double ionization potential (DIP) in $\text{Na}^+(\text{H}_2\text{O})_n$ $n=1,5$ clusters. All the values are in eV.

Cluster	IP of Na-2s			IP of Na-2p			Lowest DIP
	CAS	MSCAS	EOM	CAS	MSCAS	EOM	MSCAS
	SCF	PT2	CCSD	SCF	PT2	CCSD	PT2
$\text{Na}^+-\text{H}_2\text{O}$	80.23	79.12	79.89	45.39	45.25	45.55	53.05
$\text{Na}^+(\text{H}_2\text{O})_{2+0}$	79.10	77.61	78.70	44.37	44.01	43.70	40.16
$\text{Na}^+(\text{H}_2\text{O})_{1+1}$	80.14	78.67	—	45.39	45.74	—	40.27
Geometry A ^b	80.27	78.93	—	45.48	45.56	—	38.34
$\text{Na}^+(\text{H}_2\text{O})_{3+0}$	78.00	76.46	77.17	43.27	42.45	42.26	39.08
$\text{Na}^+(\text{H}_2\text{O})_{2+1}$	78.80	77.55	—	44.06	43.78	—	39.79
$\text{Na}^+(\text{H}_2\text{O})_{4+0}$	77.04	75.96	75.84	42.35	42.32	41.01	38.27
$\text{Na}^+(\text{H}_2\text{O})_{3+1}$	77.75	76.42	—	44.06	42.71	—	38.35
$\text{Na}^+(\text{H}_2\text{O})_{4+1}$	76.76	75.29	—	42.18	41.91	—	37.13

b: First solvation geometrical arrangement with O-Na bond distances of second solvation structure.

Note: IP of Na-2s (78.3 eV) for $\text{Na}^+-\text{H}_2\text{O}$ is reported by Stumpf et al. using ADC method²⁴⁷

number of water molecules in the first solvation shell of the Na^+ ion increases, the +1 charge of the Na^+ ion decreases. This is because the increasing number of water molecules facilitates greater charge transfer from the water molecules to the sodium ion. In other words, the water molecules effectively distribute the sodium's charge among themselves, leaving the sodium ions with a less positive charge. Natural bond order (NBO) analysis supports this hypothesis. It reveals the charge transfer between the water's lone pair and the sodium's 3s orbital stabilizes the system by 1.20 kcal/mol, $1.71 \times 2 = 3.42$ kcal/mol, $5.60 \times 3 = 16.80$ kcal/mol, and $7.68 \times 4 = 30.72$ kcal/mol for $n=1$ to $n=4$ in $\text{Na}^+(\text{H}_2\text{O})_n$, respectively. Consequently, the effective nuclear charge (ENC) experienced by the sodium's electrons in $\text{Na}^+-\text{H}_2\text{O}$ is notably higher than that experienced in $\text{Na}^+(\text{H}_2\text{O})_4$, leading to a low ENC in the latter case.

This lower ENC results in a low ionization potential (IP) since less energy is required to eject an electron. Therefore, the IP value decreases as water molecules increase in the Na^+ ion's first solvation shell in the sodium-water clusters. A similar trend is observed for Mg^{2+} - $(\text{H}_2\text{O})_{n=1-5}$ clusters. Since the Mg atom has a +2 charge and the O-Mg bond distance is smaller than the O-Na bond distance, it promotes the charge transfer even more. Because of the larger charge on Mg than Na, the ENC felt by magnesium's electrons is higher than the electrons of sodium. As a result, we found that Mg-2s and Mg-2p's IP values are larger than Na-2s and Na-2p's IP values, respectively.

Table 4.2: It shows the ionization potentials (IP) of Mg-2s and Mg-2p and the lowest double ionization potential (DIP) in Mg^{2+} - $(\text{H}_2\text{O})_n$ $n=1,5$ clusters. All the values are in eV.

Cluster	IP of Mg-2s			IP of Mg-2p			Lowest DIP
	CAS	MSCAS	EOM	CAS	MSCAS	EOM	MSCAS
	SCF	PT2	CCSD	SCF	PT2	CCSD	PT2
Mg^{2+} - H_2O	116.82	115.51	116.08	76.37	76.01	75.64	69.30
Mg^{2+} - $(\text{H}_2\text{O})_{2+0}$	114.12	113.04	113.12	73.71	73.39	72.44	55.16
Mg^{2+} - $(\text{H}_2\text{O})_{1+1}$	115.13	113.23	—	74.89	73.88	—	53.29
Mg^{2+} - $(\text{H}_2\text{O})_{3+0}$	112.03	109.80	110.59	71.70	70.86	69.99	53.77
Mg^{2+} - $(\text{H}_2\text{O})_{2+1}$	113.66	111.92	—	73.33	72.71	—	52.44
Mg^{2+} - $(\text{H}_2\text{O})_{4+0}$	110.32	107.20	107.97	70.05	69.26	—	51.32
Mg^{2+} - $(\text{H}_2\text{O})_{3+1}$	111.52	109.27	—	71.21	70.44	—	50.22
Mg^{2+} - $(\text{H}_2\text{O})_{5+0}$	109.00	102.53	107.31	68.77	68.33	—	50.05
Mg^{2+} - $(\text{H}_2\text{O})_{4+1}$	109.82	107.60	107.70	69.56	68.95	—	48.73

Note: Mg-2s IP (115.3 eV) for Na^+ - H_2O is reported by Stumpf et al. using ADC method²⁴⁷

Second, we have observed that the Na-2s/Mg-2s and Na-2p/Mg-2p's IP values are larger in the second solvation structures than in the respective first solvation structures of sodium-water and magnesium-water clusters. To illustrate this, let's consider the example of the Na^+ - $(\text{H}_2\text{O})_2$ cluster. Two water molecules are directly connected to the metal ion in the

first solvation shell ($\text{Na}^+(\text{H}_2\text{O})_{2+0}$), while only one is in the second solvation shell ($\text{Na}^+(\text{H}_2\text{O})_{1+1}$). As a result, in the first solvation shell, more charge transfer will occur between the oxygen's lone pair electrons and the sodium's 3s orbital than in the second solvation shell. Therefore, a metal ion's positive charge diffuses across two molecules in the first solvation shell, while in the second solvation shell, it diffuses over just one. As a result, the electrons of Na and Mg experience a larger ENC in their second solvation shell than in their first. Hence, the second solvation shell structures of $\text{Na}^+(\text{H}_2\text{O})_{2-4}$ and $\text{Mg}^{2+}(\text{H}_2\text{O})_{2-4}$ have larger IP values than the first. Third, we observed that the lowest DIP values decrease as the number of water molecules (n) increases. Once again, ENC plays a crucial role in this trend. Initially, all sodium-water clusters have a +1 charge. The two-hole final states formed after double ionization have a +3 total charge. This +3 charge will be on one sodium atom and one water molecule (two subunits) in $\text{Na}^+\text{-H}_2\text{O}$. In $\text{Na}^+(\text{H}_2\text{O})_5$, this +3 charge will be shared by one sodium atom and the five water molecules (six subunits). Therefore cluster electrons will experience a drop in ENC as cluster size rises. This decrease in ENC leads to smaller DIP values as the cluster size increases. Fourth, we have observed that the decay of Na-2p is not possible in all sodium-water clusters, while the decay of Mg-2p is possible in all magnesium-water clusters. This is because the IP of Mg^{2+} is larger than the lowest DIP value of magnesium-water clusters when $n=1$, while the IP of Na^+ is not. The higher charge on the magnesium ion makes the IP larger, which allows the decay of Mg-2p to occur even when there is only one water molecule in the cluster. The decay of Na-2p, on the other hand, requires at least two water molecules to be present in the cluster.

4.4.3 Solvation shell's effect on lifetimes of Na-2s and Mg-2s TBSs

We have reported the total decay width (Γ) and lifetime (τ) of Na-2s and Mg-2s TBSs in $\text{Na}^+(\text{H}_2\text{O})_{1-5}$ and $\text{Mg}^{2+}(\text{H}_2\text{O})_{1-5}$ clusters, along with the O- Na^+ and O- Mg^{2+} bond lengths, in Tables 4.3 and 4.4, respectively. We have compared our results with theoretical calculations of Stumpf *et al.*,²⁴⁷ and with the Öhrwall *et al.*'s experimental value²⁶⁵ of Na-2s and Mg-2s

Table 4.3: Shows the total decay width due to ICD and ETMD processes and the total lifetime of Na-2s TBS in $\text{Na}^+(\text{H}_2\text{O})_n$; $n=1,5$ clusters.

Cluster	Solvation	O-Na bond length (in Å)	Na-2s	
			decay width Γ (in meV)	Lifetime τ (in fs)
$\text{Na}^+\text{-H}_2\text{O}$	First	2.24	113.97	5.78
Stumpf <i>et al.</i>	First	2.21	—	5.5 ^a
Stumpf <i>et al.</i>	First	2.30	—	7.0 ^a
$\text{Na}^+(\text{H}_2\text{O})_{2+0}$	First	2.26	302.89	2.17
Geometry-A ^b	First	2.18, 4.12	209.54	3.14
$\text{Na}^+(\text{H}_2\text{O})_{1+1}$	Second	2.18, 4.12	154.66	4.25
$\text{Na}^+(\text{H}_2\text{O})_{3+0}$	First	2.29	335.25	1.96
$\text{Na}^+(\text{H}_2\text{O})_{2+1}$	Second	2.23, 3.88	260.37	2.53
$\text{Na}^+(\text{H}_2\text{O})_{4+0}$	First	2.32	400.64	1.64
$\text{Na}^+(\text{H}_2\text{O})_{3+1}$	Second	2.27, 2.29, 3.98	325.23	2.02
Stumpf <i>et al.</i>	First	2.30	365.00	1.8 ^a
$\text{Na}^+(\text{H}_2\text{O})_{4+1}$	Second	2.32, 2.30, 4.05	419.73	1.57
Experimental		—	—	3.1 ^c

Note: the O-Na Bond lengths are rounded-off to two decimal places.

a: The Fano-ADC-Stieltjes method is used for calculation with cc-pCVTZ+2s2p2d1f KBJ basis for Na & O and cc-pVTZ + 1s1p1d KBJ basis for H.²⁴⁷

b: First solvation geometry with different O-Na⁺ bond lengths

c: Experimental value by Öhrwall et al. in aqueous solutions of NaCl Ref.²⁶⁵

TBS's lifetime in NaCl and MgCl₂'s aqueous solutions. We observed that our calculated lifetime of Na-2s TBS in $\text{Na}^+\text{-H}_2\text{O}$ (5.78 fs) at 2.24 Å is in close agreement with the findings of Stumpf *et al.* (5.5 fs at 2.21 Å). They also report the decay width of 7.0 fs at 2.30 Å. The change in distance here (Stumpf et al.) is 0.09 Å, yet it brings a 21 % change in decay width values. This demonstrates the high sensitivity of decay width values to even small changes

Table 4.4: Shows the total decay width due to ICD and ETMD processes and the total lifetime of Mg-2s TBS in $\text{Mg}^{2+}-(\text{H}_2\text{O})_n$; $n=1,5$ clusters.

Cluster	Solvation	O-Mg bond length (in Å)	Mg-2s	
			decay width Γ (in meV)	Lifetime τ (in fs)
$\text{Mg}^{2+}-\text{H}_2\text{O}$	First	1.93	261.33	2.52
Stumpf <i>et al.</i>	First	2.08	178	3.6 ^a
$\text{Mg}^{2+}-(\text{H}_2\text{O})_{2+0}$	First	1.95, 1.95	442.82	1.49
$\text{Mg}^{2+}-(\text{H}_2\text{O})_{1+1}$	Second	1.84, 3.95	340.96	1.93
$\text{Mg}^{2+}-(\text{H}_2\text{O})_{3+0}$	First	1.97	525.42	1.25
$\text{Mg}^{2+}-(\text{H}_2\text{O})_{2+1}$	Second	1.92, 3.41	391.99	1.68
$\text{Mg}^{2+}-(\text{H}_2\text{O})_{4+0}$	First	2.00	593.93	1.11
$\text{Mg}^{2+}-(\text{H}_2\text{O})_{3+1}$	Second	1.95, 1.98, 3.55	493.96	1.33
Stumpf <i>et al.</i>		2.08	560	1.17 ^a
$\text{Mg}^{2+}-(\text{H}_2\text{O})_{4+1}$	Second	1.99, 2.01, 3.66	515.81	1.28
Experimental			—	1.5 ^b

Note: the O-Mg Bond lengths are rounded-off to two decimal places.

a: The Fano-ADC-Stieltjes method is used for calculation with cc-pCVTZ+2s2p2d1f KBJ basis for Mg & O and cc-pVTZ + 1s1p1d KBJ basis for H.²⁴⁷

b: Experimental value by Öhrwall *et al.* in aqueous solutions of MgCl_2 Ref.²⁶⁵

in bond length. Despite this sensitivity of decay width values to changes in bond length, we have shown that the different positions of water molecules in a cluster can also affect the decay width. We will be discussing this in the upcoming point named observation number two.

From tables 4.3 and 4.4, first, we observed that the decay width increases (or lifetime decreases) as the number of water molecules (n) grow^{39,43,299} within the first or second solvation shell in $\text{Na}^+-(\text{H}_2\text{O})_n$ and $\text{Mg}^{2+}-(\text{H}_2\text{O})_n$ clusters. As n increases, the O- Na^+ and O- Mg^{2+} bond distances increase, and a larger bond distance typically leads to a longer lifetime.

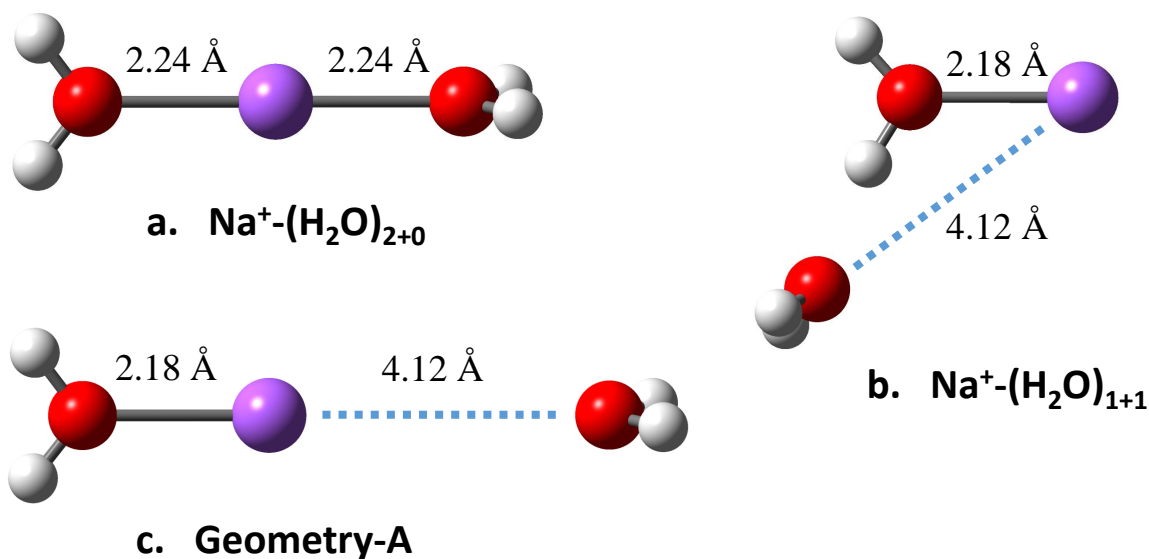


Figure 4.2: Geometries of the first (shown by a) and second solvation shells (shown by b) for $n=2$ in $\text{Na}^+(\text{H}_2\text{O})_n$ clusters. c shows the geometry-A, formed by changing the O-Na bond distances of the first solvation shell structures. The O-Na bond lengths of geometry-A are equal to those in the second solvation shell structure. A decay width (or lifetime) comparison between a and c provides the effect of bond length on decay width. In contrast, comparing b and c offers the impact of position on decay width. A decay width comparison among these geometries helps us understand what affects the lifetime of Na-2s TBS more: the O-Na bond length or the position of the water molecule. Atom colour code Violet: Sodium, Red: Oxygen, and White: Hydrogen.

Surprisingly, we observed that the Na-2s TBS's lifetime decreases instead of increasing with increasing cluster size. It implies that the effect of an increased number of water molecules dominates over the bond length effect. The decrease in Na-2s/Mg-2s TBS's lifetime is due to the non-linear increase in the number of DIPs smaller than the targeted state's IP on increasing n value. Therefore, we observed a faster decay (or a shorter lifetime) of Na-2s/Mg-2s TBS with an increase of n in $\text{Na}^+(\text{H}_2\text{O})_n$ and $\text{Mg}^{2+}(\text{H}_2\text{O})_n$.

Second, we have observed that Na-2s TBS's lifetime is longer in all the second solvation structures than its first one for a given n value. For example, the lifetime of Na-2s is longer in $\text{Na}^+(\text{H}_2\text{O})_{1+1}$ (4.26 fs) than $\text{Na}^+(\text{H}_2\text{O})_{2+0}$ (2.17 fs). These two geometries have the same number of water molecules but differ in the position of the water molecules and the O-Na bond distances. Since the number of possible decay channels is almost identical in both cases, the reason can only be explained based on the O-Na bond distance and the different positions

of water molecules. There is one more factor that can affect the Na-2s TBS's lifetime, and that is the type of non-radiative decay process. In $\text{Na}^+(\text{H}_2\text{O})_{1+1}$, ICD could be the dominant channel while ETMD could be in $\text{Na}^+(\text{H}_2\text{O})_{2+0}$ or vice-versa. To investigate this further, we have done the partial decay width calculations reported in table 4.5. The partial decay width calculations reveal that ICD and ETMD decay processes are approximately 1.9 and 2.7 times faster in $\text{Na}^+(\text{H}_2\text{O})_{2+0}$ than $\text{Na}^+(\text{H}_2\text{O})_{1+1}$. However, ICD is the dominant decay channel in both geometries. Now the question is, what affects the Na-2s TBS's lifetime more: the position of water molecules or the O-Na bond distance? To address this, we have studied one more geometry of sodium-water cluster for $n=2$, named geometry-A. The geometry-A has similar water positions as the first solvated shell structure, while the two O-Na bond lengths are the same as the second solvated structure. See Figure 4.2 for a clear understanding. The importance of geometry-A is that the comparison of Na-2s TBS's lifetime in geometry-A with that in $\text{Na}^+(\text{H}_2\text{O})_{2+0}$ will provide the effect of bond length on Na-2s TBS's lifetime because the difference in both geometries is of the O-Na bond lengths while the position of water molecules is the same in both cases. Let's call it condition-1. Furthermore, comparing the Na-2s TBS's lifetime in geometry-A with that in $\text{Na}^+(\text{H}_2\text{O})_{1+1}$ cluster will provide the effect of position on Na-2s TBS's lifetime because the difference in both geometries is of the different water molecular positions, while the O-Na bond length is the same in both cases. Let's call it condition-2. The Na-2s TBS's lifetimes are 2.17 fs, 4.25 fs, and 3.14 fs in $\text{Na}^+(\text{H}_2\text{O})_{2+0}$, $\text{Na}^+(\text{H}_2\text{O})_{1+1}$ and geometry-A, respectively. The difference in Na-2s TBS's lifetime in condition-1 and 2 are 0.97 fs and 1.11 fs. This clarifies that the effect of the positions of water molecules (1.11 fs) is slightly larger than the effect of bond length (0.97 fs) on Na-2s TBS's lifetime. Therefore we have concluded that the effect of the second water's position (or geometric effect) is more important than the bond length effect. Let's see the detailed analysis of partial decay widths. Table 4.5 presents the partial decay widths for the three geometries of $\text{Na}^+(\text{H}_2\text{O})_2$ cluster. It is observed that the influence of bond length and water molecule position on the decay width varies across different channels. Specifically,

in the $\text{Na}_{2p}^+ \text{O}_{2p}^+$ channel, the change attributed to bond length exceeds that of the position change. Conversely, in the $\text{Na}_{2p}^+ \text{H}_{1s}^+$ and $\text{O}_{2p}^+ \text{O}_{2p}^+$ channels, the position change exhibits a larger impact on the decay width compared to the bond length change. Our analysis focuses on the first two ICD channels since these channels dominate the decay process in these three geometries. Conclusively, the contribution of different positions of water molecules to the total decay width outweighs the change resulting from bond length alterations. Third, we also noticed that the lifetime of Na-2s/Mg-2s TBS is longer in the second solvation shell structures than in its first solvation shell structures. To address this, we have calculated the transition dipole moment because the decay width is proportional to the transition dipole moment.^{300,301} The transition dipole moment values have been calculated using the EOM-CCSD method with the aug-cc-pVDZ basis sets for $n=2$ (as an example case) in the sodium water cluster's first and second solvation shell structure. The left and right eigenvectors were obtained by diagonalizing the 1-hole block of the Hamiltonian matrix generated using the EOMCCSD method. The transition dipole moment is calculated for the dominant decay channel only. The calculated transition dipole moment values from Na(2p) to O(2p) are 0.123717 a.u. and 0.091239 a.u. in the first and second solvation shell structures. A large value of transition dipole moment implies that the jumping of an electron between two orbital is fast. It means the vacancy generated during the decay process can be occupied more quickly in the first solvation shell, leading to quicker decay. That's why we have observed a larger decay width (or a shorter lifetime) for the first solvation shell structures than for the second ones. Fourth, an interesting trend emerges if we compare the lifetime values of TBSs in sodium-water (5.78 fs to 1.64 fs) and magnesium-water clusters (2.52 fs to 1.11 fs). The lifetime values are dropping at a faster rate in the sodium-water clusters than magnesium-water clusters. It tells that due to a higher charge on magnesium ion than sodium ion, the decay will be slower in the magnesium water cluster than the sodium water cluster. Fifth, we also observe that the difference in the decay width between the first and second solvation gradually reduces with the increase in water molecules. For example, Na-2s TBS's lifetime

Table 4.5: Partial decay widths (for ICD and ETMD) of Na-2s ionized state in various geometries (see figure 4.2) of $\text{Na}^+(\text{H}_2\text{O})_n$ clusters for $n=2$.

Decay Type	Decay Channels	Decay Width (in meV)		
		$\text{Na}^+(\text{H}_2\text{O})_{2+0}$	Geometry-A	$\text{Na}^+(\text{H}_2\text{O})_{1+1}$
ICD	$\text{Na}_{2p}^+ \text{O}_{2p}^+$	262.7	149.00	139.33
ICD	$\text{Na}_{2p}^+ \text{H}_{1s}^+$	24.20	31.97	13.06
ETMD	$\text{O}_{2s}^+ \text{O}_{2p}^+$	5.84	3.25	2.26
ETMD	$\text{O}_{2p}^+ \text{O}_{2p}^+$	0.81	1.5	0.59

increases by 96% in $\text{Na}^+(\text{H}_2\text{O})_{1+1}$ compared to the $\text{Na}^+(\text{H}_2\text{O})_{2+0}$, whereas the increase from first to second solvation is only 29% and 10% for $n=3$ and 4, respectively. We know that the solvation shell number of sodium-ion is close to 4 in the gas phase. Therefore a difference in Na-2s TBS's lifetime in $\text{Na}^+(\text{H}_2\text{O})_{4+1}$ (1.64 fs) and $\text{Na}^+(\text{H}_2\text{O})_4$ (1.57 fs) will tell us about the effect of the solvation shell on the decay rate. In this case, Na-2s TBS's lifetime difference is 0.07 fs (4.5%), indicating that the change in the solvation shell (from first to second) affects the decay rate in a minimal. Similar results are also observed in the study of rare gas clusters by Fasshaue et al.^{302,303} They showed that apart from nearest neighbors, the second shell also contributes to an observable second peak in the spectrum of ICD electrons. However, it has little impact on the total decay width (same as our results).

In $\text{Na}^+(\text{H}_2\text{O})_4$, the lifetime of Na-2s TBS in our results (1.64 fs) and Stumpf et al. (1.80 fs) theoretical results agree well with each other. However, it is much lesser than the experimental value (3.0 fs). The difference between theoretical and experimental values is due to experimental and computational errors. The experimental errors can be due to the averaging of numerous possible structures, while the Fano-ADC method also has its limitations that introduce some errors.

4.5 Conclusions

In this chapter, we have studied the effect of solvation shells on ionization potential (IP), double ionization potential (DIP), and a lifetime of 2s ionized states using $\text{Na}^+(\text{H}_2\text{O})_{n=1-5}$ and $\text{Mg}^{2+}(\text{H}_2\text{O})_{n=1-5}$ clusters as the test systems. We have specifically looked at the impact of several variables on the lifetime of Na-2s/Mg-2s TBS, including the number of water molecules present, the solvation shell's effect, and the effect of the metal ion's charge. The decay width has been calculated using the Fano-ADC(2)X method, whereas the CAS-SCF, MS-CASPT2, and EOM-CCSD methods have been used to report the system's IP. The lowest DIPs are reported using the MS-CASPT2 method.

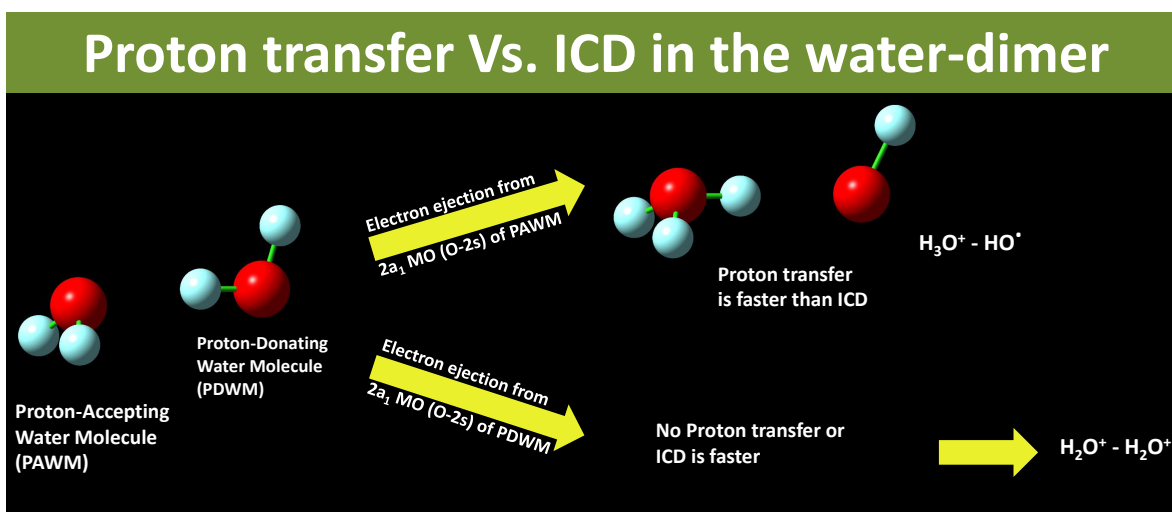
Conclusions related to IP and DIP are as follows. First, the IP of inner valence (Na-2s, Na-2p, Mg-2s, and Mg-2p) and the lowest DIP values decrease as the number of water molecules increases. The decrease in IP and DIP values with increased cluster size is due to a reduction in the effective nuclear charge (ENC). Second, we observed that the IP values would decrease continuously even after attaining the first solvation shell. However, the decrease in IP will be marginal after achieving the first solvation shell. Third, the IP of Na-2s and Mg-2s in the second solvation shell of sodium-water and magnesium-water clusters is larger than its corresponding first solvation shell. That is due to the direct connection of water molecules in the first solvation shell that stabilizes the positive charge on metal ions, which decreases the ENC. Fourth, the decay of Mg-2p occurs even when only one water molecule exists in the cluster. On the other hand, the decay of Na-2p requires at least two water molecules to be present in the cluster.

Conclusions related to the lifetime of TBS in sodium-water and magnesium-water clusters are as follows. a.) We observe that the lifetime of the TBS decreases as the number of water molecules (n) increases. This is surprising because the increase in the oxygen-metal bond length, which occurs with increasing n, typically leads to a longer lifetime. However, our results suggest that the effect of the number of water molecules dominates over the effect of bond length on the lifetime of the TBS. This is because additional water molecules

increase the number of decay channels, leading to a shorter lifetime. b.) The lifetime of Na-2s/Mg-2s TBS is longer in the second solvated shell structures than in their respective first ones. For example, Na-2s TBS's lifetime is longer in $\text{Na}^+(\text{H}_2\text{O})_{1+1}$ (4.25 fs) than in $\text{Na}^+(\text{H}_2\text{O})_{2+0}$ (2.17 fs). That is due to two reasons. (i) There is a huge increase in one of the O-Na bond lengths in $\text{Na}^+(\text{H}_2\text{O})_{1+1}$, which decreases the decay rate in the second solvation shell structure. (ii) The transition dipole moments for the first solvation were more than that for the second solvation shell, making faster decay in the first solvation shell structure. c.) A difference in Na-2s TBS's lifetime in $\text{Na}^+(\text{H}_2\text{O})_{4+1}$ (1.64 fs) and $\text{Na}^+(\text{H}_2\text{O})_4$ (1.57 fs) will tell us about the effect of solvation shell on the decay rate. This difference in lifetime is 0.07 fs (4.5%), indicating that the solvation shell's impact will be minimal after attaining the first solvation shell. d.) Fourth, the lifetime of TBSs decreases faster in sodium-water clusters (5.78 fs to 1.64 fs) than in magnesium-water clusters (2.52 fs to 1.11 fs). The lifetime values are dropping more quickly in the sodium-water clusters than in the magnesium-water clusters. This is because of the higher charge on the magnesium ion than the sodium ion, which slows down the decay process. e.) The lifetime of Na-2s TBS is longer than the Mg-2s TBS's lifetime in their corresponding clusters. For example, the lifetime of Na-2s TBS in $\text{Na}^+-\text{H}_2\text{O}$ (5.78 fs) is longer than Mg-2s TBS in $\text{Mg}^{2+}-\text{H}_2\text{O}$ (2.47 fs). The reasons for this could be (i) The number of decay channels is more in the magnesium-water clusters than in sodium-water clusters. (ii) The metal-oxygen bond lengths are smaller for magnesium-water clusters than sodium-water clusters. (iii) Due to the charge of a metal ion.

Chapter 5

Intermolecular Coulombic Decay in Water Dimer: Electronic versus Nuclear Motion



5.1 Abstract

In this article, we investigate the relaxation process of the $2a_1$ ionized state of the water in a water dimer. Usually, the relaxation occurs through the intermolecular Coulombic decay (ICD) process after inner valence ionization. We want to know whether the $2a_1$ ionized state of water would relax through a proton transfer or with ICD. We aim to understand which one will be the dominant relaxation channel. Additionally, we seek to identify conditions that may favor or inhibit proton transfer within this context. To learn about proton dynamics, we performed two Born-Oppenheimer molecular dynamics (BOMD) simulations by creating a hole in the $2a_1$ state of each water molecule in a water dimer. As for the electronic decay part, we have calculated the lifetime of $2a_1$ state of each water molecule using CAP-EOM-CCSD method with an aug-cc-pVTZ basis + 1s1p1d KBJ type continuum functions. In a water dimer system, one molecule acts as a proton-donating water molecule (PDWM) and another as a proton-accepting water molecule (PAWM). Proton transfer was observed within 14 femtoseconds (fs) when the vacancy was located in the $2a_1^{-1}$ state of a PDWM. Conversely, no proton transfer occurred when the vacancy was placed in the $2a_1^{-1}$ state of a PAWM. Using intermediate geometries of the BOMD simulation for $2a_1^{-1}$ state of PDWM and PAWM, the ionization potential (IP) and double ionization potential (DIP) are calculated using an aug-cc-pVTZ/CASPT2 method. We observed that all the decay channels get closed for the PDWM at $R_{O-H} > 1.187 \text{ \AA}$, whereas all the decay channels remain open for PAWM. After comparing the proton transfer time (14 fs) and the lifetime of $2a_1$ ionized state of PDWM (36.6 fs), we can say that proton transfer occurs faster than ICD. In contrast, ICD is the only relaxation channel for $2a_1^{-1}$ state of PAWM. In short, our study confirms that proton transfer alters the decay path and suppresses the decay channel depending on the position of the vacancy.

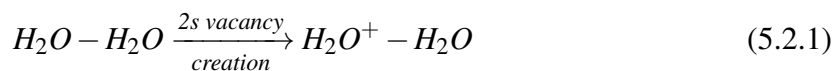
5.2 Introduction

Water is an essential molecule in chemistry and biology. It is also a universal solvent and surrounds most biological matter. Therefore, it is crucial to understand how water responds to ionizing radiation. When an inner valence state in the water clusters is ionized, it can relax through a process known as Intermolecular Coulombic decay (ICD). ICD is a non-local, non-radiative decay process.^{35,47,48,54,58} In ICD, after photoionization, the initial inner valence hole is filled by an outer valence electron of the same molecule, and the excess energy is used to ionize the neighboring molecule. It leads to a doubly ionized state (A^+B^+) where two different molecules (A and B) have a hole or a positive charge on each of them. Due to the proximity of the two positive charges, a Coulomb explosion occurs, and molecules move apart. A very similar process is electron transfer mediated decay (ETMD),⁵⁹ where the initial inner valence vacancy on molecule-A is filled by the outer valence electron of the neighboring molecule-B, and the excess energy is used to ionize the neighboring molecule-B, resulting in AB^{2+} type doubly ionized species formation.

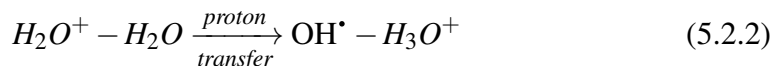
In water-rich environments such as living tissues and other biological systems, radiation-induced damage^{76,304} is predominantly observed mainly through ICD. Experimental evidence supports the occurrence of ICD in liquid water following the inner valence ionization of a water molecule.^{50,305} These non-radiative decays are highly significant as they produce low-energy electrons³⁰⁶ (LEEs) that can exert notable biological effects, including DNA damage.^{77,78,248} The prevailing belief is that DNA damage primarily arises from the interaction between ionized products of water and DNA rather than direct biomolecular ionization. Therefore, investigating ICD in liquid water is critical. However, it is theoretically challenging to replicate all potential interactions in the liquid phase. The complexity escalates dramatically with the number of interacting molecules due to the growing number of parameters influencing relaxation. This complexity hinders the study of the impact of individual parameters on relaxation processes within larger systems. To address this challenge, we have selected a water dimer as our study's test system.

The water dimer, a simple model system exhibiting hydrogen bonding, offers a unique opportunity to investigate non-local relaxation phenomena.³⁰⁷ It allows us to accurately track the dynamics of electronic and nuclear components throughout the relaxation process using quantum mechanical techniques. It is well-known that nuclear motion can alter the potential energy surfaces (PES) and affect the electronic coupling between the ionized and ground state,^{38,61,308} directly impacting the decay process.

Jahnke *et al.*³⁰⁹ studied the decay process for $2a_1$ ionized state of water dimer. They revealed that ICD is faster than proton transfer, leading the water dimer into two H_2O^+ fragments. Subsequently, Richter *et al.*²⁴⁰ employed electron-electron coincidence spectroscopy with theoretical calculations and observed proton transfer in their study of a water dimer, leading to H_3O^+ cation and OH^\bullet radical formation. Their theoretical research focused on the proton-donating water molecule (PDWM) in a water dimer system. The timescale associated with proton transfer was comparable to the ICD timescale, and experimental studies substantiated these deductions. However, Jahnke *et al.*³⁰⁹ did not observe proton transfer. Due to these two divergent conclusions, we have studied the $2a_1$ ionized state of water molecules within the water dimer system to explore the potential implications of proton transfer on relaxation pathways. Two possible scenarios can emerge in response to the removal of a $2s$ electron from a water molecule in a water dimer:

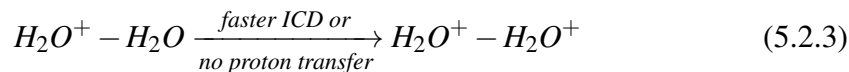


1. **Proton transfer occurs faster than ICD:** In this case, equation 5.2.2 describes the overall process.



2. **ICD occurs faster than proton transfer, or proton transfer does not occur:** In this

scenario, the overall process can be represented by equation 5.2.3.



This exploration will provide valuable insights into the fundamental mechanisms governing the relaxation dynamics of water molecules and their implications for various chemical and biological processes. The theory section of this article briefly overviews Born-Oppenheimer Molecular Dynamics (BOMD) and the CAP-EOMCCSD method. It also contains the computational details regarding calculations done in this article. The following section after the theory is the results and discussion section, where we will discuss our findings. Finally, the last section offers conclusions based on our findings.

5.3 Theory

In this section, we will briefly understand the working principles behind the various methods used in our calculation.

5.3.1 Born-Oppenheimer Molecular Dynamics

Born-Oppenheimer Molecular Dynamics (BOMD) is a simulation method based on the Born-Oppenheimer (BO) approximation used to model the dynamics of molecules. Since the mass of a nucleus is higher than that of an electron, electronic and nuclear motion can be treated separately. In BOMD simulations, the coordination of a molecular system provides the position, and the velocities are typically assigned randomly based on Boltzmann distribution for a specific temperature for the first iterative step of BOMD. These initial positions and velocities serve as starting values for the simulation. Now, the first step is to calculate the electronic ground-state energy for a given nuclear coordinates using Kohn-Sham equations ($\hat{H}_{KS}\Psi_i(r;R) = \epsilon_i\Psi_i(r;R)$). Where \hat{H}_{KS} is Kohn-Sham Hamiltonian and $\Psi_i(r;R)$ is the molec-

ular wavefunction that depends parametrically on the nuclear coordinate R . The r represents the electronic coordinate, and ϵ_i denotes the energy of the molecular system. After calculating energy, the forces get calculated on atoms. The forces for all atoms are calculated using the Hellmann-Feynman theorem, which states that the force on an atom is equal to the negative gradient of the electronic energy concerning the atom's position. The Verlet algorithm³¹⁰ is used in BOMD simulations to update the velocities (based on Newton's second law of motion) using previously calculated force, and using updated velocities, the position of the atoms also gets updated at each time step. This process was repeated iteratively. This iterative process unfolds over the simulation duration, allowing atoms to progress in time efficiently.

5.3.2 Complex Absorbing Potential (CAP)

We have used the equation of motion coupled cluster singles and doubles methods (CAP-EOM-CCSD) to calculate the lifetime of the ionized state. Now, we will briefly review the CAP part of the CAP-EOM-CCSD method and later explain the EOM-CCSD part. The CAP method helps deal with metastable states identified as eigenfunctions associated with complex eigenvalues. These complex energies are known as Siegert energy,¹⁸⁶ denoted as

$$E_{res} = E_R - i\frac{\Gamma}{2} \quad (5.3.1)$$

E_R is the real part of the energy that tells us about the orbital's energy from where electrons get ejected or attached, and the imaginary parts (represented by i in equation 5.3.1) provide information about decay width Γ . The decay width is inversely related to the lifetime τ of the system ($\Gamma = \hbar/\tau$). The complex-valued eigenvalues are obtained by adding CAP ($-i\eta\hat{W}$) to the Hamiltonian (\hat{H}), making it a complex symmetric Hamiltonian ($\hat{H}(\eta) = \hat{H} - i\eta\hat{W}$). Here, η signifies the strength of the potential, and \hat{W} represents a real-valued local potential. The CAP is always added at the periphery of the molecular system

because CAP is added to absorb the outgoing electron without disturbing the system. CAP can be added at various levels of electronic structure calculations, like the SCF, the coupled cluster level, or the EOM-CCSD levels. Adding CAP at the SCF or CCSD level calculations will perturb the N electron ground state, which is undesirable. Therefore, the CAP addition at the EOM-CCSD level (or N-1 electronic state) is the right choice. This is the CAP's advantage that it is easy to implement and can be integrated with any electronic structure method.^{40,45,311,312}

An appropriately chosen CAP causes an asymptotic damping of the Siegert eigenfunction ($\Psi(\eta)$), making wavefunction square integrable. The form of cap that we are using is a box-shaped CAP. It can be written as

$$\hat{W}(x; c) = \sum_{i=1,3} W_i(x_i; c_i) \quad (5.3.2)$$

where

$$\begin{aligned} W_i(x_i; c_i) &= \{0, x_i \leq c_i \\ &= (|x_i - c_i|)^2; |x_i| > c_i \end{aligned} \quad (5.3.3)$$

where c_i ($i=1,2,3$) represents the CAP box length in different directions and x_i ($i=1,2,3$) is the length of the molecule in different coordinate axes from the center of the coordinate axis.

The exact resonance eigenvalues (E_{res}) and eigenfunctions are obtained in the limit of $\eta \rightarrow 0$ in a complete basis set. However, the practical calculations use finite basis sets and discrete values of η . One has to solve the complex Schrödinger wave equation ($\hat{H}(\eta)\Psi(\eta) = E(\eta)\Psi(\eta)$) for various values of η to get resonance energies at each value of it. This provides the η trajectories. We calculate $\delta E/\delta\eta$ numerically and identify η_{opt} for which $|\eta_{opt} \delta E/\delta\eta_{opt}|$ is minimum.

5.3.3 Equation of Motion Coupled Cluster Singles and Doubles (EOM-CCSD) Methods for Ionization Potential

The ground state coupled cluster wavefunction for the N electron system can be written as

$$|\Psi_{cc}\rangle = \exp(\hat{T})|\Phi_o\rangle. \quad (5.3.4)$$

$|\Phi_o\rangle$ is an N electron Hartree-Fock determinant, and \hat{T} is the hole particle excitation operator, which can generate all possible excitations w.r.t $|\Phi_o\rangle$. In the coupled cluster (CC) method, if operator \hat{T} gets truncated to singles and doubles excitation, i.e., $\hat{T}=\hat{T}_1+\hat{T}_2$, then the approximation is known as CCSD method. The ground state energy and amplitudes for CCSD methods are obtained by solving the following equations.

$$\begin{aligned} \langle\Phi_o|\exp(-\hat{T})\hat{H}\exp(\hat{T})|\Phi_o\rangle &= E_{cc} \\ \langle\Phi^*|\exp(-\hat{T})\hat{H}\exp(\hat{T})|\Phi_o\rangle &= 0 \end{aligned} \quad (5.3.5)$$

where Φ_o and Φ^* represents the ground and excited state wavefunctions. We must define wavefunction for the (N-1) electronic state to get the ionization potential (IP) and lifetime values. The (N-1) state is generated by the action of a CI-like linear operator ($\hat{\mathcal{R}}(n)$) on the ground state coupled-cluster wave function ($|\Psi_{cc}\rangle$). The ionized state's wave function $|\Psi_{N-1}(n)\rangle$ can be expressed as

$$|\Psi_{N-1}(n)\rangle = \hat{\mathcal{R}}(n)|\Psi_{cc}\rangle \quad (5.3.6)$$

$\hat{\mathcal{R}}(n)$ is a linear operator which can create a hole in the n^{th} orbital. The form of the linear operator $\hat{\mathcal{R}}(n)$ for the ionized state can be written as

$$\hat{\mathcal{R}}(n) = \hat{\mathcal{R}}_1(n) + \hat{\mathcal{R}}_2(n) + \dots \quad (5.3.7)$$

$$\hat{\mathcal{R}}(n) = \sum_i r_i(n) i + \sum_{i < j, a} r_{ij}^a a^\dagger j i + \dots$$

where i, j, \dots denote the occupied orbitals, whereas a refers to the virtual or unoccupied orbital in the Hartree Fock determinant. r_i and r_{ij}^a are the amplitude of the 1h and 2h1p operators, respectively. Due to the high computational cost, we have considered the first two terms of equation 5.3.7 in our calculations. In the EOM-CCSD framework, the final ionized states are obtained by diagonalizing the coupled cluster similarity transformed Hamiltonian \bar{H}_N within $(N - 1)$ electron space, and it can be expressed as

$$\bar{H}_N \hat{\mathcal{R}}(n) |\Phi_0\rangle = \omega_i \hat{\mathcal{R}}(n) |\Phi_0\rangle \quad (5.3.8)$$

Where ω_i signifies the energy change during ionization and \bar{H}_N can be written as

$$\bar{H}_N = e^{-T} \hat{H}_N e^T - \langle \Phi_0 | e^{-T} \hat{H}_N e^T | \Phi_0 \rangle. \quad (5.3.9)$$

In the IP-EOM-CCSD approach, \bar{H}_N is constructed in a 1-hole and 2-hole 1-particle space. For the lifetime of the ionized state, we need to add CAP in the \bar{H}_N and solve the equations for various η values. CAP, being one particle term, is added to the $\bar{F}_{ab} * r_{ij}^a$ in the Hamiltonian. Then Hamiltonian, wavefunction, and eigenvalues all will become η dependent. A full diagonalization approach is used to obtain the ionization energies (from the real part of complex energy) and decay width or lifetime (from the imaginary part). A plot of the real part vs. the imaginary part of the energy is known as a η trajectory plot, and a stationary point on this plot provides the lifetime.

5.3.4 Computational details

The geometry of the water dimer is optimized using B3LYP functional^{258–260} and 6-311++G(2d,p) basis set²⁷² in Gaussian09 software.²⁵⁴ As for the accuracy of our geometry, we have compared our DFT-optimized water-dimer geometry with the CCSD(T) optimized geometry,³¹³ Our geometry is in good agreement with the CCSD(T) optimized geometry. The deMon2K software³¹⁴ was used for the BOMD simulations. We have used an aug-cc-pVTZ basis set²⁵⁷ and B3LYP functional^{258–260} for BOMD simulations. Additionally, BOMD simulations were conducted using the M06-2X functional³¹⁵ and an aug-cc-pVTZ basis set to validate the results. Remarkably, simulations with both DFT functionals yielded consistent results. We set a cutoff value for determining the completion of proton transfer during BOMD simulations, relying on the O-H bond length of the hydronium ion ($\text{H}^+ \dots \text{H}_2\text{O}$). If the O-H bond distance is below the cutoff value, we consider the proton transfer process as completed.

The ionization potential (IP) and double ionization potential (DIP) calculations were performed using the CAS-PT2 method.^{291–293} with an aug-cc-pVTZ basis set in Molcas 8.4²⁹⁴ version. To qualitatively verify the IP-DIP crossing point (see figure 5.2), additional IP and DIP calculations were performed at the cc-pVQZ/CASPT2 level. The 1s orbital of Oxygen was frozen during the IP and DIP calculations. The complete active spaces (CAS) were (15,8) for IP and (14,8) for the DIP calculations.

The decay width or lifetime calculations were done using the CAP-EOM-CCSD method. In decay width calculation, an aug-cc-pVTZ basis set + 1s1p1d Kaufmann-Baumeister-Jungen²⁵⁶ (KBJ) type continuum functions on Oxygen and an aug-cc-pVTZ basis set on Hydrogen had been implemented. In CAP-EOM-CCSD calculations,^{40,68,201} the CAP box side lengths are chosen as $C_x = C_y = C_z = 7$ au. A $\delta_c = 4$ a.u was added to the CAP box length along the molecular axis. The studied molecular system was placed at the center of the CAP box, which was the origin (0.0,0.0,0.0). To obtain the η trajectory, CAP-EOM-CCSD calculations were performed for various η values, starting from $\eta=0$ with a step size of 0.00001 au. The optimal η value for a proton-donating water molecule (PDWM) is 0.273, while for

a proton-accepting water molecule (PAWM) is 0.185. Achieving convergence of the equations ($\hat{H}(\eta)\Psi(\eta) = E(\eta)\Psi(\eta)$) for multiple η values proved challenging. Therefore, we employed full diagonalization of the matrix. We have used our in-house code to calculate the decay width. One and two-electron integrals were obtained using the GAMESS-US code.³¹⁶ We have also calculated the decay width using the FANO-ADC(2)X code, which is the in-house code of the Heidelberg group.

5.4 Results and Discussion

Numerous experimental^{317,318} and theoretical^{240,319–321} studies have already been done to study the proton transfer mechanism in water after core or valence ionization. Among these studies, only Richter *et al.*²⁴⁰ have investigated this mechanism specifically after inner-valence ionization in a water dimer. Their study involved constructing a PES for the $2a_1$ ionized state of water by stretching the O-H bond along the proton transfer coordinate, followed by ab initio molecular dynamics simulations based on this PES. Though our interest is similar, focusing on the lifetime of the $2a_1$ ionized state of water, our methodology differs from Richter *et al.*'s.²⁴⁰ Unlike their approach, which required creating a distinct potential energy surface (PES) for their simulation, our method avoids this need. We consider both scenarios: what will happen if a vacancy is generated on a PDWM and a PAWM, whereas Richter *et al.*'s²⁴⁰ study focused on a PDWM.

5.4.1 IP and DIP of PDMW and PAWM in a water dimer

To investigate the dynamics of proton transfer, we performed two BOMD simulations. In each simulation, we created a hole on the $2s$ orbital of an oxygen atom in each water molecule of the water dimer by defining the occupancy as 1. The simulations began with the optimized structure of a water dimer. Interestingly, the proton transfer occurred within the first 14 femtoseconds (fs) when the vacancy was placed on a PDWM. The O-H bonds continued to

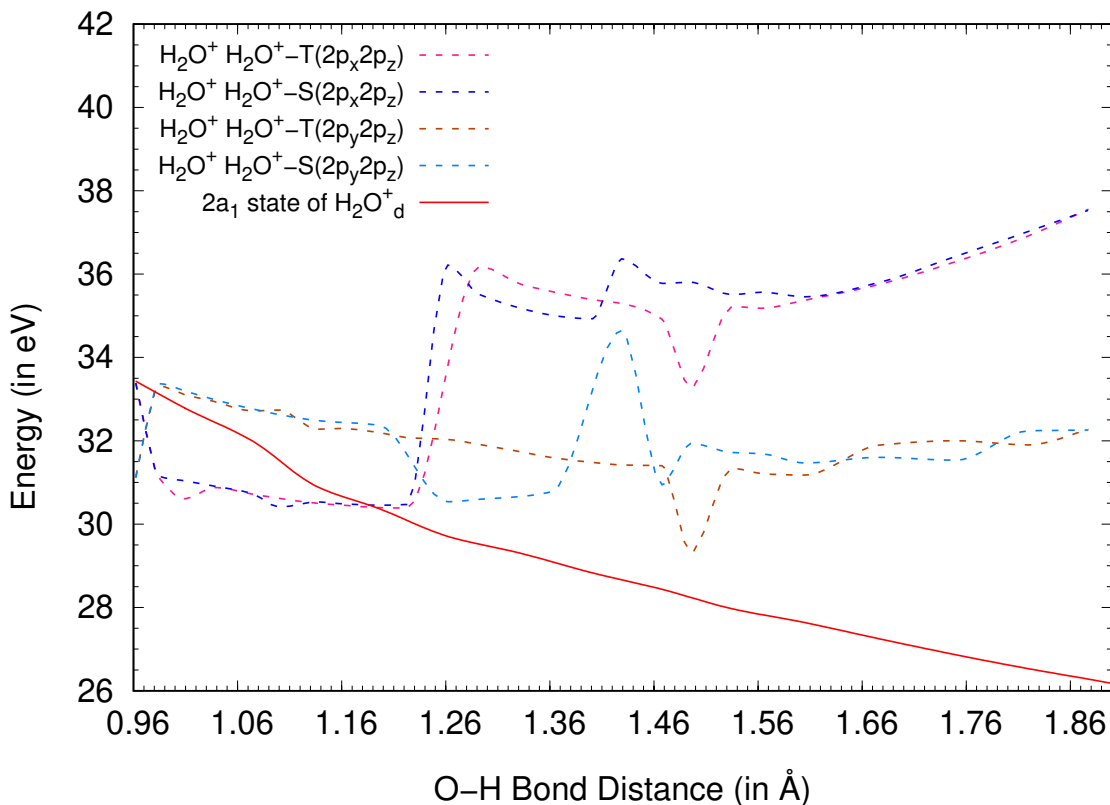


Figure 5.1: Single and double ionization potentials of water dimer along the proton transfer coordinates. These coordinates are taken from geometry obtained during the BOMD simulation when vacancy was generated in the O-2s orbital of a proton-donating water molecule (PDWM). The $2a_1$ state's IP of PDWM has been calculated using CASPT2 (15,8) and an aug-cc-pVTZ basis set, represented by a solid red line. All DIPs have been computed using state-averaged (SA-15) CASPT2(14,8) and an aug-cc-pVTZ basis set. Dashed lines of different colors show DIPs corresponding to different ICD channels. The letters S and T represent the singlet and triplet states, respectively.

stretch and vibrate throughout the remainder of the 1 ps simulation with a timestep of 1 fs. The simulation ended with the formation of an OH^\bullet radical and H_3O^+ species. In this simulation study, the O-H bond length along which proton transfer occurs ranges from 0.960 Å to 1.877 Å, while the O-O bond length varies from 2.908 Å to 2.848 Å. The geometries for each time step were recorded throughout the simulations for further analysis. The initial 15 fs of these recorded geometries were then utilized to generate the ionization potential (IP) and double ionization potential (DIP) surfaces for the PDWM (see figure 5.1). For the PAWM, geometries up to 50 fs were used to generate IP and DIP surface (see figure 5.2).

A vacancy in the inner valence state within a water dimer is known to induce multiple satellite states,^{322,323} each characterized by distinct decay rates. To ensure precision in the IP, we utilized the single-state Complete Active Space Second Order Perturbation Theory (CASPT2) method rather than taking averaging over states. The IP that we have reported is the primary peak corresponding to the $2a_1$ ionized state. By comparing the single-state CASPT2 IP results with EOM-CCSD IP values in an aug-cc-pVTZ basis set for the equilibrium geometry, it was observed that the all-electron EOM-CCSD IP value (31.84 eV) for the $2a_1^{-1}$ state in PDWM closely aligns with the corresponding all-electron CASPT2 value (32.44 eV). Notably, freezing the 1s core orbital increases the CASPT2 IP value for $2a_1^{-1}$ state of PDWM to 33.43 eV. The computed values for both IP and DIP are depicted in Figure 5.1, plotted against the O-H bond distance (R_{O-H}) relevant to proton transfer movements that occur in 15 fs. Constructing a PES through plotting IP and DIP data for these 15 geometries offers comprehensive insights beyond individual IP and DIP values. Figure 5.1 shows that the IP of the $2a_1^{-1}$ state in PDWM varies from 33.43 to 26.31 eV. The PES of the $2a_1$ ionized state (IP) of the PDWM exhibits a barrier-less potential for proton transfer. It is well known that decay is only possible if the IP of the targeted state (O-2s) is higher than the system's lowest DIP. Adhering to this principle and upon scrutiny of figure 5.1, one can readily notice that the proton transfer closes the ICD decay channel for a PDWM at $R_{O-H} > 1.185$ Å (in an aug-cc-pVTZ basis set). Using a cc-pVQZ basis, this closing of the decay channel was observed at $R_{O-H} > 1.187$ Å. The theoretical study by Richter *et al.*²⁴⁰ reported that the closure of the decay channel occurs at a distance of 1.3 Å in an aug-cc-pVTZ basis set. Notably, while our findings are based on gas-phase conditions, the results of Richter *et al.*²⁴⁰ were obtained using polarizable continuum models. The discrepancy in the bond length where ICD channels close is attributed to the surrounding medium.

Now, we will examine a scenario in which a vacancy is generated in the $2a_1$ state of PAWM during the BOMD simulation. The BOMD simulation is performed for 1 picosecond, and we do not observe any proton transfer in this time interval. Figure 5.2 shows the PES

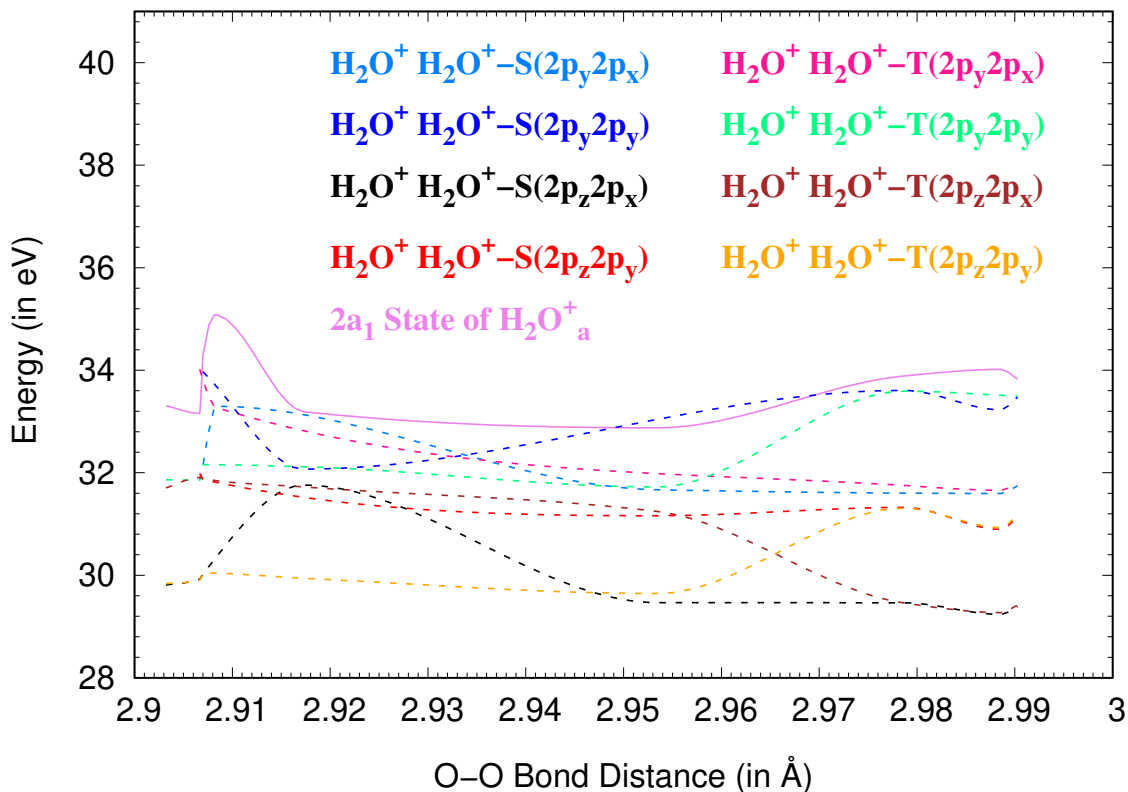


Figure 5.2: Single and Double ionization potentials of water dimer along the O-O bond coordinates. All DIPs belong to the ICD channels. The coordinates are taken from geometry obtained during the BOMD simulation when vacancy was generated in the O-2s orbital of a proton-accepting water molecule. In this case, no proton transfer occurs. The IP of $2a_1$ state of accepting water has been calculated using CASPT2 (15,8) and an aug-cc-pVTZ basis set, represented by a solid violet line. All DIPs have been computed using state-averaged (SA-15) CASPT2(14,8) and an aug-cc-pVTZ basis set. Dashed lines of different colors show DIPs corresponding to different ICD channels. The letters S and T represent the singlet and triplet states, respectively.

plot of the singly and doubly ionized states of the water dimer along O-O bond distance (R_{O-O}). The PES profiles depicted in Figure 5.2 are derived from the initial 50 intermediary geometries obtained during BOMD simulations. All the DIPs of Figure 5.2 are lower than the IP of $2a_1$ ionized state of PAWM. Consequently, ICD emerges as the sole mechanism for relaxation for the $2a_1$ ionized PAWM. In contrast to the PES associated with the $2a_1$ ionized state of PDWM, it is observed that the PES corresponding to the $2a_1$ ionized state of PAWM exhibits an initial energy barrier. Due to this barrier, we do not observe the proton transfer in this case.

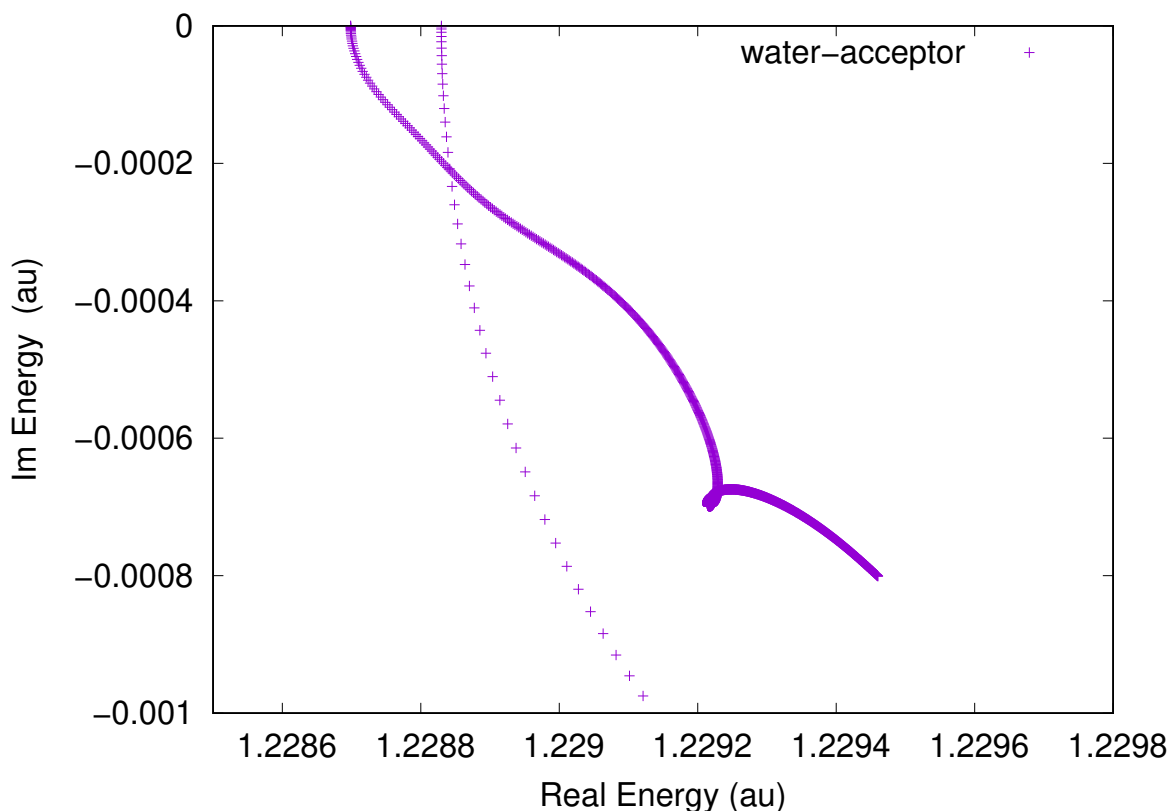


Figure 5.3: η trajectory for the $2a_1$ ionized state of proton-accepting water in the ground state geometry of a water dimer calculated using CAP-EOM-CCSD/ aug-cc-pVTZ+[1s1p1d] level of theory.

5.4.2 Decay width of PDMW and PAWM in a water dimer

The lifetime of $2a_1$ ionized states of PDWM (see figures 5.4) and PAWM (see figures 5.3) have been computed in the ground state geometry of a water dimer. It was noted that the lifetime of $2a_1$ ionized state of PDWM (36.6 fs) is twice that of the lifetime of $2a_1$ ionized state of PAWM (18 fs). This difference is because more ICD channels are available for PAWM than PDWM. After comparing the proton transfer time (14 fs) and the lifetime of $2a_1$ ionized state of PDWM (36.6 fs), we can say that proton transfer occurs faster than ICD. In addition to employing the CAP-EOM-CCSD method, we have utilized the FANO-ADC(2)X method to compute the lifetime of $2a_1$ ionized PDWM and PAWM. The FANO-ADC(2)X calculations were performed using a cc-pVTZ basis set with 5s5p5d KBJ-type continuum functions on Oxygen and cc-pVTZ+1s1p1d KBJ-type continuum functions on Hydrogen.²⁵⁶

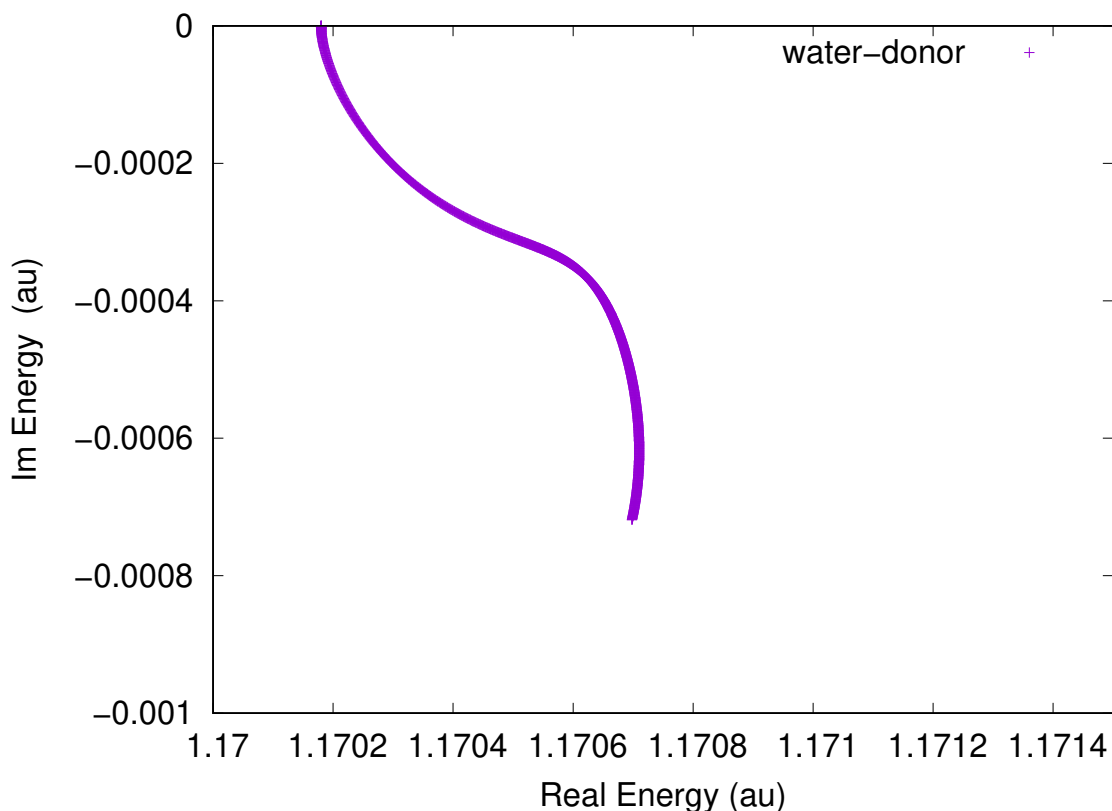


Figure 5.4: η trajectory for the $2a_1$ ionized state of proton-donating water in the ground state geometry of a water dimer calculated using CAP-EOM-CCSD/ aug-cc-pVTZ+[1s1p1d] level of theory.

It yielded a lifetime of 25 fs for PAWM and 35 fs for PDWM, which closely agrees with the corresponding values obtained from the CAP-EOM-CCSD method, 18 fs for PAWM and 36.6 fs for PDWM, respectively. The analysis based on partial decay width values for the PDWM and PAWM indicates that the singlet is the dominant decay pathway in both scenarios. Specifically, the singlet decay channels are 59% more dominant in PDWM, whereas for the PAWM, singlet decay channels are 81% more favorable than the triplet channel. It's worth noting that Richter *et al.*²⁴⁰ previously reported lifetimes of 72 fs for PDWM and 131 fs for PAWM using the FANO-CI method with a cc-pVDZ basis set + 5s5p5d KBJ type continuum functions.²⁵⁶ The difference in our and Richter *et al.*'s²⁴⁰ results is due to three reasons. First, they considered only one singlet and one triplet decay channel for each water molecule. Therefore, these lifetimes could be interpreted as the partial lifetimes related to specific decay

channels. In contrast, we have considered all decay channels for PDWM (two singlet and two triplet) and PAWM (three singlet and three triplet channels). Since PAWM has more decay channels than PDWM, it is anticipated that the former will exhibit a shorter lifetime than the latter. Second, they used a smaller basis set (cc-pVDZ), whereas we used a bigger one (cc-pVTZ). Third, the CI methodology lacks dynamic correlation compared to ADC(2)X and CC methods, potentially leading to variations in the ordering of lifetimes observed between different computational approaches. By integrating experimentation and theoretical analysis, a lifetime of 12-52 fs for small water clusters is predicted in their study. Our lifetime values for PDWM and PAWM are in this range.

Conclusion

In this article, we have studied the effect of proton transfer on ICD, a non-radiative decay process, after $2a_1$ ionization of water within a water dimer system. Two BOMD simulations were performed by ejecting an electron from the $2s$ orbital of Oxygen of PDWM and PAWM in a water dimer. The geometries resulting from these simulations were then subjected to electronic calculations to analyze the influence of nuclear motion on the ICD phenomenon.

The findings reveal that proton transfer occurs exclusively when $2s$ vacancy (or $2a_1$ ionized state) was on PDWM, with a timescale of 14 femtoseconds. The proton transfer operation effectively closes off the ICD decay pathway in this scenario. This closure is observed at $R_{O-H} > 1.185 \text{ \AA}$ with an aug-cc-pVTZ basis set and 1.187 \AA with a cc-pVQZ basis set. A comparison between the proton transfer duration (14 fs) and the electronic decay time (36.6 fs) for PDWM at ground state geometry indicates that proton transfer outpaces ICD in speed, corroborating prior findings by Richter *et al.*²⁴⁰ The decay process culminates in OH^{\bullet} radical and H_3O^+ species formation. The lifetimes reported by Richter *et al.*²⁴⁰ are partial and not the total lifetime, as they used only one of the possible decay channels for their calculation, whereas we have reported the total lifetime. Our CAP-EOM-CCSD lifetime values (18 fs for

PAWM and 36.6 fs for PDWM) are in good agreement with the FANO-ADC(2)X (25 fs for PAWM and 35 fs for PDWM) values.

When the 2s vacancy was on PAWM, no proton transfer was observed during the simulation of 1 picosecond. The lifetime of $2a_1$ ionized state of PAWM in the ground state is 18 fs. It means ICD is the only decay process through which the molecule can relax, and the final product will be $H_2O^+ - H_2O^+$. This observation aligns with the findings of Jahnke *et al.*³⁰⁹

In summary, our study confirms that proton transfer alters the decay path and suppresses the decay channel depending on the position of the vacancy. In general, each molecule can act as a proton donor and acceptor in bulk water. The dominance of proton transfer or ICD depends on whether the water molecule functions as a proton donor or a proton acceptor at that moment. If it acts as a PDWM, then proton transfer will be faster; otherwise, ICD.

Chapter 6

Summary and Future Scope

When a molecule absorbs a photon, it enters an excited state, meaning its electrons have more energy than they do in its ground state. The molecule can relax to a lower energy state by emitting a photon or other ways like non-radiative processes. Non-radiative decay processes (NRDP) are essential for understanding optoelectronic devices' efficiency, photostability of materials, energy transfer processes, chemical and biological systems, and fundamental scientific knowledge. NRDP processes involve energy transfer to the surrounding molecules or solvent molecules, which can also help us understand the surrounding environment of a molecule. We are interested in X-ray-induced NRDP. They are particularly challenging to study because they occur very quickly, on the order of femtoseconds, and due to the formation of Temporary Bound States (TBS), which form during these processes. The TBSs are the combined package of bound and continuum states, making the wavefunction of TBS non-square integrable (2nd challenge). TBSs are short-lived states that require simultaneous treatment of the continuum effect from free electrons and electron correlation. To address these challenges, we used CAP with EOM-CC methods. This method perfectly tackles the problem but is computationally expensive, making it challenging to apply to intermediate or large-sized molecules. Therefore, we also used the Fano-ADC(2)x method for larger molecules.

The significance of NRDP in chemical and biological systems becomes evident, considering their ability to generate free electrons, leading to DNA damage and the formation of reactive oxygen species, posing substantial health risks. These free electrons can also catalyze biomolecular reactions, aiding in understanding all the possible products formed after the radiolysis of a molecule. All product predictions depend on the type of NRDP and TBS that develops. Given the common occurrence of X-rays in plasma and interstellar environments, NRDP processes are widespread. Beyond catalysis, TBS in NRDP plays a vital role in exploring diverse domains, enabling investigations into plasma, multi-photon processes, and interstellar chemistry. Due to these potential applications, it is crucial to understand the factors that affect NRDP processes. In this thesis, I have studied various factors affecting NRDP processes, including bond length, different molecular surroundings, polarization, the PCM model, the increase in surrounding molecules, protonation and deprotonation, metal ion's charge, its solvation shell effect (or in other words, the position of solvent molecules in the solvation shell), and the impact of live proton dynamics of $2a^{-1}$ (or $O-2s^{-1}$) ionized water in a water dimer on NRDP.

In **1st working chapter**, I have studied the decay width of alkali metal ions as a function of different molecular environments, the increase of surrounding molecules in a system, bond distance, basis set, and polarization of the medium. using $X^+-(H_2O)_n$ $n=1-3$ & $X=Li, Na, K$ systems and CAP-IP-EOM-CCSD method. We have studied the decay of 1s, 2s, and both 2s and 2p states in Li^+ , Na^+ , and K^+ , respectively, with water. The Li 1s state undergoes ETMD, whereas the Na 2s state decays via ICD. The K 2s and 2p states undergo Auger decay.

1. To see the bond length effect on the decay width for the ICD process, we studied the 2s ionized state of Na atom in Na^+-H_2O for various bond lengths (2.2489 Å to 5.0 Å). We observed that the decay width reduces as the bond length increases, and the lifetime increases from 2.6 fs at 2.24 Å to 20 fs at 5.0 Å.
2. The Li atom's 1s ionized state has been studied using Li^+-NH_3 (81 fs) and Li^+-H_2O system to study the impact of different molecular environments. Despite being isoelec-

tronic species (NH_3 & H_2O), we found that decay is faster in Li^+-NH_3 (81 fs) than in $\text{Li}^+-\text{H}_2\text{O}$ (96 fs). This is due to the higher electronegativity of oxygen than nitrogen, and the lone pair's directional nature and orientation make electron transfer faster in Li^+-NH_3 (81 fs) than in $\text{Li}^+-\text{H}_2\text{O}$ (96 fs).

3. I have checked how the number of water molecules affects the ETMD decay using a lifetime of Li's-1s ionized state in the $\text{Li}^+(\text{H}_2\text{O})_n$ ($n = 1-3$) system. The Li-1s TBS's lifetime in $\text{Li}^+(\text{H}_2\text{O})_n$ systems are 60, 16, and 10 fs as n increases from 1 to 3. This is due to a nonlinear increase in the number of decay channels with an increasing number of surrounding atoms. A similar effect is observed for ICD, too.
4. To determine the polarization effects on the ICD and ETMD processes, we studied the decay of the Li-1s and Na-2s TBS in $\text{Li}^+-\text{H}_2\text{O}$ and $\text{Na}^+-\text{H}_2\text{O}$, respectively. In both cases, our results show that polarization provided by water solvents stabilizes the system. Hence, the decay time is increased in the liquid phase compared to the gaseous phase.
5. The Auger lifetime for the 2s and 2p ionized state of the K atom in the $\text{K}^+-\text{H}_2\text{O}$ system are 1.5 fs and 8.8 fs, respectively. The η trajectory indicates a cascade decay for the 2s ionized state of K in $\text{K}^+-\text{H}_2\text{O}$ system. It means another decay initiates after Auger decay, leading to a more stable state. Since Auger decay is localized decay, we do not expect any effect of change in bond length or number of neighbors on Auger decay.

In **2nd working chapter**, I have explained how protonation and deprotonation affect IP, DIP, and NRDP using the CAP-EOM-CCSD approach in LiH-NH_3 and $\text{LiH-H}_2\text{O}$ system with their protonated and deprotonated forms. Protonation and deprotonation can take place from the metal center (LiH) and other (NH_3 or H_2O).

1. Protonation raises IP and DIP values relative to the neutral system, while deprotonation decreases IP and DIP values. However, we do not see such a general trend for the decay width/lifetime on protonation or deprotonation.

2. We find that protonation (either from H₂O/NH₃ or from the metal center (LiH)) shuts N-2s and O-2s (inner valence) decay pathways. However, the decay channel remains open for the core state Li-1s even after protonation.
3. Li-1s TBS decays more quickly in deprotonated systems than in the corresponding neutral system because deprotonation increases the number of potential decay channels relative to the neutral system.
4. The lone pair orbital in ammonia is oriented toward Li and facilitates faster electron transmission, therefore, the Li-1s TBS decays faster in LiH-NH₃ than in LiH-H₂O.
5. Based on eigenvector analysis of the DIP, the Li-1s TBS decays in neutral and deprotonated systems through ICD and ETMD(2). However, Li-1s decays via ETMD(2 & 3) in LiH₂⁺-NH₃ and LiH₂⁺-H₂O following protonation. O-2s and N-2s TBS decay via ICD and ETMD(2) in the neutral system. But in deprotonated systems, N-2s decay via ICD (in LiH-NH₂⁻) only, whereas O-2s (in LiH-OH⁻) decay via ICD and ETMD(2). All three decays are feasible for the decay of Li-1s in LiH-NH₄⁺.
6. In general, a molecule's protonation or deprotonation impacts its structural stability, which results in noticeable changes to the system's geometry and charge distribution. For example, due to protonation/deprotonation, geometry changes dominate the decay widths in water-related systems. However, in ammonia-related systems, we observe that charge transfer makes the system stable (i.e., LiH₂⁺-NH₃), causing a significant difference in decay width. These two elements influence the difference in the decay width of the system.

In **3rd working chapter**, I have studied the effect of the charge of a metal ion, solvation shells of a metal ion on the lifetime of Na-2s and Mg-2s TBS, IP, and DIP using respective Na⁺-(H₂O)_{n=1-5} and Mg²⁺-(H₂O)_{n=1-5} clusters. We have also examined the impact of the water molecule's position on the NRDP or lifetime of Na-2s/Mg-2s TBSs. Since the system

is of intermediate size, the Fano-ADC(2)X method for decay width calculation, whereas the CAS-SCF, MS-CASPT2, and EOM-CCSD methods have been used to report the system's IP. The lowest DIPs are reported using the MS-CASPT2 method.

1. The lifetime of the TBS decreases as the number of water molecules (n) increases in $\text{Na}^+(\text{H}_2\text{O})_{n=1-5}$ and $\text{Mg}^{2+}(\text{H}_2\text{O})_{n=1-5}$ clusters. This is surprising because the increase in the oxygen-metal bond length, which occurs with increasing n , typically leads to a longer lifetime. However, our results suggest that the effect of the water molecules' number dominates over the bond length effect on the lifetime of the TBS. This is because additional water molecules increase the number of decay channels, leading to a shorter lifetime.
2. The lifetime of Na-2s/Mg-2s TBS is longer in the second solvated shell structures than in their respective first ones. For example, Na-2s TBS's lifetime is longer in $\text{Na}^+(\text{H}_2\text{O})_{1+1}$ (4.25 fs) than in $\text{Na}^+(\text{H}_2\text{O})_{2+0}$ (2.17 fs). That is due to two reasons. (i) There is a huge increase in one of the O-Na bond lengths in $\text{Na}^+(\text{H}_2\text{O})_{1+1}$, which decreases the decay rate in the second solvation shell structure. (ii) The transition dipole moments for the first solvation were more than the corresponding second solvation shell, making faster decay in the first solvation shell structure.
3. The difference in Na-2s TBS's lifetime in $\text{Na}^+(\text{H}_2\text{O})_{4+1}$ (1.64 fs) and $\text{Na}^+(\text{H}_2\text{O})_4$ (1.57 fs) is 0.07 fs (4.5%), indicating that the solvation shell's impact will be minimal after attaining the first solvation shell.
4. The lifetime values are dropping more quickly in the sodium-water clusters than in the magnesium-water clusters. This is because of the higher charge on the magnesium ion than the sodium ion, which slows down the decay process.
5. The lifetime of Na-2s TBS is longer than that of the Mg-2s TBS's lifetime in their corresponding clusters. The possible reasons could be: (i) The number of decay channels

is higher in magnesium-water clusters than in sodium-water clusters; (ii) the metal-oxygen bond lengths are smaller for magnesium-water clusters than sodium-water clusters; and (iii) the charge of the metal ion.

6. The IP of inner valence (Na-2s, Mg-2s, Na-2p, and Mg-2p) & the lowest DIP values decrease as the number of water molecules increases, which reduces the effective nuclear charge (ENC).
7. The IP values would decrease continuously even after attaining the first solvation shell. However, the decrease in IP will be marginal after achieving the first solvation shell.
8. Na-2s and Mg-2s IPs in their second solvation shells of sodium-water and magnesium-water clusters are larger than in the corresponding first solvation shell. That is due to the direct connection of water molecules in the first solvation shell that stabilizes the positive charge on metal ions, which decreases the ENC.
9. The decay of Mg-2p occurs even when only one water molecule exists in the Mg-water clusters, whereas the Na-2p decay requires at least two water molecules to be present in the cluster.

In **4th working chapter**, In this article, we have studied the effect of proton transfer on ICD, a non-radiative decay process after $2a_1$ ionization of water molecules in the water dimer. We have performed two BOMD simulations by ejecting an electron from the 2s orbital of Oxygen of PDWM and PAWM in the water dimer. We have taken geometries generated during these two simulations and did electronic structure calculations (IP and DIP) to observe the effect of nuclear motion on ICD.

1. Out of two BOMD simulations, we observed proton transfer occurs only for a $2a_1$ ionized state of PDWM or when 2s vacancy was on PDWM, which takes 14 fs. In this case, proton transfer closes the ICD decay channel for a PDWM, and the closing of the

decay channel happens at $R_{O-H} > 1.185 \text{ \AA}$ (after 4 fs) in an aug-ccpVTZ basis and 1.187 \AA in a cc-pVQZ basis set.

2. After comparing the proton transfer time (14 fs) and electronic decay time (36.6 fs) of PDWM in the ground state geometry of the water dimer, we can say that proton transfer occurs faster than ICD. In this case, the end product will be $\text{H}_3 \text{O}^+ - \text{OH}^+$.
3. when the 2s vacancy was on PAWM, no proton transfer was observed during the 1000 fs (or 1 picosecond (ps)) of simulation, and the decay channel remained open for PAWM.
4. The lifetime of $2a_1$ ionized state of PAWM in the ground state is 18 fs. It means ICD is the only decay process through which the molecule can relax, and the final product will be $\text{H}_2\text{O}^+ - \text{H}_2\text{O}^+$.
5. In bulk water, each molecule can act as a proton donor and acceptor. The dominance of proton transfer or ICD depends on whether the water molecule functions as a proton donor or acceptor at that moment. If it acts as a PDWM, then proton transfer will be faster; otherwise, ICD.

6.1 Future scope

In the future, I will study more factors like

1. The effect of the size of an element on moving along the group in a periodic table on the NRDP.
2. Effect of pKa values of amino acids on NRDP.
3. I will also study the effect of water solvent on NRDP by mimicking the actual bonding of water of bulk water solvent.

Bibliography

- [1] Kondakov, D. Y.; Sandifer, J. R.; Tang, C. W.; Young, R. H. Nonradiative recombination centers and electrical aging of organic light-emitting diodes: Direct connection between accumulation of trapped charge and luminance loss. *J. Appl. Phys.* **2003**, *93*, 1108–1119.
- [2] Luo, D.; Su, R.; Zhang, W.; Gong, Q.; Zhu, R. Minimizing non-radiative recombination losses in perovskite solar cells. *Nat. Rev. Mater.* **2020**, *5*, 44–60.
- [3] Shockley, W.; Read Jr., W. T. Statistics of the Recombinations of Holes and Electrons. *Phys. Rev.* **1952**, *87*, 835–842.
- [4] Sakar, M.; Mithun Prakash, R.; Do, T.-O. Insights into the TiO₂-Based Photocatalytic Systems and Their Mechanisms. *Catalysts* **2019**, *9*.
- [5] Zavafer, A.; Mancilla, C. Concepts of photochemical damage of Photosystem II and the role of excessive excitation. *J. Photochem. Photobiol. C: Photochem. Rev.* **2021**, *47*, 100421.
- [6] Liput, D. J.; Nguyen, T. A.; Augustin, S. M.; Lee, J. O.; Vogel, S. S. A Guide to Fluorescence Lifetime Microscopy and Förster's Resonance Energy Transfer in Neuroscience. *Curr. Protoc. Neurosci.* **2020**, *94*, e108.

- [7] Geissler, P. L.; Dellago, C.; Chandler, D.; Hutter, J.; Parrinello, M. Autoionization in Liquid Water. *Science* **2001**, *291*, 2121–2124.
- [8] Meitner, L. Über die Entstehung der β -Strahl-Spektren radioaktiver Substanzen. *Z. Physik* **1922**, *9*, 131–144.
- [9] Auger, P. Sur l' effet Photoélectrique Composé. *J. Phys. Radium* **1925**, *6*, 205–208.
- [10] Lablanquie, P.; Huttula, S.-M.; Huttula, M.; Andric, L.; Palaudoux, J.; Eland, J. H. D.; Hikosaka, Y.; Shigemasa, E.; Ito, K.; Penent, F. Multi-electron spectroscopy: Auger decays of the argon 2s hole. *Phys. Chem. Chem. Phys.* **2011**, *13*, 18355–18364.
- [11] Li, S.; Driver, T.; Rosenberger, P.; Champenois, E. G.; Duris, J.; Al-Haddad, A.; Averbukh, V.; Barnard, J. C. T.; Berrah, N.; Bostedt, C.; Bucksbaum, P. H.; Coffee, R. N.; DiMauro, L. F.; Fang, L.; Garratt, D.; Gatton, A.; Guo, Z.; Hartmann, G.; Haxton, D.; Helml, W.; Huang, Z.; LaForge, A. C.; Kamalov, A.; Knurr, J.; Lin, M.-F.; Lutman, A. A.; MacArthur, J. P.; Marangos, J. P.; Nantel, M.; Natan, A.; Obaid, R.; O'Neal, J. T.; Shivaram, N. H.; Schori, A.; Walter, P.; Wang, A. L.; Wolf, T. J. A.; Zhang, Z.; Kling, M. F.; Marinelli, A.; Cryan, J. P. Attosecond coherent electron motion in Auger-Meitner decay. *Science* **2022**, *375*, 285–290.
- [12] Kukk, E.; Bozek, J. D.; Cheng, W.-T.; Fink, R. F.; Wills, A. A.; Berrah, N. Auger decay of the C 1s⁻¹2 π^* resonance in carbon monoxide: Vibrationally and angularly resolved spectra. *J. Chem. Phys.* **1999**, *111*, 9642–9650.
- [13] Inhester, L.; Burmeister, C. F.; Groenhof, G.; Grubmüller, H. Auger spectrum of a water molecule after single and double core ionization. *J. Chem. Phys.* **2012**, *136*, 144304.
- [14] Thürmer, S.; Unger, I.; Slavíček, P.; Winter, B. Relaxation of Electronically Excited Hydrogen Peroxide in Liquid Water: Insights from Auger-Electron Emission. *J. Phys. Chem. C* **2013**, *117*, 22268–22275.

- [15] Raman, S. N.; Paul, D. F.; Hammond, J. S.; Bomben, K. D. Auger Electron Spectroscopy and Its Application to Nanotechnology. *Microscopy Today* **2011**, *19*, 12–15.
- [16] Turner, N. H.; Schreifels, J. A. Surface Analysis: X-ray Photoelectron Spectroscopy and Auger Electron Spectroscopy. *Anal. Chem.* **2000**, *72*, 99–110.
- [17] Li, S.; Zhang, H.; Liu, Z.; Xu, J.; Fan, G.; Li, W.; Li, Q.; Hu, X.; Jing, G. Auger Electron Spectroscopy (AES) and X-ray Photoelectron Spectroscopy (XPS) Profiling of Self Assembled Monolayer (SAM) Patterns Based on Vapor Deposition Technique. *Appl. Sci.* **2022**, *12*.
- [18] Baer, D.; Lea, A.; Geller, J.; Hammond, J.; Kover, L.; Powell, C.; Seah, M.; Suzuki, M.; Watts, J.; Wolstenholme, J. Approaches to analyzing insulators with Auger electron spectroscopy: Update and overview. *J. Electron Spectrosc. Relat. Phenom.* **2010**, *176*, 80–94, Charging Issues in Electron Spectroscopies.
- [19] Atzrodt, V.; Lange, H. In *Volume 79, Number 2 October 16*; Görlich,, Ed.; De Gruyter: Berlin, Boston, 1983; pp 489–497.
- [20] Debehets, J.; Miranda, S. M. C.; Homm, P.; Houssa, M.; Seefeldt, M.; Locquet, J.-P.; Seo, J. W. Auger electron spectroscopy study of semiconductor surfaces: Effect of cleaning in inert atmosphere. *J. Vac. Sci. Technol. B* **2016**, *34*, 041227.
- [21] Kim, S. C.; Kammura, W.; Iwami, M.; Hiraki, A. Application of Auger electron spectroscopy to the study of metal-semiconductor interfacial reaction. *Osaka University Technology Reports* **1980**, *30*, 81–87.
- [22] Avci, R.; Davis, B.; Rieders, N.; Lucas, K.; Nandasiri, M.; Mogk, D. Role of Metallurgy in the Localized Corrosion of Carbon Steel. *J. Minerals and Materials Characterization and Engineering* **2018**, *6*, 618–646.
- [23] Rieders, N.; Nandasiri, M.; Mogk, D.; Avci, R. New Insights into Sulfide Inclusions in 1018 Carbon Steels. *Metals* **2021**, *11*.

- [24] Coster, D.; Kronig, R. D. L. New type of auger effect and its influence on the x-ray spectrum. *Physica* **1935**, *2*, 13–24.
- [25] Fuggle, J. C.; Alvarado, S. F. Core-level lifetimes as determined by x-ray photoelectron spectroscopy measurements. *Phys. Rev. A* **1980**, *22*, 1615–1624.
- [26] Nyholm, R.; Mårtensson, N.; Lebugle, A.; Axelsson, U. Auger and Coster-Kronig broadening effects in the 2p and 3p photoelectron spectra from the metals ^{22}Ti - ^{30}Zn . *J. Phys. F: Met. Phys.* **1981**, *11*, 1727.
- [27] Agarwal, B. K. *X-ray spectroscopy : an introduction*, 2nd ed.; Springer-Verlag: Berlin, 1991.
- [28] Morishita, Y.; Liu, X.-J.; Saito, N.; Lischke, T.; Kato, M.; Prümper, G.; Oura, M.; Yamaoka, H.; Tamenori, Y.; Suzuki, I. H.; Ueda, K. Experimental Evidence of Interatomic Coulombic Decay from the Auger Final States in Argon Dimers. *Phys. Rev. Lett.* **2006**, *96*, 243402.
- [29] Kreidi, K.; Jahnke, T.; Weber, T.; Havermeier, T.; Liu, X.; Morisita, Y.; Schössler, S.; Schmidt, L. P. H.; Schöffler, M.; Odenweller, M.; Neumann, N.; Foucar, L.; Titze, J.; Ulrich, B.; Sturm, F.; Stuck, C.; Wallauer, R.; Voss, S.; Lauter, I.; Kim, H. K.; Rudloff, M.; Fukuzawa, H.; Prümper, G.; Saito, N.; Ueda, K.; Czasch, A.; Jagutzki, O.; Schmidt-Böcking, H.; Stoychev, S.; Demekhin, P. V.; Dörner, R. Relaxation processes following 1s photoionization and Auger decay in Ne_2 . *Phys. Rev. A* **2008**, *78*, 043422.
- [30] Saak, C.-M.; Unger, I.; Gopakumar, G.; Coleman, C.; Björneholm, O. Temperature Dependence of X-ray-Induced Auger Processes in Liquid Water. *J. Phys. Chem. Lett.* **2020**, *11*, 2497–2501.
- [31] Li, Z.; Becker, U. Chemical state effects on the Auger transitions in Cr, Fe, and Cu compounds. *J. Electron Spectrosc. Relat. Phenom.* **2019**, *237*, 146893.

- [32] Franz, J.; Bennett, R.; Buhmann, S. Y. Auger decay in dispersing and absorbing environments. *Phys. Rev. A* **2021**, *104*, 013103.
- [33] Dupuy, R.; Féraud, G.; Bertin, M.; Romanzin, C.; Philippe, L.; Putaud, T.; Michaut, X.; Cimino, R.; Baglin, V.; Fillion, J.-H. Desorption of neutrals, cations, and anions from core-excited amorphous solid water. *J. Chem. Phys.* **2020**, *152*, 054711.
- [34] Pokapanich, W.; Ottosson, N.; Svensson, S.; Öhrwall, G.; Winter, B.; Björneholm, O. Bond Breaking, Electron Pushing, and Proton Pulling: Active and Passive Roles in the Interaction between Aqueous Ions and Water as Manifested in the O 1s Auger Decay. *J. Phys. Chem. B* **2012**, *116*, 3–8.
- [35] Cederbaum, L. S.; Zobeley, J.; Tarantelli, F. Giant Intermolecular Decay and Fragmentation of Clusters. *Phys. Rev. Lett.* **1997**, *79*, 4778–4781.
- [36] Sisourat, N.; Sann, H.; Kryzhevoi, N. V.; Kolorenč, P.; Havermeier, T.; Sturm, F.; Jahnke, T.; Kim, H. K.; Dörner, R.; Cederbaum, L. S. Interatomic Electronic Decay Driven by Nuclear Motion. *Phys. Rev. Lett.* **2010**, *105*, 173401.
- [37] Stoychev, S. D.; Kuleff, A. I.; Cederbaum, L. S. On the Intermolecular Coulombic Decay of Singly and Doubly Ionized States of Water Dimer. *J. Chem. Phys.* **2010**, *133*, 154307.
- [38] Santra, R.; Zobeley, J.; Cederbaum, L. S.; Moiseyev, N. Interatomic Coulombic Decay in Van Der Waals Clusters and Impact of Nuclear Motion. *Phys. Rev. Lett.* **2000**, *85*, 4490–4493.
- [39] Öhrwall, G.; Tchapyguine, M.; Lundwall, M.; Feifel, R.; Bergersen, H.; Rander, T.; Lindblad, A.; Schulz, J.; Peredkov, S.; Barth, S.; Marburger, S.; Hergenbahn, U.; Svensson, S.; Björneholm, O. Femtosecond Interatomic Coulombic Decay in Free Neon Clusters: Large Lifetime Differences between Surface and Bulk. *Phys. Rev. Lett.* **2004**, *93*, 173401.

- [40] Kumar, R.; Ghosh, A.; Vaval, N. Decay Processes in Cationic Alkali Metals in Microsolvated Clusters: A Complex Absorbing Potential Based Equation-of-Motion Coupled Cluster Investigation. *J. Chem. Theory Comput* **2022**, *18*, 807–816.
- [41] Kumar, R.; Ghosh, A.; Vaval, N. Effect of charge and solvation shell on non-radiative decay processes in s-block cationic metal ion water clusters. *J. Chem. Phys.* **2023**, *159*, 054304.
- [42] Santra, R.; Cederbaum, L. S. Non-Hermitian Electronic Theory and Applications to Clusters. *Phys. Rep.* **2002**, *368*, 1–117.
- [43] Vaval, N.; Cederbaum, L. S. Ab Initio Lifetimes in the Interatomic Coulombic Decay of Neon Clusters Computed with Propagators. *J. Chem. Phys.* **2007**, *126*, 164110.
- [44] Scheit, S.; Averbukh, V.; Meyer, H.; Moiseyev, N.; Santra, R.; Sommerfeld, T.; Zobeley, J.; Cederbaum, L. S. On the Interatomic Coulombic Decay in the Ne Dimer. *J. Chem. Phys.* **2004**, *121*, 8393–8398.
- [45] Ehara, M.; Sommerfeld, T. CAP/SAC-CI Method for Calculating Resonance States of Metastable Anions. *Chem. Phys. Lett.* **2012**, *537*, 107–112.
- [46] Averbukh, V.; Müller, I. B.; Cederbaum, L. S. Mechanism of Interatomic Coulombic Decay in Clusters. *Phys. Rev. Lett.* **2004**, *93*, 263002.
- [47] Marburger, S.; Kugeler, O.; Hergenhahn, U.; Möller, T. Experimental Evidence for Interatomic Coulombic Decay in Ne Clusters. *Phys. Rev. Lett.* **2003**, *90*, 203401.
- [48] Jahnke, T.; Czasch, A.; Schöffler, M. S.; Schössler, S.; Knapp, A.; Kász, M.; Titze, J.; Wimmer, C.; Kreidi, K.; Grisenti, R. E.; Staudte, A.; Jagutzki, O.; Hergenhahn, U.; Schmidt-Böcking, H.; Dörner, R. Experimental Observation of Interatomic Coulombic Decay in Neon Dimers. *Phys. Rev. Lett.* **2004**, *93*, 163401.

- [49] Jahnke, T.; Czasch, A.; Schöffler, M.; Schössler, S.; Kász, M.; Titze, J.; Kreidi, K.; Grisenti, R. E.; Staudte, A.; Jagutzki, O.; Schmidt, L. P. H.; Weber, T.; Schmidt-Böcking, H.; Ueda, K.; Dörner, R. Experimental Separation of Virtual Photon Exchange and Electron Transfer in Interatomic Coulombic Decay of Neon Dimers. *Phys. Rev. Lett.* **2007**, *99*, 153401.
- [50] Zhang, P.; Perry, C.; Luu, T. T.; Matselyukh, D.; Wörner, H. J. Intermolecular Coulombic Decay in Liquid Water. *Phys. Rev. Lett.* **2022**, *128*, 133001.
- [51] Santra, R.; Cederbaum, L.; Meyer, H.-D. Electronic decay of molecular clusters: non-stationary states computed by standard quantum chemistry methods. *Chem. Phys. Lett.* **1999**, *303*, 413–419.
- [52] Hergenhahn, U. Interatomic and intermolecular coulombic decay: The early years. *J. Electron Spectrosc. Relat. Phenom.* **2011**, *184*, 78–90.
- [53] Hergenhahn, U. Production of low kinetic energy electrons and energetic ion pairs by Intermolecular Coulombic Decay. *Int. J. Radiat. Biol.* **2012**, *88*, 871–883.
- [54] Jahnke, T. Interatomic and Intermolecular Coulombic Decay: The Coming of Age Story. *J. Phys. B: At. Mol. Opt. Phys.* **2015**, *48*, 082001.
- [55] Dias, A. M. Interatomic coulombic decay: a short review. *Braz. J. Phys.* **2009**, *39*, 523–525.
- [56] Averbukh, V.; Demekhin, P.; Kolorenč, P.; Scheit, S.; Stoychev, S.; Kuleff, A.; Chiang, Y.-C.; Gokhberg, K.; Kopelke, S.; Sisourat, N.; Cederbaum, L. Interatomic electronic decay processes in singly and multiply ionized clusters. *J. Electron Spectrosc. Relat. Phenom.* **2011**, *183*, 36–47.
- [57] Frühling, U.; Trinter, F.; Karimi, F.; Williams, J.; T., J. Time-resolved studies of interatomic Coulombic decay. *J. Electron Spectrosc. Relat. Phenom.* **2015**, *204*, 237–244.

- [58] Jahnke, T.; Hergenbahn, U.; Winter, B.; Dörner, R.; Frühling, U.; Demekhin, P. V.; Gokhberg, K.; Cederbaum, L. S.; Ehresmann, A.; Knie, A.; Dreuw, A. Interatomic and Intermolecular Coulombic Decay. *Chem. Rev.* **2020**, *120*, 11295–11369.
- [59] Zobeley, J.; Santra, R.; Cederbaum, L. S. Electronic Decay in Weakly Bound Heteroclusters: Energy Transfer versus Electron Transfer. *J. Chem. Phys.* **2001**, *115*, 5076–5088.
- [60] Förstel, M.; Mucke, M.; Arion, T.; Bradshaw, A. M.; Hergenbahn, U. Autoionization Mediated by Electron Transfer. *Phys. Rev. Lett.* **2011**, *106*, 033402.
- [61] Slavíček, P.; Winter, B.; Cederbaum, L. S.; Kryzhevoi, N. V. Proton-Transfer Mediated Enhancement of Nonlocal Electronic Relaxation Processes in X-ray Irradiated Liquid Water. *J. Am. Chem. Soc.* **2014**, *136*, 18170–18176.
- [62] Sakai, K.; Stoychev, S.; Ouchi, T.; Higuchi, I.; Schöffler, M.; Mazza, T.; Fukuzawa, H.; Nagaya, K.; Yao, M.; Tamenori, Y.; Kuleff, A. I.; Saito, N.; Ueda, K. Electron-Transfer-Mediated Decay and Interatomic Coulombic Decay from the Triply Ionized States in Argon Dimers. *Phys. Rev. Lett.* **2011**, *106*, 033401.
- [63] Stumpf, V.; Kryzhevoi, N. V.; Gokhberg, K.; Cederbaum, L. S. Enhanced One-Photon Double Ionization of Atoms and Molecules in an Environment of Different Species. *Phys. Rev. Lett.* **2014**, *112*, 193001.
- [64] Buth, C.; Santra, R.; Cederbaum, L. S. Impact of interatomic electronic decay processes on Xe 4d hole decay in the xenon fluorides. *J. Chem. Phys.* **2003**, *119*, 10575–10584.
- [65] Stumpf, V.; Kolorenč, P.; Gokhberg, K.; Cederbaum, L. S. Efficient Pathway to Neutralization of Multiply Charged Ions Produced in Auger Processes. *Phys. Rev. Lett.* **2013**, *110*, 258302.

- [66] Ghosh, A.; Cederbaum, L. S.; Gokhberg, K. Electron transfer mediated decay in HeLi₂ cluster: Potential energy surfaces and decay widths. *J. Chem. Phys.* **2019**, *150*, 164309.
- [67] Ghosh, A.; Cederbaum, L. S.; Gokhberg, K. Signature of the neighbor's quantum nuclear dynamics in the electron transfer mediated decay spectra. *Chem. Sci.* **2021**, *12*, 9379–9385.
- [68] Kumar, R.; Vaval, N. Effect of Protonation and Deprotonation on Electron Transfer Mediated Decay and Interatomic Coulombic Decay. *ChemPhysChem* **2023**, *24*, e202200340.
- [69] Müller, I. B.; Cederbaum, L. S. Electronic decay following ionization of aqueous Li⁺ microsolvation clusters. *J. Chem. Phys.* **2005**, *122*, 094305.
- [70] Pohl, M. N.; Richter, C.; Lugovoy, E.; Seidel, R.; Slavíček, P.; Aziz, E. F.; Abel, B.; Winter, B.; Hergenbahn, U. Sensitivity of Electron Transfer Mediated Decay to Ion Pairing. *J. Phys. Chem. B* **2017**, *121*, 7709–7714.
- [71] Unger, I.; Seidel, R.; Thürmer, S.; Pohl, M. N.; Aziz, E. F.; Cederbaum, L. S.; Muchová, E.; Slavíček, P.; Winter, B.; Kryzhevoi, N. V. Observation of electron-transfer-mediated decay in aqueous solution. *Nat. Chem.* **2017**, *9*, 708–714.
- [72] Pernpointner, M.; Kryzhevoi, N. V.; Urbaczek, S. Possible electronic decay channels in the ionization spectra of small clusters composed of Ar and Kr: A four-component relativistic treatment. *J. Chem. Phys.* **2008**, *129*, 024304.
- [73] Barth, S.; Joshi, S.; Marburger, S.; Ulrich, V.; Lindblad, A.; Öhrwall, G.; Björneholm, O.; Hergenbahn, U. Observation of resonant Interatomic Coulombic Decay in Ne clusters. *J. Chem. Phys.* **2005**, *122*, 241102.
- [74] Aoto, T.; Ito, K.; Hikosaka, Y.; Shigemasu, E.; Penent, F.; Lablanquie, P. Properties of Resonant Interatomic Coulombic Decay in Ne Dimers. *Phys. Rev. Lett.* **2006**, *97*, 243401.

- [75] Gokhberg, K.; Averbukh, V.; Cederbaum, L. S. Interatomic decay of inner-valence-excited states in clusters. *J. Chem. Phys.* **2006**, *124*, 144315.
- [76] Ren, X.; Wang, E.; Skitnevskaya, A. D.; Trofimov, A. B.; Gokhberg, K.; Dorn, A. Experimental evidence for ultrafast intermolecular relaxation processes in hydrated biomolecules. *Nat. Phys.* **2018**, *14*, 1062–1066.
- [77] Boudaïffa, B.; Cloutier, P.; Hunting, D.; Huels, M. A.; Sanche, L. Resonant Formation of DNA Strand Breaks by Low-Energy (3 to 20 eV) Electrons. *Science* **2000**, *287*, 1658–1660.
- [78] Hanel, G.; Gstir, B.; Denifl, S.; Scheier, P.; Probst, M.; Farizon, B.; Farizon, M.; Illenberger, E.; Märk, T. D. Electron Attachment to Uracil: Effective Destruction at Subexcitation Energies. *Phys. Rev. Lett.* **2003**, *90*, 188104.
- [79] Howell, R. W. Auger processes in the 21st century. *Int. J. Radiat. Biol.* **2008**, *84*, 959–975.
- [80] Surdutovich, E.; Solov'yov, A. Double strand breaks in DNA resulting from double ionization events. *Eur. Phys. J. D* **2012**, *66*, 206.
- [81] Alizadeh, E.; Orlando, T. M.; Sanche, L. Biomolecular Damage Induced by Ionizing Radiation: The Direct and Indirect Effects of Low-Energy Electrons on DNA. *Annu. Rev. Phys. Chem.* **2015**, *66*, 379–398.
- [82] Märk, T. D.; Scheier, P. Unexpected electrons. *Nat. Phys.* **2010**, *6*, 82–83.
- [83] Sonntag, C. *Free-Radical-Induced DNA Damage and Its Repair: A Chemical Perspective*; Springer Science & Business Media, 2006.
- [84] Kumar, A.; Sevilla, M. D. In *Handbook of Computational Chemistry*; Leszczynski, J., Ed.; Springer Netherlands: Dordrecht, 2016; pp 1–63.

- [85] Gu, J.; Wang, J.; Leszczynski, J. Electron attachment-induced DNA single-strand breaks at the pyrimidine sites. *Nucleic Acids Res.* **2010**, *38*, 5280–5290.
- [86] Rackwitz, J.; Bald, I. Low-Energy Electron-Induced Strand Breaks in Telomere-Derived DNA Sequences—Influence of DNA Sequence and Topology. *Chem. Eur. J.* **2018**, *24*, 4680–4688.
- [87] Baccarelli, I.; Bald, I.; Gianturco, F. A.; Illenberger, E.; Kopyra, J. Electron-induced damage of DNA and its components: Experiments and theoretical models. *Phys. Rep.* **2011**, *508*, 1–44.
- [88] Chen, W.; Chen, S.; Dong, Y.; Cloutier, P.; Zheng, Y.; Sanche, L. Absolute cross-sections for DNA strand breaks and crosslinks induced by low energy electrons. *Phys. Chem. Chem. Phys.* **2016**, *18*, 32762–32771.
- [89] Gu, J.; Wang, J.; Leszczynski, J. Electron Attachment-Induced DNA Single Strand Breaks: C_{3'}-O_{3'} σ -Bond Breaking of Pyrimidine Nucleotides Predominates. *J. Am. Chem. Soc.* **2006**, *128*, 9322–9323.
- [90] Ebel, K.; Bald, I. Low-Energy (5–20 eV) Electron-Induced Single and Double Strand Breaks in Well-Defined DNA Sequences. *J. Phys. Chem. Lett.* **2022**, *13*, 4871–4876.
- [91] Simons, J. How Do Low-Energy (0.1-2 eV) Electrons Cause DNA-Strand Breaks? *Acc. Chem. Res.* **2006**, *39*, 772–779.
- [92] Khorsandgolchin, G.; Sanche, L.; Cloutier, P.; Wagner, J. R. Strand Breaks Induced by Very Low Energy Electrons: Product Analysis and Mechanistic Insight into the Reaction with TpT. *J. Am. Chem. Soc.* **2019**, *141*, 10315–10323.
- [93] Tripathi, D.; Dutta, A. K. Electron Attachment to DNA Base Pairs: An Interplay of Dipole- and Valence-Bound States. *J. Phys. Chem. A* **2019**, *123*, 10131–10138.

- [94] Davis, D.; Vysotskiy, V. P.; Sajeev, Y.; Cederbaum, L. S. Electron Impact Catalytic Dissociation: Two-Bond Breaking by a Low-Energy Catalytic Electron. *Angew. Chem. Int. Ed.* **2011**, *50*, 4119–4122.
- [95] Davis, D.; Vysotskiy, V. P.; Sajeev, Y.; Cederbaum, L. S. A One-Step Four-Bond-Breaking Reaction Catalyzed by an Electron. *Angew. Chem. Int. Ed.* **2012**, *51*, 8003–8007.
- [96] Davis, D.; Sajeev, Y. Low energy electron catalyst: the electronic origin of catalytic strategies. *Phys. Chem. Chem. Phys.* **2016**, *18*, 27715–27720.
- [97] Davis, D.; Sajeev, Y. Communication: Low-energy free-electron driven molecular engineering: In situ preparation of intrinsically short-lived carbon-carbon covalent dimer of CO. *J. Chem. Phys.* **2017**, *146*, 081101.
- [98] Davis, D.; Kundu, S.; Prabhudesai, V. S.; Sajeev, Y.; Krishnakumar, E. Formation of CO₂ from formic acid through catalytic electron channel. *J. Chem. Phys.* **2018**, *149*, 064308.
- [99] Davis, D.; Bhushan, K. G.; Sajeev, Y.; Cederbaum, L. S. A Concerted Synchronous [2 + 2] Cycloreversion Repair Catalyzed by Two Electrons. *J. Phys. Chem. Lett.* **2018**, *9*, 6973–6977.
- [100] Lozano, A. I.; Kossoski, F.; Blanco, F.; Limão Vieira, P.; Varella, M. T. d. N.; García, G. Observation of Transient Anions That Do Not Decay through Dissociative Electron Attachment: New Pathways for Radiosensitization. *J. Phys. Chem. Lett.* **2022**, *13*, 7001–7008.
- [101] Denifl, S.; Ptasińska, S.; Probst, M.; Hrušák, J.; Scheier, P.; Märk, T. D. Electron Attachment to the Gas-Phase DNA Bases Cytosine and Thymine. *J. Phys. Chem. A* **2004**, *108*, 6562–6569.

- [102] Cipriani, M.; Ingólfsson, O. HF Formation through Dissociative Electron Attachment- A Combined Experimental and Theoretical Study on Pentafluorothiophenol and 2-Fluorothiophenol. *Int. J. Mol. Sci.* **2022**, *23*, 2430.
- [103] Boulanouar, O.; Fromm, M.; Mavon, C.; Cloutier, P.; Sanche, L. Dissociative electron attachment to DNA-diamine thin films: Impact of the DNA close environment on the OH⁻ and O⁻ decay channels. *J. Chem. Phys.* **2013**, *139*, 055101.
- [104] Ma, J.; Kumar, A.; Muroya, Y.; Yamashita, S.; Sakurai, T.; Denisov, S. A.; Sevilla, M. D.; Adhikary, A.; Seki, S.; Mostafavi, M. Observation of dissociative quasi-free electron attachment to nucleoside via excited anion radical in solution. *Nat. Commun.* **2019**, *10*, 102.
- [105] Fock, V. Näherungsmethode zur Lösung des quantenmechanischen Mehrkörperproblems. *Z. Physik* **1930**, *61*, 126–148.
- [106] Hartree, D. R. The Wave Mechanics of an Atom with a Non-Coulomb Central Field. Part I. Theory and Methods. *Math. Proc. Camb. Philos. Soc.* **1928**, *24*, 89–110.
- [107] Slater, J. C. Note on Hartree's Method. *Phys. Rev.* **1930**, *35*, 210–211.
- [108] Szabó, A.; Ostlund, N. S. *Modern quantum chemistry : introduction to advanced electronic structure theory*, first edition ed.; Dover publications: Mineola, New York, 1996.
- [109] Roothaan, C. C. J. New Developments in Molecular Orbital Theory. *Rev. Mod. Phys.* **1951**, *23*, 69–89.
- [110] Roothaan, C. C. J. Self-Consistent Field Theory for Open Shells of Electronic Systems. *Rev. Mod. Phys.* **1960**, *32*, 179–185.
- [111] Fast, P. L.; Corchado, J.; Sanchez, M. L.; Truhlar, D. G. Optimized Parameters for Scaling Correlation Energy. *J. Phys. Chem. A* **1999**, *103*, 3139–3143.

- [112] Kelly, H. P. Correlation Effects in Atoms. *Phys. Rev.* **1963**, *131*, 684–699.
- [113] Pople, J. A.; Binkley, J. S.; Seeger, R. Theoretical models incorporating electron correlation. *Int. J. Quantum Chem.* **1976**, *10*, 1–19.
- [114] Bartlett, R. J. Many-Body Perturbation Theory and Coupled Cluster Theory for Electron Correlation in Molecules. *Annu. Rev. Phys. Chem.* **1981**, *32*, 359–401.
- [115] Mukhopadhyay, D.; Mukhopadhyay, S.; Chaudhuri, R.; Mukherjee, D. Aspects of separability in the coupled cluster based direct methods for energy differences. *Theoret. Chim. Acta* **1991**, *80*, 441–467.
- [116] Handy, N. Multi-root configuration interaction calculations. *Chem. Phys. Lett.* **1980**, *74*, 280–283.
- [117] Siegbahn, P. E. A new direct CI method for large CI expansions in a small orbital space. *Chem. Phys. Lett.* **1984**, *109*, 417–423.
- [118] Knowles, P.; Handy, N. A new determinant-based full configuration interaction method. *Chem. Phys. Lett.* **1984**, *111*, 315–321.
- [119] Knowles, P. J.; Handy, N. C. Unlimited full configuration interaction calculations. *J. Chem. Phys.* **1989**, *91*, 2396–2398.
- [120] Olsen, J.; Jørgensen, P.; Simons, J. Passing the one-billion limit in full configuration-interaction (FCI) calculations. *Chem. Phys. Lett.* **1990**, *169*, 463–472.
- [121] David Sherrill, C.; Schaefer, H. F. In *The Configuration Interaction Method: Advances in Highly Correlated Approaches*; Löwdin, P.-O., Sabin, J. R., Zerner, M. C., Brändas, E., Eds.; Advances in Quantum Chemistry; Academic Press, 1999; Vol. 34; pp 143–269.
- [122] Eriksen, J. J. The Shape of Full Configuration Interaction to Come. *J. Phys. Chem. Lett.* **2021**, *12*, 418–432.

-
- [123] Coe, J. P. Machine Learning Configuration Interaction. *J. Chem. Theory Comput* **2018**, *14*, 5739–5749.
- [124] Paige, C. Accuracy and effectiveness of the Lanczos algorithm for the symmetric eigenproblem. *Linear Algebra Appl.* **1980**, *34*, 235–258.
- [125] *Lanczos Algorithms for Large Symmetric Eigenvalue Computations*; Chapter 7, pp 210–251.
- [126] Wu, K.; Simon, H. D. A parallel Lanczos method for symmetric generalized eigenvalue problems. *Comput. Vis. Sci.* **1999**, *2*, 37–46.
- [127] Davidson, E. R. The iterative calculation of a few of the lowest eigenvalues and corresponding eigenvectors of large real-symmetric matrices. *J. Comput. Phys.* **1975**, *17*, 87–94.
- [128] Sommerfeld, T.; Tarantelli, F. Subspace iteration techniques for the calculation of resonances using complex symmetric Hamiltonians. *J. Chem. Phys.* **2000**, *112*, 2106–2110.
- [129] Crouzeix, M.; Philippe, B.; Sadkane, M. The Davidson Method. *SIAM J. Sci. Comput.* **1994**, *15*, 62–76.
- [130] Kalamboukis, T. Z. Davidson’s algorithm with and without perturbation corrections. *J. Phys. A Math.* **1980**, *13*, 57.
- [131] Löwdin, P. A Note on the QuantumMechanical Perturbation Theory. *J. Chem. Phys.* **2004**, *19*, 1396–1401.
- [132] Löwdin, P. Studies in perturbation theory XIII. Treatment of constants of motion in resolvent method, partitioning technique, and perturbation theory. *Int. J. Quantum Chem.* **1968**, *2*, 867–931.

- [133] Brouder, C.; Duchamp, G. H.; Patras, F.; Tóth, G. Z. The Rayleigh-Schrödinger perturbation series of quasi-degenerate systems. *Int. J. Quantum Chem.* **2012**, *112*, 2256–2266.
- [134] Hirschfelder, J. O. Formal Rayleigh–Schrödinger perturbation theory for both degenerate and non-degenerate energy states. *Int. J. Quantum Chem.* **1969**, *3*, 731–748.
- [135] Arteca, G. A.; Fernández, F. M.; Castro, E. A. *Large Order Perturbation Theory and Summation Methods in Quantum Mechanics*; Springer Berlin Heidelberg: Berlin, Heidelberg, 1990; pp 45–71.
- [136] Møller, C.; Plesset, M. S. Note on an Approximation Treatment for Many-Electron Systems. *Phys. Rev.* **1934**, *46*, 618–622.
- [137] Frisch, M. J.; Head-Gordon, M.; Pople, J. A. A direct MP2 gradient method. *Chem. Phys. Lett.* **1990**, *166*, 275–280.
- [138] Frisch, M. J.; Head-Gordon, M.; Pople, J. A. Semi-direct algorithms for the MP2 energy and gradient. *Chem. Phys. Lett.* **1990**, *166*, 281–289.
- [139] Head-Gordon, M.; Pople, J. A.; Frisch, M. J. MP2 energy evaluation by direct methods. *Chem. Phys. Lett.* **1988**, *153*, 503–506.
- [140] Sæbø, S.; Almlöf, J. Avoiding the integral storage bottleneck in LCAO calculations of electron correlation. *Chem. Phys. Lett.* **1989**, *154*, 83–89.
- [141] Head-Gordon, M.; Head-Gordon, T. Analytic MP2 frequencies without fifth-order storage. Theory and application to bifurcated hydrogen bonds in the water hexamer. *Chem. Phys. Lett.* **1994**, *220*, 122–128.
- [142] Grüneis, A.; Marsman, M.; Kresse, G. Second-order Møller–Plesset perturbation theory applied to extended systems. II. Structural and energetic properties. *J. Chem. Phys.* **2010**, *133*, 074107.

- [143] Pople, J. A.; Seeger, R.; Krishnan, R. Variational configuration interaction methods and comparison with perturbation theory. *Int. J. Quantum Chem.* **1977**, *12*, 149–163.
- [144] Grimme, S. Improved third-order Møller–Plesset perturbation theory. *J. Comput. Chem.* **2003**, *24*, 1529–1537.
- [145] Krishnan, R.; Pople, J. A. Approximate fourth-order perturbation theory of the electron correlation energy. *Int. J. Quantum Chem.* **1978**, *14*, 91–100.
- [146] Krishnan, R.; Frisch, M. J.; Pople, J. A. Contribution of triple substitutions to the electron correlation energy in fourth order perturbation theory. *J. Chem. Phys.* **1980**, *72*, 4244–4245.
- [147] Leininger, M. L.; Allen, W. D.; Schaefer III, H. F.; Sherrill, C. D. Is Møller–Plesset perturbation theory a convergent ab initio method? *J. Chem. Phys.* **2000**, *112*, 9213–9222.
- [148] Forsberg, B.; He, Z.; He, Y.; Cremer, D. Convergence behavior of the Møller–Plesset perturbation series: Use of Feenberg scaling for the exclusion of backdoor intruder states. *Int. J. Quantum Chem.* **2000**, *76*, 306–330.
- [149] Cremer, D. Møller–Plesset perturbation theory: from small molecule methods to methods for thousands of atoms. *WIREs Comput. Mol. Sci.* **2011**, *1*, 509–530.
- [150] Coester, F. Bound states of a many-particle system. *Nucl. Phys.* **1958**, *7*, 421–424.
- [151] Coester, F.; Kümmel, H. Short-range correlations in nuclear wave functions. *Nucl. Phys.* **1960**, *17*, 477–485.
- [152] Čížek, J. On the Correlation Problem in Atomic and Molecular Systems. Calculation of Wavefunction Components in UrsellType Expansion Using QuantumField Theoretical Methods. *J. Chem. Phys.* **1966**, *45*, 4256–4266.

- [153] Čížek, J. *Advances in Chemical Physics*; John Wiley & Sons, Ltd, 1969; Vol. 14; Chapter 2, pp 35–89.
- [154] Paldus, J.; Čížek, J.; Shavitt, I. Correlation Problems in Atomic and Molecular Systems. IV. Extended Coupled-Pair Many-Electron Theory and Its Application to the BH₃ Molecule. *Phys. Rev. A* **1972**, *5*, 50–67.
- [155] Purvis III, G. D.; Bartlett, R. J. A full coupled-cluster singles and doubles model: The inclusion of disconnected triples. *J. Chem. Phys.* **1982**, *76*, 1910–1918.
- [156] Raghavachari, K.; Trucks, G. W.; Pople, J. A.; Head-Gordon, M. A fifth-order perturbation comparison of electron correlation theories. *Chem. Phys. Lett.* **1989**, *157*, 479–483.
- [157] Noga, J.; Bartlett, R. J. The full CCSDT model for molecular electronic structure. *J. Chem. Phys.* **1987**, *86*, 7041–7050.
- [158] Salter, E. A.; Sekino, H.; Bartlett, R. J. Property evaluation and orbital relaxation in coupled cluster methods. *J. Chem. Phys.* **1987**, *87*, 502–509.
- [159] Bartlett, R. J.; Musiał, M. Coupled-cluster theory in quantum chemistry. *Rev. Mod. Phys.* **2007**, *79*, 291–352.
- [160] Lyakh, D. I.; Musiał, M.; Lotrich, V. F.; Bartlett, R. J. Multireference Nature of Chemistry: The Coupled-Cluster View. *Chem. Rev.* **2012**, *112*, 182–243.
- [161] Lindgren, I.; Mukherjee, D. On the connectivity criteria in the open-shell coupled-cluster theory for general model spaces. *Phys. Rep.* **1987**, *151*, 93–127.
- [162] Mukherjee, D.; Pal, S. In *Use of Cluster Expansion Methods in the Open-Shell Correlation Problem*; Löwdin, P.-O., Ed.; Advances in Quantum Chemistry; Academic Press, 1989; Vol. 20; pp 291–373.

- [163] Rowe, D. J. Equations-of-Motion Method and the Extended Shell Model. *Rev. Mod. Phys.* **1968**, *40*, 153–166.
- [164] Nooijen, M.; Bartlett, R. J. Similarity Transformed Equation-of-Motion Coupled-Cluster Theory: Details, Examples, and Comparisons. *J. Chem. Phys.* **1997**, *107*, 6812–6830.
- [165] Musiał, M.; Bartlett, R. J. Charge Transfer Separability and Size Extensivity in the Equation-of-Motion Coupled Cluster Method: EOM-CCx. *J. Chem. Phys.* **2011**, *134*, 034106.
- [166] Sekino, H.; Bartlett, R. J. A linear response, coupled-cluster theory for excitation energy. *Int. J. Quantum Chem.* **1984**, *26*, 255–265.
- [167] Stanton, J. F.; Bartlett, R. J. The Equation-of-Motion Coupled Cluster Method. A Systematic Biorthogonal Approach to Molecular Excitation Energies, Transition Probabilities, and Excited State Properties. *J. Chem. Phys.* **1993**, *98*, 7029–7039.
- [168] Bartlett, R. J.; Stanton, J. F. *Reviews in Computational Chemistry*; John Wiley & Sons, Ltd, 1994; Vol. 5; Chapter ch2, pp 65–169.
- [169] Bomble, Y. J.; Saeh, J. C.; Stanton, J. F.; Szalay, P. G.; Kállay, M.; Gauss, J. Equation-of-motion coupled-cluster methods for ionized states with an approximate treatment of triple excitations. *J. Chem. Phys.* **2005**, *122*, 154107.
- [170] Nooijen, M.; Bartlett, R. J. Equation-of-Motion Coupled Cluster Method for Electron Attachment. *J. Chem. Phys.* **1995**, *102*, 3629–3647.
- [171] Watts, J. D.; Bartlett, R. J. Economical triple excitation equation-of-motion coupled-cluster methods for excitation energies. *Chem. Phys. Lett.* **1995**, *233*, 81–87.
- [172] Watts, J. D.; Bartlett, R. J. Iterative and non-iterative triple excitation corrections in

- coupled-cluster methods for excited electronic states: the EOM-CCSDT-3 and EOM-CCSD(\tilde{T}) methods. *Chem. Phys. Lett.* **1996**, 258, 581–588.
- [173] Musiał, M.; Kucharski, S. A.; Bartlett, R. J. *Approximate Inclusion of the T_3 and R_3 Operators in the Equation-of-motion Coupled-cluster Method*; Advances in Quantum Chemistry; Academic Press, 2004; Vol. 47; pp 209–222.
- [174] Kowalski, K.; Piecuch, P. The active-space equation-of-motion coupled-cluster methods for excited electronic states: Full EOMCCSDt. *J. Chem. Phys.* **2001**, 115, 643–651.
- [175] Watts, J. D.; Bartlett, R. J. The inclusion of connected triple excitations in the equation-of-motion coupled-cluster method. *J. Chem. Phys.* **1994**, 101, 3073–3078.
- [176] Kucharski, S. A.; Włoch, M.; Musiał, M.; Bartlett, R. J. Coupled-cluster theory for excited electronic states: The full equation-of-motion coupled-cluster single, double, and triple excitation method. *J. Chem. Phys.* **2001**, 115, 8263–8266.
- [177] Hirata, S. Higher-order equation-of-motion coupled-cluster methods. *J. Chem. Phys.* **2004**, 121, 51–59.
- [178] Musiał, M.; Kucharski, S. A.; Bartlett, R. J. Equation-of-Motion Coupled Cluster Method with Full Inclusion of the Connected Triple Excitations for Ionized States: IP-EOM-CCSDT. *J. Chem. Phys.* **2003**, 118, 1128–1136.
- [179] Kamiya, M.; Hirata, S. Higher-order equation-of-motion coupled-cluster methods for ionization processes. *J. Chem. Phys.* **2006**, 125, 074111.
- [180] Gour, J. R.; Piecuch, P. Efficient formulation and computer implementation of the active-space electron-attached and ionized equation-of-motion coupled-cluster methods. *J. Chem. Phys.* **2006**, 125, 234107.

- [181] Musiał, M.; Bartlett, R. J. Equation-of-motion coupled cluster method with full inclusion of connected triple excitations for electron-attached states: EA-EOM-CCSDT. *J. Chem. Phys.* **2003**, *119*, 1901–1908.
- [182] Kamiya, M.; Hirata, S. Higher-order equation-of-motion coupled-cluster methods for electron attachment. *J. Chem. Phys.* **2007**, *126*, 134112.
- [183] Moiseyev, N. *Non-Hermitian Quantum Mechanics*; Cambridge University Press, 2011; p 116–173.
- [184] Moiseyev, N. *Non-Hermitian Quantum Mechanics*; Cambridge University Press, 2011; p 211–249.
- [185] Moiseyev, N. *Non-Hermitian Quantum Mechanics*; Cambridge University Press, 2011; pp 84–115.
- [186] Siegert, A. J. F. On the Derivation of the Dispersion Formula for Nuclear Reactions. *Phys. Rev.* **1939**, *56*, 750–752.
- [187] Riss, U. V.; Meyer, H. D. Calculation of Resonance Energies and Widths using the Complex Absorbing Potential Method. *J. Phys. B: At. Mol. Opt. Phys.* **1993**, *26*, 4503–4535.
- [188] Sommerfeld, T.; Riss, U. V.; Meyer, H. D.; Cederbaum, L. S.; Engels, B.; Suter, H. U. Temporary Anions - Calculation of Energy and Lifetime by Absorbing Potentials: The N_2^- $^2\Pi_g$ Resonance. *J. Phys. B: At. Mol. Opt. Phys.* **1998**, *31*, 4107–4122.
- [189] Muga, J.; Palao, J.; Navarro, B.; Egusquiza, I. Complex Absorbing Potentials. *Phys. Rep.* **2004**, *395*, 357–426.
- [190] Moiseyev, N. Derivations of universal exact complex absorption potentials by the generalized complex coordinate method. *J. Phys. B: At. Mol. Opt. Phys.* **1998**, *31*, 1431.

- [191] P., B.; Sajeev, Y.; Moiseyev, N. Ab-initio complex molecular potential energy surfaces by the back-rotation transformation method. *Chem. Phys. Lett.* **2012**, *524*, 84–89.
- [192] Masui, H.; Ho, Y. K. Resonance states with the complex absorbing potential method. *Phys. Rev. C* **2002**, *65*, 054305.
- [193] Santra, R. Why complex absorbing potentials work: A discrete-variable-representation perspective. *Phys. Rev. A* **2006**, *74*, 034701.
- [194] Jolicard, G.; Zucconi, J.-M.; Drira, I.; Spielfieldel, A.; Feautrier, N. The photodissociation of SiO. *J. Chem. Phys.* **1997**, *106*, 10105–10112.
- [195] Ghosh, A.; Vaval, N.; Pal, S. Equation-of-motion coupled-cluster method for the study of shape resonance. *J. Chem. Phys.* **2012**, *136*, 234110.
- [196] Ghosh, A.; Karne, A.; Pal, S.; Vaval, N. CAP/EOM-CCSD method for the study of potential curves of resonant states. *Phys. Chem. Chem. Phys.* **2013**, *15*, 17915–17921.
- [197] Ghosh, A.; Pal, N., Souravand Vaval Interatomic Coulombic decay in HF_n ($n = 2-3$) clusters using CAP/EOM-CCSD method. *Mol. Phys.* **2014**, *112*, 669–673.
- [198] Ghosh, A.; Vaval, N. Geometry-dependent lifetime of Interatomic coulombic decay using equation-of-motion coupled cluster method. *J. Chem. Phys.* **2014**, *141*, 234108.
- [199] Ghosh, A.; Pal, S.; Vaval, N. Lifetime of inner-shell hole states of Ar (2p) and Kr (3d) using equation-of-motion coupled cluster method. *J. Chem. Phys.* **2015**, *143*, 024305.
- [200] Ghosh, A.; Vaval, N.; Pal, S. Auger decay rates of core hole states using equation of motion coupled cluster method. *Chem. Phys.* **2017**, *482*, 160–164.
- [201] Ghosh, A.; Pal, S.; Vaval, N. Study of Interatomic Coulombic Decay of $\text{Ne}(\text{H}_2\text{O})_n$ ($n=1,3$) Clusters Using Equation-of-Motion Coupled Cluster Method. *J. Chem. Phys.* **2013**, *139*, 064112.

- [202] Ghosh, A.; Vaval, N.; Pal, S.; Bartlett, R. J. Complex Absorbing Potential Based Equation-of-Motion Coupled Cluster Method for the Potential Energy Curve of CO_2^- Anion. *J. Chem. Phys.* **2014**, *141*, 164113.
- [203] Jagau, T. C.; Zuev, D.; Bravaya, K. B.; Epifanovsky, E.; Krylov, A. I. A Fresh Look at Resonances and Complex Absorbing Potentials: Density Matrix-Based Approach. *J. Phys. Chem. Lett.* **2014**, *5*, 310–315.
- [204] Zuev, D.; Jagau, T. C.; Bravaya, K. B.; Epifanovsky, E.; Shao, Y.; Sundstrom, E.; Head-Gordon, M.; Krylov, A. I. Complex Absorbing Potentials within EOM-CC Family of Methods: Theory, Implementation, and Benchmarks. *J. Chem. Phys.* **2014**, *141*, 024102.
- [205] Jagau, T. C.; Krylov, A. I. Complex Absorbing Potential Equation-of-Motion Coupled-Cluster Method Yields Smooth and Internally Consistent Potential Energy Surfaces and Lifetimes for Molecular Resonances. *J. Phys. Chem. Lett.* **2014**, *5*, 3078–3085.
- [206] Sajeev, Y.; Ghosh, A.; Vaval, N.; Pal, S. Coupled Cluster Methods for Autoionisation Resonances. *Int. Rev. Phys. Chem.* **2014**, *33*, 397–425.
- [207] Sajeev, Y.; Santra, R.; Pal, S. Correlated Complex Independent Particle Potential for Calculating Electronic Resonances. *J. Chem. Phys.* **2005**, *123*, 204110.
- [208] Sajeev, Y.; Pal, S. A General Formalism of the Fock Space Multireference Coupled Cluster Method for Investigating Molecular Electronic Resonances. *Mol. Phys.* **2005**, *103*, 2267–2275.
- [209] Sajeev, Y.; Vysotskiy, V.; Cederbaum, L. S.; Moiseyev, N. Continuum remover-complex absorbing potential: Efficient removal of the nonphysical stabilization points. *J. Chem. Phys.* **2009**, *131*, 211102.

- [210] Sajeev, Y. Real-valued continuum remover potential: An improved L_2 -stabilization method for the chemistry of electronic resonance states. *Chem. Phys. Lett.* **2013**, 587, 105–112.
- [211] Riss, U. V.; D., M. H. Reflection-free complex absorbing potentials. *J. Phys. B: At. Mol. Opt. Phys.* **1995**, 28, 1475.
- [212] Sajeev, Y.; Moiseyev, N. Reflection-free complex absorbing potential for electronic structure calculations: Feshbach-type autoionization resonances of molecules. *J. Chem. Phys.* **2007**, 127, 034105.
- [213] Sajeev, Y.; Sindelka, M.; Moiseyev, N. Reflection-free complex absorbing potential for electronic structure calculations: Feshbach type autoionization resonance of Helium. *Chem. Phys.* **2006**, 329, 307–312, Electron Correlation and Multimode Dynamics in Molecules.
- [214] Riss, U. V.; Meyer, H. D. The Transformative Complex Absorbing Potential Method: A Bridge between Complex Absorbing Potentials and Smooth Exterior Scaling. *J. Phys. B: At. Mol. Opt. Phys.* **1998**, 31, 2279–2304.
- [215] Sommerfeld, T.; Ehara, M. Complex Absorbing Potentials with Voronoi Isosurfaces Wrapping Perfectly around Molecules. *J. Chem. Theory Comput* **2015**, 11, 4627–4633.
- [216] Gayvert, J. R.; Bravaya, K. B. Application of Box and Voronoi CAPs for Metastable Electronic States in Molecular Clusters. *J. Phys. Chem. A* **2022**, 126, 5070–5078.
- [217] Ehara, M.; Fukuda, R.; Sommerfeld, T. Projected CAP/SAC-CI method with smooth Voronoi potential for calculating resonance states. *J. Comput. Chem.* **2016**, 37, 242–249.
- [218] Jolicard, G.; Austin, E. J. Optical Potential Stabilisation Method for Predicting Resonance Levels. *Chem. Phys. Lett.* **1985**, 121, 106–110.

- [219] Aguilar, J.; Combes, J. M. A class of analytic perturbations for one-body Schrödinger Hamiltonians. *Commun. Math. Phys.* **1971**, *22*, 269–279.
- [220] Balslev, E.; Combes, J. M. Spectral properties of many-body Schrödinger operators with dilatation-analytic interactions. *Commun. Math. Phys.* **1971**, *22*, 280–294.
- [221] Simon, B. Quadratic form techniques and the Balslev-Combes theorem. *Commun. Math. Phys.* **1972**, *27*, 1–9.
- [222] Reinhardt, W. P. Complex Coordinates in the Theory of Atomic and Molecular Structure and Dynamics. *Annu. Rev. Phys. Chem.* **1982**, *33*, 223–255.
- [223] Moiseyev, N. Quantum theory of resonances: calculating energies, widths and cross-sections by complex scaling. *Phys. Rep.* **1998**, *302*, 212–293.
- [224] Moiseyev, N.; Certain, P.; Weinhold, F. Resonance properties of complex-rotated hamiltonians. *Mol. Phys.* **1978**, *36*, 1613–1630.
- [225] McCurdy, C. W.; Rescigno, T. N. Extension of the Method of Complex Basis Functions to Molecular Resonances. *Phys. Rev. Lett.* **1978**, *41*, 1364–1368.
- [226] Moiseyev, N.; Corcoran, C. Autoionizing states of H_2 and H_2^- using the complex-scaling method. *Phys. Rev. A* **1979**, *20*, 814–817.
- [227] Ho, Y. The method of complex coordinate rotation and its applications to atomic collision processes. *Phys. Rep.* **1983**, *99*, 1–68.
- [228] Lipkin, N.; Moiseyev, N.; Brändas, E. Resonances by the exterior-scaling method within the framework of the finite-basis-set approximation. *Phys. Rev. A* **1989**, *40*, 549–553.
- [229] Katō, K. Resonances and continuum states in the complex scaling method. *J. Phys.: Conf. Ser.* **2006**, *49*, 73.

- [230] Bardsley, J. N. Complex scaling: An introduction. *Int. J. Quantum Chem.* **1978**, *14*, 343–352.
- [231] Myo, T.; Katō, K. Complex scaling: Physics of unbound light nuclei and perspective. *Prog. Theor. Exp. Phys* **2020**, *2020*, 12A101.
- [232] Fano, U. Effects of Configuration Interaction on Intensities and Phase Shifts. *Phys. Rev.* **1961**, *124*, 1866–1878.
- [233] Feshbach, H. A unified theory of nuclear reactions. II. *Ann. Phys.* **1962**, *19*, 287–313.
- [234] Kolorenč, P.; Averbukh, V.; Gokhberg, K.; Cederbaum, L. S. Ab initio calculation of interatomic decay rates of excited doubly ionized states in clusters. *J. Chem. Phys.* **2008**, *129*, 244102.
- [235] Averbukh, V.; Cederbaum, L. S. Ab initio calculation of interatomic decay rates by a combination of the Fano ansatz, Green's-function methods, and the Stieltjes imaging technique. *J. Chem. Phys.* **2005**, *123*, 204107.
- [236] Kolorenč, P.; Averbukh, V. Fano-ADC(2,2) method for electronic decay rates. *J. Chem. Phys.* **2020**, *152*, 214107.
- [237] Averbukh, V.; Cederbaum, L. S. Calculation of interatomic decay widths of vacancy states delocalized due to inversion symmetry. *J. Chem. Phys.* **2006**, *125*, 094107.
- [238] Martín, F.; Riera, A.; Yáñez, M. Continuum versus discretized wavefunctions. The importance of being well normalized. *Comput. Phys. Commun.* **1988**, *149*, 85–88.
- [239] Zhang, P.; Perry, C.; Luu, T. T.; Wörner, H. Observation of intermolecular Coulombic decay in liquid water. The 22nd International Conference on Ultrafast Phenomena 2020. 2020; p M3B.4.

- [240] Richter, C.; Hollas, D.; Saak, C.-M.; Förstel, M.; Miteva, T.; Mucke, M.; Björneholm, O.; Sisourat, N.; Slavíček, P.; Hergenbahn, U. Competition between proton transfer and intermolecular Coulombic decay in water. *Nat Commun.* **2018**, *9*, 4988.
- [241] Fasshauer, E.; Förstel, M.; Mucke, M.; Arion, T.; Hergenbahn, U. Theoretical and experimental investigation of Electron Transfer Mediated Decay in ArKr clusters. *Chem. Phys.* **2017**, *482*, 226–238.
- [242] Yan, S.; Zhang, P.; Ma, X.; Xu, S.; Li, B.; Zhu, X. L.; Feng, W. T.; Zhang, S. F.; Zhao, D. M.; Zhang, R. T.; Guo, D. L.; Liu, H. P. Observation of interatomic Coulombic decay and electron-transfer-mediated decay in high-energy electron-impact ionization of Ar₂. *Phys. Rev. A* **2013**, *88*, 042712.
- [243] LaForge, A. C.; Stumpf, V.; Gokhberg, K.; von Vangerow, J.; Stienkemeier, F.; Kryzhevoi, N. V.; O’Keeffe, P.; Ciavardini, A.; Krishnan, S. R.; Coreno, M.; Prince, K. C.; Richter, R.; Moshhammer, R.; Pfeifer, T.; Cederbaum, L. S.; Mudrich, M. Enhanced Ionization of Embedded Clusters by Electron-Transfer-Mediated Decay in Helium Nanodroplets. *Phys. Rev. Lett.* **2016**, *116*, 203001.
- [244] Kryzhevoi, N. V.; Averbukh, V.; Cederbaum, L. S. High Activity of Helium Droplets Following Ionization of Systems Inside Those Droplets. *Phys. Rev. B* **2007**, *76*, 094513.
- [245] Ben Ltaief, L.; Shcherbinin, M.; Mandal, S.; Krishnan, S. R.; Richter, R.; Pfeifer, T.; Bauer, M.; Ghosh, A.; Mudrich, M.; Gokhberg, K.; LaForge, A. C. Electron Transfer Mediated Decay of Alkali Dimers Attached to He Nanodroplets. *Phys. Chem. Chem. Phys.* **2020**, *22*, 8557–8564.
- [246] Stumpf, V.; Gokhberg, K.; Cederbaum, L. S. The Role of Metal Ions in X-ray Induced Photochemistry. *Nat. Chem.* **2016**, *8*, 237–241.

- [247] Stumpf, V.; Brunken, C.; Gokhberg, K. Impact of Metal Ion's Charge on the Interatomic Coulombic Decay Widths in Microsolvated Clusters. *J. Chem. Phys.* **2016**, *145*, 104306.
- [248] Brun, E.; Cloutier, P.; Sicard-Roselli, C.; Fromm, M.; Sanche, L. Damage Induced to DNA by Low-Energy (0-30 eV) Electrons under Vacuum and Atmospheric Conditions. *J. Phys. Chem. B* **2009**, *113*, 10008–10013.
- [249] Sussman, F.; Weinstein, H. On the Ion Selectivity in Ca-Binding Proteins: The Cyclo(-L-Pro-Gly-)3 Peptide as a Model. *Proc. Natl. Acad. Sci. USA* **1989**, *86*, 7880–7884.
- [250] Dill, K. A. Dominant Forces in Protein Folding. *Biochemistry* **1990**, *29*, 7133–7155.
- [251] Forrest, M. D. The Sodium-Potassium Pump is an Information Processing Element in Brain Computation. *Front. Physiol.* **2014**, *5*, 472.
- [252] Clausen, M. V.; Hilbers, F.; Poulsen, H. The Structure and Function of the Na,K-ATPase Isoforms in Health and Disease. *Front. Physiol.* **2017**, *8*, 371.
- [253] Tomasi, J.; Mennucci, B.; Cammi, R. Quantum Mechanical Continuum Solvation Models. *Chem. Rev.* **2005**, *105*, 2999–3094.
- [254] Frisch, M. J.; Trucks, G. W.; Schlegel, H. B.; Scuseria, G. E.; Robb, M. A.; Cheeseman, J. R.; Scalmani, G.; Barone, V.; Mennucci, B.; Petersson, G. A.; Nakatsuji, H.; Caricato, M.; Li, X.; Hratchian, H. P.; Izmaylov, A. F.; Bloino, J.; Zheng, G.; Sonnenberg, J. L.; Hada, M.; Ehara, M.; Toyota, K.; Fukuda, R.; Hasegawa, J.; Ishida, M.; Nakajima, T.; Honda, Y.; Kitao, O.; Nakai, H.; Vreven, T.; Montgomery, J., J. A.; Peralta, J. E.; Ogliaro, F.; Bearpark, M.; Heyd, J. J.; Brothers, E.; Kudin, K. N.; Staroverov, V. N.; Kobayashi, R.; Norm and, J.; Raghavachari, K.; Rendell, A.; Burant, J. C.; Iyengar, S. S.; Tomasi, J.; Cossi, M.; Rega, N.; Millam, J. M.; Klene, M.; Knox, J. E.; Cross, J. B.; Bakken, V.; Adamo, C.; Jaramillo, J.; Gomperts, R.; Stratmann, R. E.; Yazyev, O.; Austin, A. J.; Cammi, R.; Pomelli, C.; Ochterski, J. W.;

- Martin, R. L.; Morokuma, K.; Zakrzewski, V. G.; Voth, G. A.; Salvador, P.; Dannenberg, J. J.; Dapprich, S.; Daniels, A. D.; Farkas, O.; Foresman, J. B.; Ortiz, J. V.; Cioslowski, J.; Fox, D. J. Gaussian-09 Gaussian Inc.: Wallingford CT, 2009.
- [255] Dunning, T. H. Gaussian Basis Sets for Use in Correlated Molecular Calculations. I. The Atoms Boron Through Neon and Hydrogen. *J. Chem. Phys.* **1989**, *90*, 1007–1023.
- [256] Kaufmann, K.; Baumeister, W.; Jungen, M. Universal Gaussian Basis Sets for an Optimum Representation of Rydberg and Continuum Wavefunctions. *J. Phys. B: At. Mol. Opt. Phys.* **1989**, *22*, 2223–2240.
- [257] Kendall, R. A.; Dunning Jr., T. H.; Harrison, R. J. Electron Affinities of the First-Row Atoms Revisited. Systematic Basis Sets and Wave Functions. *J. Chem. Phys.* **1992**, *96*, 6796–6806.
- [258] Becke, A. D. Density-Functional Thermochemistry. III. The Role of Exact Exchange. *J. Chem. Phys.* **1993**, *98*, 5648–5652.
- [259] Lee, C.; Yang, W.; Parr, R. G. Development of the Colle-Salvetti Correlation-Energy Formula into a Functional of the Electron Density. *Phys. Rev. B* **1988**, *37*, 785–789.
- [260] Stephens, P. J.; Devlin, F. J.; Chabalowski, C. F.; Frisch, M. J. Ab Initio Calculation of Vibrational Absorption and Circular Dichroism Spectra Using Density Functional Force Fields. *J. Phys. Chem.* **1994**, *98*, 11623–11627.
- [261] Vosko, S. H.; Wilk, L.; Nusair, M. Accurate Spin-Dependent Electron Liquid Correlation Energies for Local Spin Density Calculations: A Critical Analysis. *Can. J. Phys.* **1980**, *58*, 1200–1211.
- [262] Müller, I. B.; Cederbaum, L. S.; Tarantelli, F. Microsolvation of Li⁺ in Water Analyzed by Ionization and Double Ionization. *J. Phys. Chem. A* **2004**, *108*, 5831–5844.

- [263] Papajak, E.; Leverentz, H. R.; Zheng, J.; Truhlar, D. G. Efficient Diffuse Basis Sets: cc-pVxZ+ and maug-cc-pVxZ. *J. Chem. Theory Comput.* **2009**, *5*, 3330–3330.
- [264] Pritchard, B. P.; Altarawy, D.; Didier, B.; Gibson, T. D.; Windus, T. L. New Basis Set Exchange: An Open, Up-to-Date Resource for the Molecular Sciences Community. *J. Chem. Inf. Model.* **2019**, *59*, 4814–4820.
- [265] Öhrwall, G.; Ottosson, N.; Pokapanich, W.; Legendre, S.; Svensson, S.; Björneholm, O. Charge Dependence of Solvent-Mediated Intermolecular Coster-Kronig Decay Dynamics of Aqueous Ions. *J. Phys. Chem. B* **2010**, *114*, 17057–17061.
- [266] McLean, A. D.; Chandler, G. S. Contracted Gaussian Basis Sets for Molecular Calculations. I. Second Row Atoms, Z=11-18. *J. Chem. Phys.* **1980**, *72*, 5639–5648.
- [267] Blaudeau, J.-P.; McGrath, M. P.; Curtiss, L. A.; Radom, L. Extension of Gaussian-2 (G2) Theory to Molecules Containing Third-Row Atoms K and Ca. *J. Chem. Phys.* **1997**, *107*, 5016–5021.
- [268] Hill, J. G.; Peterson, K. A. Gaussian Basis Sets for Use in Correlated Molecular Calculations. XI. Pseudopotential-Based and All-Electron Relativistic Basis Sets for Alkali Metal (K-Fr) and Alkaline Earth (Ca-Ra) Elements. *J. Chem. Phys.* **2017**, *147*, 244106.
- [269] Pokapanich, W.; Bergersen, H.; Bradeanu, I. L.; Marinho, R. R. T.; Lindblad, A.; Legendre, S.; Rosso, A.; Svensson, S.; Björneholm, O.; Tchapyguine, M.; Öhrwall, G.; Kryzhevoi, N. V.; Cederbaum, L. S. Auger Electron Spectroscopy as a Probe of the Solution of Aqueous Ions. *J. Am. Chem. Soc.* **2009**, *131*, 7264–7271.
- [270] Pokapanich, W.; Kryzhevoi, N. V.; Ottosson, N.; Svensson, S.; Cederbaum, L. S.; Öhrwall, G.; Björneholm, O. Ionic-Charge Dependence of the Intermolecular Coulombic Decay Time-Scale for Aqueous Ions Probed by the Core-Hole Clock. *J. Am. Chem. Soc.* **2011**, *133*, 13430–13436.

- [271] Kryzhevoi, N. V.; Cederbaum, L. S. Using pH Value to Control Intermolecular Electronic Decay. *Angew. Chem. Int. Ed.* **2011**, *50*, 1306–1309.
- [272] Krishnan, R.; Binkley, J. S.; Seeger, R.; Pople, J. A. Self-Consistent Molecular Orbital Methods. XX. A Basis Set for Correlated Wave Functions. *J. Chem. Phys.* **1980**, *72*, 650–654.
- [273] Viering, D. H. H. M.; de Baaij, J. H. F.; Walsh, S. B.; Kleta, R.; Bockenbauer, D. Genetic Causes of Hypomagnesemia, a Clinical Overview. *Pediatr. Nephrol.* **2017**, *32*, 1123–1135.
- [274] Swaminathan, R. Magnesium Metabolism and its Disorders. *Clin. Biochem. Rev.* **2003**, *24*, 47–66.
- [275] Horowitz, M.; Al Alawi, A. M.; Majoni, S. W.; Falhammar, H. Magnesium and Human Health: Perspectives and Research Directions. *Int. J. Endocrinol.* **2018**, *2018*, 9041694.
- [276] Rao, J. S.; Dinadayalane, T. C.; Leszczynski, J.; Sastry, G. N. Comprehensive Study on the Solvation of Mono- and Divalent Metal Cations: Li^+ , Na^+ , K^+ , Be^{2+} , Mg^{2+} and Ca^{2+} . *J. Phys. Chem. A* **2008**, *112*, 12944–12953, PMID: 18834092.
- [277] Hartke, B.; Charvat, A.; Reich, M.; Abel, B. Experimental and Theoretical Investigation of Microsolvation of Na^+ -Ions in the Gas Phase by High Resolution Mass Spectrometry and Global Cluster Geometry Optimization. *J. Chem. Phys.* **2002**, *116*, 3588–3600.
- [278] Fifen, J. J.; Agmon, N. Structure and Spectroscopy of Hydrated Sodium Ions at Different Temperatures and the Cluster Stability Rules. *J. Chem. Theory Comput.* **2016**, *12*, 1656–1673, PMID: 26913993.
- [279] Miteva, T.; Wenzel, J.; Klaiman, S.; Dreuw, A.; Gokhberg, K. X-Ray Absorption Spectra of Microsolvated Metal Cations. *Phys. Chem. Chem. Phys.* **2016**, *18*, 16671–16681.

- [280] Wang, P.; Shi, R.; Su, Y.; Tang, L.; Huang, X.; Zhao, J. Hydrated Sodium Ion Clusters $[\text{Na6}+(\text{H}_2\text{O})_n$ ($n = 1-6$): An Ab Initio Study on Structures and Non-covalent Interaction. *Front. Chem.* **2019**, *7*, 624.
- [281] Hemmerich, J. L.; Bennett, R.; Buhmann, S. Y. The influence of retardation and dielectric environments on interatomic Coulombic decay. *Nat. Commun.* **2018**, *9*, 2934.
- [282] Reinhardt, W. P. L^2 discretization of atomic and molecular electronic continua: Moment, quadrature and J-matrix techniques. *Comput. Phys. Commun.* **1979**, *17*, 1–21.
- [283] Roos, B. O.; Taylor, P. R.; Siegbahn, P. E. M. A complete active space SCF method (CASSCF) using a density matrix formulated super-CI approach. *Chem. Phys.* **1980**, *48*, 157–173.
- [284] Siegbahn, P. E. M.; Almlöf, J.; Heiberg, A.; Roos, B. O. The complete active space SCF (CASSCF) method in a Newton–Raphson formulation with application to the HNO molecule. *J. Chem. Phys.* **1981**, *74*, 2384–2396.
- [285] Siegbahn, P.; Heiberg, A.; Roos, B.; Levy, B. A Comparison of the Super-CI and the Newton-Raphson Scheme in the Complete Active Space SCF Method. *Phys. Scr.* **1980**, *21*, 323.
- [286] Roos, B. O. *Advances in Chemical Physics*; John Wiley & Sons, Ltd, 1987; Chapter 7, pp 399–445.
- [287] Frisch, M.; Ragazos, I. N.; Robb, M. A.; Bernhard Schlegel, H. An evaluation of three direct MC-SCF procedures. *Chem. Phys. Lett.* **1992**, *189*, 524–528.
- [288] Eade, R. H.; Robb, M. A. Direct minimization in mc scf theory. the quasi-newton method. *Chem. Phys. Lett.* **1981**, *83*, 362–368.
- [289] Siegbahn, P. E. A new direct CI method for large CI expansions in a small orbital space. *Chem. Phys. Lett.* **1984**, *109*, 417–423.

- [290] Olsen, J. The CASSCF method: A perspective and commentary. *International Journal of Quantum Chemistry* **2011**, *111*, 3267–3272.
- [291] Andersson, K.; Malmqvist, P. Å.; Roos, B. O.; Sadlej, A. J.; Wolinski, K. Second-order Perturbation Theory with a CASSCF Reference Function. *J. Phys. Chem.* **1990**, *94*, 5483–5488.
- [292] Werner, H.; Knowles, P. J. A Second Order Multiconfiguration SCF Procedure with Optimum Convergence. *J. Chem. Phys.* **1985**, *82*, 5053–5063.
- [293] Andersson, K.; Malmqvist, P. Å.; Roos, B. O. Second-order Perturbation Theory with a Complete Active Space Self-Consistent Field Reference Function. *J. Chem. Phys.* **1992**, *96*, 1218–1226.
- [294] Aquilante, F.; Autschbach, J.; Carlson, R. K.; Chibotaru, L. F.; Delcey, M. G.; De Vico, L.; Fdez. Galván, I.; Ferré, N.; Frutos, L. M.; Gagliardi, L.; Garavelli, M.; Giussani, A.; Hoyer, C. E.; Li Manni, G.; Lischka, H.; Ma, D.; Malmqvist, P. Å.; Müller, T.; Nenov, A.; Olivucci, M.; Pedersen, T. B.; Peng, D.; Plasser, F.; Pritchard, B.; Reiher, M.; Rivalta, I.; Schapiro, I.; Segarra-Martí, J.; Stenrup, M.; Truhlar, D. G.; Ungur, L.; Valentini, A.; Vancoillie, S.; Veryazov, V.; Vysotskiy, V. P.; Weingart, O.; Zapata, F.; Lindh, R. Molcas 8: New Capabilities for Multiconfigurational Quantum Chemical Calculations Across the Periodic Table. *J. Comput. Chem.* **2016**, *37*, 506–541.
- [295] Widmark, P.-O.; Persson, B. J.; Roos, B. O. Density Matrix Averaged Atomic Natural Orbital (ANO) Basis Sets for Correlated Molecular Wave Functions. II. Second Row Atoms. *Theor. Chim. Acta* **1991**, *79*, 419–432.
- [296] Stanton, J. F.; Gauss, J. Perturbative treatment of the similarity transformed Hamiltonian in equationofmotion coupledcluster approximations. *J. Chem. Phys.* **1995**, *103*, 1064–1076.

- [297] Cederbaum, L. S.; Domcke, W.; Schirmer, J.; Niessen, W. V. *Adv. Chem. Phys.*; John Wiley & Sons, Ltd, 1986; Chapter 3, pp 115–159.
- [298] Phillips, J. C. Generalized Koopmans' Theorem. *Phys. Rev.* **1961**, *123*, 420–424.
- [299] Küstner-Wetekam, C.; Marder, L.; Bloß, D.; Honisch, C.; Kiefer, N.; Richter, C.; Rubik, S.; Schaf, R.; Zindel, C.; Förstel, M.; Gokhberg, K.; Knie, A.; Hergenbahn, U.; Ehresmann, A.; Kolorenč, P.; Hans, A. Experimental quantification of site-specific efficiency of Interatomic Coulombic Decay after inner shell ionization. *Commun. Phys.* **2023**, *6*, 50.
- [300] Fasshauer, E. Effect of spin–orbit coupling on decay widths of electronic decay processes. *J. Chem. Phys.* **2020**, *152*, 224307.
- [301] Cederbaum, L. S.; Kuleff, A. I. Impact of cavity on interatomic Coulombic decay. *Nat. Commun.* **2021**, *12*, 4083.
- [302] Fasshauer, E. Non-nearest neighbour ICD in clusters. *New J. Phys.* **2016**, *18*, 043028.
- [303] Fasshauer, E.; Förstel, M.; Pallmann, S.; Pernpointner, M.; Hergenbahn, U. Using ICD for structural analysis of clusters: a case study on NeAr clusters. *New J. Phys.* **2014**, *16*, 103026.
- [304] Stoychev, S. D.; Kuleff, A. I.; Cederbaum, L. S. Intermolecular Coulombic Decay in Small Biochemically Relevant Hydrogen-Bonded Systems. *J. Am. Chem. Soc.* **2011**, *133*, 6817.
- [305] Marsalek, O.; Elles, C. G.; Pieniasek, P. A.; Pluhařová, E.; VandeVondele, J.; Bradforth, S. E.; Jungwirth, P. Chasing Charge Localization and Chemical Reactivity Following Photoionization in Liquid Water. *J. Chem. Phys.* **2011**, *135*, 224510.
- [306] Mucke, M.; Braune, M.; Barth, S.; Förstel, M.; Lischke, T.; Ulrich, V.; Arion, T.;

- Becker, U.; Bradshaw, A.; Hergenbahn, U. A Hitherto Unrecognized Source of Low-energy Electrons in Water. *Nat. Phys.* **2010**, *6*, 143–146.
- [307] Jordan, I.; Huppert, M.; Rattenbacher, D.; Peper, M.; Jelovina, D.; Perry, C.; Von Conta, A.; Schild, A.; Wörner, H. J. Attosecond science in liquid phase. *Science* **2020**, *369*, 974–979.
- [308] Slavíček, P.; Kryzhevoi, N. V.; Aziz, E. F.; Winter, B. Relaxation processes in aqueous systems upon X-ray ionization: entanglement of electronic and nuclear dynamics. *J. Phys. Chem. Lett.* **2016**, *7*, 234–243.
- [309] Jahnke, T.; Sann, H.; Havermeier, T.; Kreidi, K.; Stuck, C.; Meckel, M.; Schöffler, M.; Neumann, N.; Wallauer, R.; Voss, S.; Czasch, A.; Jagutzki, O.; Malakzadeh, A.; Afaneh, F.; Weber, T.; Schmidt-Böcking, H.; Dörner, R. Ultrafast Energy Transfer between Water Molecules. *Nat. Phys.* **2010**, *6*, 139–142.
- [310] Verlet, L. Computer "experiments" on classical fluids. I. Thermodynamical properties of Lennard-Jones molecules. *Phys. Rev.* **1967**, *159*, 98.
- [311] Santra, R.; Cederbaum, L. S. Complex Absorbing Potentials in the Framework of Electron Propagator Theory. I. General Formalism. *J. Chem. Phys.* **2002**, *117*, 5511–5521.
- [312] Jagau, T.-C.; Zuev, D.; Bravaya, K. B.; Epifanovsky, E.; Krylov, A. I. A Fresh Look at Resonances and Complex Absorbing Potentials: Density Matrix-based Approach. *J. Phys. Chem. Lett.* **2014**, *5*, 310–315.
- [313] Lane, J. R. CCSDTQ Optimized Geometry of Water Dimer. *J. Chem. Theory Comput.* **2013**, *9*, 316–323.
- [314] Koster, A. M.; Geudtner, G.; Alvarez Ibarra, A.; Calaminici, P.; Casida, M. E.; Carmona-Espindola, J.; Dominguez, V. D.; Flores-Moreno, R.; Gamboa, G. U.; Goursoot, A.; Heine, T.; Ipatov, A.; de la Lande, A.; Janetzko, F.; del Campo, J. M.; Mejia-Rodriguez, D.; Reveles, J. U.; Vasquez-Perez, J.; Vela, A.; Zuniga-Gutierrez, B.;

- Salahub, D. deMon2k, Version 6, The deMon developers, Cinvestav, Mexico City, 2018.
- [315] Zhao, Y.; Truhlar, D. G. The M06 Suite of Density Functionals for Main Group Thermochemistry, Thermochemical Kinetics, Noncovalent Interactions, Excited States, and Transition Elements: Two New Functionals and Systematic Testing of Four M06-class Functionals and 12 Other Functionals. *Theor. Chem. Account.* **2008**, *120*, 215–241.
- [316] Barca, G. M. J.; Bertoni, C.; Carrington, L.; Datta, D.; De Silva, N.; Deustua, J. E.; Fedorov, D. G.; Gour, J. R.; Gunina, A. O.; Guidez, E.; Harville, T.; Irle, S.; Ivanic, J.; Kowalski, K.; Leang, S. S.; Li, H.; Li, W.; Lutz, J. J.; Magoulas, I.; Mato, J.; Mironov, V.; Nakata, H.; Pham, B. Q.; Piecuch, P.; Poole, D.; Pruitt, S. R.; Rendell, A. P.; Roskop, L. B.; Ruedenberg, K.; Sattasathuchana, T.; Schmidt, M. W.; Shen, J.; Slipchenko, L.; Sosonkina, M.; Sundriyal, V.; Tiwari, A.; Galvez Vallejo, J. L.; Westheimer, B.; Włoch, M.; Xu, P.; Zahariev, F.; Gordon, M. S. Recent Developments in the General Atomic and Molecular Electronic Structure System. *J. Chem. Phys.* **2020**, *152*, 154102.
- [317] Thürmer, S.; Ončák, M.; Ottosson, N.; Seidel, R.; Hergenbahn, U.; Bradforth, S. E.; Slavíček, P.; Winter, B. On the Nature and Origin of Dicationic, Charge-Separated Species Formed in Liquid Water on X-ray Irradiation. *Nat. Chem.* **2013**, *5*, 590–596.
- [318] Schnorr, K.; Belina, M.; Augustin, S.; Lindenblatt, H.; Liu, Y.; Meister, S.; Pfeifer, T.; Schmid, G.; Treusch, R.; Trost, F.; Slavíček, P.; Moshhammer, R. Direct tracking of ultrafast proton transfer in water dimers. *Sci. Adv.* **2023**, *9*, eadg7864.
- [319] Svoboda, O.; Hollas, D.; Ončák, M.; Slavíček, P. Reaction Selectivity in an Ionized Water Dimer: Nonadiabatic Ab Initio Dynamics Simulations. *Phys. Chem. Chem. Phys.* **2013**, *15*, 11531–11542.

-
- [320] Kamarchik, E.; Kostko, O.; Bowman, J. M.; Ahmed, M.; Krylov, A. I. Spectroscopic Signatures of Proton Transfer Dynamics in the Water Dimer Cation. *J. Chem. Phys.* **2010**, *132*, 194311.
- [321] Pieniazek, P. A.; VandeVondele, J.; Jungwirth, P.; Krylov, A. I.; Bradforth, S. E. Electronic Structure of the Water Dimer Cation. *J. Phys. Chem. A* **2008**, *112*, 6159–6170.
- [322] Müller, I. B.; Cederbaum, L. S. Ionization and double ionization of small water clusters. *J. Chem. Phys.* **2006**, *125*, 204305.
- [323] Moitra, T.; Paul, A. C.; Decleva, P.; Koch, H.; Coriani, S. Multi-electron excitation contributions towards primary and satellite states in the photoelectron spectrum. *Phys. Chem. Chem. Phys.* **2022**, *24*, 8329–8343.

ABSTRACT

Name of the Student: Ravi Kumar

Registration No.: 10CC18A26018

Faculty of Study: Chemical Science

Year of Submission: 2023

AcSIR academic centre/CSIR Lab: CSIR

Name of the Supervisor: Dr. Nayana Vaval

-National Chemical Laboratory, Pune

Title of the thesis: Study of non-radiative decay processes in weakly bound systems using post Hartree-Fock methods.

When a molecule absorbs a photon, it enters an excited state. It means its electrons have more energy than they do in its ground state. The molecule can relax to a lower energy state by emitting a photon and other non-radiative processes. The non-radiative decay processes (NRDP) are essential for many reasons. They can help us understand optoelectronic devices' efficiency, materials' photostability, energy transfer processes, chemical and biological systems, and fundamental scientific knowledge. NRD processes involve energy transfer to the surrounding molecules or solvent molecules; therefore, it also helps us to understand more about the surrounding environment of a molecule. X-ray-induced NRD processes are particularly challenging to study because they occur very quickly, on the order of femtoseconds. During these processes, Temporary Bound States (TBS) form. TBSs are short-lived states requiring simultaneous treatment of electron correlation and continuum effect from free electrons. On top of that, we have to make the wavefunction of TBS square integrable. That is why we have used Complex absorbing potential (CAP) with equation of motion Coupled-cluster methods. This method tackles the problem perfectly. However, the problem is that this method is computationally expensive, making it hard to apply to intermediate or large-size molecules. That's why we have also used the Fano-ADC(2)X method for larger molecules.

The other importance of NRDP in chemical and biological systems is that they generate free electrons that can cause DNA damage and create reactive oxygen species or free radicals within the human body. This poses significant health risks. Free electrons can also act as catalysts in biomolecules. It means NRDP also helps us to understand the product formed after the radiolysis of the molecules. All this product prediction depends upon the type of NRDP and TBS's type that will develop. Beyond catalysis, TBSs play a pivotal role in exploring diverse domains. They facilitate the investigation of plasma, multi-photon processes, and even interstellar chemistries. Therefore, it is crucial to understand the factors that affect NRD processes. In this thesis, I have studied various factors affecting NRD processes, including bond length, different molecular surroundings, polarization, the PCM model, the increase in surrounding molecules, protonation and deprotonation, metal ion's charge, and its solvation shell effect or in other word position of solvent molecules in the solvation shell. Lastly, we have also studied the impact of live proton dynamics of $2a^{-1}$ (or $O-2s^{-1}$) ionized water in a water dimer on NRDP.

List of Publication(s) in SCI Journals Emanating from the Thesis Work

1. **Ravi Kumar**, Aryya Ghosh, and Nayana Vaval; “Decay Processes in Cationic Alkali Metals in Microsolvated Clusters: A Complex Absorbing Potential Based Equation-of-Motion Coupled Cluster Investigation” *J. Chem. Theory Comput.* **2022**, 18, 2, 807–816. <https://doi.org/10.1021/acs.jctc.1c01036>
2. **Ravi Kumar**, Aryya Ghosh, and Nayana Vaval; “Effect of Protonation and Deprotonation on Electron Transfer Mediated Decay and Interatomic Coulombic Decay.” *ChemPhysChem* **2023**, 24, e202200340. <https://doi.org/10.1002/cphc.202200340>
3. **Ravi Kumar**, Aryya Ghosh, Nayana Vaval; “Effect of charge and solvation shell on non-radiative decay processes in s-block cationic metal ion water clusters.” *J. Chem. Phys.* **2023**, 159 (5), 054304. <https://doi.org/10.1063/5.0153598>
4. **Ravi Kumar**, Aryya Ghosh, Nayana Vaval; “Intermolecular Coulombic Decay in Water Dimer: A Coupling of Electronic and Nuclear Motion” (communicated)
5. **Ravi Kumar**, Aryya Ghosh, Nayana Vaval; “Effect of pKa value on Non radiative decay processes using Alanine amino acid” (manuscript in preparation)
6. **Ravi Kumar**, Aryya Ghosh, Nayana Vaval; “Role of water in Auger decay of Pyrrole-(H₂O)_{n=0-3}.” (manuscript in preparation)

List of Publications Non-Emanating from the Thesis Work

1. Gargi Kundu, Soumya Ranjan Dash, **Ravi Kumar**, Kumar Vanka, Aryya Ghosh, and Sakya S. Sen; “Enhancing Diradical Character of Chichibabin's Hydrocarbon through Fluoride Substitution.” *ChemPlusChem*, **2023**, 88, e202300273. <https://doi.org/10.1002/cplu.202300273>.
2. George Devasia, **Ravi Kumar**, Nayana Vaval, Sailaja Krishnamurty. Insights into adsorption of various gases on extra-framework cations of zeolite: A dispersion corrected DFT study on zeolite cluster models with Li⁺, Na⁺ and K⁺ charge compensating ions, *Microporous and Mesoporous Materials*, **2023**, 361, 112739. <https://doi.org/10.1016/j.micromeso.2023.112739>.
3. Pradnya M. Bodhankar, Dattatray S. Dhawale, Sarbjit Giddey, **Ravi Kumar** and Pradip B. Sarawade Well-defined hierarchical teddy bear sunflower-like NiCo₂O₄ electrocatalyst for superior water oxidation. *Sustainable Energy Fuels*, **2022**, 6, 5491. <https://doi.org/10.1039/D2SE01111E>
4. Asma H. Maneri, Chandrodai Pratap Singh, **Ravi Kumar**, Ashakiran Maibam, and Sailaja Krishnamurty; “Mapping the Finite-Temperature Behavior of Conformations to Their Potential Energy Barriers: Case Studies on Si₆B and Si₅B

Clusters.” *ACS Omega*, **2022**, *7*, *7*, 6167–6173.
<https://doi.org/10.1021/acsomega.1c06654>

5. Gargi Kundu, Debjit Pramanik, Soumya Ranjan Dash, **Ravi Kumar**, Srinu Tothadi, Aryya Ghosh*, Kumar Vanka*, and Sakya S. Sen*. A Kekulé Diradicaloid Featuring a Naphthalene Spacer, and A Distinct Cobalt Complex along with its Perfluoro Analogue. (Communicated to journal)
6. Ashwin D. Gedam, Manish M. Katiya, Kapil S. Ganorkar, Vijay J. Thakare, Prashant R. Mandlik, **Ravi Kumar**, Nayana Vaval, Prof. Madhukar Dhonde. Green Chromogenic Reagent & Green Sensor for Detection & Identification of Dichlorvos. (Communicated to journal)

List of papers with abstract presented (oral or poster) at national or international conferences/seminars.

1. Poster presentation in “**DAE Symposium on Current Trends in Theoretical Chemistry (CTTC-2020)**” Organised by Chemistry Division, Bhabha Atomic Research Centre (BARC) Mumbai, India held via online mode during 23-25 September, 2021.
2. Oral poster presentation in “**NCL Research Foundation-2021**” organised by CSIR-NCL Pune.
3. Poster presentation in “**Theoretical Chemistry Symposium, TCS - 2021**” organized by IISER Kolkata.

Achievements

1. Best oral presentation award in “**NCL Research Foundation-2021**” organised by CSIR-NCL Pune.
2. Best Poster presentation award in “**DAE Symposium on Current Trends in Theoretical Chemistry (CTTC-2020)**” Organised by Chemistry Division, BARC Mumbai, India held via online mode during 23-25 September, 2021.

Decay Processes in Cationic Alkali Metals in Microsolvated Clusters: A Complex Absorbing Potential Based Equation-of-Motion Coupled Cluster Investigation

Ravi Kumar, Aryya Ghosh, and Nayana Vaval*



Cite This: *J. Chem. Theory Comput.* 2022, 18, 807–816



Read Online

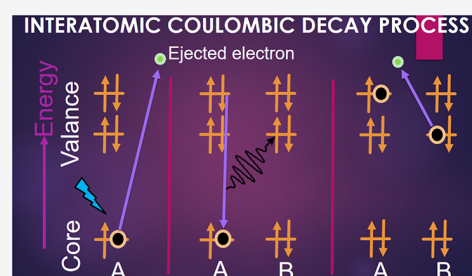
ACCESS |

Metrics & More

Article Recommendations

Supporting Information

ABSTRACT: We have employed the highly accurate complex absorbing potential based ionization potential equation-of-motion coupled cluster singles and doubles (CAP-IP-EOM-CCSD) method to study the various intermolecular decay processes in ionized metals (Li^+ , Na^+ , K^+) microsolvated by water molecules. For the Li atom, the electron is ionized from the 1s subshell. However, for Na and K atoms, the electron is ionized from 2s and both 2s and 2p subshells, respectively. We have investigated decay processes for the $\text{Li}^+(\text{H}_2\text{O})_n$ ($n = 1-3$) systems, as well as $\text{Na}^+(\text{H}_2\text{O})_n$ ($n = 1, 2$), and $\text{K}^+(\text{H}_2\text{O})_n$. The lithium cation in water can decay only via electron transfer mediated decay (ETMD) as there are no valence electrons in lithium. We have investigated how the various decay processes change in the presence of different alkali metal atoms and how the increasing number of water molecules play a significant role in the decay of microsolvated systems. To see the effect of the environment, we have studied Li^+-NH_3 in comparison to $\text{Li}^+-\text{H}_2\text{O}$. In the case of $\text{Na}^+-\text{H}_2\text{O}$, we have studied the impact of bond distance on the decay width. The effect of polarization on decay width was checked for the $\text{X}^+-\text{H}_2\text{O}$ ($\text{X} = \text{Li}, \text{Na}$) systems. We used the PCM model to study the polarization effect. We have compared our results with existing theoretical and experimental results wherever available in the literature.



INTRODUCTION

There are various ways in which an excited or ionized atom or molecule can relax. It can relax either via radiative processes or nonradiative decay processes. Radiative decay like fluorescence or a nonradiative process like Auger decay has been exceptionally well-known for a long time. Auger spectroscopy¹ has various applications in material and surface science. In 1997, Cederbaum et al.^{2,3} proposed a new decay mechanism for inner valence ionized or excited states, called interatomic or molecular Coulomb decay (ICD). This nonlocal complex relaxation process happens in atomic or molecular clusters. In the original formulation of this process, a single inner-valence hole state in an atom or molecule, which cannot decay locally via the Auger mechanism due to energetic considerations, decays through energy transfer to the neighboring atom. This knocks out an outer valence electron from the adjacent atom or molecule. Contrary to the Auger decay process, ICD is driven by the correlation between electrons located on different species, often a few nanometers apart. The ejected ICD electrons have low energy, the value of which strongly depends on the initial state and chemical nature of the neighbor. In the ICD process, two positive charges are produced in close proximity to each other, leading to a Coulomb explosion.

Electron transfer mediated decay (ETMD)⁴ is another interatomic decay process initiated by ionizing radiation. In this process, not energy but electron transfer between two

subunits acts as a mediator. In ETMD, a neighbor donates an electron to an initially ionized atom or molecule, while excess energy is transferred either to the donor or to another neighbor, which emits a secondary electron to the continuum. Li^+ has electrons only in its core orbital, so it is the best example to study the ETMD process. Being an electron transfer process, ETMD is usually considerably slower than energy transfer driven ICD process. However, it becomes a vital decay pathway in a medium if ICD is energetically forbidden. Since its original formulation, ICD has been investigated theoretically⁵⁻⁷ and experimentally⁸⁻¹¹ in a variety of systems such as rare-gas clusters,^{12,13} hydrogen bonded clusters,¹⁴ and water solutions.^{15,16} It has been found that not only inner-valence ionized states may undergo ICD, but any localized electronic excitation the energy of which lies above the ionization potential of a neighbor can undergo ICD. Thus, the ICD of ionized-excited, doubly ionized, or neutral-excited states of clusters have been observed and investigated theoretically. Moreover, it turns out that this decay process can be initiated not only by photons but also by energetic electrons

Received: October 16, 2021

Published: January 12, 2022



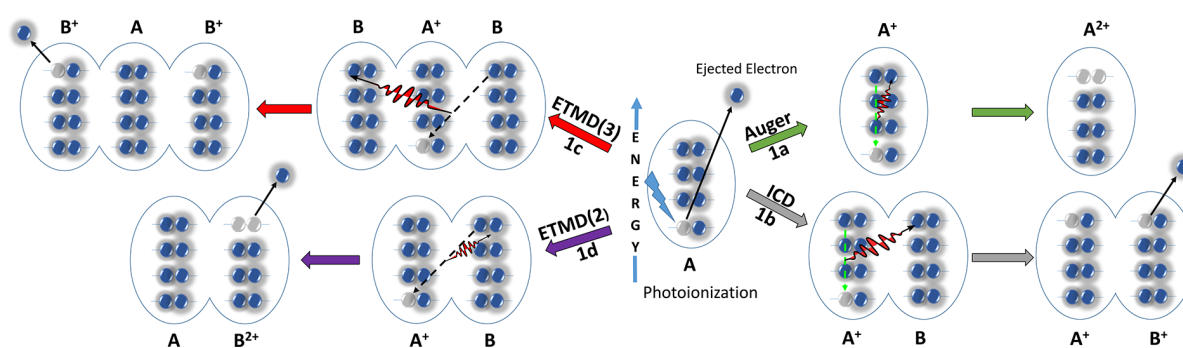


Figure 1. Various nonradiative decay processes: (a) Auger decay, (b) ICD, (c, d) ETMD processes (3 and 2 represent the number of atoms in each process).

and positive heavy ions. Experimentally, the ETMD process has been observed in rare gas clusters^{17–20} and alkali doped helium droplets.^{21–24} Recently, Unger et al.²⁵ have investigated the ETMD process in LiCl aqueous solution. The ETMD process has been studied theoretically in hydrogen bonded clusters.^{26,27} Recently, Ghosh et al.²⁸ have investigated the ETMD process in the HeLi₂ cluster. Their investigation, has shown that multimode nuclear dynamics play a significant role in the ETMD process. The ETMD process has also been investigated theoretically in microsolvated clusters.²⁹

The high efficiency of interatomic decay processes (i.e., ICD, ETMD) makes it imperative to take these interatomic decay processes into account for proper understanding of physicochemical phenomena induced in biological systems by ionizing radiation and related to radiation damage. First, ICD and ETMD result in the production of low energy electrons (LEEs) through ionization of the medium. LEEs are known to be very effective in causing DNA strand breaks through the resonant dissociative attachment mechanism.³⁰ Second, the ionization of the medium produces genotoxic radicals such as the hydroxyl radical, •OH. Third, both LEEs and radicals are produced locally close to where an ionizing particle initially deposits energy. If this happens close to the DNA molecule, the probability of the complex being damaged significantly increases. The feasibility of ICD and ETMD among biologically relevant species was investigated theoretically.^{31,32} Microsolvated clusters with alkali metal cations serve as a model system for a natural biological system because ions can impact intracellular and extracellular activities, that is, the movement of enzymes³³ and activities and conformers of proteins.³⁴ Na⁺ and K⁺ ions are the key components of the sodium–potassium pump in the human body. These ions also help to transmit signals inside the brain.³⁵ The proper functioning of Na⁺ and K⁺ ions helps us to avoid neurological diseases.³⁶ Therefore, the investigation of interatomic or intermolecular decay processes in microsolvated clusters will shed light on chemistry related to radiation damage. The decay rate of the interatomic decay process specifically depends on the energy of the initially ionized or excited state. Therefore, the proper treatment of the initially ionized or excited state is necessary to calculate the lifetime of the interatomic decay process. The ionization potential equation-of-motion coupled cluster method augmented by complex absorbing potential (CAP-IP-EOM-CC)^{37–43} provides proper treatment of ionized states or excited states with the inclusion of correlation effects (dynamic and nondynamic), as well as continuum ones. Therefore, the CAP-IP-EOM-CCSD (SD = singles, doubles

amplitude) method is promising to describe the interatomic decay process efficiently.

In this article, we have reported the implementation of the highly correlated CAP-IP-EOM-CCSD method, which is a combination of the CAP approach and the equation-of-motion coupled cluster^{44–50} approach, to study the ETMD decay mechanism in microsolvated Li⁺–(H₂O)_n (*n* = 1,3) systems, ICD in Na⁺–(H₂O)_n (*n* = 1, 2), and Auger decay in K⁺–(H₂O) (Figure 1). To see the effect of the environment on the decay of the Li 1s state, we have chosen two isoelectronic systems, Li⁺–NH₃ and Li⁺–H₂O. We compare our results with the available theoretical and experimental results. This article is organized as follows; in the Theory section, we briefly discuss the equation-of-motion coupled cluster theory along with the CAP approach. Results and discussion of them are presented in the next section. In the final section, we conclude our findings.

THEORY

To calculate the position and lifetime of the decaying state, we have used the CAP-IP-EOM-CCSD method. In this section, we discuss the CAP-IP-EOM-CCSD method briefly. The decaying states are associated with the complex eigenvalues within the formulation of Siegert.⁵¹

$$E_{\text{res}} = E_{\text{R}} - i\frac{\Gamma}{2} \quad (1)$$

where E_{R} represents the resonance position and Γ is the decay width. The relation between decay width and lifetime, τ , is given by

$$\tau = \frac{\hbar}{\Gamma} \quad (2)$$

The metastable states are not square-integrable. They can also be seen as discrete states embedded into the continuum. Hence to describe the metastable states, we require a method that can simultaneously treat electron correlation and the continuum. CAP and complex scaling^{52–54} are two well-known methods used for the calculation of resonance energies. Complex absorbing potential (CAP),^{54–59} along with quantum chemical methods, is one of the simplest and is the favored approach. CAP has been implemented in many of the quantum chemical methods for the calculation of resonance states.^{6,7,37–43,60,61} CAP along with EOM-CCSD has been used very successfully for the study of ICD and the shape resonance phenomena.

In the CAP approach, a one-particle potential, $i\eta W$, is added to the physical Hamiltonian, making the original Hamiltonian

complex symmetric and nonhermitian (i.e., $\mathbf{H}(\eta) = \mathbf{H} - i\eta W$). As a result, we obtain complex eigenvalues from the CAP augmented Hamiltonian ($\mathbf{H}(\eta)$). The real part denotes the resonance position, and the imaginary part gives half of the decay width. In $\mathbf{H}(\eta) = \mathbf{H} - i\eta W$, η represents the CAP strength, and W is a local positive-semidefinite one-particle operator. With the appropriate choice of CAP, the eigenfunctions of the complex symmetric Hamiltonian become square-integrable, and eigenvalues are discrete. $\mathbf{H}(\eta)$ is solved for various values of η . The resonance energy is obtained by diagonalizing the complex Hamiltonian matrix $\mathbf{H}(\eta)$ for multiple values of η . The η trajectory is obtained by plotting the real part vs imaginary part of energy. The local minimum of trajectory is associated with the position and half decay width of the decaying state.

$$\nu_i(\eta) = \eta \frac{\delta E_i}{\delta \eta} \quad (3)$$

The value of η for which $\nu_i(\eta)$ is minimum gives the optimal CAP strength. We have used a box shape CAP. CAP is applied in the peripheral region so that the target remains unperturbed yet scattered electrons are absorbed.

In the equation of motion coupled cluster approach, the target state is generated by the action of a configuration interaction (CI)-like linear operator onto the initial reference state (closed shell coupled cluster reference state). The wave function for the k^{th} ionized state, $|\Psi_k\rangle$, is expressed as

$$|\Psi_k\rangle = R(k)|\Phi_{\text{cc}}\rangle \quad (4)$$

where $R(k)$ is an ionization operator. The form of the linear operator for the electron ionized state can be written as

$$R(k) = \sum_i r_i(k)i + (1/2) \sum_{ija} r_{ij}^a(k)a^\dagger ji \quad (5)$$

The reference CC wave function, $|\Phi_{\text{cc}}\rangle$, can be written as

$$|\Phi_{\text{cc}}\rangle = e^T|\Phi_0\rangle \quad (6)$$

where $|\Phi_0\rangle$ is the N -electron closed shell reference determinant (restricted Hartree–Fock determinant (RHF)) and T is the cluster operator. In the coupled cluster singles and doubles (CCSD) approximation, the T operator can be defined as follows:

$$T = \sum_{ia} t_i^a a_a^\dagger a_i + 1/4 \sum_{ab} \sum_{ij} t_{ij}^{ab} a_a^\dagger a_b^\dagger a_i a_j \quad (7)$$

The indices a and b represent the virtual spin orbitals and the indices i and j represent the occupied spin orbitals. In the IP-EOM-CCSD framework, the final ionized states are obtained by diagonalizing the coupled cluster similarity transformed Hamiltonian within an $(N - 1)$ electron space.

$$\bar{H}_N R(k)|\Phi_0\rangle = \omega_k R(k)|\Phi_0\rangle \quad (8)$$

where

$$\bar{H}_N = e^{-T} H_N e^T - E_{\text{cc}} \quad (9)$$

\bar{H}_N is the similarity transformed Hamiltonian and ω_k is the energy change connected with the ionization process. In the IP-EOM-CCSD approach, the matrix is generated in the 1 hole and 2 hole–1 particle (2h–1p) subspace. Diagonalization of the matrix gives us ionization potential (IP) values.

In principle, CAP can be implemented at the self-consistent field (SCF)/Hartree–Fock, coupled cluster (CC) or EOM-CC level. Adding CAP at the coupled cluster level makes the cluster amplitudes complex, and hence all the further calculations are complex. The N electron ground state should be unperturbed. Adding CAP at the CC or SCF level perturbs the N electron ground state itself. Then to get the correct decay width, we need to correct the N electron ground state by removing the perturbation.

$$|\Phi_{\text{cc}}(\eta)\rangle = e^{T(\eta)}|\Phi_0\rangle \quad (10)$$

$$\bar{H}_N(\eta) = e^{T(\eta)} H_N(\eta) e^{T(\eta)} - \langle \Phi_0 | e^{T(\eta)} H_N(\eta) e^{T(\eta)} | \Phi_0 \rangle \quad (11)$$

The resonance energy is obtained as

$$E_{\text{res}}(\eta) = \omega_k(\eta) - E_{\text{cc}}(\eta) - E_{\text{cc}}(\eta = 0) \quad (12)$$

Thus, we lose the advantage of computing resonance energy as the direct energy difference is obtained as eigenvalues of $\bar{H}_N(\eta)$ using the IP-EOM-CCSD approach. Our previous study of resonance⁶² shows that the results are not affected when we implement CAP at the IP-EOM-CCSD level. In our calculation for the decay width, we have added the CAP potential in the particle–particle block of the one-particle \bar{H}_N matrix, leaving our N electron ground state unaffected. Therefore, the $\bar{H}_N(\eta)$ can be written as

$$\bar{H}_N(\eta) = e^{T(\eta=0)} H_N(\eta) e^{T(\eta=0)} - \langle \Phi_0 | e^{T(\eta=0)} H_N(\eta = 0) e^{T(\eta=0)} | \Phi_0 \rangle \quad (13)$$

To generate the η trajectory for locating the stationary point, we need to run the CAP-IP-EOM-CCSD calculations thousands of times. We start with $\eta = 0$ and then proceed with small incremental η values. Since IP-EOM-CCSD scales as N^6 , it makes our calculations computationally intensive. Convergence of the equations for various η values may be difficult because we are interested in the inner valence state and the presence of metal ion may add to the problem. Hence we have used the full diagonalization of the matrix using BLAS routines. The dimension of the matrix usually is $NH + NH \times NH \times NP$ in a given basis for a system where NH and NP represent the number of occupied and unoccupied orbitals.

RESULTS AND DISCUSSION

This work has studied the decay mechanism of microsolvated clusters of small cations (Li^+ , Na^+ , K^+) with water. The bond distance, different environments, and number of neighbors play important roles in the decay process. So, we have studied the behavior of the decay width in microsolvated clusters as a function of the following parameters: (a) Effect of different molecular environments on decay width for ETMD. We have studied the decay of the lithium 1s state in Li^+ –water and Li^+ –ammonia. Ammonia resembles the amino group found in biomolecules, and it is isoelectronic with water also. This is the main reason to choose these systems to study the effect of different environments on the ETMD process. (b) Impact of an increasing number of surrounding molecules on the decay width for ETMD. We have studied the decay of the Li^+ 1s state in Li^+ – $(\text{H}_2\text{O})_n$ ($n = 1$ –3). (c) Effect of bond distance on the decay width for ICD. We have studied the decay of the 2s state of Na^+ in Na^+ – H_2O at various bond lengths. The distance between sodium and oxygen is varied. (d) Effect of polarization on the decay width. We have studied Li^+ –water

and Na⁺–water systems in the gaseous and liquid phases. We have used the PCM model⁶³ to study the liquid phase.

We have studied ICD of the sodium 2s state in Na⁺–(H₂O)_n (*n* = 1, 2) and Auger decay of potassium 2s and 2p states in K⁺–(H₂O). The details of the geometries used in this work are available in the Supporting Information along with the basis set and method used for the geometry optimization. Geometries were optimized using the Gaussian09⁶⁴ software package. For the rest of the calculations, the codes used are homemade.

Choice of Basis Set for ETMD Process of 1s State of Li⁺ in Li⁺–H₂O. We have studied Li⁺–water in four different basis sets: Basis A is an aug-cc-pVDZ basis set.⁶⁵ Basis B is constructed by adding an extra Rydberg type f function on the oxygen atom of the water molecule in basis A. In the Li⁺–water system, after ionizing the electron from the 1s orbital of lithium, an electron will be transferred from oxygen to fill the 1s vacancy created on lithium. The excess energy will be used to knock out a secondary electron from oxygen. Thus, it is important to have a Rydberg type function on oxygen to get the continuum effect. The exponent of the f function is constructed according to the method of Kaufmann et al.⁶⁶ Basis C is an aug-cc-pVTZ basis set.⁶⁷ Basis D is constructed using the aug-cc-pVTZ basis set on lithium and oxygen atoms and the cc-pVTZ basis set for the hydrogen atom. In basis D, an extra Rydberg f function is added to the oxygen atom similar to basis B. The CAP box side lengths are chosen to be $C_x = C_y = \delta c$ and $C_z = \delta c + R/2$ au. The δc value is chosen to be 5.0 au for the aug-cc-pVDZ basis set and 6 au for the aug-cc-pVTZ basis set. Table 1 reports the resonance position and

Table 1. Effect of Variation of Basis Set on Decay Width of the Li 1s State in Li⁺–H₂O for ETMD Process

basis	energy (eV)	width (meV)	lifetime (fs)
aug-cc-pVDZ	72.36	11	60
aug-cc-pVDZ+F(O)	72.32	12	56
aug-cc-pVTZ	71.89	6.6	98
aug-cc-pVTZ+F(O)	72.16	7	96

decay width and lifetime for the lithium 1s state in all four basis sets. The triple- ζ (TZ) quality basis reduces the decay position by 0.5 eV. The addition of the Rydberg f function on oxygen has minimal effect on the decay position (i.e., ionization potential) and the decay width in double- ζ and triple- ζ basis sets. For the Li⁺–water dimer and –water trimer study, we have used basis A (i.e., aug-cc-pVDZ basis⁶⁵) since the method scales N^6 , making it computationally expensive with the higher basis set.

Effect of Different Molecular Environments on the ETMD Process. To see the impact of different molecular environments on the decay of the lithium 1s state, we have chosen Li⁺–NH₃ and Li⁺–H₂O as study systems. Since they are isoelectronic systems, they are relevant systems to study the effect of different molecular environments on the decay width of lithium 1s state for the ETMD process. We have used the aug-cc-pVTZ + Rydberg 1f function on oxygen and nitrogen. The δc value was chosen to be 6.0 au. We have presented our results in Table 2.

The ionization potential of the Li 1s state is 71.89 and 71.18 eV in Li⁺–H₂O and Li⁺–NH₃, respectively. The decay widths are 7 and 8 meV, respectively. The decay is faster in Li⁺–NH₃ (lifetime of 81 fs) than Li⁺–H₂O (lifetime of 96 fs). This means that the transfer of the electron to the 1s vacant position

Table 2. Effect of Different Molecular Surroundings on ETMD Process for Li 1s State in Li⁺–H₂O and Li⁺–NH₃ Using aug-cc-pVTZ+1f Basis Set

system	energy (eV)	width (meV)	lifetime (fs)
Li ⁺ –H ₂ O	71.89	7	96
Li ⁺ –NH ₃	71.18	8	81

of the Li atom is faster in the case of ammonia than water. This can be explained on the following basis. (a) Electronegativity: Oxygen is a more electronegative atom than nitrogen, making the electron transfer slower in case of water than ammonia. (b) Position of the lone pair electron: The lone pair electron in Li⁺–NH₃ is between Li⁺ and nitrogen. In Li⁺–H₂O, the lone pair is perpendicular to the Li⁺–H₂O molecular plane (not between Li⁺ and oxygen); see Figure 2. Because of the

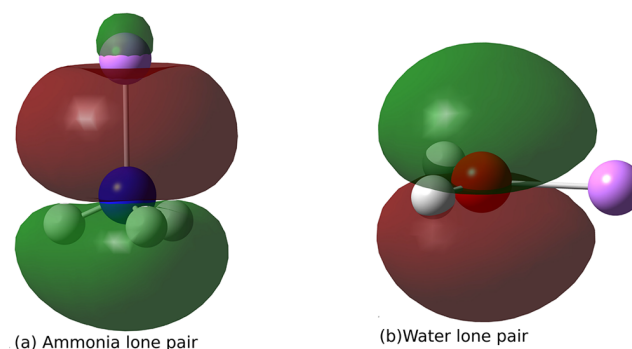


Figure 2. (a) Orientation of the lone pair in Li⁺–NH₃ toward Li atom, making electron transfer easier and hence producing a shorter lifetime. (b) Direction of the lone pair in Li⁺–H₂O perpendicular to the molecular plane, making electron transfer difficult and thus producing a longer lifetime. Image is generated for isosurface value 0.02 e Å⁻³. Atom color code: pink, lithium; blue, nitrogen; red, oxygen; white, hydrogen.

directional nature of the p-orbital and the lone pair's orientation toward lithium, electron transfer is much faster in case of ammonia than water. Orbitals of Figure 2 are generated with the Gaussian09⁶⁴ software package using density functional theory with B3LYP functional^{68–71} and aug-cc-pVTZ basis set.⁶⁷ The error of the IP-EOM-CCSD method is larger than 1 meV. However, the trend should remain the same. To confirm this, we have calculated the ionization potential (IP) for both systems using CCSD(T) method. The IP values are 71.81 and 71.18 eV for Li⁺–H₂O and Li⁺–NH₃, respectively with partial inclusion of triples. We hope that the qualitative trend for decay width will be similar; hence we conclude that the Li⁺–NH₃ decaying faster than the Li⁺–H₂O should remain the same.

Li⁺–Water Clusters: Effect of the Increasing Number of Water Molecules in Surrounding Environment on the ETMD Process. We have used the aug-cc-pVDZ basis set for the Li⁺–water dimer and –water trimer. The CAP box size used for the dimer is $C_x = 8$ au, $C_y = C_z = 5$ au, and $C_x = C_y = 10$ au, $C_z = 5$ au for the trimer. The Li⁺ ion is a good example to study the ETMD process since it has only core electrons. Therefore, ICD and Auger decay processes cannot take place in this system.

If the Li⁺–water cluster is ionized by removing an electron from the 1s subshell of the Li⁺ ion, then the molecule relaxes via the ETMD process. The ETMD process of Li²⁺(1s⁻¹2s⁻¹)

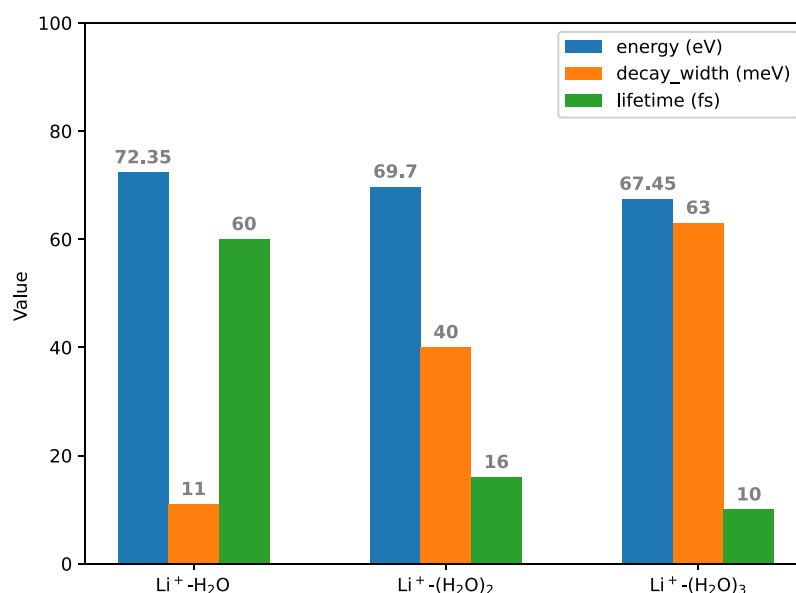


Figure 3. Effect of the increased number of surrounding water molecules on ETMD process using an aug-cc-pVDZ basis set.

state in Li⁺–water clusters can be described as follows. After removing an electron from the 1s orbital of Li⁺ ion in Li⁺–H₂O (i.e., formation of Li²⁺–H₂O), the 1s vacancy of Li²⁺(1s⁻¹2s⁻¹) ion is filled by a 2p outer valence electron of the oxygen atom of one of the water molecules. Then the released energy emits a secondary outer valence electron from the same water molecule or another water molecule. Therefore, the final state (Li⁺–H₂O²⁺ or H₂O⁺–Li⁺–H₂O⁺) of the ETMD process is a double-ionized state (with respect to our initial system, Li⁺–H₂O). The Li⁺–H₂O²⁺ final state is produced via an ETMD(2) process, where both the positive charges are present on one water molecule. The H₂O⁺–Li⁺–H₂O⁺ double-ionized final state (with respect to our initial system, Li⁺–H₂O) is produced via ETMD(3). The ETMD channel is open for the 1s ionized state of Li⁺ ion because the energy of the Li²⁺(1s⁻¹2s⁻¹) state lies above that of the double-ionized final states (i.e., Li⁺–H₂O²⁺ or H₂O⁺–Li⁺–H₂O⁺). Thus, the positively charged water molecules will repel the positively charged lithium ion leading to a Coulomb explosion. Different variants of ETMD (i.e., ETMD(2) or ETMD(3)) may be possible with an increasing number of water molecules surrounding the Li⁺ ion. The 1s ionization energy of the Li⁺ ion in the Li⁺–water cluster varies from 72.35 to 67.45 eV depending on the number of water molecules present in the surroundings of the Li⁺ ion. Here, we have calculated the lifetime of 1s ionized state of Li⁺ ion in various Li⁺–water clusters.

In Figure 3, we have plotted the decay values for the Li⁺–(H₂O)_n (n = 1–3) system. In this case, we have used the aug-cc-pVDZ basis set for the study. As we move from the monomer to the trimer, the decay position reduces from 72.35 to 67.45 eV. On the other hand, the decay width increases from 11 to 63 meV. There are two factors that can affect the decay width: first the bond distance between the Li⁺ and H₂O molecules and second the number of surrounding water molecules. The bond length does not seem to have much effect as we move from the monomer (1.867 Å) to the dimer (1.86 Å). Therefore, the number of decay channels play a significant role in increasing the decay width as we move from monomer to dimer. From Figure 3, we have noticed that the decay width

increases nonlinearly. The possible reason for the nonlinear growth of the decay width is that the number of decay channels increases nonlinearly with an increasing number of water molecules surrounding the Li⁺ ion. Cederbaum and Müller²⁶ have studied Li⁺–H₂O with up to five water molecules using a perturbation theory ansatz with SCF integrals. They estimated lifetimes in the range of 100–20 fs. Our results give decay time in the range from 60 to 10 fs from monomer to trimer in the aug-cc-pVDZ basis.⁶⁵ In the aug-cc-pVTZ basis set,⁶⁷ we obtained a lifetime of 98 fs, which is in good agreement with the results from Cederbaum and Müller. See ref 72 for details of the IP and DIP spectra of the Li⁺–(H₂O)_n complex.

Na⁺–Water Cluster: Effect of Distance and Increasing Number of Water Molecules on the ICD Process. The 2s ionized state of the Na atom in the Na⁺–H₂O system can relax via the ICD process. The ICD process of the 2s ionized state of the Na atom in the Na⁺–H₂O system can be described as follows: after removal of an electron from the 2s subshell of the Na atom, the 2s vacancy of the Na atom in the Na²⁺–H₂O is filled by a 2p outer valence electron of the Na atom. Then the released energy is transferred to the neighboring H₂O molecule, which emits a secondary electron. Therefore, the final state of the ICD process is characterized by the Na²⁺(2p⁻¹3s⁻¹) O⁺H₂(2p⁻¹) triple ionized state. Energetically, the ICD process is possible in the Na⁺–H₂O system because the energy of the 2s ionized state of the Na atom lies above the energy of the Na²⁺(2p⁻¹3s⁻¹) O⁺H₂(2p⁻¹) final state.

The decay of the sodium 2s state in the Na⁺–H₂O system is studied in a modified maug-cc-pV(T+d)Z⁷³ basis set (taken from the basis set exchange library,⁷⁴ then modified) augmented by 3s3p1d functions for oxygen and 1s1p for sodium and cc-pVDZ⁶⁵ for hydrogen. The detailed basis set used for the system is described in Supporting Information. To see the effect of bond length on the decay width, we have studied the Na⁺–water system for various bond lengths, 2.249 88–5.0 Å between the sodium and the oxygen atom. The geometry was optimized using the CCSD method in the aug-cc-pVDZ basis,⁶⁵ and the bond distance between sodium and oxygen was found to be 2.249 88 Å. Thus, we have used

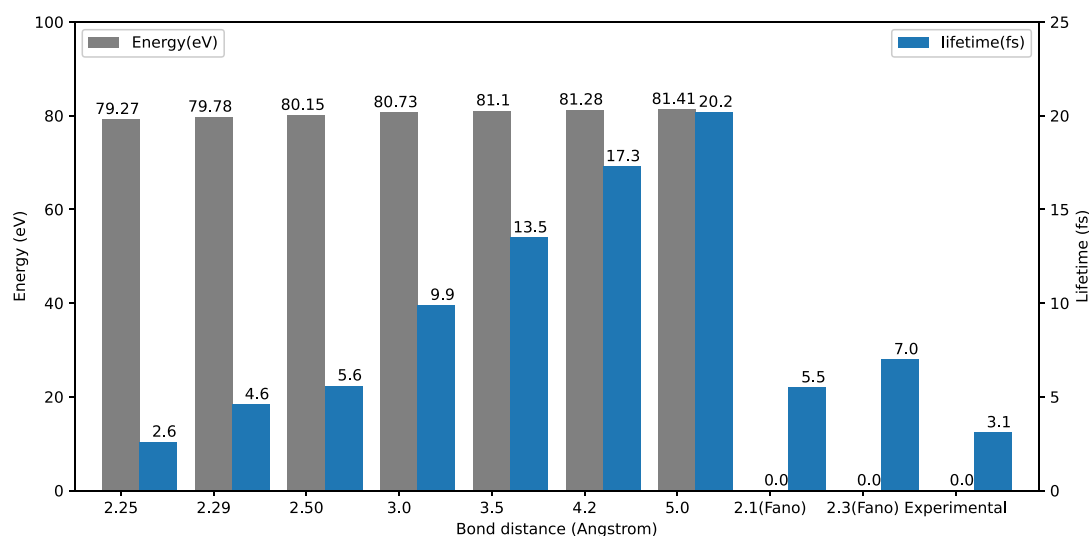


Figure 4. Effect of bond length on ICD process for the 2s state of Na in $\text{Na}^+-\text{H}_2\text{O}$ using maug-cc-pV(T+d)Z basis set.

this bond distance. The CAP box size used in our calculation is $C_x = 8.7$, $C_y = 6.5$, and $C_z = 5.0$ au. Figure 4 summarizes the results for various bond lengths. We know from eq 2 that the decay width and lifetime of a temporary bound state (TBS) are inversely proportional to each other. We observe that the lifetime increases rapidly as bond length increases or the decay width rapidly decreases with an increase in the bond length. A sharp change in decay width from 251 meV (2.6 fs) at 2.249 88 Å to 142 meV (4.6 fs) at 2.29 Å is observed. Then it saturates at 33 meV (20 fs) at 5.0 Å. It may become bound with a further increase in the bond length. We also report the Fano-ADC²⁹ results at 2.30 Å. The basis set used in that calculation is cc-pCVTZ+2s2p2d1f KBJ⁶⁶ for sodium and oxygen and cc-pVTZ+1s1p1d KBJ⁶⁶ for hydrogen. The lifetime of 7 fs was reported using the Fano-ADC method. The experimental⁷⁵ value of the decay time of the Na 2s state is 3.1 fs. Our results predict the decay time to be 2.6 fs at the equilibrium bond length, which shows good agreement with the experimental value.

To see the effect of the increased number of surrounding molecules on the decay width in the ICD process, we also studied the Na^+-water dimer. The optimized geometry was obtained using the B3LYP functional^{68–71} and the 6-311++g(3d,2p) basis set⁷⁶ in the Gaussian09⁶⁴ software package. The CAP box size used for the Na^+-water system in our calculation is $C_x = 12$, $C_y = 7$, and $C_z = 7$ au. We have used a spherical basis set for the Na^+-water dimer due to scaling of the CC equations (i.e., in a Cartesian basis, the Na^+-water dimer is computationally very expensive). To compare $\text{Na}^+-\text{(H}_2\text{O)}_2$ with $\text{Na}^+-\text{H}_2\text{O}$, we again ran $\text{Na}^+-\text{H}_2\text{O}$ in a spherical basis set. The bond distance between sodium and oxygen is 2.2453 Å in $\text{Na}^+-\text{(H}_2\text{O)}_2$ and 2.249 88 Å in $\text{Na}^+-\text{H}_2\text{O}$. The decay width of the 2s state of sodium in $\text{Na}^+-\text{(H}_2\text{O)}_2$ is 305 meV (2.1 fs) compared to 129 meV (5.1 fs) in $\text{Na}^+-\text{H}_2\text{O}$.

Auger Decay Process for the 2s and 2p Ionized States of K in K^+-Water . The 2s and 2p ionized states of the K atom in the $\text{K}^+-\text{H}_2\text{O}$ can relax via the Auger process. In our calculations, we have used the optimized geometry for $\text{K}^+-\text{H}_2\text{O}$ obtained using the B3LYP functional^{68–71} and the 6-311++g(3d,2p) basis set⁷⁷ in the Gaussian09⁶⁴ software package. For the computation of the decay width, we have employed the aug-cc-pVDZ-X2C basis set⁷⁸ for potassium,

aug-cc-pVDZ⁶⁵ for oxygen, and the cc-pVDZ basis set⁶⁵ for hydrogen. The results for the 2s and 2p ionized states are presented in Table 3 along with $\text{Li}^+-\text{(H}_2\text{O)}_n$ and Na^+-

Table 3. Different Decay Processes in Different Systems: Auger Decay in $\text{K}^+-\text{H}_2\text{O}$, ICD in $\text{Na}^+-\text{(H}_2\text{O)}_n$, and ETMD in $\text{Li}^+-\text{(H}_2\text{O)}_n$ ($n = 1, 2$)

basis	system	energy (eV)	width in meV (fs)
maug-cc-pV(T+d)Z ^a	$\text{Li}^+-\text{H}_2\text{O}$	71.81	7.64 (86)
maug-cc-pV(T+d)Z ^a	$\text{Li}^+-\text{(H}_2\text{O)}_2$	69.03	16.12 (40.8)
maug-cc-pV(T+d)Z ^b	$\text{Na}^+-\text{H}_2\text{O}$	79.49	129(5.1)
maug-cc-pV(T+d)Z ^b	$\text{Na}^+-\text{(H}_2\text{O)}_2$	78.19	305(2.1)
aug-cc-pVDZ-X2C	$\text{K}^+-\text{H}_2\text{O}$ (2s)	396	423(1.5) 278(2.4) ^c
aug-cc-pVDZ-X2C	$\text{K}^+-\text{H}_2\text{O}$ (2p)	315	74.86 (8.8) 246(2.7) ^c

^aThe maug-cc-pV(T+d)Z + 3s3p1d on O atom in Cartesian basis.

^bThe maug-cc-pV(T+d)Z + 3s3p1d on O atom in spherical basis.

^cSecond decay value observed for the system.

$\text{(H}_2\text{O)}_n$ ($n = 1, 2$). Here, for the $\text{Li}^+-\text{(H}_2\text{O)}_n$ ($n = 1, 2$), we have used the maug-cc-pV(T+d)Z⁷³ + 3s3p1d basis set on oxygen, while for Li, we have used maug-cc-pV(T+d)Z basis set⁷³ to maintain consistency. The CAP box size used for K^+-water system in our calculation is $C_x = 7$, $C_y = 4$, and $C_z = 4$ au. In the case of the $\text{K}^+-\text{H}_2\text{O}$ system, we observed two stationary points on the η trajectory indicating decay through a cascade mechanism. Experimentally, a similar kind of two stationary points (cascade decay type effect) was observed.⁷⁹ The η trajectory shows only one stationary point for the other two systems ($\text{Li}^+-\text{H}_2\text{O}$, $\text{Na}^+-\text{H}_2\text{O}$).

The Auger process of the 2s, 2p ionized state of the K atom in $\text{K}^+-\text{H}_2\text{O}$ ($4s^{-1}$) can be rationalized as follows: After removal of an electron from the 2s or 2p subshell of the K atom in $\text{K}^+-\text{H}_2\text{O}$ (formation of $\text{K}^{2+}-\text{H}_2\text{O}(2s^{-1}4s^{-1}$ or $2p^{-1}4s^{-1})$), the 2s or 2p vacancy is filled by a 3p or 3s outer valence electron of the K atom. Then the released energy is used to knock out another secondary outer valence electron from the 3p or 3s subshell of the K atom (formation of $\text{K}^{3+}-\text{H}_2\text{O}$). This two-hole state ($\text{K}^{3+}(3p^{-2}4s^{-1})-\text{H}_2\text{O}$ or $\text{K}^{3+}(3p^{-1}3s^{-1}4s^{-1})-\text{H}_2\text{O}$ or $\text{K}^{3+}(3s^{-2}4s^{-1})-\text{H}_2\text{O}$, which is with respect to our initial

system K^+-H_2O) is unstable and further relaxes via another decay process, which is a three-hole state. Energetically the Auger process will be viable if the energy of the 2s or 2p ionized state of the K atom lies above the triple ionized final states. The calculation of the three-hole state is beyond the scope of this work.

The Auger decay width for the 2p ionized state is 74.86 meV (i.e., 8.8 fs), and then the system undergoes further decay with a decay width of 246 meV corresponding to a lifetime of 2.7 fs. Similarly, the Auger decay width for the 2s ionized state is 423 meV with a lifetime of 1.5 fs, and then the system undergoes further decay with a decay width of 278 meV corresponding to a lifetime of 2.4 fs. Pokapanich et al.¹⁶ have studied the Auger decay in potassium chloride surrounded by water molecules.

Polarized Surrounding Effect on ETMD and ICD. We have studied the Li^+ -water and Na^+ -water in the gaseous and aqueous medium to see the effect of a polarized surrounding on the decay width in the ETMD and ICD processes, respectively. We have used the PCM model⁶³ for the aqueous phase, where water is the solvent. The bond distance and CAP box size were kept identical for the gaseous and aqueous phases. The results are presented in Table 4. For the Li^+ -water

Table 4. Polarization Effect on Decay Width in ETMD and ICD Processes for X^+-H_2O Systems ($X = Li, Na$)

basis	system	medium	energy (eV)	width in meV (fs)
aug-cc-pVDZ+F(O)	Li^+-H_2O	gas	72.36	12 (56)
aug-cc-pVDZ+F(O)	Li^+-H_2O	PCM	72.3	9.7 (67)
m-aug-cc-PV(T+d)Z	Na^+-H_2O	gas	79.78	143 (4.6)
m-aug-cc-PV(T+d)Z	Na^+-H_2O	PCM	79.73	108 (6.0)

1s state, the decay position remains almost identical; however, the decay width changes from 12 meV (56 fs) for the gaseous medium to 9.7 meV (67 fs) for the aqueous medium. The decay is slower in the aqueous medium compared to the gaseous medium. A similar trend was observed for the Na^+ -water 2s state, and the decay width changes from 143 meV (4.6) for the gaseous medium to 108 meV (6 fs) for the aqueous medium. The slow decay in the aqueous medium is due to the polarization provided by the medium, which makes the ionized state more stable than the gaseous medium.

CONCLUSIONS

This work has used the CAP-IP-EOM-CCSD method to study the various decay processes in microsolvated alkali metal ions, that is, Li^+ , Na^+ , and K^+ . The CAP-IP-EOM-CCSD method is used for the first time to explore the ETMD lifetimes for the Li 1s state in Li^+-H_2O clusters. It is observed that the decay widths are sensitive to the bond length, surrounding atoms, medium (gas or liquid), and number of neighboring molecules. We have studied the effect of all these parameters on the decay width of Li^+-H_2O and Na^+-H_2O clusters.

We have studied the decay of 1s, 2s, and both 2s and 2p states in Li^+ , Na^+ , and K^+ , respectively, with water. The Li 1s state undergoes ETMD, whereas the Na 2s state decays via ICD. The K 2s and 2p states undergo Auger decay. To study the impact of different molecular environments, the 1s ionized state of the Li atom was studied in Li^+-NH_3 and Li^+-H_2O . Since water and ammonia are isoelectronic, it would be interesting to study the effect of the environment on the decay

width. We found that decay is faster in Li^+-NH_3 (81 fs) than in Li^+-H_2O (96 fs). The possible explanation for this could be first the higher electronegativity of oxygen than nitrogen, making electron transfer more difficult than with nitrogen, and second the location of the lone pair. In Li^+-NH_3 , it is between Li^+ and nitrogen, whereas in Li^+-H_2O , it is perpendicular to the molecular plane. Because of the directional nature of p-orbitals and the orientation of the lone pair toward lithium, electron transfer is much faster in the case of ammonia than water (See Figure 2 for details).

We have studied the ETMD lifetime for the 1s ionized state of the Li atom in the $Li^+-(H_2O)_n$ ($n = 1-3$) system to see the effect of the number of water molecules on the decay. The lifetime obtained for the $Li^+-(H_2O)_n$ system is 60 fs, 16 fs, and drops further to 10 fs as n increases from 1 to 3. As a characteristic feature of ETMD, the lifetime decreases strongly with an increasing number of neighbors. This is due to a nonlinear increase in the number of decay channels with an increasing number of surrounding atoms.

To see the effect of bond length on the decay width for the ICD process, we studied the 2s ionized state of Na atom in Na^+-H_2O at various bond lengths, 2.2489 Å to 5.0 Å. We observed that as the bond length increases, the decay width reduces and the lifetime increases from 2.6 fs at 2.24 Å to 20 fs at 5.0 Å. A similar trend was observed using the Fano ADC method.²⁹ The authors reported a lifetime of 5.5 fs at 2.21 Å and 7 fs at 2.30 Å. Our results for sodium 2s state are in good agreement with the experiment⁷⁵ and the Fano ADC²⁹ method. We have also investigated the ICD lifetime for the 2s ionized state of the Na atom in the $Na^+-(H_2O)_n$ ($n = 1, 2$) systems to study the effect of increased water molecules in the surroundings on ICD. The computed ICD lifetime for the Na^+-H_2O system is 5.1 fs, and it decreases strongly to 2.1 fs for the $Na^+-(H_2O)_2$ system. We have used a spherical Gaussian basis set here for monomer and dimer to have a proper comparison. Sensitivity of the decay width to the spherical or Cartesian basis is also observed. We have investigated the Auger lifetime for the 2s and 2p ionized state of the K atom in the K^+-H_2O system. The computed Auger lifetimes for the 2s and 2p ionized states are 1.5 and 8.8 fs, respectively. The η trajectory indicates a cascade decay for the K^+-H_2O system. The Auger decay initiates another decay after a short-lived state leading to a more stable state. Since the Auger decay is a localized decay, we do not expect much change with bond length or number of neighbors.

To determine the polarization effects on the ICD and ETMD processes, we studied the decay of the 1s state of the Li atom and the 2s state of Na in $Li^+-(H_2O)$ and $Na^+-(H_2O)$, respectively. We used the PCM model⁶³ in our study. In both cases, our results show that polarization stabilizes the system, that is, decay time is increased in the liquid phase compared to the gaseous phase. In this work, we studied the decay width of alkali metal ions as a function of different molecular environments, increase of surrounding molecules in a system, bond distance, basis set, and polarization of the medium.

ASSOCIATED CONTENT

Supporting Information

The Supporting Information is available free of charge at <https://pubs.acs.org/doi/10.1021/acs.jctc.1c01036>.

Data that support the findings of this study (PDF)

AUTHOR INFORMATION

Corresponding Author

Nayana Vaval – *Electronic Structure Theory Group, Physical Chemistry Division, CSIR-National Chemical Laboratory, Pune 411008, India*; orcid.org/0000-0002-5107-1875;
Email: np.vaval@ncl.res.in

Authors

Ravi Kumar – *Academy of Scientific and Innovative Research, CSIR-Human Resource Development Center (CSIR-HRDC) Campus, Ghaziabad, Uttar Pradesh 201002, India*;
Electronic Structure Theory Group, Physical Chemistry Division, CSIR-National Chemical Laboratory, Pune 411008, India

Aryya Ghosh – *Department of Chemistry, Ashoka University, Sonapat, Haryana 131029, India*

Complete contact information is available at:
<https://pubs.acs.org/10.1021/acs.jctc.1c01036>

Notes

The authors declare no competing financial interest.

ACKNOWLEDGMENTS

N.V. acknowledges financial support from Department of Science and Technology. R.K. acknowledges financial support from Council of Scientific and Industrial Research. Authors acknowledge the computational facility at the CSIR-National Chemical Laboratory. We dedicate this paper to Prof. Sourav Pal on his 65th birthday.

REFERENCES

- (1) Auger, P. Sur l' effet Photoélectrique Composé. *J. Phys. Radium* **1925**, *6*, 205–208.
- (2) Cederbaum, L. S.; Zobeley, J.; Tarantelli, F. Giant Intermolecular Decay and Fragmentation of Clusters. *Phys. Rev. Lett.* **1997**, *79*, 4778–4781.
- (3) Santra, R.; Cederbaum, L. S. Non-Hermitian Electronic Theory and Applications to Clusters. *Phys. Rep.* **2002**, *368*, 1–117.
- (4) Zobeley, J.; Santra, R.; Cederbaum, L. S. Electronic Decay in Weakly Bound Heteroclusters: Energy Transfer versus Electron Transfer. *J. Chem. Phys.* **2001**, *115*, 5076–5088.
- (5) Scheit, S.; Averbukh, V.; Meyer, H.; Moiseyev, N.; Santra, R.; Sommerfeld, T.; Zobeley, J.; Cederbaum, L. S. On the Interatomic Coulombic Decay in the Ne Dimer. *J. Chem. Phys.* **2004**, *121*, 8393–8398.
- (6) Vaval, N.; Cederbaum, L. S. Ab Initio Lifetimes in the Interatomic Coulombic Decay of Neon Clusters Computed with Propagators. *J. Chem. Phys.* **2007**, *126*, 164110.
- (7) Ehara, M.; Sommerfeld, T. CAP/SAC-CI Method for Calculating Resonance States of Metastable Anions. *Chem. Phys. Lett.* **2012**, *537*, 107–112.
- (8) Jahnke, T. Interatomic and Intermolecular Coulombic Decay: The Coming of Age Story. *J. Phys. B: At. Mol. Opt. Phys.* **2015**, *48*, 082001.
- (9) Marburger, S.; Kugeler, O.; Hergenbahn, U.; Möller, T. Experimental Evidence for Interatomic Coulombic Decay in Ne Clusters. *Phys. Rev. Lett.* **2003**, *90*, 203401.
- (10) Jahnke, T.; Czasch, A.; Schöffler, M. S.; Schössler, S.; Knapp, A.; Käsz, M.; Titze, J.; Wimmer, C.; Kreidi, K.; Grisenti, R. E.; Staudte, A.; Jagutzki, O.; Hergenbahn, U.; Schmidt-Böcking, H.; Dörner, R. Experimental Observation of Interatomic Coulombic Decay in Neon Dimers. *Phys. Rev. Lett.* **2004**, *93*, 163401.
- (11) Öhrwall, G.; Tchapyguine, M.; Lundwall, M.; Feifel, R.; Bergersen, H.; Rander, T.; Lindblad, A.; Schulz, J.; Peredkov, S.; Barth, S.; Marburger, S.; Hergenbahn, U.; Svensson, S.; Björneholm, O. Femtosecond Interatomic Coulombic Decay in Free Neon Clusters: Large Lifetime Differences between Surface and Bulk. *Phys. Rev. Lett.* **2004**, *93*, 173401.
- (12) Santra, R.; Zobeley, J.; Cederbaum, L. S.; Moiseyev, N. Interatomic Coulombic Decay in Van Der Waals Clusters and Impact of Nuclear Motion. *Phys. Rev. Lett.* **2000**, *85*, 4490–4493.
- (13) Sisourat, N.; Sann, H.; Kryzhevoi, N. V.; Kolorenč, P.; Havermeier, T.; Sturm, F.; Jahnke, T.; Kim, H. K.; Dörner, R.; Cederbaum, L. S. Interatomic Electronic Decay Driven by Nuclear Motion. *Phys. Rev. Lett.* **2010**, *105*, 173401.
- (14) Stoychev, S. D.; Kuleff, A. I.; Cederbaum, L. S. On the Intermolecular Coulombic Decay of Singly and Doubly Ionized States of Water Dimer. *J. Chem. Phys.* **2010**, *133*, 154307.
- (15) Thürmer, S.; Unger, I.; Slavíček, P.; Winter, B. Relaxation of Electronically Excited Hydrogen Peroxide in Liquid Water: Insights from Auger-Electron Emission. *J. Phys. Chem. C* **2013**, *117*, 22268–22275.
- (16) Pokapanich, W.; Kryzhevoi, N. V.; Ottosson, N.; Svensson, S.; Cederbaum, L. S.; Öhrwall, G.; Björneholm, O. Ionic-Charge Dependence of the Intermolecular Coulombic Decay Time-Scale for Aqueous Ions Probed by the Core-Hole Clock. *J. Am. Chem. Soc.* **2011**, *133*, 13430–13436.
- (17) Fasshauer, E.; Förstel, M.; Mucke, M.; Arion, T.; Hergenbahn, U. Theoretical and Experimental Investigation of Electron Transfer Mediated Decay in ArKr Clusters. *Chem. Phys.* **2017**, *482*, 226–238.
- (18) Förstel, M.; Mucke, M.; Arion, T.; Bradshaw, A. M.; Hergenbahn, U. Autoionization Mediated by Electron Transfer. *Phys. Rev. Lett.* **2011**, *106*, 033402.
- (19) Yan, S.; Zhang, P.; Ma, X.; Xu, S.; Li, B.; Zhu, X. L.; Feng, W. T.; Zhang, S. F.; Zhao, D. M.; Zhang, R.; Guo, D.; Liu, H. P. Observation of Interatomic Coulombic Decay and Electron Transfer Mediated Decay in High Energy Electron Impact Ionization of Ar₂. *Phys. Rev. A* **2013**, *88*, 042712.
- (20) Sakai, K.; Stoychev, S.; Ouchi, T.; Higuchi, I.; Schöffler, M.; Mazza, T.; Fukuzawa, H.; Nagaya, K.; Yao, M.; Tamenori, Y.; Kuleff, A. I.; Saito, N.; Ueda, K. Electron Transfer Mediated Decay and Interatomic Coulombic Decay from the Triply Ionized States in Argon Dimers. *Phys. Rev. Lett.* **2011**, *106*, 033401.
- (21) LaForge, A. C.; Stumpf, V.; Gokhberg, K.; von Vangerow, J.; Stienkemeier, F.; Kryzhevoi, N. V.; O'Keeffe, P.; Ciavardini, A.; Krishnan, S. R.; Coreno, M.; Prince, K. C.; Richter, R.; Moshhammer, R.; Pfeifer, T.; Cederbaum, L. S.; Mudrich, M. Enhanced Ionization of Embedded Clusters by Electron-Transfer-Mediated Decay in Helium Nanodroplets. *Phys. Rev. Lett.* **2016**, *116*, 203001.
- (22) Ghosh, A.; Cederbaum, L. S.; Gokhberg, K. Electron Transfer Mediated Decay in HeLi₂ Cluster: Potential Energy Surfaces and Decay Widths. *J. Chem. Phys.* **2019**, *150*, 164309.
- (23) Kryzhevoi, N. V.; Averbukh, V.; Cederbaum, L. S. High Activity of Helium Droplets Following Ionization of Systems Inside Those Droplets. *Phys. Rev. B* **2007**, *76*, 094513.
- (24) Ben Ltaief, L.; Shcherbinin, M.; Mandal, S.; Krishnan, S. R.; Richter, R.; Pfeifer, T.; Bauer, M.; Ghosh, A.; Mudrich, M.; Gokhberg, K.; LaForge, A. C. Electron Transfer Mediated Decay of Alkali Dimers Attached to He Nanodroplets. *Phys. Chem. Chem. Phys.* **2020**, *22*, 8557–8564.
- (25) Unger, I.; Seidel, R.; Thürmer, S.; Pohl, M. N.; Aziz, E. F.; Cederbaum, L. S.; Muchová, E.; Slavíček, P.; Winter, B.; Kryzhevoi, N. V. Observation of Electron Transfer Mediated Decay in Aqueous Solution. *Nat. Chem.* **2017**, *9*, 708–714.
- (26) Müller, I. B.; Cederbaum, L. S. Electronic Decay Following Ionization of Aqueous Li⁺ Microsolvation Clusters. *J. Chem. Phys.* **2005**, *122*, 094305.
- (27) Stumpf, V.; Gokhberg, K.; Cederbaum, L. S. The Role of Metal Ions in X-ray Induced Photochemistry. *Nat. Chem.* **2016**, *8*, 237–241.
- (28) Ghosh, A.; Cederbaum, L. S.; Gokhberg, K. Signature of the Neighbor's Quantum Nuclear Dynamics in the Electron Transfer Mediated Decay Spectra. *Chem. Sci.* **2021**, *12*, 9379–9385.

- (29) Stumpf, V.; Brunken, C.; Gokhberg, K. Impact of Metal Ion's Charge on the Interatomic Coulombic Decay Widths in Microsolvated Clusters. *J. Chem. Phys.* **2016**, *145*, 104306.
- (30) Brun, E.; Cloutier, P.; Sicard-Roselli, C.; Fromm, M.; Sanche, L. Damage Induced to DNA by Low-Energy (0–30 eV) Electrons under Vacuum and Atmospheric Conditions. *J. Phys. Chem. B* **2009**, *113*, 10008–10013.
- (31) Alizadeh, E.; Orlando, T. M.; Sanche, L. Biomolecular Damage Induced by Ionizing Radiation: The Direct and Indirect Effects of Low-Energy Electrons on DNA. *Annu. Rev. Phys. Chem.* **2015**, *66*, 379–398.
- (32) Ren, X.; Wang, E.; Skitnevskaya, A. D.; Trofimov, A. B.; Gokhberg, K.; Dorn, A. Experimental Evidence for Ultrafast Interatomic Relaxation Processes in Hydrated Biomolecules. *Nat. Phys.* **2018**, *14*, 1062–1066.
- (33) Sussman, F.; Weinstein, H. On the Ion Selectivity in Ca-Binding Proteins: The Cyclo(-L-Pro-Gly-)3 Peptide as a Model. *Proc. Natl. Acad. Sci. U.S.A.* **1989**, *86*, 7880–7884.
- (34) Dill, K. A. Dominant Forces in Protein Folding. *Biochemistry* **1990**, *29*, 7133–7155.
- (35) Forrest, M. D. The Sodium-Potassium Pump is an Information Processing Element in Brain Computation. *Front. Physiol.* **2014**, *5*, 472.
- (36) Clausen, M. V.; Hilbers, F.; Poulsen, H. The Structure and Function of the Na,K-ATPase Isoforms in Health and Disease. *Front. Physiol.* **2017**, *8*, 371.
- (37) Ghosh, A.; Vaval, N. Geometry-Dependent Lifetime of Interatomic Coulombic Decay using Equation-of-Motion Coupled Cluster Method. *J. Chem. Phys.* **2014**, *141*, 234108.
- (38) Ghosh, A.; Pal, S.; Vaval, N. Study of Interatomic Coulombic Decay of $\text{Ne}(\text{H}_2\text{O})_n$ ($n = 1, 3$) Clusters Using Equation-of-Motion Coupled Cluster Method. *J. Chem. Phys.* **2013**, *139*, 064112.
- (39) Ghosh, A.; Vaval, N.; Pal, S.; Bartlett, R. J. Complex Absorbing Potential Based Equation-of-Motion Coupled Cluster Method for the Potential Energy Curve of CO_2^- Anion. *J. Chem. Phys.* **2014**, *141*, 164113.
- (40) Jagau, T. C.; Zuev, D.; Bravaya, K. B.; Epifanovsky, E.; Krylov, A. I. A Fresh Look at Resonances and Complex Absorbing Potentials: Density Matrix-Based Approach. *J. Phys. Chem. Lett.* **2014**, *5*, 310–315.
- (41) Zuev, D.; Jagau, T. C.; Bravaya, K. B.; Epifanovsky, E.; Shao, Y.; Sundstrom, E.; Head-Gordon, M.; Krylov, A. I. Complex Absorbing Potentials within EOM-CC Family of Methods: Theory, Implementation, and Benchmarks. *J. Chem. Phys.* **2014**, *141*, 024102.
- (42) Jagau, T. C.; Krylov, A. I. Complex Absorbing Potential Equation-of-Motion Coupled-Cluster Method Yields Smooth and Internally Consistent Potential Energy Surfaces and Lifetimes for Molecular Resonances. *J. Phys. Chem. Lett.* **2014**, *5*, 3078–3085.
- (43) Sajeev, Y.; Ghosh, A.; Vaval, N.; Pal, S. Coupled Cluster Methods for Autoionisation Resonances. *Int. Rev. Phys. Chem.* **2014**, *33*, 397–425.
- (44) Bartlett, R. J.; Musiał, M. Coupled Cluster Theory in Quantum Chemistry. *Rev. Mod. Phys.* **2007**, *79*, 291–352.
- (45) Lyakh, D. I.; Musiał, M.; Lotrich, V. F.; Bartlett, R. J. Multireference Nature of Chemistry: The Coupled Cluster View. *Chem. Rev.* **2012**, *112*, 182–243.
- (46) Nooijen, M.; Bartlett, R. J. Equation-of-Motion Coupled Cluster Method for Electron Attachment. *J. Chem. Phys.* **1995**, *102*, 3629–3647.
- (47) Stanton, J. F.; Bartlett, R. J. The Equation-of-Motion Coupled Cluster Method. A Systematic Biorthogonal Approach to Molecular Excitation Energies, Transition Probabilities, and Excited State Properties. *J. Chem. Phys.* **1993**, *98*, 7029–7039.
- (48) Nooijen, M.; Bartlett, R. J. Similarity Transformed Equation-of-Motion Coupled-Cluster Theory: Details, Examples, and Comparisons. *J. Chem. Phys.* **1997**, *107*, 6812–6830.
- (49) Musiał, M.; Bartlett, R. J. Charge Transfer Separability and Size Extensivity in the Equation-of-Motion Coupled Cluster Method: EOM-CCx. *J. Chem. Phys.* **2011**, *134*, 034106.
- (50) Musiał, M.; Kucharski, S. A.; Bartlett, R. J. Equation-of-Motion Coupled Cluster Method with Full Inclusion of the Connected Triple Excitations for Ionized States: IP-EOM-CCSDT. *J. Chem. Phys.* **2003**, *118*, 1128–1136.
- (51) Siegert, A. J. F. On the Derivation of the Dispersion Formula for Nuclear Reactions. *Phys. Rev.* **1939**, *56*, 750–752.
- (52) Moiseyev, N.; Corcoran, C. Autoionizing States of H_2 and H_2^- using the Complex-Scaling Method. *Phys. Rev. A* **1979**, *20*, 814–817.
- (53) Moiseyev, N. Quantum Theory of Resonances: Calculating Energies, Widths and Cross-Sections by Complex Scaling. *Phys. Rep.* **1998**, *302*, 212–293.
- (54) Moiseyev, N. Derivations of Universal Exact Complex Absorption Potentials by the Generalized Complex Coordinate Method. *J. Phys. B: At. Mol. Opt. Phys.* **1998**, *31*, 1431–1441.
- (55) Sommerfeld, T.; Riss, U. V.; Meyer, H. D.; Cederbaum, L. S.; Engels, B.; Suter, H. U. Temporary Anions - Calculation of Energy and Lifetime by Absorbing Potentials: The Resonance. *J. Phys. B: At. Mol. Opt. Phys.* **1998**, *31*, 4107–4122.
- (56) Jolicard, G.; Austin, E. J. Optical Potential Stabilisation Method for Predicting Resonance Levels. *Chem. Phys. Lett.* **1985**, *121*, 106–110.
- (57) Riss, U. V.; Meyer, H. D. Calculation of Resonance Energies and Widths using the Complex Absorbing Potential Method. *J. Phys. B: At. Mol. Opt. Phys.* **1993**, *26*, 4503–4535.
- (58) Muga, J.; Palao, J.; Navarro, B.; Egusquiza, I. Complex Absorbing Potentials. *Phys. Rep.* **2004**, *395*, 357–426.
- (59) Riss, U. V.; Meyer, H. D. The Transformative Complex Absorbing Potential Method: A Bridge between Complex Absorbing Potentials and Smooth Exterior Scaling. *J. Phys. B: At. Mol. Opt. Phys.* **1998**, *31*, 2279–2304.
- (60) Sajeev, Y.; Santra, R.; Pal, S. Correlated Complex Independent Particle Potential for Calculating Electronic Resonances. *J. Chem. Phys.* **2005**, *123*, 204110.
- (61) Sajeev, Y.; Pal, S. A General Formalism of the Fock Space Multireference Coupled Cluster Method for Investigating Molecular Electronic Resonances. *Mol. Phys.* **2005**, *103*, 2267–2275.
- (62) Ghosh, A.; Karne, A.; Pal, S.; Vaval, N. CAP/EOM-CCSD Method for the Study of Potential Curves of Resonant States. *Phys. Chem. Chem. Phys.* **2013**, *15*, 17915–17921.
- (63) Tomasi, J.; Mennucci, B.; Cammi, R. Quantum Mechanical Continuum Solvation Models. *Chem. Rev.* **2005**, *105*, 2999–3094.
- (64) Frisch, M. J.; Trucks, G. W.; Schlegel, H. B.; Scuseria, G. E.; Robb, M. A.; Cheeseman, J. R.; Scalmani, G.; Barone, V.; Mennucci, B.; Petersson, G. A.; Nakatsuji, H.; Caricato, M.; Li, X.; Hratchian, H. P.; Izmaylov, A. F.; Bloino, J.; Zheng, G.; Sonnenberg, J. L.; Hada, M.; Ehara, M.; Toyota, K.; Fukuda, R.; Hasegawa, J.; Ishida, M.; Nakajima, T.; Honda, Y.; Kitao, O.; Nakai, H.; Vreven, T.; Montgomery, J. A., Jr.; Peralta, J. E.; Ogliaro, F.; Bearpark, M.; Heyd, J. J.; Brothers, E.; Kudin, K. N.; Staroverov, V. N.; Kobayashi, R.; Normand, J.; Raghavachari, K.; Rendell, A.; Burant, J. C.; Iyengar, S. S.; Tomasi, J.; Cossi, M.; Rega, N.; Millam, J. M.; Klene, M.; Knox, J. E.; Cross, J. B.; Bakken, V.; Adamo, C.; Jaramillo, J.; Gomperts, R.; Stratmann, R. E.; Yazyev, O.; Austin, A. J.; Cammi, R.; Pomelli, C.; Ochterski, J. W.; Martin, R. L.; Morokuma, K.; Zakrzewski, V. G.; Voth, G. A.; Salvador, P.; Dannenberg, J. J.; Dapprich, S.; Daniels, A. D.; Farkas, O.; Foresman, J. B.; Ortiz, J. V.; Cioslowski, J.; Fox, D. J. *Gaussian 09*, revision C.01; Gaussian, Inc.: Wallingford, CT, 2009.
- (65) Dunning, T. H. Gaussian Basis Sets for Use in Correlated Molecular Calculations. I. The Atoms Boron Through Neon and Hydrogen. *J. Chem. Phys.* **1989**, *90*, 1007–1023.
- (66) Kaufmann, K.; Baumeister, W.; Jungen, M. Universal Gaussian Basis Sets for an Optimum Representation of Rydberg and Continuum Wavefunctions. *J. Phys. B: At. Mol. Opt. Phys.* **1989**, *22*, 2223–2240.
- (67) Kendall, R. A.; Dunning, T. H.; Harrison, R. J. Electron Affinities of the First-Row Atoms Revisited. Systematic Basis Sets and Wave Functions. *J. Chem. Phys.* **1992**, *96*, 6796–6806.

- (68) Becke, A. D. Density-Functional Thermochemistry. III. The Role of Exact Exchange. *J. Chem. Phys.* **1993**, *98*, 5648–5652.
- (69) Lee, C.; Yang, W.; Parr, R. G. Development of the Colle-Salvetti Correlation-Energy Formula into a Functional of the Electron Density. *Phys. Rev. B* **1988**, *37*, 785–789.
- (70) Stephens, P. J.; Devlin, F. J.; Chabalowski, C. F.; Frisch, M. J. Ab Initio Calculation of Vibrational Absorption and Circular Dichroism Spectra Using Density Functional Force Fields. *J. Phys. Chem.* **1994**, *98*, 11623–11627.
- (71) Vosko, S. H.; Wilk, L.; Nusair, M. Accurate Spin-Dependent Electron Liquid Correlation Energies for Local Spin Density Calculations: A Critical Analysis. *Can. J. Phys.* **1980**, *58*, 1200–1211.
- (72) Müller, I. B.; Cederbaum, L. S.; Tarantelli, F. Microsolvation of Li^+ in Water Analyzed by Ionization and Double Ionization. *J. Phys. Chem. A* **2004**, *108*, 5831–5844.
- (73) Papajak, E.; Leverentz, H. R.; Zheng, J.; Truhlar, D. G. Efficient Diffuse Basis Sets: cc-pVxZ+ and maug-cc-pVxZ. *J. Chem. Theory Comput.* **2009**, *5*, 3330.
- (74) Pritchard, B. P.; Altarawy, D.; Didier, B.; Gibson, T. D.; Windus, T. L. New Basis Set Exchange: An Open, Up-to-Date Resource for the Molecular Sciences Community. *J. Chem. Inf. Model.* **2019**, *59*, 4814–4820.
- (75) Öhrwall, G.; Ottosson, N.; Pokapanich, W.; Legendre, S.; Svensson, S.; Björneholm, O. Charge Dependence of Solvent-Mediated Intermolecular Coster-Kronig Decay Dynamics of Aqueous Ions. *J. Phys. Chem. B* **2010**, *114*, 17057–17061.
- (76) McLean, A. D.; Chandler, G. S. Contracted Gaussian Basis Sets for Molecular Calculations. I. Second Row Atoms, $Z = 11-18$. *J. Chem. Phys.* **1980**, *72*, 5639–5648.
- (77) Blaudeau, J.-P.; McGrath, M. P.; Curtiss, L. A.; Radom, L. Extension of Gaussian-2 (G2) Theory to Molecules Containing Third-Row Atoms K and Ca. *J. Chem. Phys.* **1997**, *107*, 5016–5021.
- (78) Hill, J. G.; Peterson, K. A. Gaussian Basis Sets for Use in Correlated Molecular Calculations. XI. Pseudopotential-Based and All-Electron Relativistic Basis Sets for Alkali Metal (K-Fr) and Alkaline Earth (Ca-Ra) Elements. *J. Chem. Phys.* **2017**, *147*, 244106.
- (79) Pokapanich, W.; Bergersen, H.; Bradeanu, I. L.; Marinho, R. R. T.; Lindblad, A.; Legendre, S.; Rosso, A.; Svensson, S.; Tchapyguine, M.; Kryzhevoi, N. V.; Cederbaum, L. S. Auger Electron Spectroscopy as a Probe of the Solution of Aqueous Ions. *J. Am. Chem. Soc.* **2009**, *131*, 7264–7271.

Recommended by ACS

Multi-state and Multi-mode Vibronic Coupling Effects in the Photoionization Spectroscopy of Acetaldehyde

Vadala Jhansi Rani, S. Mahapatra, *et al.*

SEPTEMBER 20, 2022
THE JOURNAL OF PHYSICAL CHEMISTRY A

READ 

Time-Resolved Optical Pump-Resonant X-ray Probe Spectroscopy of 4-Thiouracil: A Simulation Study

Yeonsig Nam, Shaul Mukamel, *et al.*

APRIL 27, 2022
JOURNAL OF CHEMICAL THEORY AND COMPUTATION

READ 

Hydrated Electrons in High-Concentration Electrolytes Interact with Multiple Cations: A Simulation Study

Wilberth A. Narvaez, Benjamin J. Schwartz, *et al.*

MAY 11, 2022
THE JOURNAL OF PHYSICAL CHEMISTRY B

READ 

Development, Validation, and Pilot Application of a Generalized Fluctuating Charge Model for Computational Spectroscopy in Solution

Vincenzo Barone, Marco Pagliai, *et al.*

APRIL 06, 2022
ACS OMEGA

READ 

Get More Suggestions >

Effect of Protonation and Deprotonation on Electron Transfer Mediated Decay and Interatomic Coulombic Decay

R. Kumar^[a, b] and N. Vaval^{*[a, b]}

Electronically excited atoms or molecules in an environment are often subject to interatomic/intermolecular Coulombic decay (ICD) and/or electron transfer mediated decay (ETMD) mechanisms. A few of the numerous variables that can impact these non-radiative decay mechanisms include bond distance, the number of nearby atoms or molecules, and the polarisation effect. In this paper, we have studied the effect of protonation and deprotonation on the ionization potential (IP), double ionization potential (DIP), and lifetime (or decay width) of the temporary bound state in these non-radiative decay processes. We have chosen LiH-NH₃ and LiH-H₂O as test systems. The equation of motion coupled cluster singles and doubles method augmented by complex absorbing potential (CAP-

EOM-CCSD) has been used in calculating the energetic position of the decaying state and the system's decay rate. Deprotonation of LiH-NH₃/LiH-H₂O either from the metal center (LiH) or from ammonia/water lowers the IP and DIP compared to the neutral systems. In contrast, protonation increases these quantities compared to neutral systems. The protonation closes the inner valence state relaxation channels for ICD/ETMD. For example, the decay of the O-2s/N-2s state stops in protonated systems (LiH₂⁺-H₂O, LiH₂⁺-NH₃, and LiH-NH₄⁺). Our study also shows that the efficiency, i.e., the rate of ICD/ETMD, can be altered by protonation and deprotonation. It is expected to have implications for chemical and biological systems.

Introduction

The knowledge on the importance of non-radiative processes like interatomic and intermolecular coulombic decay (ICD)^[1,2] and electron transfer mediated decay (ETMD)^[3-5] has substantially increased over the past two decades. ICD, first proposed by Cederbaum *et al.*,^[1,2] is a nonlocal and efficient decay mechanism that occurs at the femtosecond timescale. During this process, when an ionized/excited system relaxes non-radiatively in an environment, an outer valence electron fills the vacancy in the inner valence, resulting in a virtual photon emission which knocks out a valence electron from an adjacent atom or molecule. This situation leads to a Coulomb explosion due to the proximity of two positively charged species. The energy transfer happens quickly, i.e. in a few to a hundred femtoseconds. ICD was initially studied theoretically^[6-8] and experimentally^[9-14] in hydrogen-bonded,^[15] and weakly bound rare gas clusters.^[16,17] In ETMD, an electron is transferred from a neighboring atom to an initially ionized atom or molecule. The excess energy can knock out a second electron from the same donor atom/molecule in ETMD(2) process. While in ETMD(3),

secondary electron ejection occurred from the second adjacent atom/molecule. Since ETMD involves the transfer of electrons from a neighboring species to an initially ionized species, it is usually slower than the ICD. See Figure 1 for a better understanding of the difference between ICD and ETMD. The low energy electrons generated during ICD and ETMD have different kinetic energies. One can use this information to identify

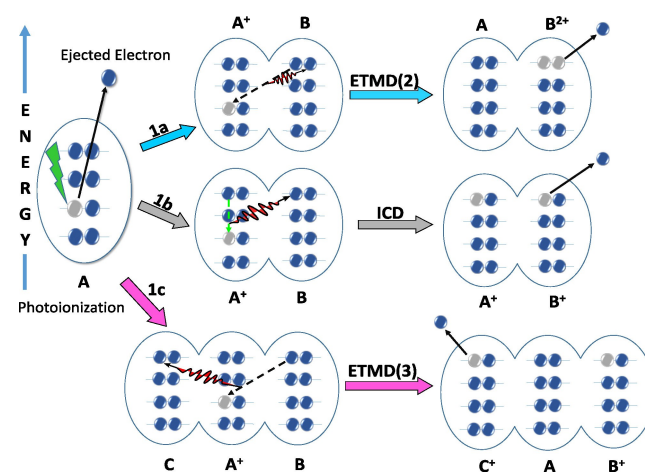


Figure 1. Visual representation of electronic decay processes. (1a.) In ETMD(2), an inner valence vacancy is filled by an outer valence electron of the neighboring molecule B, and another valence electron is emitted from the same molecule B leaving a final AB²⁺ molecular state. (1b.) ICD, a valence electron from molecule A, fills the vacancy, and the released energy is transferred to an outer valence electron of neighboring molecule B. Thus, forming A⁺B⁺ as the final state. (1c.) ETMD(3) process in which the vacancy in molecule A is filled by an outer valence electron of the neighboring molecule B, and ejection of the second electron occurs from another adjacent molecule C, leaving AB⁺C⁺ as the final state. The number 2 and 3 represents the number of molecule involved in the ETMD process.

[a] R. Kumar, Dr. N. Vaval
Academy of Scientific and Innovative Research,
CSIR-Human Resource Development Center (CSIR-HRDC) Campus,
Postal staff College Area, Ghaziabad,
Uttar Pradesh, 201002, India
E-mail: np.vaval@ncl.res.in

[b] R. Kumar, Dr. N. Vaval
Electronic Structure Theory Group,
Physical and Materials Chemistry Division,
CSIR-National Chemical Laboratory,
Pune, 411008, India

the specific local environment. Thus, the study of ICD and ETMD is essential to understand the decay of the ionized inner valence state in an environment. Recent studies^[18,19] show that various factors influence the ICD/ETMD process, like the number of surrounding atoms or molecules, bond distance, geometry, and the medium in which energy/electron transfer happens. The environment can change the lifetime of a temporary bound state (TBS) undergoing ICD/ETMD by stabilizing or destabilizing it. Thus, environmental effects/properties play a particularly relevant role. In this paper, we explore an important environmental effect: the protonation and deprotonation effect on ICD and ETMD. Specifically, we will study the impact of protonation and deprotonation on ionization potential (IP), Double ionization potential (DIP), and decay width (or the lifetime of TBS). Recently, the effect of protonation and deprotonation on IP and DIP in pure ammonia clusters^[20] has been studied. Still, the impact of protonation and deprotonation on the lifetime of TBS has not been studied. We are the first ones to learn it through this study.

Our aim is to understand the effect of protonation/deprotonation on the ICD/ETMD using alkali metal ions micro-solvated in water and ammonia. Understanding this may help us control the relevant process in a chemical environment. This tells us how a change in surrounding and protonation/deprotonation affects the decay process and lifetime of the TBS. The first step towards this will be doing these calculations accurately for a metal ion-water system and its protonated/deprotonated form with the coupled-cluster methods, which scale as N^6 . To get the decay width, we need to solve the CC equation thousands of times, which makes it computationally expensive. Thus, we wanted to study the smallest possible metal-related system. Therefore, we chose Lithium, although we know that the alkali metals Na^+ , K^+ , etc., are more relevant biologically. Also, as the first step towards this, gas-phase calculations are done. We may have to implement some approximate method for the actual interesting systems. We have discussed our finding and their possible reasons in the Results and Discussion Section, followed by the Conclusion. Last, we have discussed the Computational and Theoretical Details of the Equation of motion coupled cluster methods.

Results and Discussion

We will study the effect of protonation and deprotonation on the IP, DIP, and lifetime of O-2s, N-2s, and Li-1s TBS in the gaseous state. We have chosen $\text{LiH-H}_2\text{O}$ and LiH-NH_3 as test systems for our study. Protonation and deprotonation can occur either from LiH (metal center) or $\text{H}_2\text{O}/\text{NH}_3$. Thus, $\text{LiH}_2^+-\text{NH}_3$ and LiH-NH_4^+ will be formed by the protonation of LiH-NH_3 and Li^--NH_3 and LiH-NH_2^- by deprotonation. Similarly, for the $\text{LiH-H}_2\text{O}$ system, we have $\text{Li}^--\text{H}_2\text{O}$ and LiH-OH^- as deprotonated and $\text{LiH}_2^+-\text{H}_2\text{O}$ only as a protonated system. Due to the instability of $\text{LiH-H}_3\text{O}^+$, global minima could not be found. Understanding the impact of deprotonation and protonation on ICD and ETMD in microsolvated systems is a step toward helping us control these relevant and abundant processes in various chemical

environments and may also be in biological systems. We will first study, analyze and then compare the effect of the protonation and deprotonation on IP and DIP for LiH-NH_3 , $\text{LiH-H}_2\text{O}$, along with their protonated and deprotonated systems. Later, we will examine the factors that affect TBS lifetime and whether it is possible to find a general trend in the lifetime of TBS on protonation and deprotonation.

Effect of Protonation and Deprotonation on the IP and DIP

Figures 2 and 3 display the all IP (except O-1s) and the lowest DIP values of the neutral, protonated, and deprotonated $\text{LiH-H}_2\text{O}$ and LiH-NH_3 systems, respectively. We have written down a few observations from both figures (2nd and 3rd) and will provide possible explanations for them. First, we observe the decrease in system's IP and DIP values with deprotonation and an increase after protonation. This is due to the decrease and increase in effective nuclear charge on deprotonation and protonation, respectively. Protonation increases the effective nuclear charge (ENC) while deprotonation decreases it. Electron ejection becomes challenging as ENC rises. As a result, we saw that IP and DIP value increased on protonation and decreased after protonation.

Second, from Figure 3, if we compare the IP values of the two deprotonated systems of LiH-NH_3 , i.e., Li^--NH_3 and LiH-NH_2^- . The IP values for all the states of Li^--NH_3 are higher than the corresponding LiH-NH_2^- , except for the IP of HOMO. HOMO's IP of LiH-NH_2^- (3.06 eV) is more than HOMO's IP of Li^--NH_3 (0.33 eV), which is just opposite of the rest of the IP trend. A similar trend is observed between deprotonated systems of $\text{LiH-H}_2\text{O}$.

The IP values of HOMO in the metal-centered deprotonated systems (Li^--NH_3 and $\text{Li}^--\text{H}_2\text{O}$) almost drop to zero. The lowest

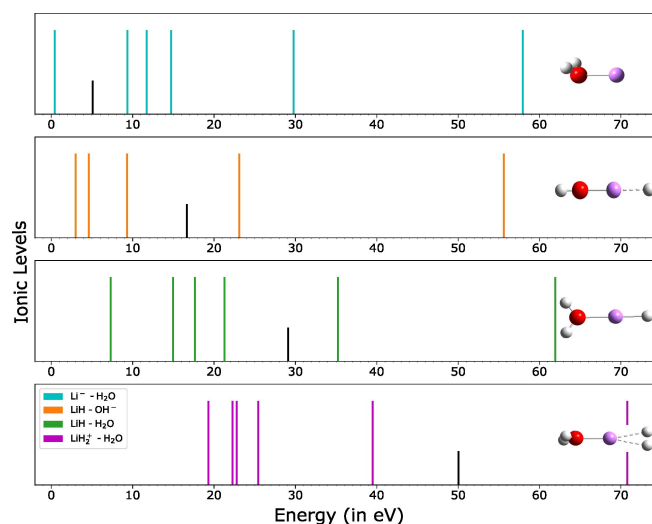


Figure 2. The IPs of neutral $\text{LiH-H}_2\text{O}$ and its deprotonated and protonated species. The smaller black line denotes the lowest DIP value. The structure of the respective system is shown on the right of each panel. Atom color code: Red: Oxygen, Pink: Lithium, and White: Hydrogen.

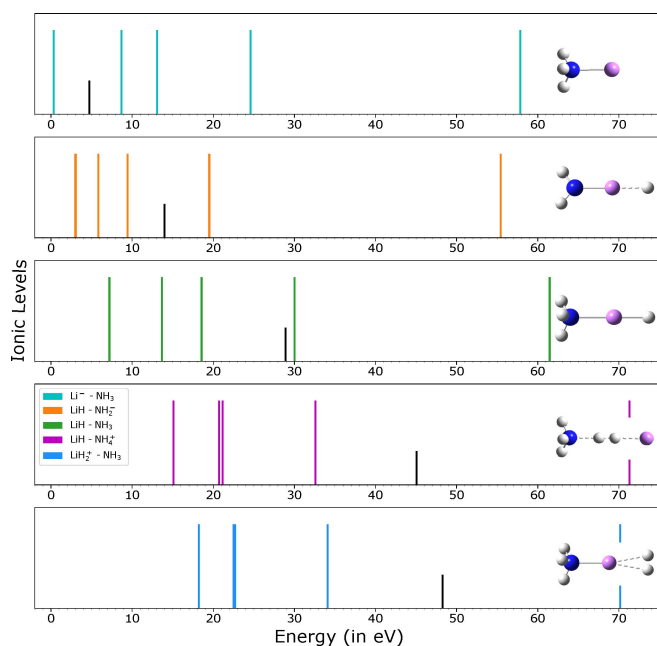


Figure 3. The IPs of deprotonated, protonated, and neutral LiH-NH₃. The smaller black line denotes the lowest DIP value. The structure of the respective system is shown on the right of each panel. Atom color code: Blue: Nitrogen, Pink: Lithium, and White: Hydrogen.

IP (HOMO's IP) values of metal-centered deprotonated systems are so small that both systems may lose their outer-valence electron vibrationally. To know that, we have calculated these system's ionization energy (IE) and zero point energy. The IE value was found to be 0.54 eV and 0.46 eV for the Li⁻-H₂O and Li⁻-NH₃, respectively. But the zero point energy is 0.62 eV for Li⁻-H₂O and 0.99 eV for Li⁻-NH₃. It is clear that the zero-point energy of the metal-centered deprotonated systems is higher than its ionization energy. Thus, we conclude that the metal-centered deprotonated systems can lose electrons vibrationally in their ground state and are not electronically stable. Therefore, we will not further study the metal-centered deprotonated systems for the decay width. We have used the CCSD(T) method (a gold standard in theory) for the ionization energy and zero-point energy with the aug-cc-pVTZ basis set.^[21]

Till now, it's clear that electrons can lose vibrationally, but it does not tell why the HOMO's IP values of metal-centered deprotonated systems are so low than HOMO's IP of their respective neutral systems and other deprotonated systems (LiH-NH₂⁻ and LiH-OH⁻). To understand that, we will discuss both systems' geometric and electronic structures before returning to the ionization spectra. Our primary focus will be the HOMO since HOMO does not fit the rest of the IP trend.

We must know about the HOMO and its constituting atomic orbitals in neutral and metal-centered deprotonated systems to understand the changes clearly. Lithium-2s and hydrogen-1s atomic orbitals form the HOMO in neutral systems (LiH-NH₃ and LiH-H₂O). After deprotonation from the metal center, HOMO is mainly Li-2s in metal-centered deprotonated systems (Li⁻-NH₃ and Li⁻-H₂O). However, the HOMO of other deprotonated

systems (LiH-NH₂⁻/LiH-OH⁻) is similar to the corresponding neutral systems. The LiH bond is ionic, so electron density is mainly towards the more electronegative atom in the Li-H bond, which is the hydrogen atom. Figure 4 (a, b, and c) shows the location of HOMO (Li-2s), the lowest unoccupied molecular orbital (LUMO) (N-H antibonding), and both in one frame for Li⁻-NH₃. There is a partial overlapping in space between the HOMO and LUMO, which indicates the possibility of electron density transfer from HOMO to LUMO. Natural bond order (NBO) analysis proves this possibility, showing that the system stabilizes by $8.66 \times 3 = 25.98$ kcal/mol by delocalizing the electron density to 3 degenerate N-H antibonding orbitals from HOMO. Since the HOMO of Li-2s is spherical, all three delocalizations can happen simultaneously. One more interaction stabilizing the system by 3.61 kcal/mol occurs between HOMO and Rydberg states (3s orbital) of N. Resulting in HOMO will have negligible electron density. Hence, the IP of HOMO is lowered dramatically to 0.33 eV in Li⁻-NH₃. The NBO analysis has been done using the CCSD(T) level of theory and aug-cc-pVTZ basis set^[21] in the Gaussian09 software package.^[22] MOs in Figure 4, has been generated after NBO analysis. A similar interaction between HOMO and LUMO did not observe in the rest of the systems.

A similar kind of partial overlapping in space (shown in Figure 4d) and interaction between HOMO and LUMO is observed in Li⁻-H₂O. Here, the system stabilizes by $17.18 \times 2 = 34.36$ kcal/mol by delocalizing Li-2s electron density to 2 O-H antibonding orbitals, drastically lowering the IP of HOMO to 0.42 eV.

In Li⁻-NH₃ and Li⁻-H₂O, we have seen delocalization of the electron density. However, despite the fact that both LiH-OH⁻ and LiH-NH₂⁻ are deprotonated systems, why is there no delocalization in these systems? This can be explained by the fact that lithium is less electronegative than oxygen and nitrogen in water and ammonia, respectively. As a result, the lone pair stays close to the oxygen/nitrogen atoms. Second, Li is bound to the p_z-orbitals of nitrogen and oxygen in LiH-OH⁻ and LiH-NH₂⁻. The electron density after deprotonation is still present in the p_x and p_y orbitals of nitrogen/oxygen. Unlike the s-orbital of Li-2s in Li⁻-NH₃ and Li⁻-H₂O, which is spherical, p-

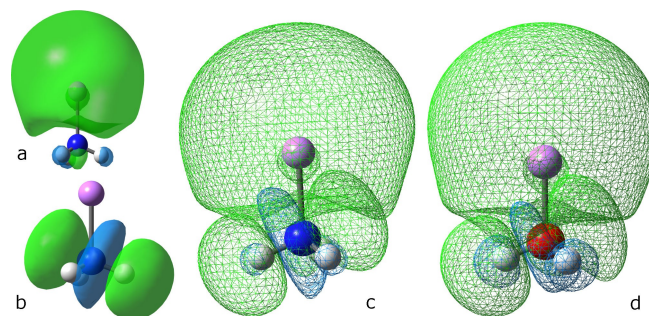


Figure 4. a and b show HOMO and LUMO in Li⁻-NH₃, c shows HOMO and LUMO are together in one picture in Li⁻-NH₃, d shows the same for Li⁻-H₂O. This Figure (c and d) demonstrates these orbitals partially overlap in space. Images are generated for 0.02 eÅ⁻³ isosurface value. Atom color code: Blue: Nitrogen, Red: Oxygen, Pink: Lithium, and White: Hydrogen.

orbitals are directional. Therefore, in LiH-OH^- and LiH-NH_2^- , we do not observe delocalization on deprotonation from ammonia/water.

Third, we noted that the IP was increased more by protonation from the metal center (IP's in $\text{LiH}_2^+-\text{NH}_3$) than by protonation from ammonia (IP's in LiH-NH_4^+). For example, the IP of HOMO is higher in $\text{LiH}_2^+-\text{NH}_3$ (18.24 eV) than in LiH-NH_4^+ (15.10 eV). The reason is the charge transfer. The location of a H^+ ion is critical within the molecule because it can help promote and demote the charge transfer between lithium and nitrogen. Let's understand how the H^+ ion affects charge transfer. As discussed earlier, HOMO in LiH-NH_3 is more localized on hydrogen than lithium. An extra added H^+ ion shifts the lithium's 2s electron density. Thus, almost all-electron density will be on H_2^+ in $\text{LiH}_2^+-\text{NH}_3$ and LiH-NH_4^+ , and lithium will be left with nearly nothing. However, the direct sharing of a lone pair of ammonia in $\text{LiH}_2^+-\text{NH}_3$ overcomes this lack of electron density on Li and stabilizes the system. $\text{LiH}_2^+-\text{NH}_3$ geometry shows that the additional H^+ ion is located far from the ammonia, facilitating charge transfer even more. Such direct electron sharing is impossible from ammonia to lithium in LiH-NH_4^+ since H_2^+ is between lithium and nitrogen. Fourth, we observe that the DIP value is the lowest (4.73 eV for Li^--NH_3) and highest (48.26 eV for $\text{LiH}_2^+-\text{NH}_3$) when deprotonation and protonation occur from the metal center (LiH), respectively. That's because HOMO, which corresponds to the lowest DIP orbital, is a combination of lithium and hydrogen atomic orbitals. Thus, any change to these orbitals can lead to a considerable shift in DIP.

We have so far talked about how protonation and deprotonation affect IP and DIP values. We have observed that protonation increases the IP and DIP values, resulting in a few decay (inner valence) channels closing. For example, N-2s TBS in $\text{LiH}_2^+-\text{NH}_3$ and LiH-NH_4^+ , and O-2s TBS in $\text{LiH}_2^+-\text{H}_2\text{O}$ stop showing the decay. Note that the IP and DIP of the protonated/deprotonated system tell us whether a system is temporarily bound or not. In other words, if decay is possible or not. This means whether a lifetime of a decaying state will increase or decrease on protonation or deprotonation cannot be concluded based only on the IP and DIP values. To know that, we will now study how the protonation and deprotonation affect the decay width (in meV) and lifetime (in fs) of the TBS, along with the possible reasons.

Effect of Protonation and Deprotonation on the Lifetime of Li-1s and O-2s/N-2s TBSs in $\text{LiH-H}_2\text{O}$ and LiH-NH_3

The visual representation of the ICD and ETMD processes for a general system ABC is shown in Figure 1. Since ICD and ETMD(2) include two atoms/molecules, we are not mentioning molecule C there. You can distinguish between various decay mechanisms by identifying their final DIP states. The final two-hole states are localized on two separate molecules in ICD, i.e., A^+B^+ , but in ETMD(2), they are localized on one atom/molecules, i.e., AB^{2+} or A^{2+}B . The two-hole localization in ETMD(3) is on the pair of neighboring molecules, i.e., C^+AB^+ .

DIP eigenvalues and eigenvectors offer information on the localization of two holes in molecules. Specifically, eigenvalues tell us whether decay is feasible, whereas eigenvectors predict whether a process will be ICD, ETMD(2), or ETMD(3). In the following section, we will compare the systems in Tables 1 & 2 and examine potential explanations for any variations in the lifetime of Li-1s and O-2s/N-2s TBS on protonation and deprotonation.

Lifetime of Li-1s TBS in $\text{LiH-H}_2\text{O}$, LiH-NH_3 and their Deprotonated Systems

When we compare the lifetime of Li-1s TBS in deprotonated LiH-OH^- and neutral $\text{LiH-H}_2\text{O}$ systems in Table 1, we observe a decrease in the lifetime of Li-1s TBS. That's due to an increase in the orbital's partial overlapping in space (see Figure 5a and 5b) that facilitates a faster electron transfer between p-orbitals of oxygen to Li-1s orbital. This partial orbital overlap is influenced by three different causes. First is the charge. In LiH-OH^- , oxygen

Table 1. Energetic position of the decaying state and the decay width after Li-1s and O-2s ionization of $\text{LiH-H}_2\text{O}$ along with its protonated and deprotonated systems.

System	Li-1s		O-2s	
	Energy (eV)	Width in meV (fs)	Energy (eV)	Width in meV (fs)
LiH-OH^-	55.56	64.27 (10.24)	23.10	16.6 (39.62)
$\text{LiH-H}_2\text{O}$	61.93	13.41 (49)	35.22	4.7 (139.6)
$\text{LiH}_2^+-\text{H}_2\text{O}$	70.79	50.17 (13.17)	–	–

Table 2. Energetic position of the decaying state and the decay width after Li-1s and N-2s ionization of LiH-NH_3 along with its protonated and deprotonated systems.

System	Li-1s		N-2s	
	Energy (eV)	Width in meV (fs)	Energy (eV)	Width in meV (fs)
LiH-NH_3	61.48	39.18 (16.79)	30.00	7.19 (91.48)
$\text{LiH}_2^+-\text{NH}_3$	70.17	10.39 (63.32)	–	–
	protonation and deprotonation on nitrogen			
LiH-NH_2^-	55.50	65.52 (10.45)	19.51	7.48 (87.90)
LiH-NH_3	61.48	39.18 (16.79)	30.00	7.19 (91.48)
LiH-NH_4^+	71.01	144.06 (4.57)	–	–

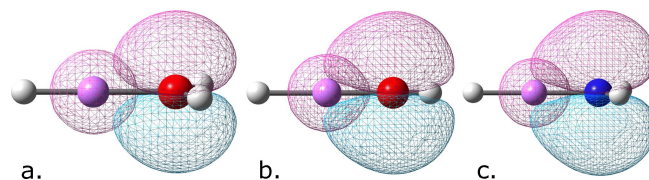


Figure 5. a, b, and c show the partially overlapping in space between Li-1s orbital and the lone pair orbital of oxygen/nitrogen, which are perpendicular to the molecular axis in $\text{LiH-H}_2\text{O}$, LiH-OH^- , and LiH-NH_2^- , respectively. It shows that the orbital's partial overlapping in space increases from $\text{LiH-H}_2\text{O}$ to LiH-OH^- . Images are generated for 0.02 $\text{e}\text{\AA}^{-3}$ isosurface value. Atom color code: Red: Oxygen, Pink: Lithium, Blue: Nitrogen, and White: Hydrogen.

has an entirely negative charge, while lithium has a high positive charge. Here two adjacent atoms have opposite charges on them. We know opposite charges attract each other. Therefore, there will be an increase in attraction force (or partial overlapping of orbitals). The O–Li bond distance is the second. We observed a reduction in the O–Li bond length while switching from LiH–H₂O (1.924 Å) to LiH–OH[−] (1.690 Å). This further increases the partial overlapping between orbitals. The third is electron–electron repulsion. After LiH–H₂O deprotonated, an additional lone pair appeared on OH[−] in LiH–OH[−], which is perpendicular to the molecular plane. The Li–H bond's electron density is mostly on hydrogen (more electronegative than Li) because it is an ionic bond. Therefore, an incoming oxygen's electrons may feel substantially less repulsion from Li-2s electrons. This makes the shift of lone pair electrons of oxygen toward lithium more favorable. This shift of lone pairs increases further when there is a vacancy formation on Li during the decay, making electron transfer faster between oxygen and lithium. Thus, we are getting a low lifetime for Li-1s TBS in LiH–OH[−] than LiH–H₂O. Similar reasoning can explain a decrease in Li-1s TBS lifespan in LiH–NH₂[−] compared to LiH–NH₃.

Additionally, we've seen that the decrease in Li-1s TBS lifetime in LiH–NH₂[−] relative to its neutral system is less pronounced than the decrease in Li-1s TBS lifetime in LiH–OH[−] relative to its neutral system. Two factors can explain this. First is the number of lone pairs. LiH–OH[−] has two lone pairs, which are perpendicular to the molecular plane, while LiH–NH₂[−] has one such lone pair. As a result, electron transfer from the oxygen/nitrogen lone pair to the Li-1s orbital will happen twice as quickly in LiH–OH[−] as in LiH–NH₂[−]. Bond distance is the second. The O–Li bond distance (1.69 Å) in LiH–OH[−] is shorter than the N–Li bond distance (1.85 Å) in LiH–NH₂[−]. Therefore, the partial overlapping between the lone pair orbital of oxygen and the lithium 1s orbital will be greater than that between the lone pair orbital of nitrogen and the lithium 1s orbital. This strong partial overlapping makes electron transfer faster between O/N and Li-1s in LiH–OH[−] than in LiH–NH₂[−]. The lone pair of oxygen/nitrogen that we are talking about are the ones that are perpendicular to the molecular axis of each system. Hence, observing a significant reduction in LiH–OH[−] than in LiH–NH₂[−] compared to their neutral systems.

Lifetime of O-2s and N-2s TBS in LiH–H₂O, LiH–NH₃ and their Deprotonated Systems

We have seen a large shift in the lifetime of O-2s TBS and a minor decrease in N-2s TBS in LiH–OH[−] and LiH–NH₂[−] compared to their respective neutral systems. There are three reasons for that. First, LiH–OH[−] has two lone pairs, which are perpendicular to the molecular plane, while LiH–NH₂[−] has one such lone pair. It means LiH–OH[−] and LiH–NH₂[−] each have one lone pair extra than their respective neutral systems. We are aware that bonded electron density is governed by two attractive forces from two separate nuclei, whereas lone pair electrons are affected by one nucleus (atom specific). It means the O-2s or N-2s vacancy can be filled faster in deprotonated systems than in

respective neutral systems. Hence, we observed that the decay becomes faster, and the lifetime will reduce. Second, oxygen is more electronegative than nitrogen. Thus, attraction felt by electrons is higher in LiH–OH[−] than LiH–NH₂[−], making decay faster. The third is the eigenvector analysis. We observe that N-2s have two possible decay channels in LiH–NH₂[−], while O-2s have four possible decay channels in LiH–OH[−]. Based on eigenvector analysis, N-2s TBS decays by the ICD process only. In contrast, O-2s TBS decays by ETMD and ICD. Besides these three reasons, huge geometry and symmetry change may also be the reason for a large drop in the lifetime of O-2s in LiH–OH[−] and a minor change in the lifetime of N-2s in LiH–NH₂[−] compared to their respective neutral systems. In water-related systems, the H–O–Li bond angle changes from 126.6 (in LiH–H₂O) to 180 (in LiH–OH[−]), and symmetry changes from C_{2v} to C_{∞v}. While in ammonia-related systems, the H–N–Li bond angle changes from 112.4 (in LiH–NH₃) to 127.9 (in LiH–NH₂[−]), and symmetry changes from C_{3v} to C_{2v}. This change in the geometry of the ammonia-related system is not profound compared to the geometry change of LiH–OH[−] form LiH–H₂O.

Lifetime of Li-1s TBS in LiH–H₂O, LiH–NH₃ and their Protonated Systems

The situation changes in LiH₂⁺–H₂O and LiH₂⁺–NH₃ because the molecule can be seen as three separate units, namely H₂O/NH₃, Li⁺, and H₂. You might wonder if it makes a difference whether a molecule has two or three subunits. It matters because the prerequisites for the ETMD(3) process are met (two nearby atoms or molecules in addition to the atom or molecule that forms the TBS). The ETMD(3) decay process can be described for Li-1s TBS in LiH₂⁺–H₂O and LiH₂⁺–NH₃, as the lithium atom receives a second positive charge due to photoionization (Li-1s vacancy formation). Then an electron from the H₂ subunit will fill the Li-1s vacancy, and the released virtual photon will eject a secondary electron from either NH₃ or H₂O. The directional nature of p-orbitals is critical in explaining increases and decreases in lifetime of the Li-1s TBS in the protonated systems (LiH₂⁺–H₂O, LiH₂⁺–NH₃, and LiH–NH₄⁺). The nitrogen/oxygen lone pair orbital is oriented toward the Li-1s TBS in LiH₂⁺–NH₃ and perpendicular to the molecular plane in LiH₂⁺–H₂O. As a result, charge transfer in LiH₂⁺–NH₃ is eased, and we can observe that lone pairs of ammonia stabilize Li-1s TBS while LiH₂⁺–H₂O does not experience this stabilization from water. This explains why the Li-1s TBS lifetime in LiH₂⁺–H₂O and LiH₂⁺–NH₃ differs from those of their neutral systems. Since H₂ sits between Li and ammonia in LiH–NH₄⁺, there is no direct stabilizing effect by ammonia's lone pair in this compound. As a result, LiH–NH₄⁺ has a lower Li-1s TBS lifetime than LiH–NH₃. Protonation raises the IP and DIP values, which shuts the decay channel for the O-2s and N-2s in their respective protonated systems (LiH₂⁺–H₂O, LiH–NH₄⁺, and LiH₂⁺–NH₃). This explains the absence of N-2s and O-2s peaks in their respective protonated systems.

Conclusion

The impact of protonation and deprotonation on the system's IP, DIP, and lifetime has been examined in this paper. LiH-NH₃ and LiH-H₂O have been selected as test systems. For our research, we employed the EOM-CCSD approach with CAP potential. Our investigation found that protonation raises IP and DIP values relative to the neutral system, while deprotonation decreases IP and DIP values. However, we do not see such a general trend for the decay width/lifetime on protonation or deprotonation. In general, a molecule's protonation or deprotonation impacts its structural stability, which results in noticeable changes to the system's geometry and charge distribution. For example, due to protonation/deprotonation, geometry changes dominate the decay widths in water-related systems. However, in ammonia-related systems, we observe that charge transfer makes the system stable (i.e., LiH₂⁺-NH₃), causing a significant difference in decay width. These two elements influence the difference in the decay width of the system. We cannot state that protonation or deprotonation will cause an increase or decrease in decay width, unlike the IP/DIP values. We find that protonation (either from the metal center (LiH) or from H₂O/NH₃) shuts N-2s and O-2s (inner valence) decay pathways. However, the decay channel remains open for the core state Li-1s even after protonation. Li-1s TBS decays more quickly in deprotonated systems than in the corresponding neutral system because deprotonation increases the number of potential decay channels relative to the neutral system. Since the ammonia lone pair orbital is oriented toward Li and facilitates faster electron transmission, the Li-1s TBS decays in LiH-NH₃ more quickly than in LiH-H₂O. We draw the conclusion that the Li-1s TBS decays in neutral and deprotonated systems through ICD and ETMD(2) based on eigenvector analysis of the DIP. However, Li-1s decays via ETMD(2 & 3) in LiH₂⁺-NH₃ and LiH₂⁺-H₂O following protonation. O-2s and N-2s TBS decay via ICD and ETMD(2) in the neutral system. But in deprotonated systems, N-2s decay via ICD (in LiH-NH₂⁻) only, whereas O-2s (in LiH-OH⁻) decay via ICD and ETMD(2). All three decays are feasible for the decay of Li-1s in LiH-NH₄⁺.

Theory and Computational Details

We will initially examine the computational specifics before going through the decay processes' theory and procedures. Geometries of all molecules were optimized in the Gaussian09 software package^[22] using B3LYP^[23–26] functional and 6-311++g(2d,p) basis set.^[27] The IPs of neutral, protonated, and deprotonated clusters are calculated using the equation of motion coupled-cluster singles and doubles (EOM-CCSD) method.^[28–31] The DIP values are computed using the diagonalization of the 2-hole block of EOM-CCSD. The decay position and width of the system are calculated using the EOM-CCSD method augmented by the complex absorbing potential (CAP).^[32–37] We have used the aug-cc-pVTZ basis set^[21] for CAP-EOM-CCSD calculations. For information on the CAP-EOM-CCSD technique for ICD, ETMD(2), and ETMD(3), see reference.^[18] For both neutral systems, the CAP-EOM-CCSD computations have been performed with various box sizes. The dimension of optimum box size was found to be C_x=C_y=C_z=9 a.u and δC in protonated, deprotonated, and neutral LiH-NH₃. δC=R/2 was added along the

molecular axis. For protonated, deprotonated, and neutral LiH-H₂O systems, box dimensions were C_x=C_y=C_z=11 a.u and δC. Again, the δC=R/2 value was added along the molecular axis. Calculations of IP, DIP, and decay widths are done using homegrown codes. We will now quickly go over the CAP-EOM-CCSD methodology.

The target state, which is one hole state, is generated by the action of a linear operator $R(k)$ on the ground state wavefunction. The equation for the target state $|\Psi_k\rangle$ can be written as

$$|\Psi_k\rangle = R(k)|\Phi_{cc}\rangle \quad (1)$$

where $|\Phi_{cc}\rangle$ is the coupled-cluster wavefunction. It can be defined as

$$|\Phi_{cc}\rangle = e^T|\Phi_0\rangle \quad (2)$$

Where $|\Phi_0\rangle$ is the ground state Hartree-Fock wavefunction, $R(k)$ is an ionization operator, and T 's ($T=T_1+T_2$ for CCSD) are hole-particle excitation operators. T and R commute with each other. The linear operator $R(k)$ within singles and doubles approximation is written as

$$R(k) = \sum_i r_i(k)i + \sum_{ij,a} r_{ij}^a(k)a^\dagger j i \quad (3)$$

The similarity transformed Hamiltonian \bar{H}_N is formed as below.

$$\bar{H}_N = e^{-T}H_N e^T - \langle \Phi_0 | e^{-T}H_N e^T | \Phi_0 \rangle \quad (4)$$

The ionization potential values are obtained by diagonalizing the coupled-cluster similarity transformed Hamiltonian within $(N-1)$ electron space. This similarity transformed Hamiltonian is formed within 1-hole and 2-hole one particle space.

$$\bar{H}_N R(k)|\Phi_0\rangle = \omega_k R(k)|\Phi_0\rangle \quad (5)$$

Where ω_k is the difference between the N and $(N-1)$ electronic state, which is the IP of the k^{th} state.

The position and lifetime of the decaying state are obtained by augmenting the EOM-CCSD by complex absorbing potential (CAP). CAP approach adds a one-particle potential to the physical Hamiltonian $-i\eta W$. This makes the original Hamiltonian complex and non-hermitian $H(\eta) = H - i\eta W$. Where W is the real potential and η is the strength of CAP. The complex eigenvalues of the non-hermitian Hamiltonian give us the system's position and half decay width. In CAP-EOM-CCSD, we get the total decay width, i.e., the contribution from all possible decay channels. We do not get the decay width for the individual decay process.

We solve the $H(\eta) = H - i\eta W$ equation for various values of η to obtain complex energies that are η dependent. Real part vs. imaginary part of energy plotted in energy plot that shows the η trajectory. The stationary point on the trajectory provides the stabilization point.

Acknowledgements

RK acknowledges financial support from Council of scientific and Industrial Research. Authors acknowledge the computational facility at the CSIR-National Chemical Laboratory and IISER-Pune.

Authors acknowledge Prof. L. S. Cederbaum for critical reading of the manuscript and the valuable suggestions.

Conflict of Interest

The authors declare no conflict of interest.

Data Availability Statement

The data that support the findings of this study are available from the corresponding author upon reasonable request.

- [1] L. S. Cederbaum, J. Zobeley, F. Tarantelli, *Phys. Rev. Lett.* **1997**, *79*, 4778.
[2] R. Santra, L. S. Cederbaum, *Phys. Rep.* **2002**, *368*, 1.
[3] J. Zobeley, R. Santra, L. S. Cederbaum, *J. Chem. Phys.* **2001**, *115*, 5076.
[4] I. B. Müller, L. S. Cederbaum, *J. Chem. Phys.* **2005**, *122*, 094305.
[5] V. Stumpf, K. Gokhberg, L. S. Cederbaum, *Nat. Chem.* **2016**, *8*, 237.
[6] S. Scheit, V. Averbukh, H. Meyer, N. Moiseyev, R. Santra, T. Sommerfeld, J. Zobeley, L. S. Cederbaum, *J. Chem. Phys.* **2004**, *121*, 8393.
[7] N. Valal, L. S. Cederbaum, *J. Chem. Phys.* **2007**, *126*, 164110.
[8] M. Ehara, T. Sommerfeld, *Chem. Phys. Lett.* **2012**, *537*, 107.
[9] T. Jahnke, *J. Phys. B: At. Mol. Opt. Phys.* **2015**, *48*, 082001.
[10] S. Marburger, O. Kugeler, U. Hergenhahn, T. Möller, *Phys. Rev. Lett.* **2003**, *90*, 203401.
[11] T. Jahnke, A. Czasch, M. S. Schöffler, S. Schössler, A. Knapp, M. Kász, J. Titze, C. Wimmer, K. Kreidi, R. E. Grisenti, A. Staudte, O. Jagutzki, U. Hergenhahn, H. Schmidt-Böcking, R. Dörner, *Phys. Rev. Lett.* **2004**, *93*, 163401.
[12] I. Unger, R. Seidel, S. Thürmer, M. N. Pohl, E. F. Aziz, L. S. Cederbaum, E. Muchová, P. Slaviček, B. Winter, N. V. Kryzhevoi, *Nat. Chem.* **2017**, *9*, 708.
[13] M. N. Pohl, C. Richter, E. Lugovoy, R. Seidel, P. Slaviček, E. F. Aziz, B. Abel, B. Winter, U. Hergenhahn, *J. Phys. Chem. B* **2017**, *121*, 7709, pMID: 28696722.
[14] P. Zhang, C. Perry, T. T. Luu, D. Matselyukh, H. J. Wörner, *Phys. Rev. Lett.* **2022**, *128*, 133001.
[15] S. D. Stoychev, A. I. Kuleff, L. S. Cederbaum, *J. Chem. Phys.* **2010**, *133*, 154307.
[16] R. Santra, J. Zobeley, L. S. Cederbaum, N. Moiseyev, *Phys. Rev. Lett.* **2000**, *85*, 4490.
[17] N. Sisourat, H. Sann, N. V. Kryzhevoi, P. Kolorenč, T. Havermeier, F. Sturm, T. Jahnke, H. K. Kim, R. Dörner, L. S. Cederbaum, *Phys. Rev. Lett.* **2010**, *105*, 173401.
[18] R. Kumar, A. Ghosh, N. Valal, *J. Chem. Theory Comput.* **2022**, *18*, 807, pMID: 35019266.
[19] T. Jahnke, U. Hergenhahn, B. Winter, R. Dörner, U. Fröhling, P. V. Demekhin, K. Gokhberg, L. S. Cederbaum, A. Ehresmann, A. Knie, A. Dreuw, *Chem. Rev.* **2020**, *120*, 11295, pMID: 33035051.
[20] N. V. Kryzhevoi, L. S. Cederbaum, *Angew. Chem. Int. Ed.* **2011**, *50*, 1306.
[21] R. A. Kendall, T. H. Dunning, R. J. Harrison, *J. Chem. Phys.* **1992**, *96*, 6796.
[22] M. J. Frisch, G. W. Trucks, H. B. Schlegel, G. E. Scuseria, M. A. Robb, J. R. Cheeseman, G. Scalmani, V. Barone, B. Mennucci, G. A. Petersson, H. Nakatsuji, M. Caricato, X. Li, H. P. Hratchian, A. F. Izmaylov, J. Bloino, G. Zheng, J. L. Sonnenberg, M. Hada, M. Ehara, K. Toyota, R. Fukuda, J. Hasegawa, M. Ishida, T. Nakajima, Y. Honda, O. Kitao, H. Nakai, T. Vreven, J. Montgomery, J. A., J. E. Peralta, F. Ogliaro, M. Bearpark, J. J. Heyd, E. Brothers, K. N. Kudin, V. N. Staroverov, R. Kobayashi, J. Normand, K. Raghavachari, A. Rendell, J. C. Burant, S. S. Iyengar, J. Tomasi, M. Cossi, N. Rega, J. M. Millam, M. Klene, J. E. Knox, J. B. Cross, V. Bakken, C. Adamo, J. Jaramillo, R. Gomperts, R. E. Stratmann, O. Yazyev, A. J. Austin, R. Cammi, C. Pomelli, J. W. Ochterski, R. L. Martin, K. Morokuma, V. G. Zakrzewski, G. A. Voth, P. Salvador, J. J. Dannenberg, S. Dapprich, A. D. Daniels, O. Farkas, J. B. Foresman, J. V. Ortiz, J. Cioslowski, D. J. Fox, *Gaussian-09*, Gaussian Inc., Wallingford CT **2009**.
[23] P. J. Stephens, F. J. Devlin, C. F. Chabalowski, M. J. Frisch, *J. Phys. Chem.* **1994**, *98*, 11623.
[24] A. D. Becke, *J. Chem. Phys.* **1993**, *98*, 5648.
[25] C. Lee, W. Yang, R. G. Parr, *Phys. Rev. B* **1988**, *37*, 785.
[26] S. H. Vosko, L. Wilk, M. Nusair, *Can. J. Phys.* **1980**, *58*, 1200.
[27] R. Krishnan, J. S. Binkley, R. Seeger, J. A. Pople, *J. Chem. Phys.* **1980**, *72*, 650.
[28] R. J. Bartlett, M. Musiał, *Rev. Mod. Phys.* **2007**, *79*, 291.
[29] D. I. Lyakh, M. Musiał, V. F. Lotrich, R. J. Bartlett, *Chem. Rev.* **2012**, *112*, 182.
[30] M. Nooijen, R. J. Bartlett, *J. Chem. Phys.* **1995**, *102*, 3629.
[31] J. F. Stanton, R. J. Bartlett, *J. Chem. Phys.* **1993**, *98*, 7029.
[32] T. Sommerfeld, U. V. Riss, H. D. Meyer, L. S. Cederbaum, B. Engels, H. U. Suter, *J. Phys. B: At. Mol. Opt. Phys.* **1998**, *31*, 4107.
[33] G. Jolicard, E. J. Austin, *Chem. Phys. Lett.* **1985**, *121*, 106.
[34] U. V. Riss, H. D. Meyer, *J. Phys. B: At. Mol. Opt. Phys.* **1993**, *26*, 4503.
[35] J. Muga, J. Palao, B. Navarro, I. Egusquiza, *Phys. Rep.* **2004**, *395*, 357.
[36] N. Moiseyev, *J. Phys. B: At. Mol. Opt. Phys.* **1998**, *31*, 1431.
[37] U. V. Riss, H. D. Meyer, *J. Phys. B: At. Mol. Opt. Phys.* **1998**, *31*, 2279.

Manuscript received: May 19, 2022

Revised manuscript received: September 7, 2022

Accepted manuscript online: September 10, 2022

Version of record online: October 18, 2022

Effect of charge and solvation shell on non-radiative decay processes in s-block cationic metal ion water clusters

Ravi Kumar ; Aryya Ghosh ; Nayana Vaval  

 Check for updates

J. Chem. Phys. 159, 054304 (2023)

<https://doi.org/10.1063/5.0153598>



View
Online



Export
Citation

CrossMark

Articles You May Be Interested In

Electron transfer mediated decay in HeLi₂ cluster: Potential energy surfaces and decay widths

J. Chem. Phys. (April 2019)

Electronic decay following ionization of aqueous Li + microsolvation clusters

J. Chem. Phys. (February 2005)

Entangled trajectory molecular dynamics in multidimensional systems: Two-dimensional quantum tunneling through the Eckart barrier

J. Chem. Phys. (July 2012)

23 August 2023 06:21:54

Webinar

Boost Your Signal-to-Noise
Ratio with Lock-in Detection



Sep. 7th – Register now



Zurich
Instruments

Effect of charge and solvation shell on non-radiative decay processes in s-block cationic metal ion water clusters

Cite as: J. Chem. Phys. 159, 054304 (2023); doi: 10.1063/5.0153598

Submitted: 10 April 2023 • Accepted: 14 July 2023 •

Published Online: 3 August 2023



View Online



Export Citation



CrossMark

Ravi Kumar,^{1,a)} Aryya Ghosh,^{2,b)} and Nayana Vaval^{1,a),c)}

AFFILIATIONS

¹Academy of Scientific and Innovative Research (AcSIR), Ghaziabad 201002, India

²Department of Chemistry, Ashoka University, Sonapat, Haryana 131029, India

^{a)}Also at: Physical and Materials Chemistry Division, CSIR-National Chemical Laboratory, Dr. Homi Bhabha Road, Pune, 411008, India.

^{b)}Electronic mail: aryya.ghosh@ashoka.edu.in

^{c)}Author to whom correspondence should be addressed: np.vaval@ncl.res.in

ABSTRACT

Intermolecular Coulombic decay or electron transfer-mediated decay are the autoionization processes through which a molecule can relax. This relaxation is only possible if the inner valence's ionization potential (IP) exceeds the system's double ionization potential (DIP). To study the effects of charge and solvation shell, we have calculated the IP, DIP values, and lifetime of Na-2s and Mg-2s temporary bound states in various optimized structures of Na⁺-(H₂O)_n and Mg²⁺-(H₂O)_n ($n = 1-5$) micro-solvated clusters, where n water molecules are distributed in a way that some are directly bound to the metal ion and the rest to the water molecules. The first and second solvation shells are the names for the former and the latter water-binding positions, respectively. For a given n , the lifetime of decaying states is longer when water molecules are in the second solvation shell. We found that the Mg-2p state can decay for all n values in Mg²⁺-(H₂O)_n clusters, whereas the Na-2p state's decay is possible for $n \geq 2$ in Na⁺-(H₂O)_n clusters. Our findings highlight the influence of metal ions' charge, different solvation shell structures, and the number of water molecules on the decay rate. These systems are relevant to the human body, which makes this study significant.

Published under an exclusive license by AIP Publishing. <https://doi.org/10.1063/5.0153598>

I. INTRODUCTION

In nature, we find various metal ions that act as catalysts and are necessary for enzymatic activity. A few metal ions play an essential role in many biological processes. Sodium and magnesium ions are two of a few (i.e., Na, Mg, K, Ca, Zn, Fe, Cu, etc.) that are essential for the human body. Studies¹⁻³ have shown that magnesium ions alone have been involved in more than 300 enzymatic systems as cofactors. For example, magnesium is required in the human body for making proteins, maintaining the health of muscles and neurons, controlling blood glucose levels, and promoting the structural development of bones. Additionally, magnesium aids in the active movement of calcium and potassium ions across cell membranes, which is necessary for the conduction of nerve impulses, the contraction of muscles, and a regular heartbeat. Magnesium also helps in adenosine triphosphate (ATP) production (the energy currency of the human body).

Three sodium and two potassium ions use this energy currency to move in and out of the cells. The Na⁺ ion is one of the main elements of the sodium-potassium pump in the human body. The Na⁺ ion also plays an important role in neural signaling⁴ and preventing brain disease.⁵ Studying non-radiative decay processes in micro-solvated clusters will provide insight into the chemistry involved in radiation damage in the human body.

Most of the human body's chemical and biological reactions occur in the liquid phase. However, studying the reactions in the liquid phase is more challenging than in the gaseous phase because of the large number of solvent molecules and weak interactions (solvent-solute and solvent-solvent weak interactions) between these large numbers of molecules in the liquid phase. However, understanding these weak interactions is essential for more accurate results. Thus, one can use the concept of micro-solvation, where calculations are performed in the gaseous phase using a few molecules

of solvent (at least up to the first solvation shell). Micro-solvation includes weak interactions, is not too computationally expensive, and provides good-quality results.

Our chosen study system is so versatile that many studies^{6–11} have been conducted. Most of these investigations target the spectra, thermal stability, and global minimum for the ground state structure of the clusters. Micro-solvated metal ions can serve as a valuable model for studying solution chemistry at the molecular level. These studies are essential for solvation chemistry, electron transfer, charge-induced reactivity, and other properties. However, only a few studies^{10,12} have explored the non-radiative decay process using micro-solvated cationic metal ion water systems. Non-radiative decay processes, characterized by the absence of radiation or photon emission, have short lifetimes in the femtosecond range, making them challenging to detect. Intermolecular or interatomic Coulombic decay^{13,14} (ICD) and electron transfer-mediated decay¹⁵ (ETMD) are examples of non-radiative decay processes. In ICD, the initial vacancy of the inner valence subshell is filled by an electron from the outer valence shell of the same molecule (molecule-A). The excess energy knocks out an electron from the nearby molecule's valence shell (molecule B). The A^+B^+ type of final state will be formed in ICD. Since there is a +1 charge on each molecule, the coulomb explosion will happen, leading molecules to move apart. On the contrary, in ETMD, an adjacent molecule's electron (the electron from molecule B) fills the initial vacancy. The energy released from this process knocks out an electron from the valence shell of neighboring molecules. In ETMD, the AB^{2+} and AB^+C^+ double ionized states will be the final states. For more details on non-radiative decay, you can see Fig. 1.

Recently, various factors^{7,14,16,17} that affect the non-radiative decay process have been studied, for example, the effects of protonation and deprotonation,^{16,18} bond length,^{19,20} polarization, different molecular environment effects,⁷ etc. Stumpf *et al.*²⁰ studied the decay width of the $Na^+(H_2O)_n$ ($n = 1, 4$), and $Mg^{2+}(H_2O)_m$ ($m = 1, 6$) clusters as a function of metal-oxygen distance and the number of nearest neighbors. They initiated their study with the optimized geometry of the cluster containing the highest number of water molecules, namely $Na^+(H_2O)_4$ and $Mg^{2+}(H_2O)_6$. They gradually removed one water molecule at a time while maintaining the high number of *cis*-pairs to retain the position and bond distance for subsequent geometries. There is no unique way to remove water molecules from these clusters; one can follow any method. However, removing the water molecules from various positions in a cluster will lead to different geometries. It is known that bond length⁷ and geometry affect the decay width. Using three different geometries of $Na^+(H_2O)_2$, our study shows that the position of the water molecules contributes significantly to the decay width. In this study, we have used the various optimized structures of $Na^+(H_2O)_n$ and $Mg^{2+}(H_2O)_n$ ($n = 1–5$) micro-solvated clusters, where the n water molecules are distributed such that some are directly bound to the metal ion and the rest to water molecules. We refer to the former arrangement as the first solvation shell and the latter as the second. Check Sec. III A for further details regarding different solvation shell structures. In this paper, our primary goal is to understand the influence of metal ions' charge, different solvation shell structures (water molecules positions), and the number of water molecules on the decay rate using $Na^+(H_2O)_n$ and $Mg^{2+}(H_2O)_n$ clusters. How all these factors affect the ionization potential

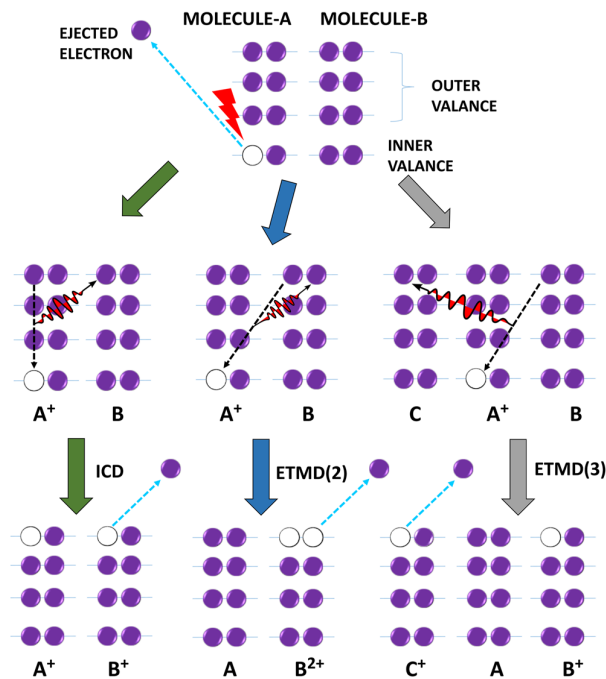


FIG. 1. Different types of non-radiative decay processes are represented visually. A vacancy in the inner valence shell (mainly in 2s orbitals) is created due to high-energy electron or x-ray bombardment. (a) In ICD, the vacancy is filled by a valence electron of molecule A, and the released energy will knock out molecule B's valence electron. The A^+B^+ type molecular state will be the final state. (b) In ETMD(2), an outer valence electron from the nearby molecule B fills an inner valence vacancy. The virtual photon will eject another valence electron from molecule B, resulting in the final molecular state of the AB^{2+} type. (c) In the ETMD(3) process, a neighboring molecule B's outer valence electron fills the hole in molecule A, and the virtual photon ejects a second electron from molecule C. The AB^+C^+ type molecular state will be the final state. In ETMD(2) and ETMD(3), 2 and 3 are the number of molecules involved in the ETMD process.

(IP) and double ionization potential (DIP) trends within clusters has also been studied.

II. COMPUTATIONAL METHODS

A. Fano approach for decay width

The metastable states generated via photoionization can decay through Auger decay, ICD, and ETMD. The decay happens through two-electron autoionization mechanisms; hence, these processes can belong to Feshbach-type resonance states. The characteristic of these metastable states is governed by the system's decay width Γ . According to Fano–Feshbach's theory, the resonance state can be described as a combination of bound and continuum states. The coupling between the bound and continuum parts of the resonance state gives us the decay width. The decay width Γ in this approach is provided by

$$\Gamma = 2\pi \sum_f |\langle \phi | H | \chi_{f,e} \rangle|^2, \quad (1)$$

where H is the total electronic Hamiltonian, f indicates open decay channels that belong to the continuum subspace, and ϵ is the asymptotic kinetic energy of the ICD/ETMD electron. To construct the bound and continuum parts of the resonance state, we have divided the Hilbert space into the Q subspace for bound configurations and the P subspace for continuum configurations. The P and Q subspaces would have to fulfill the following conditions: $P + Q = 1$ and $P * Q = 0$. We have obtained the bound part of the resonance state through the diagonalization of H projected on the Q subspace. The Q subspace included

$$QHQ|\phi\rangle = E_b|\phi\rangle. \quad (2)$$

We have obtained the continuum part of the resonance state through the diagonalization of H projected on the P subspace,

$$PHP|\chi_{f,\epsilon}\rangle = E_f|\chi_{f,\epsilon}\rangle. \quad (3)$$

The continuum states we obtained using Eq. (3) are not true continuums because the L^2 basis set has been used in our calculations. They show incorrect normalization and asymptotic behavior. Therefore, they are pseudo-continuums in nature. To obtain the correct normalization and accurate value of decay width, we have employed the Stieltjes imaging technique.²¹

For the construction of H , we have used the extended second-order algebraic diagrammatic construction [ADC(2)X] scheme of the Green's function [defined within the space spanned by the one-hole (1h) and two-hole one particle (2h1p) configurations]. In the ADC(2)X approach,^{22–25} the coupling between the 1h configurations is treated as the second order of perturbation theory. However, the coupling between 1h and 2h1p configurations and the coupling between 2h1p configurations are treated according to first-order perturbation theory. We considered the 2h1p configurations to construct the P subspace, representing the final double-ionized state with an outgoing free electron. In one hole block (part of the Q subspace), we include all occupied orbitals except for the core orbitals of the metal and oxygen atoms. The 2h1p configurations are partitioned in such a way that the ones that are open decay channels (i.e., DIPs lower than IP) are in the P subspace, and the rest are in the Q subspace. In this approach, we can get the total and partial decay widths. For details on the Fano-ADC method, please see Refs. 22–25.

III. RESULTS AND DISCUSSION

A. Cluster geometries and basis set

We must familiarize ourselves with the solvation shell's concept since we are examining its impact in this article. The solute's solvation shell refers to the number of water molecules (solvent molecules) surrounding the solute (a metal ion in our case). The distinction between these two structures (first and second solvation) lies in the positioning of water molecules within the cluster. In the first solvation shell structure, all the water molecules are directly connected to the metal ion. Conversely, in the second solvation shell structure, a few water molecules are not directly linked to the metal ion but rather connected to the water molecules of the first solvation shell. To denote the different solvation shell structures in our clusters, we use a general notation: $\text{Na}^+(\text{H}_2\text{O})_{p+q}$ and $\text{Mg}^{2+}(\text{H}_2\text{O})_{p+q}$, where p and q represent the number of water molecules in the first and second solvation shells, respectively. The sum of p and q is n ,

the total number of water molecules in any cluster. To illustrate this notation with examples of sodium-water clusters, let us consider the case when $n = 2$. The $\text{Na}^+(\text{H}_2\text{O})_{2+0}$ cluster denotes the first solvation shell geometry, where both water molecules directly interact with the Na^+ ion. On the other hand, $\text{Na}^+(\text{H}_2\text{O})_{1+1}$ is the second solvation shell geometry, where one water molecule is directly connected to Na^+ (present in the first solvation shell). The second water molecule is linked to the first water molecule or indirectly connected to a metal ion (making it part of the second solvation shell). Similarly, for $n = 3$, $\text{Na}^+(\text{H}_2\text{O})_{3+0}$ and $\text{Na}^+(\text{H}_2\text{O})_{2+1}$ are the first and second solvation geometries, respectively. Numerous structural possibilities⁹ exist for the first and second solvation shells when $n \geq 3$. We solely consider the lowest energy structure for each solvation shell.

The number of water molecules in the first solvation shell of the Na^+ ion is reported differently in different articles. You can find these studies in Ref. 9 and the references within it. The coordination number of the Na^+ ion in the gaseous phase is close to 4, while in bulk, it is between 5 and 6. This means that in the gaseous phase, the first solvation shell structure for $n \leq 4$ will be the lowest minimum structure, whereas the second solvation shell structure will be the lowest energy structure for $n \geq 5$ in $\text{Na}^+(\text{H}_2\text{O})_n$. As for $\text{Mg}^{2+}(\text{H}_2\text{O})_n$ clusters, the coordination number is close to 6. The Mg^{2+} 's coordination number in $\text{Mg}^{2+}(\text{H}_2\text{O})_n$ tells us that the first solvation shell structure will be the lowest minimum structure up to $n \leq 6$.

Geometries of $\text{Na}^+(\text{H}_2\text{O})_n$ and $\text{Mg}^{2+}(\text{H}_2\text{O})_n$ clusters were optimized using the Gaussian09 software package²⁶ with B3LYP^{27–30} functional and 6-311++g(2d,p) basis sets.³¹ Grimme's GD3 dispersion correction has been used while optimizing geometries. To ensure accurate results, we employed tight convergence criteria for optimizing all structures in our study. The maximum and RMS forces were constrained below 15×10^{-6} and 10×10^{-6} atomic units,

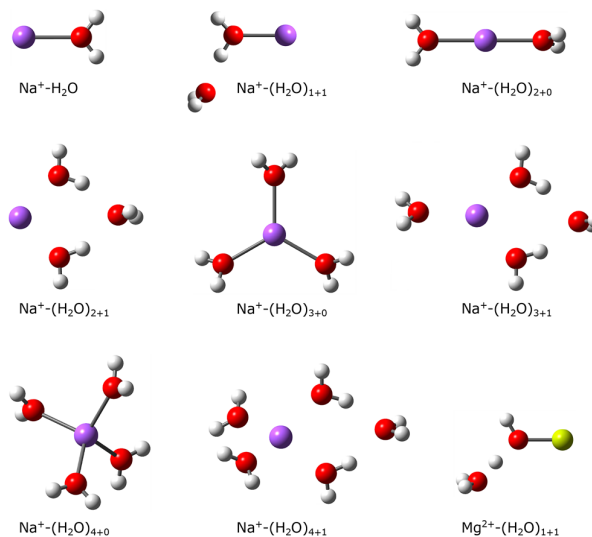


FIG. 2. Geometries of $\text{Mg}^{2+}(\text{H}_2\text{O})_{1+1}$ cluster and the first and second solvation shells of the $\text{Na}^+(\text{H}_2\text{O})_{n=1-5}$ clusters. Atom color code: yellow: magnesium, violet: sodium, red: oxygen, and white: hydrogen.

respectively, while the maximum and RMS displacements were limited to 60×10^{-6} and 40×10^{-6} atomic units. Symmetry was not enforced during the optimization process, allowing for unrestricted exploration of the cluster geometries. Figure 2 shows sodium-water clusters' optimized first and second solvation shell structures for different n values. The optimized geometries of magnesium-water clusters' are similar to the corresponding geometries of sodium-water clusters, except for the second solvation shell geometry when $n = 2$. The $\text{Mg}^{2+}-(\text{H}_2\text{O})_{1+1}$ geometry differs significantly from $\text{Na}^+-(\text{H}_2\text{O})_{1+1}$ even though both have the same symmetry, as depicted in the second and last geometries shown in Fig. 2. The bonding between two water molecules is different in both structures. In $\text{Mg}^{2+}-(\text{H}_2\text{O})_{1+1}$, because of the +2 charge of magnesium, the water molecule in the first solvation shell gets a partial charge, and the O–H bond becomes elongated, which is stabilized by the water in the second solvation shell. Considering the significance of symmetry in determining a cluster's geometry, let us delve into the symmetries observed in sodium and magnesium water clusters. Except for $p = 2$, where $\text{Na}^+-(\text{H}_2\text{O})_{2+0}$ and $\text{Mg}^{2+}-(\text{H}_2\text{O})_2$ exhibit D_2 and D_{2d} symmetries, respectively, the symmetries of $\text{Na}^+-(\text{H}_2\text{O})_{p+0}$ and $\text{Mg}^{2+}-(\text{H}_2\text{O})_{p+0}$ are identical for $p = 1, 3, \text{ and } 4$, which are C_{2v} , D_3 , and S_4 . Symmetries of $\text{Na}^+-(\text{H}_2\text{O})_{p+0}$ for $p = 5$ and 6 are C_1 and S_6 , whereas for $\text{Mg}^{2+}-(\text{H}_2\text{O})_{p+0}$ they are C_{2v} and T_H . The second solvation shell structures of sodium and magnesium-water clusters [$\text{Na}^+-(\text{H}_2\text{O})_{p+1}$ and $\text{Mg}^{2+}-(\text{H}_2\text{O})_{p+1}$] were also found to have the same symmetries. The symmetries are C_s for $p = 1$, C_{2v} for $p = 2$, C_2 for $p = 3$, and C_2 for $p = 4$. In the second solvation shell structure for $n = 6$, the $4 + 2$ structure type ($p = 4, q = 2$) has smaller energy than the $5 + 1$ type structure ($p = 5, q = 1$). D_{2d} is the symmetry for the $4 + 2$ type structure of Na^+ and Mg^{2+} water clusters. The coordinates of the $\text{Na}^+-(\text{H}_2\text{O})_n$ and $\text{Mg}^{2+}-(\text{H}_2\text{O})_n$ clusters first and second solvation geometries and the counterpoise correction [or basis set superposition error (BSSE)] for these structures are given in the supplementary material.

We have already discussed the basis for geometry optimization. The CAS-SCF³² and MS-CASPT2 methods^{33–35} have been used to calculate the IP and DIP in the MOLCAS 8.4 version.³⁶ We have used the cc-pVTZ basis³⁷ for the hydrogen atom, the aug-cc-pVTZ basis³⁷ for the oxygen atom, and the ANO-L basis³⁸ for Mg^{2+} and Na^+ metal ions. We have used the aug-cc-pVTZ basis set³⁷ for all chemical species (H, O, Na^+ , and Mg^{2+}) while computing IP values using the EOM-CCSD method.³⁹ We have used the FANO-ADC(2)X approach^{22–25} for the decay width calculations. Decay widths are very sensitive to the basis set. The accurate calculation of decay width requires a proper description of the continuum wave function. Therefore, we added 4s-type 4p-type 4d-type continuum-like basis functions (4s4p4d) to the cc-pVTZ basis set for oxygen and sodium atoms, and the cc-pVTZ basis set augmented by 1s1p1d functions is used for the hydrogen atom in $\text{Na}^+-(\text{H}_2\text{O})_{1-3}$ clusters. Basis function addition is done using the Kaufmann–Baumeister–Jungen (KBJ)⁴⁰ continuum-like basis function approach. Adding the extra functions will provide a good description of the pseudo-continuum. However, adding extra KBJ functions also increases the calculation's cost. Thus, one has to choose the basis set by keeping the cost of calculation and the result's accuracy in mind. Therefore, for the decay width calculation of $\text{Na}^+-(\text{H}_2\text{O})_{4,5}$ clusters, the cc-pVTZ basis set augmented with 2s2p KBJ continuum-like basis functions for oxygen, the cc-pVTZ basis set for hydrogen, and the cc-pVTZ basis

set plus 3s3p1d KBJ continuum-like basis functions for the sodium atom have been used. For $\text{Mg}^{2+}-(\text{H}_2\text{O})_{1-5}$ clusters, we have used the cc-pVTZ basis set for hydrogen, the cc-pCVTZ basis set + 2s2p KBJ functions for oxygen, and the cc-pCVTZ basis set⁴¹ + 3s3p1d KBJ functions for magnesium atoms.

B. Solvation shell's effect on IP and DIP of $\text{Na}^+-(\text{H}_2\text{O})_{1-5}$ and $\text{Mg}^{2+}-(\text{H}_2\text{O})_{1-5}$ clusters

It is well known that the core IP is dominated by relaxation, whereas the outer valence IP is governed by correlation. In the case of inner valence ionization, relaxation, and correlation⁴² both play an important role. In some cases, the interplay of these effects causes Koopmans' approximation⁴³ to fail. The inner valence ionized state in a surrounding environment has a finite lifetime and decays via ICD or ETMD. These decay processes form double-ionized states, resulting in significant reorganization and relaxation within the system. Shake-up states usually accompany the double ionization potentials, highlighting the importance of considering many-body effects in DIP calculations. There are two possibilities within double ionized states. First are the single site double ionized states (ss-DIP), where two holes are confined to a single site (A^+B or AB^{2+}). Second are two sited-doubly ionized states (ts-DIP), where two holes are localized on two different sites (A^+B^+ or AB^+C^+). You can see these two types of two-hole states in Fig. 1. The ss-DIP states are usually larger in energy than the ts-DIP states because two positive charges repel each other more strongly if they are on the same molecule rather than two different molecules. The ts-DIP states are usually responsible for the non-radiative decay process since they are likely to be smaller than the IP of the inner valence state. This implies that decay occurs only when the lowest DIP is smaller than the target state's IP. The count of DIPs smaller than the target state's IP provides the number of potential decay channels. The IPs (Na^+-2s , Na^+-2p , $\text{Mg}^{2+}-2s$, and $\text{Mg}^{2+}-2p$) and the lowest DIPs of $\text{Na}^+-(\text{H}_2\text{O})_{1-5}$ and $\text{Mg}^{2+}-(\text{H}_2\text{O})_{1-5}$ clusters are reported in Tables I and II, respectively. The CASSCF and MS-CASPT2 methods involve CAS-active space, which contains the number of active orbitals and active electrons. The details of the active space for $\text{Na}^+-(\text{H}_2\text{O})_n$ and $\text{Mg}^{2+}-(\text{H}_2\text{O})_n$ clusters are described in the supplementary material. To ensure the accuracy of the IP values obtained from the MS-CASPT2 method, we also performed IP calculations using the EOM-CCSD method. The trend observed in the IP values obtained from both methods is consistent. It also supports the reliability of the MS-CASPT2 results. However, it should be noted that calculating double ionization potentials (DIPs) using the EOM-CCSD method is computationally expensive. Consequently, we employed the MS-CASPT2 method to calculate the DIP values, as it balances accuracy and computational cost. One will need two different solvation shell structures to study the solvation shell effect. The construction of the first and second solvation shells requires a minimum of two water molecules. Therefore, we focused on the lowest energy structures of the first and second solvation for our study. For $\text{Na}^+-(\text{H}_2\text{O})_{2-4}$ and $\text{Mg}^{2+}-(\text{H}_2\text{O})_{2-4}$, we have studied two different geometries that correspond to the first and second solvations.

Tables I and II provide valuable insights, leading to the following observations: We will try to understand the reasons behind them.

TABLE I. It shows the ionization potentials (IP) of Na-2s and Na-2p and the lowest double ionization potential (DIP) in $\text{Na}^+(\text{H}_2\text{O})_n$, $n = 1, 5$ clusters. All the values are in eV. Note: The IP of Na-2s (78.3 eV) for $\text{Na}^+\text{-H}_2\text{O}$ is reported by Stumpf *et al.* using the ADC method.²⁰

Cluster	IP of Na-2s			IP of Na-2p			Lowest DIP MSCAS PT2
	CAS SCF	MSCAS PT2	EOM CCSD	CAS SCF	MSCAS PT2	EOM CCSD	
$\text{Na}^+\text{-H}_2\text{O}$	80.23	79.12	79.89	45.39	45.25	45.55	53.05
$\text{Na}^+(\text{H}_2\text{O})_{2+0}$	79.10	77.61	78.70	44.37	44.01	43.70	40.16
$\text{Na}^+(\text{H}_2\text{O})_{1+1}$	80.14	78.67	...	45.39	45.74	...	40.27
Geometry A ^a	80.27	78.93	...	45.48	45.56	...	38.34
$\text{Na}^+(\text{H}_2\text{O})_{3+0}$	78.00	76.46	77.17	43.27	42.45	42.26	39.08
$\text{Na}^+(\text{H}_2\text{O})_{2+1}$	78.80	77.55	...	44.06	43.78	...	39.79
$\text{Na}^+(\text{H}_2\text{O})_{4+0}$	77.04	75.96	75.84	42.35	42.32	41.01	38.27
$\text{Na}^+(\text{H}_2\text{O})_{3+1}$	77.75	76.42	...	44.06	42.71	...	38.35
$\text{Na}^+(\text{H}_2\text{O})_{4+1}$	76.76	75.29	...	42.18	41.91	...	37.13

^aFirst solvation geometrical arrangement with O–Na bond distances of the second solvation structure (see Fig. 3).

TABLE II. It shows the ionization potentials (IP) of Mg-2s and Mg-2p and the lowest double ionization potential (DIP) in $\text{Mg}^{2+}(\text{H}_2\text{O})_n$, $n = 1, 5$ clusters. All the values are in eV. Note: Mg-2s IP (115.3 eV) for $\text{Mg}^{2+}\text{-H}_2\text{O}$ is reported by Stumpf *et al.* using the ADC method.²⁰

Cluster	IP of Mg-2s			IP of Mg-2p			Lowest DIP MSCAS PT2
	CAS SCF	MSCAS PT2	EOM CCSD	CAS SCF	MSCAS PT2	EOM CCSD	
$\text{Mg}^{2+}\text{-H}_2\text{O}$	116.82	115.51	116.08	76.37	76.01	75.64	69.30
$\text{Mg}^{2+}(\text{H}_2\text{O})_{2+0}$	114.12	113.04	113.12	73.71	73.39	72.44	55.16
$\text{Mg}^{2+}(\text{H}_2\text{O})_{1+1}$	115.13	113.23	...	74.89	73.88	...	53.29
$\text{Mg}^{2+}(\text{H}_2\text{O})_{3+0}$	112.03	109.80	110.59	71.70	70.86	69.99	53.77
$\text{Mg}^{2+}(\text{H}_2\text{O})_{2+1}$	113.66	111.92	...	73.33	72.71	...	52.44
$\text{Mg}^{2+}(\text{H}_2\text{O})_{4+0}$	110.32	107.20	107.97	70.05	69.26	...	51.32
$\text{Mg}^{2+}(\text{H}_2\text{O})_{3+1}$	111.52	109.27	...	71.21	70.44	...	50.22
$\text{Mg}^{2+}(\text{H}_2\text{O})_{5+0}$	109.00	102.53	107.31	68.77	68.33	...	50.05
$\text{Mg}^{2+}(\text{H}_2\text{O})_{4+1}$	109.82	107.60	107.70	69.56	68.95	...	48.73

First, in sodium-water clusters, we observe a decreasing trend in IP values as the number of water molecules in the first solvation shell of the Na^+ ion increases. The decrease in effective nuclear charge (ENC) is the key here. As the number of water molecules in the first solvation shell of the Na^+ ion increases, the +1 charge of the Na^+ ion decreases. This is because the increasing number of water molecules facilitates greater charge transfer from the water molecules to the sodium ion. In other words, the water molecules effectively distribute the sodium's charge among themselves, leaving the sodium ions with a less positive charge. Natural bond order (NBO) analysis supports this hypothesis. It reveals the charge transfer between the water's lone pair and the sodium's 3s orbital stabilizes the system by 1.20 kcal/mol, $1.71 \times 2 = 3.42$ kcal/mol, $5.60 \times 3 = 16.80$ kcal/mol, and $7.68 \times 4 = 30.72$ kcal/mol for $n = 1$ to $n = 4$ in $\text{Na}^+(\text{H}_2\text{O})_n$,

respectively. Consequently, the effective nuclear charge (ENC) experienced by the sodium's electrons in $\text{Na}^+\text{-H}_2\text{O}$ is notably higher than that experienced in $\text{Na}^+(\text{H}_2\text{O})_4$, leading to a low ENC in the latter case. This lower ENC results in a low IP, since less energy is required to eject an electron. Therefore, the IP value decreases as water molecules increase in the Na^+ ion's first solvation shell in the sodium-water clusters. A similar trend is observed for $\text{Mg}^{2+}(\text{H}_2\text{O})_{n=1-5}$ clusters. Since the Mg atom has a +2 charge and the O–Mg bond distance is smaller than the O–Na bond distance, it promotes the charge transfer even more. Because of the larger charge on Mg than Na, the ENC felt by magnesium's electrons is higher than the electrons of sodium. As a result, we found that Mg-2s and Mg-2p's IP values are larger than Na-2s and Na-2p's IP values for a given value of n , respectively.

TABLE III. Shows the total decay width due to ICD and ETMD processes and the total lifetime of Na-2s TBS in $\text{Na}^+(\text{H}_2\text{O})_n$; $n = 1, 5$ clusters. Note: the O–Na Bond lengths are rounded-off to two decimal places.

Cluster	Solvation	O–Na bond Length (in Å)	Na-2s	
			Decay width Γ (in meV)	Lifetime τ (in fs)
$\text{Na}^+-\text{H}_2\text{O}$	First	2.24	113.97	5.78
Stumpf <i>et al.</i>	First	2.21	...	5.5 ^a
Stumpf <i>et al.</i>	First	2.30	...	7.0 ^a
$\text{Na}^+(\text{H}_2\text{O})_{2+0}$	First	2.26	302.89	2.17
Geometry-A ^b	First	2.18, 4.12	209.54	3.14
$\text{Na}^+(\text{H}_2\text{O})_{1+1}$	Second	2.18, 4.12	154.66	4.25
$\text{Na}^+(\text{H}_2\text{O})_{3+0}$	First	2.29	335.25	1.96
$\text{Na}^+(\text{H}_2\text{O})_{2+1}$	Second	2.23, 3.88	260.37	2.53
$\text{Na}^+(\text{H}_2\text{O})_{4+0}$	First	2.32	400.64	1.64
$\text{Na}^+(\text{H}_2\text{O})_{3+1}$	Second	2.27, 2.29, 3.98	325.23	2.02
Stumpf <i>et al.</i>	First	2.30	365.00	1.8 ^a
$\text{Na}^+(\text{H}_2\text{O})_{4+1}$	Second	2.32, 2.30, 4.05	419.73	1.57
Experimental		3.1 ^c

^aThe Fano-ADC-Stieltjes method is used for calculation with cc-pCVTZ + 2s2p2d1f KBJ basis for Na and O and cc-pVTZ + 1s1p1d KBJ basis for H.²⁰

^bFirst solvation geometry with different O–Na⁺ bond lengths (see Fig. 3).

^cExperimental value by Öhrwall *et al.* in aqueous solutions of NaCl (Ref. 44).

Second, we have observed that the Na-2s/Mg-2s and Na-2p/Mg-2p's IP values are larger in the second solvation structures than in the respective first solvation structures of sodium-water and magnesium-water clusters. To illustrate this, let us consider the example of the $\text{Na}^+(\text{H}_2\text{O})_2$ cluster. Two water molecules are directly connected to the metal ion in the first solvation shell ($\text{Na}^+(\text{H}_2\text{O})_{2+0}$), while only one is in the second solvation shell ($\text{Na}^+(\text{H}_2\text{O})_{1+1}$). As a result, in the first solvation shell, more charge transfer will occur between the oxygen's lone pair electrons and the sodium's 3s orbital than in the second solvation shell. Therefore, a metal ion's positive charge diffuses across two molecules in the first solvation shell, while in the second solvation shell, it diffuses over just one. As a result, the electrons of Na and Mg experience a larger ENC in their second solvation shell than in their first. Hence, the second solvation shell structures of $\text{Na}^+(\text{H}_2\text{O})_{2-4}$ and $\text{Mg}^{2+}(\text{H}_2\text{O})_{2-4}$ have larger IP values than the first. Third, we observed that the lowest DIP values decrease as the number of water molecules (n) increases. Once again, ENC plays a crucial role in this trend. Initially, all sodium-water clusters have a +1 charge. The two-hole final states formed after double ionization have a +3 total charge. This +3 charge will be on one sodium atom and one water molecule (two subunits) in $\text{Na}^+-\text{H}_2\text{O}$. In $\text{Na}^+(\text{H}_2\text{O})_5$, this +3 charge will be shared by one sodium atom and the five water molecules (six subunits). Therefore, cluster electrons will experience a drop in ENC as cluster size increases. This decrease in ENC leads to smaller DIP values as the cluster size increases. Fourth, we have observed that the decay of Na-2p is not possible in all sodium-water clusters, while the decay of Mg-2p is possible in all magnesium-water clusters. This is because the IP of Mg^{2+} is larger than the lowest DIP value of magnesium-

water clusters when $n = 1$, while the IP of Na^+ is not. The higher charge on the magnesium ion makes the IP larger, which allows the decay of Mg-2p to occur even when there is only one water molecule in the cluster. The decay of Na-2p, on the other hand, requires at least two water molecules to be present in the cluster.

C. Solvation shell's effect on lifetimes of Na-2s and Mg-2s TBSs

We have reported the total decay width (Γ) and lifetime (τ) of Na-2s and Mg-2s TBSs in $\text{Na}^+(\text{H}_2\text{O})_{1-5}$ and $\text{Mg}^{2+}(\text{H}_2\text{O})_{1-5}$ clusters, along with the O–Na⁺ and O–Mg²⁺ bond lengths, in Tables III and IV, respectively. We have compared our results with the theoretical calculations of Stumpf *et al.*²⁰ and with the Öhrwall *et al.*'s experimental value⁴⁴ of Na-2s and Mg-2s TBS's lifetime in NaCl and MgCl₂'s aqueous solutions. We observed that our calculated lifetime of Na-2s TBS in $\text{Na}^+-\text{H}_2\text{O}$ (5.78 fs) at 2.24 Å is in close agreement with the findings of Stumpf *et al.* (5.5 fs at 2.21 Å). They also report a decay width of 7.0 fs at 2.30 Å. The change in distance here (Stumpf *et al.*) is 0.09 Å, yet it brings a 21% change in decay width values. This demonstrates the high sensitivity of decay width values to even small changes in bond length. Despite this sensitivity of decay width values to changes in bond length, we have shown that the different positions of water molecules in a cluster can also affect the decay width. We will be discussing this in the upcoming point named observation number two.

From Tables III and IV, first, we observed that the decay width increases (or lifetime decreases) as the number of water molecules

TABLE IV. Shows the total decay width due to ICD and ETMD processes and the total lifetime of Mg-2s TBS in $\text{Mg}^{2+}-(\text{H}_2\text{O})_n$; $n = 1, 5$ clusters. Note: the O–Mg Bond lengths are rounded-off to two decimal places.

Cluster	Solvation	O–Mg bond Length (in Å)	Mg-2s	
			Decay width Γ (in meV)	Lifetime τ (in fs)
$\text{Mg}^{2+}-\text{H}_2\text{O}$ Stumpf <i>et al.</i>	First	1.93	261.33	2.52
	First	2.08	178	3.6 ^a
$\text{Mg}^{2+}-(\text{H}_2\text{O})_{2+0}$ $\text{Mg}^{2+}-(\text{H}_2\text{O})_{1+1}$	First	1.95, 1.95	442.82	1.49
	Second	1.84, 3.95	340.96	1.93
$\text{Mg}^{2+}-(\text{H}_2\text{O})_{3+0}$ $\text{Mg}^{2+}-(\text{H}_2\text{O})_{2+1}$	First	1.97	525.42	1.25
	Second	1.92, 3.41	391.99	1.68
$\text{Mg}^{2+}-(\text{H}_2\text{O})_{4+0}$ $\text{Mg}^{2+}-(\text{H}_2\text{O})_{3+1}$ Stumpf <i>et al.</i>	First	2.00	593.93	1.11
	Second	1.95, 1.98, 3.55	493.96	1.33
		2.08	560	1.17 ^a
$\text{Mg}^{2+}-(\text{H}_2\text{O})_{4+1}$	Second	1.99, 2.01, 3.66	515.81	1.28
Experimental			...	1.5 ^b

^aThe Fano-ADC-Stieltjes method is used for calculation with cc-pCVTZ + 2s2p2d1f KBJ basis for Mg and O and cc-pVTZ + 1s1p1d KBJ basis for H.²⁰

^bExperimental value by Öhrwall *et al.* in aqueous solutions of MgCl_2 (Ref. 44).

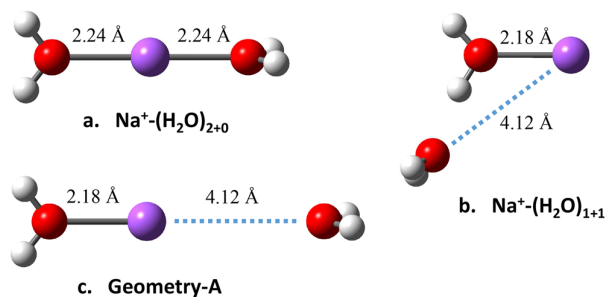
(n) grow^{45–47} within the first or second solvation shell in $\text{Na}^+(\text{H}_2\text{O})_n$ and $\text{Mg}^{2+}-(\text{H}_2\text{O})_n$ clusters. As n increases, the O– Na^+ and O– Mg^{2+} bond distances increase, and a larger bond distance typically leads to a longer lifetime. Surprisingly, we observed that the Na-2s TBS's lifetime decreases instead of increasing with increasing cluster size. It implies that the effect of an increased number of water molecules dominates over the bond length effect. The decrease in Na-2s/Mg-2s TBS's lifetime is due to the non-linear increase in the number of DIPs smaller than the targeted state's IP with increasing n values. Therefore, we observed a faster decay (or a shorter lifetime) of Na-2s/Mg-2s TBS with an increase in n in $\text{Na}^+(\text{H}_2\text{O})_n$ and $\text{Mg}^{2+}-(\text{H}_2\text{O})_n$.

Second, we have observed that Na-2s TBS's lifetime is longer in all the second solvation structures than its first one for a given n value. For example, the lifetime of Na-2s is longer in $\text{Na}^+(\text{H}_2\text{O})_{1+1}$ (4.26 fs) than in $\text{Na}^+(\text{H}_2\text{O})_{2+0}$ (2.17 fs). These two geometries have the same number of water molecules but differ in the position of the water molecules and the O–Na bond distances. Since the number of possible decay channels is almost identical in both cases, the reason can only be explained based on the O–Na bond distance and the different positions of water molecules. There is one more factor that can affect the Na-2s TBS's lifetime, and that is the type of non-radiative decay process. In $\text{Na}^+(\text{H}_2\text{O})_{1+1}$, ICD could be the dominant channel while ETMD could be in $\text{Na}^+(\text{H}_2\text{O})_{2+0}$ or vice versa. To investigate this further, we have done the partial decay width calculations reported in Table V. The partial decay width calculations reveal that ICD and ETMD decay processes are ~ 1.9 and 2.7 times faster in $\text{Na}^+(\text{H}_2\text{O})_{2+0}$ than in $\text{Na}^+(\text{H}_2\text{O})_{1+1}$, respectively. However, ICD is the dominant decay channel in both geometries. Now the question is: what affects the Na-2s TBS's lifetime more: the position of water molecules or the O–Na bond

distance? To address this, we have studied one more geometry of sodium-water cluster for $n = 2$, named geometry-A. The geometry-A has similar water positions as the first solvated shell structure, while the two O–Na bond lengths are the same as the second solvated structure. See Fig. 3 for a clear understanding. The importance of geometry-A is that the comparison of Na-2s TBS's lifetime in geometry-A with that in the $\text{Na}^+(\text{H}_2\text{O})_{2+0}$ will provide the effect of bond length on the Na-2s TBS's lifetime because the difference in both geometries is of the O–Na bond lengths while the position of water molecules is the same in both cases. Let us call it condition-1. Furthermore, comparing the Na-2s TBS's lifetime in geometry-A with that in the $\text{Na}^+(\text{H}_2\text{O})_{1+1}$ cluster will provide the effect of position on Na-2s TBS's lifetime because the difference in both geometries is due to the different water molecular positions, while the O–Na bond length is the same in both cases. Let us call it condition-2. The Na-2s TBS's lifetimes are 2.17, 4.25, and 3.14 fs in $\text{Na}^+(\text{H}_2\text{O})_{2+0}$, $\text{Na}^+(\text{H}_2\text{O})_{1+1}$ and geometry-A, respectively. The difference in Na-2s TBS's lifetime in condition-1 and 2 are 0.97 and 1.11 fs, respectively. This clarifies that the effect of the positions of water molecules (1.11 fs) is slightly larger than the effect of bond length (0.97 fs) on Na-2s TBS's lifetime. Therefore, we have concluded that the effect of the second water's position (or geometric effect) is more important than the bond length effect. Let us see the detailed analysis of partial decay widths. Table V presents the partial decay widths for the three geometries of the $\text{Na}^+(\text{H}_2\text{O})_2$ cluster. It is observed that the influence of bond length and water molecule position on the decay width varies across different channels. In particular, in the $\text{Na}_{2p}^+\text{O}_{2p}^+$ channel, the change attributed to bond length exceeds that of the position change. Conversely, in the $\text{Na}_{2p}^+\text{H}_1^+$ and $\text{O}_{2p}^+\text{O}_{2p}^+$ channels, the position change exhibits a larger impact on the decay width compared to the bond length change. Our analysis

TABLE V. Partial decay widths (for ICD and ETMD) of the Na-2s ionized state in various geometries (see Fig. 3) of $\text{Na}^+(\text{H}_2\text{O})_n$ clusters for $n = 2$.

Decay type	Decay channels	Decay width (in meV)		
		$\text{Na}^+(\text{H}_2\text{O})_{2+0}$	Geometry-A	$\text{Na}^+(\text{H}_2\text{O})_{1+1}$
ICD	$\text{Na}_{2p}^+ \text{O}_{2p}^+$	262.7	149.00	139.33
ICD	$\text{Na}_{2p}^+ \text{H}_{1s}^+$	24.20	31.97	13.06
ETMD	$\text{O}_{2s}^+ \text{O}_{2p}^+$	5.84	3.25	2.26
ETMD	$\text{O}_{2p}^+ \text{O}_{2p}^+$	0.81	1.5	0.59

**FIG. 3.** Geometries of the first [shown by (a)] and second solvation shells [shown by (b)] for $n = 2$ in $\text{Na}^+(\text{H}_2\text{O})_n$ clusters. (c) Shows the geometry-A, formed by changing the O-Na bond distances of the first solvation shell structures. The O-Na bond lengths of geometry-A are equal to those in the second solvation shell structure. A decay width (or lifetime) comparison between (a) and (c) provides the effect of bond length on decay width. In contrast, comparing (b) and (c) offers the impact of position on decay width. A decay width comparison among these geometries helps us understand what affects the lifetime of Na-2s TBS more: the O-Na bond length or the position of the water molecule. Atom color code: violet: sodium; red: oxygen; and white: hydrogen.

focuses on the first two ICD channels since these channels dominate the decay process in these three geometries. Conclusively, the contribution of different positions of water molecules to the total decay width outweighs the change resulting from bond length alterations. To address why the lifetime of Na-2s/Mg-2s TBS is longer in the second solvation shell structures than in the first solvation shell structures, we have calculated the transition dipole moment because the decay width is proportional to the transition dipole moment.^{48,49} The transition dipole moment values have been calculated using the EOM-CCSD method with the aug-cc-pVDZ basis sets for $n = 2$ (as an example case) in the sodium water cluster's first and second solvation shell structures. The left and right eigenvectors were obtained by diagonalizing the one-hole block of the Hamiltonian matrix generated using the EOMCCSD method. The transition dipole moment is calculated for the dominant decay channel only. The calculated transition dipole moment values from $\text{Na}(2p)$ to $\text{O}(2p)$ are 0.123 717 and 0.091 239 a.u. in the first and second solvation shell structures, respectively. A large value of the transition dipole moment implies that the jumping of an electron between two orbitals is fast. It means the vacancy generated during the decay process can be filled more quickly in the first solvation shell, leading to quicker decay. That is why we have observed a larger decay width (or a shorter lifetime) for the first solvation shell structures than for the second ones. Third,

an interesting trend emerges if we compare the lifetime values of TBSs in sodium-water (5.78 to 1.64 fs) and magnesium-water clusters (2.52 to 1.11 fs). The lifetime values are dropping at a faster rate in the sodium-water clusters than in the magnesium-water clusters. It says that due to a higher charge on magnesium ions than sodium ions, the decay will be slower in the magnesium water cluster than in the sodium water cluster. Fourth, we also observe that the difference in the decay width between the first and second solvations gradually reduces with the increase in water molecules. For example, Na-2s TBS's lifetime increases by 96% in $\text{Na}^+(\text{H}_2\text{O})_{1+1}$ compared to $\text{Na}^+(\text{H}_2\text{O})_{2+0}$, whereas the increase from first to second solvation is only 29% and 10% for $n = 3$ and 4, respectively. We know that the solvation shell number of sodium-ions is close to 4 in the gas phase. Therefore, a difference in Na-2s TBS's lifetime in $\text{Na}^+(\text{H}_2\text{O})_{4+1}$ (1.64 fs) and $\text{Na}^+(\text{H}_2\text{O})_4$ (1.57 fs) will tell us about the effect of the solvation shell on the decay rate. In this case, Na-2s TBS's lifetime difference is 0.07 fs (4.5%), indicating that the change in the solvation shell (from first to second) affects the decay rate in a minimal way. Similar results were also observed in the study of rare gas clusters by Fasshauer *et al.*^{50,51} They showed that, apart from its nearest neighbors, the second shell also contributes to an observable second peak in the spectrum of ICD electrons. However, it has little impact on the total decay width (the same as our results).

In $\text{Na}^+(\text{H}_2\text{O})_4$, the lifetime of Na-2s TBS in our results (1.64 fs) and Stumpf *et al.*'s (1.80 fs) theoretical results agree well with each other. However, it is much lower than the experimental value (3.0 fs). The difference between theoretical and experimental values is due to experimental and computational errors. The experimental errors can be due to the averaging of numerous possible structures, while the Fano-ADC method also has its limitations that introduce some errors.

IV. CONCLUSIONS

In this article, we have studied the effect of solvation shells on ionization potential (IP), double ionization potential (DIP), and a lifetime of 2s ionized states using $\text{Na}^+(\text{H}_2\text{O})_{n=1-5}$ and $\text{Mg}^{2+}(\text{H}_2\text{O})_{n=1-5}$ clusters as the test systems. We have specifically looked at the impact of several variables on the lifetime of Na-2s/Mg-2s TBS, including the number of water molecules present, effect of solvation shell, and metal ion's charge. The decay width has been calculated using the Fano-ADC(2)X method, whereas the CAS-SCF, MS-CASPT2, and EOM-CCSD methods have been used to report the system's IP. The lowest DIPs are reported using the MS-CASPT2 method.

Conclusions related to IP and DIP are as follows: First, the IP of inner valence (Na-2s, Na-2p, Mg-2s, and Mg-2p) and the lowest DIP values decrease as the number of water molecules increases. The decrease in IP and DIP values with increased cluster size is due to a reduction in the effective nuclear charge (ENC). Second, we observed that the IP values would decrease continuously even after attaining the first solvation shell. However, the decrease in IP will be marginal after achieving the first solvation shell. Third, the IP of Na-2s and Mg-2s in the second solvation shell of sodium-water and magnesium-water clusters is larger than its corresponding first solvation shell. That is due to the direct connection of water molecules in the first solvation shell, which stabilizes the positive charge on metal ions and decreases the ENC. Fourth, the decay of Mg-2p occurs even when only one water molecule exists in the cluster. On the other hand, the decay of Na-2p requires at least two water molecules to be present in the cluster.

Conclusions related to the lifetime of TBSs in sodium-water and magnesium-water clusters are as follows: (a) We observe that the lifetime of the TBS decreases as the number of water molecules (n) increases. This is surprising because the increase in the oxygen-metal bond length, which occurs with increasing n , typically leads to a longer lifetime. However, our results suggest that the effect of the number of water molecules dominates over the effect of bond length on the lifetime of the TBS. This is because additional water molecules increase the number of decay channels, leading to a shorter lifetime. (b) The lifetime of Na-2s/Mg-2s TBS is longer in the second solvated shell structures than in their respective first ones. For example, Na-2s TBS's lifetime is longer in $\text{Na}^+(\text{H}_2\text{O})_{1+1}$ (4.25 fs) than in $\text{Na}^+(\text{H}_2\text{O})_{2+0}$ (2.17 fs). That is due to two reasons. (i) There is a huge increase in one of the O–Na bond lengths in $\text{Na}^+(\text{H}_2\text{O})_{1+1}$, which decreases the decay rate in the second solvation shell structure. (ii) The transition dipole moments for the first solvation were higher than those for the second solvation shell, resulting in faster decay in the first solvation shell structure. (c) A difference in Na-2s TBS's lifetime in $\text{Na}^+(\text{H}_2\text{O})_{4+1}$ (1.64 fs) and $\text{Na}^+(\text{H}_2\text{O})_4$ (1.57 fs) will tell us about the effect of the solvation shell on the decay rate. This difference in lifetime is 0.07 fs (4.5%), indicating that the solvation shell's impact will be minimal after attaining the first solvation shell. (d) Fourth, the lifetime of TBSs decreases faster in sodium-water clusters (5.78 to 1.64 fs) than in magnesium-water clusters (2.52 to 1.11 fs). The lifetime values are dropping more quickly in the sodium-water clusters than in the magnesium-water clusters. This is because of the higher charge on the magnesium ion than the sodium ion, which slows down the decay process. (e) The lifetime of Na-2s TBS is longer than that of the Mg-2s TBS's lifetime in their corresponding clusters. For example, the lifetime of Na-2s TBS in $\text{Na}^+\text{-H}_2\text{O}$ (5.78 fs) is longer than Mg-2s TBS in $\text{Mg}^{2+}\text{-H}_2\text{O}$ (2.47 fs). The reasons for this could be: (i) The number of decay channels is higher in magnesium-water clusters than in sodium-water clusters; (ii) the metal-oxygen bond lengths are smaller for magnesium-water clusters than sodium-water clusters; and (iii) the charge of the metal ion.

SUPPLEMENTARY MATERIAL

Supplementary data include optimized coordinates of $\text{Na}^+(\text{H}_2\text{O})_n$ and $\text{Mg}^{2+}(\text{H}_2\text{O})_n$ clusters with basis set superposition error

(BSSE) or counterpoise correction for each cluster and the CAS active space information for IP and DIP calculations.

ACKNOWLEDGMENTS

R.K. acknowledges financial support from the Council of Scientific and Industrial Research (CSIR). The authors acknowledge the computational facilities at the CSIR-National Chemical Laboratory and Ashoka University. A.G. acknowledges financial support from SERB (Grant No. SRG/2022/001115).

AUTHOR DECLARATIONS

Conflict of Interest

The authors have no conflicts to disclose.

Author Contributions

Ravi Kumar: Data curation (equal); Formal analysis (equal); Investigation (equal); Writing – original draft (equal). **Aryya Ghosh:** Data curation (equal); Methodology (equal); Software (equal); Writing – review & editing (equal). **Nayana Vaval:** Conceptualization (equal); Software (equal); Supervision (equal); Validation (equal); Writing – review & editing (equal).

DATA AVAILABILITY

The data that support the findings of this study are available within the article and its supplementary material.

REFERENCES

- 1 D. H. H. M. Viering, J. H. F. de Baaij, S. B. Walsh, R. Kleta, and D. Bockenbauer, *Pediatr. Nephrol.* **32**, 1123–1135 (2017).
- 2 R. Swaminathan, *Clin. Biochem. Rev.* **24**(2), 47–66 (2003).
- 3 M. Horowitz, A. M. Al Alawi, S. W. Majoni, and H. Falhammar, *Int. J. Endocrinol.* **2018**, 9041694.
- 4 M. D. Forrest, *Front. Physiol.* **5**, 472 (2014).
- 5 M. V. Clausen, F. Hilbers, and H. Poulsen, *Front. Physiol.* **8**, 371 (2017).
- 6 J. S. Rao, T. C. Dinadayalane, J. Leszczynski, and G. N. Sastry, *J. Phys. Chem. A* **112**, 12944–12953 (2008).
- 7 R. Kumar, A. Ghosh, and N. Vaval, *J. Chem. Theory Comput.* **18**, 807–816 (2022).
- 8 B. Hartke, A. Charvat, M. Reich, and B. Abel, *J. Chem. Phys.* **116**, 3588–3600 (2002).
- 9 J. J. Fifen and N. Agmon, *J. Chem. Theory Comput.* **12**, 1656–1673 (2016).
- 10 T. Miteva, J. Wenzel, S. Klaiman, A. Dreuw, and K. Gokhberg, *Phys. Chem. Chem. Phys.* **18**, 16671–16681 (2016).
- 11 P. Wang, R. Shi, Y. Su, L. Tang, X. Huang, and J. Zhao, *Front. Chem.* **7**, 624 (2019).
- 12 V. Stumpf, K. Gokhberg, and L. S. Cederbaum, *Nat. Chem.* **8**, 237–241 (2016).
- 13 L. S. Cederbaum, J. Zobeley, and F. Tarantelli, *Phys. Rev. Lett.* **79**, 4778 (1997).
- 14 T. Jahnke, U. Hergenbahn, B. Winter, R. Dörner, U. Fröhling, P. V. Demekhin, K. Gokhberg, L. S. Cederbaum, A. Ehresmann, A. Knie, and A. Dreuw, *Chem. Rev.* **120**, 11295–11369 (2020).
- 15 J. Zobeley, R. Santra, and L. S. Cederbaum, *J. Chem. Phys.* **115**, 5076 (2001).
- 16 R. Kumar and N. Vaval, *ChemPhysChem* **24**, e202200340 (2023).
- 17 J. L. Hemmerich, R. Bennett, and S. Y. Buhmann, *Nat. Commun.* **9**, 2934 (2018).

- ¹⁸N. V. Kryzhevoi and L. S. Cederbaum, *Angew. Chem., Int. Ed.* **50**, 1306 (2011).
- ¹⁹A. Ghosh and N. Vaval, *J. Chem. Phys.* **141**, 234108 (2014).
- ²⁰V. Stumpf, C. Brunken, and K. Gokhberg, *J. Chem. Phys.* **145**, 104306 (2016).
- ²¹W. P. Reinhardt, *Comput. Phys. Commun.* **17**, 1–21 (1979).
- ²²P. Kolorenč, V. Averbukh, K. Gokhberg, and L. S. Cederbaum, *J. Chem. Phys.* **129**, 244102 (2008).
- ²³V. Averbukh and L. S. Cederbaum, *J. Chem. Phys.* **123**, 204107 (2005).
- ²⁴P. Kolorenč and V. Averbukh, *J. Chem. Phys.* **152**, 214107 (2020).
- ²⁵V. Averbukh and L. S. Cederbaum, *J. Chem. Phys.* **125**, 094107 (2006).
- ²⁶M. J. Frisch, G. W. Trucks, H. B. Schlegel, G. E. Scuseria, M. A. Robb, J. R. Cheeseman, G. Scalmani, V. Barone, B. Mennucci, G. A. Petersson, H. Nakatsuji, M. Caricato, X. Li, H. P. Hratchian, A. F. Izmaylov, J. Bloino, G. Zheng, J. L. Sonnenberg, M. Hada, M. Ehara, K. Toyota, R. Fukuda, J. Hasegawa, M. Ishida, T. Nakajima, Y. Honda, O. Kitao, H. Nakai, T. Vreven, J. A. Montgomery, J. E. Peralta, F. Ogliaro, M. Bearpark, J. J. Heyd, E. Brothers, K. N. Kudin, V. N. Staroverov, R. Kobayashi, J. Norm, K. Raghavachari, A. Rendell, J. C. Burant, S. S. Iyengar, J. Tomasi, M. Cossi, N. Rega, J. M. Millam, M. Klene, J. E. Knox, J. B. Cross, V. Bakken, C. Adamo, J. Jaramillo, R. Gomperts, R. E. Stratmann, O. Yazyev, A. J. Austin, R. Cammi, C. Pomelli, J. W. Ochterski, R. L. Martin, K. Morokuma, V. G. Zakrzewski, G. A. Voth, P. Salvador, J. J. Dannenberg, S. Dapprich, A. D. Daniels, O. Farkas, J. B. Foresman, J. V. Ortiz, J. Cioslowski, and D. J. Fox, Gaussian-09, Gaussian, Inc., Wallingford, CT, 2009.
- ²⁷P. J. Stephens, F. J. Devlin, C. F. Chabalowski, and M. J. Frisch, *J. Phys. Chem.* **98**, 11623–11627 (1994).
- ²⁸A. D. Becke, *J. Chem. Phys.* **98**, 5648–5652 (1993).
- ²⁹C. Lee, W. Yang, and R. G. Parr, *Phys. Rev. B* **37**, 785–789 (1988).
- ³⁰S. H. Vosko, L. Wilk, and M. Nusair, *Can. J. Phys.* **58**, 1200–1211 (1980).
- ³¹R. Krishnan, J. S. Binkley, R. Seeger, and J. A. Pople, *J. Chem. Phys.* **72**, 650–654 (1980).
- ³²B. O. Roos, P. R. Taylor, and P. E. M. Sigbahn, *Chem. Phys.* **48**, 157–173 (1980).
- ³³K. Andersson, P. Å. Malmqvist, B. O. Roos, A. J. Sadlej, and K. Wolinski, *J. Phys. Chem.* **94**, 5483–5488 (1990).
- ³⁴H.-J. Werner and P. J. Knowles, *J. Chem. Phys.* **82**, 5053–5063 (1985).
- ³⁵K. Andersson, P. Å. Malmqvist, and B. O. Roos, *J. Chem. Phys.* **96**, 1218–1226 (1992).
- ³⁶F. Aquilante, J. Autschbach, R. K. Carlson, L. F. Chibotaru, M. G. Delcey, L. De Vico, I. Fdez Galván, N. Ferré, L. M. Frutos, L. Gagliardi, M. Garavelli, A. Giussani, C. E. Hoyer, G. Li Manni, H. Lischka, D. Ma, P. Å. Malmqvist, T. Müller, A. Nenov, M. Olivucci, T. B. Pedersen, D. Peng, F. Plasser, B. Pritchard, M. Reiher, I. Rivalta, I. Schapiro, J. Segarra-Martí, M. Stenrup, D. G. Truhlar, L. Ungur, A. Valentini, S. Vancoillie, V. Velyazov, V. P. Vysotskiy, O. Weingart, F. Zapata, and R. Lindh, *J. Comput. Chem.* **37**, 506–541 (2016).
- ³⁷T. H. Dunning, *J. Chem. Phys.* **90**, 1007–1023 (1989).
- ³⁸P.-O. Widmark, B. J. Persson, and B. O. Roos, *Theor. Chim. Acta* **79**, 419–432 (1991).
- ³⁹J. F. Stanton and J. Gauss, *J. Chem. Phys.* **103**, 1064–1076 (1995).
- ⁴⁰K. Kaufmann, W. Baumeister, and M. Jungen, *J. Phys. B: At., Mol. Opt. Phys.* **22**, 2223–2240 (1989).
- ⁴¹K. L. Schuchardt, B. T. Didier, T. Elsethagen, L. Sun, V. Gurumoorthi, J. Chase, J. Li, and T. L. Windus, *J. Chem. Inf. Model.* **47**, 1045–1052 (2007).
- ⁴²L. S. Cederbaum, W. Domcke, J. Schirmer, and W. V. Niessen, *Adv. Chem. Phys.* (John Wiley & Sons, Ltd., 1986), Chap. 3, pp. 115–159.
- ⁴³J. C. Phillips, *Phys. Rev.* **123**, 420–424 (1961).
- ⁴⁴G. Öhrwall, N. Ottosson, W. Pokapanich, S. Legendre, S. Svensson, and O. Björneholm, *J. Phys. Chem. B* **114**, 17057–17061 (2010).
- ⁴⁵N. Vaval and L. S. Cederbaum, *J. Chem. Phys.* **126**, 164110 (2007).
- ⁴⁶G. Öhrwall, M. Tchapyguine, M. Lundwall, R. Feifel, H. Bergersen, T. Rander, A. Lindblad, J. Schulz, S. Peredkov, S. Barth, S. Marburger, U. Hergenhahn, S. Svensson, and O. Björneholm, *Phys. Rev. Lett.* **93**, 173401 (2004).
- ⁴⁷C. Küstner-Wetekam, L. Marder, D. Bloß, C. Honisch, N. Kiefer, C. Richter, S. Rubik, R. Schaf, C. Zindel, M. Förstel, K. Gokhberg, A. Knie, U. Hergenhahn, A. Ehresmann, P. Kolorenč, and A. Hans, *Commun. Phys.* **6**, 50 (2023).
- ⁴⁸E. Fasshauer, *J. Chem. Phys.* **152**, 224307 (2020).
- ⁴⁹L. S. Cederbaum and A. I. Kuleff, *Nat. Commun.* **12**, 4083 (2021).
- ⁵⁰E. Fasshauer, *New J. Phys.* **18**, 043028 (2016).
- ⁵¹E. Fasshauer, M. Förstel, S. Pallmann, M. Pernpointner, and U. Hergenhahn, *New J. Phys.* **16**, 103026 (2014).